Investigating the molecular and physiological roles of BUD23-dependent protein translation

Maria Voronkov

St. Cross College

University of Oxford

A thesis submitted for the degree of

Doctor of Philosophy

Michaelmas 2021

Acknowledgements

This work was funded by the Medical Research Council and the Radcliffe Department of Medicine.

I would like to thank my supervisory team - Prof. David Ray, Prof. Leanne Hodson, Prof. David Bechtold and Dr. Matthew Baxter - for their guidance over the years.

I would also like thank all my colleagues for their assistance, and for many sources of laughter over the years.

Outside of the academic world, I am eternally grateful to my family and friends, who kept me somewhat sane while I wrote this manuscript.

Preface

Whilst this thesis is written as 'we', all data and analysis presented are my own work unless otherwise stated.

Abstract

The human ribosome is extensively modified, containing at least 288 distinct modification sites. Current literature suggests that most ribosomal modifications serve to stabilise the tertiary structure of the ribosome, however this fails to explain why ribosomal RNA (rRNA) modifications tend to cluster in functionally important regions that are vital for translation. Their spatial organisation and high level of conservation throughout all eukaryotes strongly suggest that rRNA modifications are instead responsible for the regulation of ribosomal function. BUD23 is a putative methyltransferase that is responsible for modifying a key residue on the small ribosomal subunit. It also has a second independent function in small ribosomal subunit biogenesis, where its presence is essential for correct ribosomal maturation. While BUD23's role in small ribosomal subunit maturation has been well characterised, studies have failed to determine any functional consequences of its methylation activity. This has led to the idea that the methylation event may be non-essential, or is imparted simply as a quality control marker. Over the course of this project, I aimed to investigate the role of BUD23, with particular focus on the *in vivo* consequences of its function.

By generating two unique mouse models of BUD23, I have established that BUD23 attenuates mitochondrial and metabolic function, and have implicated that this is as a result of its methylation activity. In addition, I have generated a homology model of human BUD23 to explore the mechanisms underlying its core functions, and point to a functional purpose for the existence of the methyl mark on the small ribosomal subunit. Overall, this thesis implicates that BUD23 is responsible for the regulation of tissue and organismal energy balance in a highly selective manner, promoting a selective translational advantage to metabolic transcripts. Its loss has profound implications, resulting in global metabolic defects as a consequence of ribosomal failure.

Contents

List of Figures

1 Introduction

Contents

The human ribosome is heavily modified, constituting the second most modified type of RNA (Sloan et al., 2017). To date, 288 distinct modification sites have been identified (Fig. 1.1; Taoka et al., 2018), which equates to approximately 2% of all ribosomal RNA (rRNA) nucleotides. Modification of nucleotides is a common

occurrence, and has been identified across all three phylogenetic kingdoms (Cantara et al., 2011). While it is generally accepted that most rRNA modifications serve to stabilise the ribosome, aiding in forming its tertiary structure (Polikanov et al., 2015), many studies have hypothesised that rRNA modifications may serve a much greater role.

rRNA modifications tend to occupy functionally important sites, such as the transfer RNA (tRNA) binding sites and the decoding site of the ribosome, which are essential to the correct function of translational machinery. In addition, modifications are under high conservative stress, suggesting that they should encompass a more central function than simply assisting with stability. Recent studies have identified that not all rRNA modifications show full penetrance, and instead their expression is heterogeneous (Andersen et al., 2004; Birkedal et al., 2014; Taoka et al., 2016). This provided the first look into how modification of nucleotides could potentially be altered in a dynamic fashion, providing a mechanism by which they could attenuate translation in response to a wide array of context-driven stimuli, such as time of day, or even by subcellular location.

This unexplored aspect of translational control poses an exciting field in which to learn more about the mechanisms governing cellular protein production. Over the course of this thesis, the effect of rRNA modifications on ribosomal function is studied in greater detail. In particular, the physiological and mechanistic roles of BUD23, a methyltransferase responsible for modification of the small ribosomal subunit, are explored.

1.1 Epigenetics and modifications

Although little is known about the functions of rRNA modifications, modifications of other nucleic and amino acid residues provide cells with the ability to adapt rapidly to changes in their environment and to regulate biological processes in a dynamic fashion (Morgan et al., 2005). While all the cells within an organism contain the same genetic code, the way this information is used varies from cell to

cell without any alteration to the primary DNA sequence (Portela & Esteller, 2010). Instead, plasticity is introduced via the differential regulation of gene expression through a process termed 'epigenetics' (Waddington, 1956). Thus processes such as development, differentiation and physiology can be controlled (Li, 2002; Ringrose & Paro, 2004; Reik, 2007).

Post-translation modifications (PTMs) add another level of malleability to cells

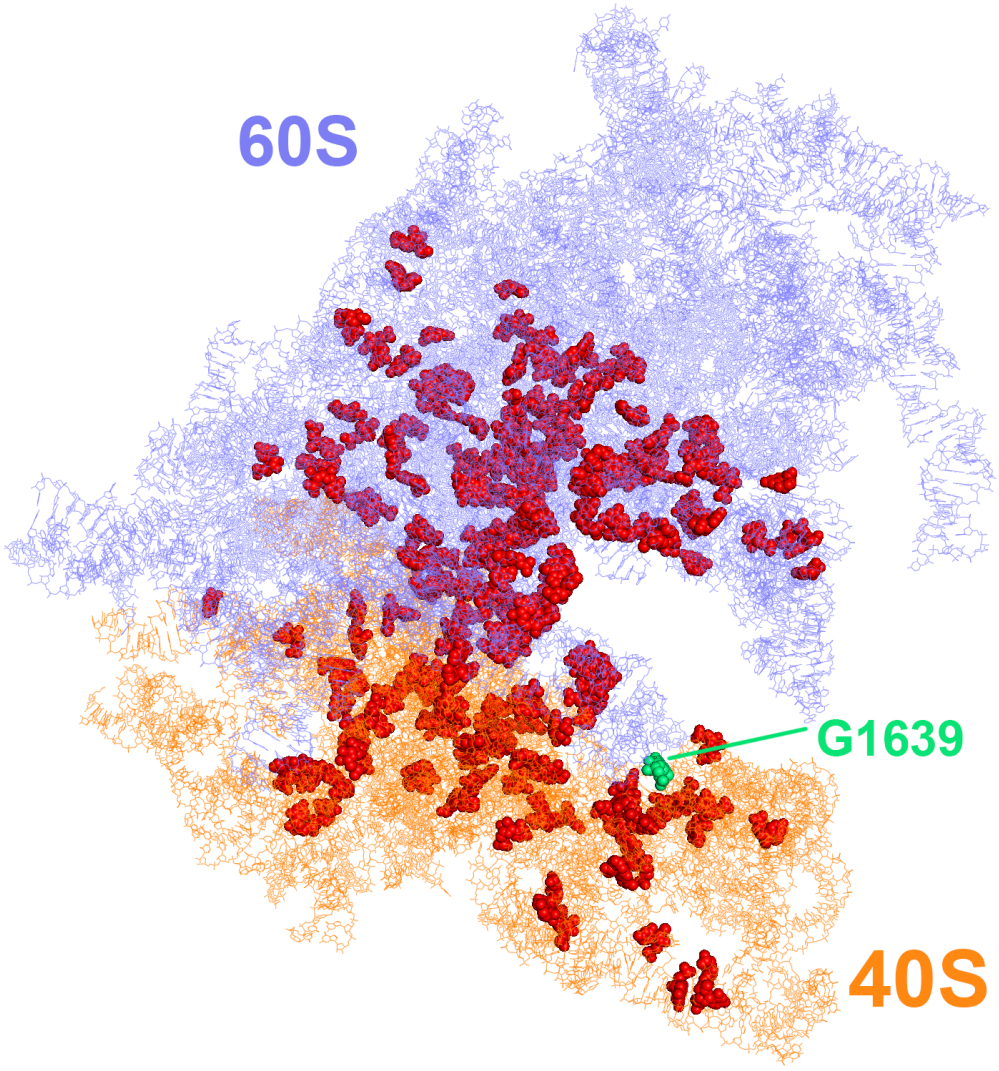

Figure 1.1: Modification landscape of the mammalian ribosome. Graphical representation of the 3D structure of the mammalian ribosome (PDB 7O7Y; Bhatt et al., 2021). The ribosome is extensively modified, containing upwards of 250 known modification sites. Modified nucleotides are indicated in red. BUD23 is responsible for the methylation of G1639, which is indicated in green.

through the covalent modification of proteins (Prabakaran et al., 2012). The addition or removal of specific PTMs permits for the properties of an amino acid residue to be altered, thus potentially impacting upon tertiary protein structure and protein interactions (Jensen, 2006). The activity of proteins can therefore be modulated in real-time without the need for transcriptional repression via epigenetic modifications. PTMs are widely spread and conserved across multiple domains of life, making them interesting targets to study (Krishna & Wold, 1993; Eichler & Adams, 2005).

While historically modifications were studied at single residue levels, with the assumption that a single modification is responsible for regulating a single specific function, more recently the importance of multi-site modification events has been elucidated (Yang, 2005). In some instances, while an individual modification may have little to no apparent effect on function, its summative effect with other modifications will serve to attenuate substrate stability and activity (Gunawardena, 2005). In particular, phosphorylation of proteins such as MAPKK (Ferrell, 1996), Sic1 (Nash et al., 2001), and cyclin E (Welcker et al., 2003) requires that a specific threshold number of phosphorylation events must occur in order to have an effect on substrate activity, and any modifications made that are under the threshold value will consequently have no effect. Histone proteins are also extensively modified via ubiquitination, methylation, phosphorylation and acetylation in a complex, multi-site fashion that permits for dynamic reorganisation of genetic material (Fischle et al., 2005; Pokholok et al, 2005).

The heterogeneity of protein and DNA modification states exponentially increases the number of products that can exist within each cell, despite the limited nature of the DNA code. This permits the specialisation and differentiation of cells and tissue types, as demonstrated by the number of modifications that are cell-type specific (Wang et al., 2014). The exact importance of many modifications remains unknown, opening an interesting field of study.

1.1.1 Types of modifications

Advances in mass spectrometry and proteomics have provided key frameworks to aid in the identification of PTMs and epigenetic markers (Doll & Burlingame, 2015). To date, over 200 distinct types of modifications have been discovered (Fig. 1.2), with yet more still being reported (Bidlingmaier & Liu, 2016). Previous estimates have indicated that glycosylated proteins are the highest abundant PTMs, with around half of all proteins carrying a glycosyl modification (Apweiler et al., 1999). However, systemic searching of the Swiss-Prot database reveals that the actual figure is closer to only one fifth of total proteins (Khoury et al., 2011). Glycosylation events often occur on the cell surface, and are vital for correct cell-cell recognition (Ohtsubo & Marth, 2006). They are significantly deregulated during disease states, especially in cancer and inflammation (Christiansen et al, 2014). Not only are some glycans over- or under-expressed in malignant tissues, but aberrant expression of developmental glycans can also be seen, usually as a result of alterations in glysosyltransferase levels (Jurianz et al., 1999). Glycosylation patterns also change in response to chronic inflammatory diseases (Renkonen et al., 2002), such as asthma and arthritis, providing a useful tool for diagnostic and therapeutic purposes.

Phosphorylation is the most prominent PTM, with up to 30% of all proteins containing at least one phosphorylated residue (Cohen, 2000). It plays key roles in virtually all cellular processes, including growth, motility, intracellular trafficking, and metabolism (Manning et al., 2002). Roughly 500 human protein kinases have been identified, and their specificities vary from hundreds of sites, as in the case of cyclin-dependent kinases, to only a single site (Ubersax & Ferrell, 2007). Atypical activation of kinases is a common phenomenon in many cancer types, resulting in a severe deregulation of many basic processes (Arena et al., 2005).

Some modifications can have varying effects depending on the location of their covalent bonds. For example, single ubiquitin modifications are responsible for regulating crucial protein-binding interactions (Rape, 2018). This is particularly important during development, where aberrant monoubiquitylation can cause severe

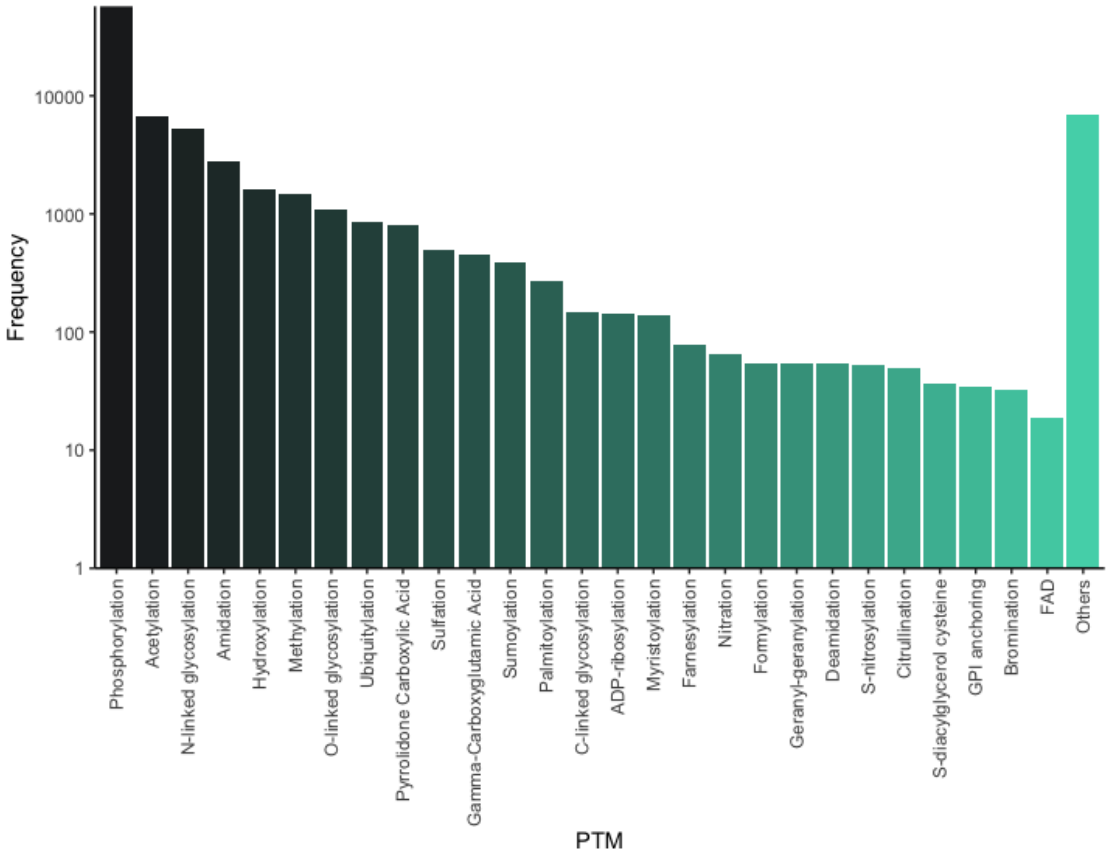

Figure 1.2: A summary of experimentally validated post-translational modifications. Post-translational modifications were identified using the Swiss-Prot database. Data collected from Khoury et al., 2011.

craniofacial abnormalities (Zou et al., 2011; Jin et al., 2012; Werner et al., 2015). However, ubiquitin molecules can also be chained together to modify their effect. K11 and K48-linked chains mark a protein for degradation (Chau et al., 1989; Jin et al., 2008), while K63 and M1 linkage are essential for protein complex assembly during signalling and autophagy (Tokunaga et al., 2009). Furthermore, ubiquitin can itself be further modified via phosphorylation, deamination and acetylation to further modulate these functions (Cui et al., 2010; Koyano et al., 2014; Ohtake et al., 2015). This reveals just how complex modification networks can be, and how vital they are in controlling biological processes.

Deregulation of PTMs can cause severe disease phenotypes. For example, accumulation of carbamylated proteins has been linked to autoimmune disease

(Pruijn, 2015), kidney disruption (Koeth et al., 2013), cataract formation (Lapko et al., 2001), and atherosclerosis (Sun et al., 2016).

Nucleic acids can also be altered, with cytosine methylation being the most widespread epigenetic modifier (Portela & Esteller, 2010). It is usually highly clustered in CpG dinucleotide islands, where methylation is responsible for the disruption of gene transcription (Deaton & Bird, 2011). Global loss of DNA methylation is a hallmark sign of cancer, with malignant cells showing up to a 60% reduction in 5-methyl-cytosine levels (Goelz et al., 1985). For example, IGF2 methylation is lost in breast, colon, liver and lung malignancies (Ito et al., 2008); S100P in pancreatic cancers (Irizarry et al., 2009); and LINE family member L1 in bladder, liver, breast and lung cancers (Wilson et al., 2007). Interestingly, certain CpG islands have instead been shown to be hypermethylated, in particular ones that control tumour suppressor genes such as BRCA1, P15, p73, and SFRP1 (Esteller, 2007). Identification of such sites could be an important diagnostic tool for future biomedical research.

The prevalence of PTMs and epigenetic markers reveals how crucial they are in maintaining cellular processes, providing insight into how cells regulate their various functions. As perturbation of modification machinery can create a severe phenotype, understanding the underlying mechanisms of action of various modifications will allow for the development of effective treatments to counter such scenarios.

1.1.2 Chromatin remodelling

Genomic material is typically considered to be in one of two organisational states: euchromatin or heterochromatin. The former is regarded to be transcriptionally active, and is characterised by the presence of trimethyl marks on H3K4, H3K36, and H3K79, as well as high levels of acetylation, including marks on H3K56 and H4K16 (Li et al., 2007). Histone tails tend to be highly targeted for modification, as opposed to the main body. Conversely, heterochromatin is much more densely packaged and

so is transcriptionally repressive, with typically low levels of acetylation but with high levels of monomethylated H3K27 and H4K20 (Li et al., 2007).

However, as previously described, chromatin modifications form a complex, multi-site network where some modifications may have very little effect, or only have an effect if multiple other modifications are also present. Therefore, describing individual markers is not as useful at looking at the overall chromatin state. Based on the different epigenetic modification profiles, Ernst and Kellis (2010) identified 51 unique chromatin states, each with distinct biological functions, challenging the simple euchromatin and heterochromatin model. Modifications are not restricted to acting upon immediately adjacent histones, and can modify the functions of marks on other tails and in different sites, significantly increasing the complexity of the system (Nakanishi et al., 2009).

Epigenetic control of histone modifications is a rapid, highly dynamic process, permitting the genome to switch between the various 'open' and 'closed' conformation states as necessary. To facilitate this, hundreds of enzymes have been identified that are capable of both writing and erasing PTMs in a very fluid manner (Kouzarides, 2007).

Because of their importance in regulating gene transcription, epigenetic histone markers are often perturbed during tumourigenesis. In prostate cancer, overexpression of histone deacetylase 1 promotes rampant growth (Noonan et al., 2009) due to the removal of modifications such as acetylation of H4K16 (Fraga et al., 2005). Similarly, histone demethylases have also been shown to be upregulated in both squamous cell carcinomas and in prostate cancers (Shi, 2007). However, not all histone markers tend to be removed during cancer. EZH2 is often upregulated, causing disrupted hypermethylation of its targets, promoting proliferation and cancer progression through chromatin remodelling (Varambally et al., 2008).

1.1.3 Metabolism

Cellular metabolism is responsible for the generation of many consumable substrates that are essential for epigenetic modifications and PTMs. Therefore, any factors that can affect metabolism, including nutrition and oxygen levels, will have a direct impact on modification capacity (Kaelin & McKnight, 2013). Conversely, epigenetic modifications can also play a role in controlling the genes responsible for attenuating metabolic functions, thereby creating a feedback cycle. For example, PPARγ expression is reduced as a consequence of promoter methylation in diabetic mice (Fujiki et al., 2009).

Fluctuations in levels of metabolically derived enzymatic substrates occur rhythmically within cells, and provide a rate-limiting step for modifying enzymes (Klevecz, 2004; Tu & McKnight, 2009). Levels of acetyl-CoA, the substrate required for acetylation, peak at the transition stage between oxidation and reductive building (Cai et al., 2011). Consequently, acetyl marks on H3 and H4 become rapidly saturated at this time point. As the half-life of histone acetyl marks is very short, estimated to be as low as 3 minutes (Waterborg, 2002), this reveals just how dynamic modification networks are. In some cases, much larger fluctuations occur as part of specific cell-type signalling. Undifferentiated embryonic stem cells contain unusually high levels of acetyl-CoA, which drop as the cells differentiate (Wang et al., 2009).

S-adenosylmethionine (SAM) is the high-energy donor for most methyltransferases (Fig. 1.3). Its production is dependent upon methionine and ATP levels within the cell. Interestingly, it is possible that SAM generation can be locally induced within the nucleus to provide cells with sufficient levels of methylation to maintain a correct epigenetic state (Kaelin & McKnight, 2013). This is supported by evidence that MAFK (Muto et al., 1998), a transcription factor, can recruit methionine adenosyltransferase enzymes directly to the targets of methylation (Katoh et al., 2011). Methionine adenosyltransferases are responsible for generating SAM (Sakata et al., 1993), thereby providing methyltransferases with their metabolic substrate directly at their target sites.

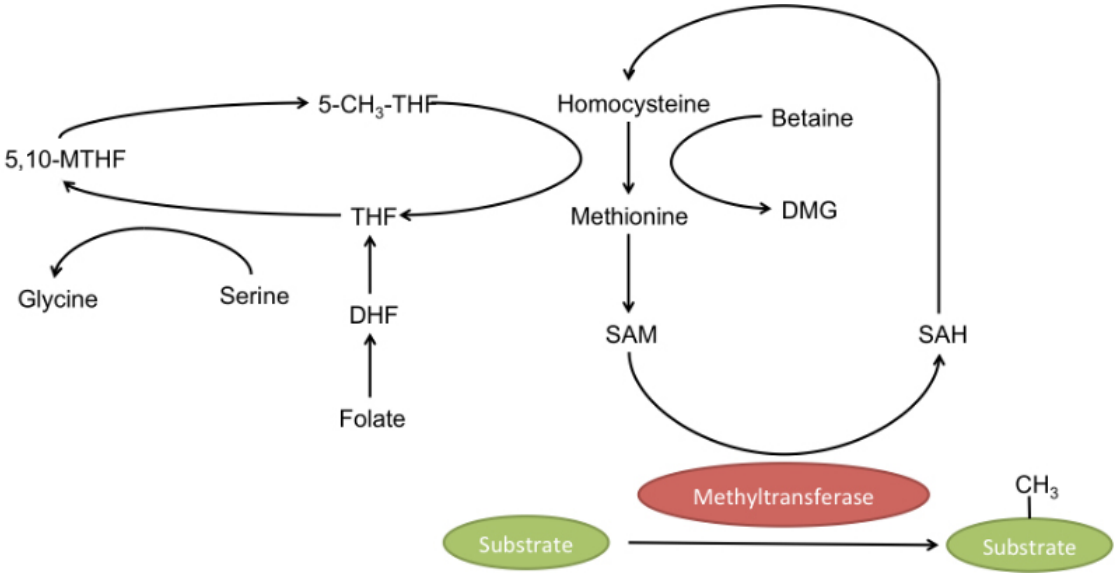

Figure 1.3: Metabolic signalling pathways responsible for controlling levels of SAM. THF, tetrahydrofolate; MTHF, methylene tetrahydrofolate; DHF, dihydrofolate; DMG dimethylglycine.

1.2 Methylation

The process of methylation refers to the covalent transfer of a methyl group from SAM to a target substrate by a methyltransferase, yielding methylated substrate and S-adenosylhomocysteine (SAH). The most commonly studied epigenetic modification is methylation of DNA cytosine residues, which is usually associated with gene silencing. However, methylation can also occur in proteins, on lysine or arginine residues, or in various forms of RNA. Interestingly, although most PTMs are highly dynamic, methylation is a comparatively stable modification, even being retained across generations in some cases (Greer et al., 2014).

Under specific circumstances, it can be rapidly induced and removed, however. For example, instigation of the DNA damage response triggers rapid remodelling of methylation profiles in apoptotic and repair pathways (Dhami et al., 2013). In addition, the methyltransferase MLL3 is responsible for epigenetic changes as part of the circadian cycle, playing a key role in maintaining transcriptional oscillation (Valekunja et al, 2013).

1.2.1 DNA methylation

Eukaryotic genomes contain low levels of methylated residues. The majority of these are C5-methylcytosine (m5C) bases, although N6-methyladenine (m6A) modifications have also been identified (Zemach et al., 2010; Koziol et al., 2016). The latter is much more prominent in prokaryotic genomes (Liu et al., 2016), which also contain a unique N4-methylcytosine modification not present in eukaryotes (Sánchez-Romero et al., 2015). The functions of m6A modifications have not been characterised in humans yet, but m5C has been very well studied. Purkinje and granule cells have also been found to contain 5-hydroxymethyl-2'-deoxycitidine, an epigenetic mark associated with the brain only (Kriaucionis & Heintz, 2009).

CpG dinulceotides are rapidly converted into m5C modifications in vertebrate genomes (Coulondre et al., 1978). The notable exception to this is in CpG islands, which are defined as long stretches (roughly 1000 base pairs) of DNA containing an elevated GC content (Deaton & Bird, 2011). These are typically associated with transcription promoter sites, and are characterised by their typical lack of methylation. Only approximately 6% of all CpG islands become methylated at some point during development or differentiation, and even then only in tissue-specific manners (Straussman et al., 2009). The remaining 94% are mainly composed of promoters for housekeeping genes (Larsen et al., 1992).

CpG island methylation is associated with gene silencing. It plays an essential role during genomic imprinting, permitting the monoallelic expression of a parental gene (Kacem & Feil, 2009). Interestingly, during X-chromosome inactivation, methylation does not initiate gene silencing but instead promotes long-term lock-in of the silencing phenotype, preventing the genes from becoming reactivated in the future (Sado et al., 2000). Other epigenetic modifications, such as H2K27 trimethylation, are responsible for initiation of silencing in this situation.

Methylation of some CpG islands occurs during neuronal development, taking place at the point of differentiation from embryonic stem cells into neurones (Mohn

et al., 2008). Some germline-expressed genes also become methylated at their associated CpG island promoter, for example MAGE genes are expressed only in the testes but are silenced in somatic tissue (De Smet et al., 1999). Once again, there is evidence that the associated genes are already silenced prior to methylation occurring (Mohn et al., 2008). This points to methylation being a long term DNA modification that is much more stable than other types of epigenetic modifications.

However, DNA methylation is not limited to CpG islands only. Methylation of CpG island shores, which are regions that lie close to CpG islands but have a lower ratio of CpG dinucleotides, also promotes gene silencing (Irizarry et al., 2009). This is responsible for significant tissue-specific reprogramming, encompassing over 70% of differentially methylated areas linked with reprogramming (Doi et al., 2009).

In some cases, DNA methylation occurs within a gene body, in which case it is often transcriptionally active instead (Hellman & Chess, 2007). It is thought that this might play a role in modifying the efficiency of elongation, thereby hindering inappropriate transcriptional initiation (Zilberman et al., 2007). It may also help regulate alternative gene splicing (Kornblihht, 2006).

De novo methylation, catalysed by DNMT3, is not limited to CpG dinucleotides. Initially, it was thought to be an accidental, non-specific methylation event (Ramsahoye et al., 2000), but recent studies have revealed that these modifications may instead have an independent purpose (Keown et al., 2017). In particular, MECP2, a neuronal transcriptional repressor, is selectively recruited to sites of non-CpG methylation, which is essential during neuronal maturation (Chen et al., 2015).

Overall, although DNA methylation appears to be a stable silencing mechanism, the system is a lot more complex than it appears and methylation may serve many more purposes that we are not yet aware of.

1.2.2 Protein methylation

Over 4,000 distinct protein methylation sites have been identified so far (Cao et al., 2013), with the vast majority lying in non-histone proteins. However, their functions remain largely unknown.

Proteins can be methylated in a variety of ways. Lysine residues can be methylated up to three times on a single nitrogen atom by lysine-specific methyltransferases (KMTs), while arginine residues can only be modified twice, but in either a symmetrical or asymmetrical fashion, by protein arginine methyltransferases (PRMTs; Smith & Denu, 2009). While the enzymes responsible for removal of lysine methyl marks have been known for a while, with KDM1A being the first to be identified (Shi et al., 2004), arginine demethylases have only been characterised very recently, and are actually formed by a subset of the lysine demethylase family JmjC (Walport et al., 2016). The ability of methyl marks to be added and consequently removed creates a malleable modification system.

Functional characterisation of various methyltransferases has shown that they have broad specificity ranges. SETD7 can methylate over 30 protein targets (Wang et al., 2001a), while PRMT5 has the capacity to modify 25 different non-histone substrates, in addition to histone marks (Wang et al., 2001b). It is possible that this is a falsely inflated figure, as the *in vivo* cellular environment may constraint or modify their actions. Biochemical assays also reveal that many substrates contain multiple methylation sites, giving rise to potential cross-talk mechanisms between the different marks. For example, p53 can be methylated by: G9a at K373 (Huang et al., 2010); SMYD2 at K370 (Huang et al., 2006); SETD8 at K382 (Shi et al., 2007); and SETD7 at K372 (Campaner et al., 2011). Some of these mechanisms have been elucidated. Dimethylation at K370 activates p53 as a transcription factor (Roy et al., 2010), while monomethylation represses this function (Huang et al., 2006). Meanwhile, K372 methylation prevents modification at the K370 site, revealing a complex underlying network (Huang et al., 2006).

Some locations can be methylated by multiple enzymes, such as K4 on histone H3, which can be modified by at least three different KMTs: MLL1, SETD7, and PRDM9 (Biggar & Li, 2015), revealing a certain amount of redundancy in this network. It is possible that the various enzymes become activated by different factors, but necessitate the same outcome. The specific mechanisms for this co-ordination are yet to be elucidated.

The function of protein methylation can vary, depending on cross-talk with other modifications. Methylation of MAP3K2 at K260 inhibits its interaction with PP2A, which causes a downstream increase in the activity of MEK1, MEK2, ERK1 and ERK2 (Mazur et al., 2014). This is a key step in pancreatic ductal adenocarcinoma development, and blocking this methylation step may provide a new therapeutic strategy. Meanwhile, methylation of Yes-associated protein, a transcriptional cofactor, prevents its nuclear translocation and forces it to be retained within the cytoplasm, preventing its action (Oudhoff et al., 2013). Methylation plays important roles in many cell signalling pathways, including differentiation, growth, and proliferation, and as such is often commonly disrupted in cancer. For example, STAT3 is important for maintenance of glioblastoma stem cells, and methylation of STAT3 encourages subsequent phosphorylation, thus promoting its activation (Kim et al., 2013).

1.2.3 RNA methylation

All types of RNA, from messenger to transfer to non-coding, can be modified with methyl groups in multiple locations. This affects not only the charge of the modified residue, but also its stability and steric properties. Adenine can be methylated to either 1-methyladenine (m1A) or m6A (Chawla et al., 2015). This permits the bases to adopt non-Watson-Crick base pairing, with m1A capable of forming bonds with unmodified adenine in addition to uracil, and m6A capable of binding to guanine instead. Both of these modifications can be found in several tRNA species, with m1A seemingly stabilising tRNA(iMet) in yeast (Anderson et al., 1998). Whether it serves the same functions in human tRNAs is yet to be established.

Guanine can be methylated in three different locations, including: 1-methylguanine, which was also identified in yeast tRNA(iMet); N2-methylguanine, in ribosomal RNA and various tRNAs; and 7-methylguanine (m7G), in ribosomal RNA (Chawla et al., 2015). Again, this alters the properties of the base and enables variant base pairs to form. Finally, cytosine can be modified into m5C, as previously described under DNA modifications. Many of these occur in areas that define RNA tertiary shapes, and are likely to play an important role in the formation and maintenance of their structure. In support of this theory, dimethylation of m2G has been proposed to stabilise human tRNA(Asn) at position 26 by blocking canonical Watson-Crick pairing that would contort the shape (Steinberg & Cedergren, 1995).

The role of m6A has been studied in the context of mRNA, where it has been found to localise strongly to both the 3' untranslated region and to stop codons in a reversible fashion (Meyer et al., 2012). A complex of METTL3, METTL14 and WTAP are responsible for catalysing this methylation reaction at Pu(G>A)m6AC(A/C/U) consensus sequences, though not all consensus sites are saturated (Dominissini et al., 2012; Liu et al., 2014). m6A has shown a large range of functionalities *in vitro*, in particular regarding embryonic stem cell fate via regulation of mRNA stability, but *in vivo* studies have struggled to replicate them (Batista et al., 2014). A recent study by Li et al. (2017) has identified that m6A is an important player in regulation of T cell proliferation by controlling IL-7 signalling via Socs mRNA degradation. It was suggested that m6A might play a more thorough role in controlling early response genes via modulation of mRNA degradation rates in response to environmental factors.

Studies have also shown that m6A is essential for correct regulation of the circadian cycle. Knock down of METTL3 results in clock dysregulation, driven by a lack of m6A mRNA methylation that therefore affects the nuclear exit timing of vital clock genes such as PER2 and ARNTL (Fustin et al., 2013). Inhibition of m7G has also been show to extend the period within a cell, through an independent mechanism to that of m6A. However, this mechanism has not yet been elucidated.

1.3 Methyltransferases

Methyltransferases are a group of enzymes responsible for catalysing the transfer of a methyl group from a metabolic SAM donor to their target substrate, which can be either DNA, RNA or protein in nature. They are highly conserved across multiple domains of life, where they can play differing roles based on the organism (Boye & Løbner-Olesen, 1990; Niu et al., 2013). In eukaryotes, they have essential functions in chromatin reorganisation, as well as for various PTMs. Prokaryotes lack chromatin, but still contain methyltransferases. These can directly methylate genomic material, as well as proteins, and it has also been suggested that these may serve to remodel eukaryotic chromatin during infection by pathogenic bacteria (Aravind et al., 2011). Methylation of DNA can also help to protect it from endonuclease activity, preserving the host genome during restriction-modification defence systems against phages (Bickle & Krüger, 1993).

Methyltransferases fall into three main families, those with SET domains, often referred to as the KMTs (lysine methyltransferases), those with a SPOUT domain, and those with a Rossmann-fold. While all three use the universal SAM donor, they have evolved different mechanisms for catalysing the transfer reaction.

1.3.1 SET domains

The SET domain superfamily encompasses all KMTs with the notable exception of DOT1L, which seems to have evolved lysine specificity independently (Feng et al., 2002). It contains seven main families within it, plus some orphan KMTs such as SET8 (Dillon et al., 2005). All have a similar SET domain in terms of structure, but proteins within the same family show higher levels of homology at the sequence level, and a greater similarity between other domains.

It is thought that the SET domain arose as a duplication event from a simple three-stranded unit dimer, with one of the units diverging to become a SAM acceptor, and the other gaining specificity for the methylation substrate (Aravind & Iyer, 2003). The middle ‘barrel’ of the domain also arose from a dimer pair,

but diverged heavily to form a psuedoknot that was formed due to looping of the C-terminal through another part of the sequence, bringing the two vital consensus sequence motifs into contact to form the binding pocket – RFINHXCXPN and ELXFDY (Aravind & Iyer, 2003).

SET domain proteins are strikingly different from other methyltransferases in that the binding sites for the SAM donor and the substrate occur on opposite sides of the SET domain (Trievel et al., 2002). A deep barrel through the domain provides a channel down which the methyl group can transfer from SAM to the amino group on the target lysine residue. This configuration permits multiple methylation events to occur on the same lysine residue without requiring dissociation of the substrate (Zhang et al., 2003).

1.3.2 SPOUT domains

The SPOUT methyltransferase superfamily is one of the largest methyltransferase groups, second only to Rossmann-fold type methyltransferases (Bujnicki, 1999). It was first identified from predicted structures of bacterial TrmD and SpoU methyltransferases (Anantharaman et al., 2002), and then confirmed via crystallisation of two of its members, RrmA and RlmB (Michel et al., 2002; Das et al., 2004). Interestingly, all of its constituent members seem to methylate RNA exclusively. Phylogenetic analyses of SPOUT methyltransferases have revealed that it is an ancient superfamily, with predictions stating that the Last Universal Common Ancestor likely had three separate SPOUT proteins, responsible for m1G, 3-methyluracil and 2'-O-ribose methylation respectively (Tkaczuk et al., 2007).

SPOUT domains are characterised by their very deep trefoil knot at their C-terminus, which is responsible for SAM binding (Nureki et al., 2004). The core of the domain is assembled from five β strands aligned in a 5-3-4-1-2 parallel configuration, which is flanked by two groups of helices (Petrossian & Clarke, 2009). These helices vary significantly between members of the superfamily, not only in terms of size but also angle relative to the rest of the core. The N-terminus is formed from a

Rossmannoidal α/β fold, with some members of the family containing extra α/β modules compared to others (Tkaczuk et al., 2007).

To enable enzymatic activity, all SPOUT proteins must dimerise (Tkaczuk et al., 2007). The nature of this interaction varies depending on the specific structure of the constituent members, as they can align in either a perpendicular or antiparallel configuration. This is supported by the fact that the enzymatic site is formed in between the two monomers, with essential points of contact formed by individual residues from both proteins. This also serves to help stabilise the co-factor binding loops within each monomer.

1.3.3 Rossmann-fold methyltransferases

Rossmann-fold methyltransferases, also called seven β strand methyltransferases, are the largest described group of methyltransferases (Martin & McMillan, 2002). They contain a large variety of proteins, and unlike SET and SPOUT domains, which can methylate only a single substrate type, show a large diversity in their substrate ranges. It contains the NOP2/Sun RNA methyltransferase family, PRMTs, tRNA methyltransferases, methyltransferase-like proteins, as well as various *de novo* and maintenance DNA methyltransferases (Okano et al., 1999; Horwich et al., 2007; Richon et al., 2011; Haag et al., 2015).

Their shape is mainly formed by a Rossmann-like-fold, consisting of a sheet of 7 β-strands arranged in a 3-2-1-4-5-7-6 configuration, sandwiched between three helices on either side (Fig. 1.4; Martin & McMillan, 2002). The seventh strand is generally antiparallel relative to the others. The N-terminal side of the sheet contains the SAM binding site, which is formed from a few highly conserved loops. Interestingly, though structurally all members of the family are very similar around the binding domain, they diverge heavily at the sequence level. Some have a binding site enriched with phenylalanines, some with tyrosines, and some with methionines, to name a few. Only one loop, named motif I, has a conserved sequence E/DXGXGXG, responsible for interacting with SAM's amino group. SAM itself forms three separate hydrogen

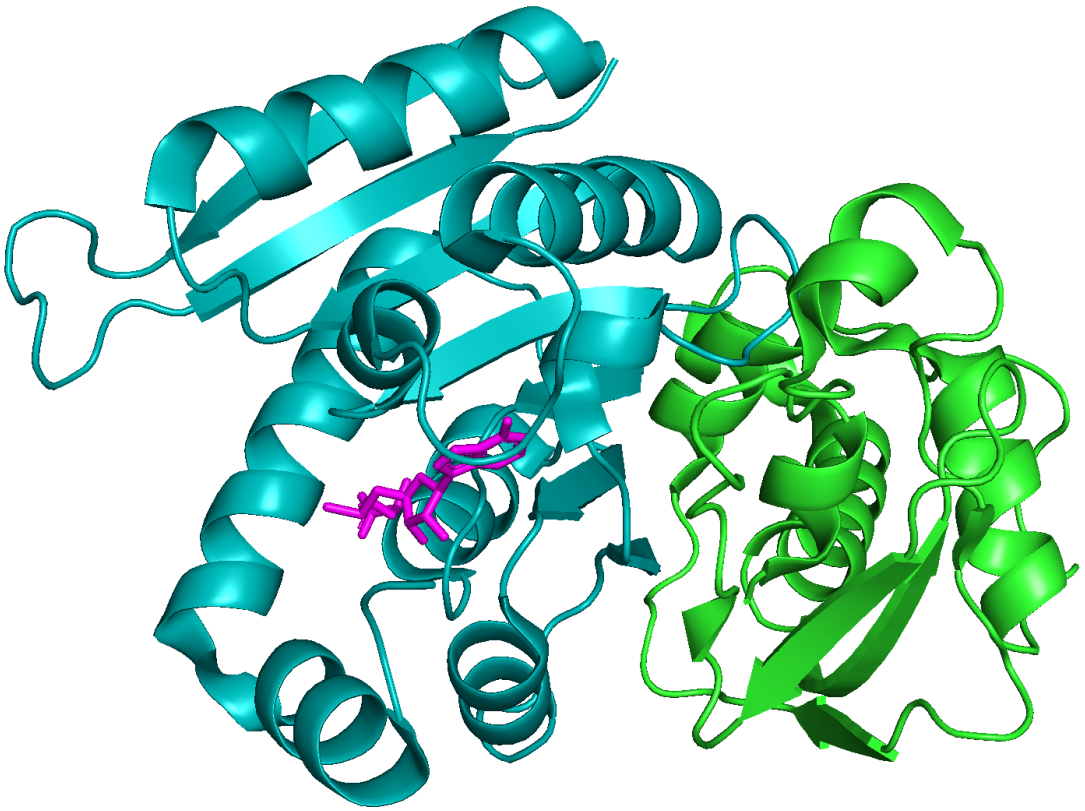

Figure 1.4: 3D structure of yeast Bud23 in complex with TRM112. Bud23 (blue) shows the typical 7 β strand structure common to the Rossmann-fold methyltransferase family. SAM is indicated in pink; TRM112 in green. (PDB 4QTU; Létoquart et al., 2014)

bonds with the protein, one in this glycine-rich motif I, and two in other areas of the protein. Although the other two bonds seem to form with very different residues from protein to protein, including isoleucine, valine, proline, cysteine, etc..., the interaction here is actually with the backbone of the amino acid, and so structurally and chemically is very similar despite initial appearances.

The C-terminus is responsible for conferring substrate specificity, and related protein members bear very little homology to each other here in terms of either structure or sequence (Martin & McMillan, 2002).

1.3.4 Chemogenetic tree

A study by Richon et al. (2011) attempted to create family trees for two groups of methyltransferases – the KMTs and PRMTs. Systematic searches of the human

genome were performed to identify putative KMT and PRMT members, and identified sequences were aligned based on the structure of their catalytically active domains.

One of the initial findings was that the two families could not be grouped onto the same tree regardless of which parameters were applied, indicating that they strongly diverged some time ago. Given the strong differences observed in the catalytic sites of both SET (the family which KMTs belong to) and Rossmann-fold (the family which PRMTs belong to) methyltransferases, this is in many ways not a surprising result.

However, DOT1L, a known KMT that characteristically lacks a SET domain could not be included on the KMT tree, but could be included in the PRMT tree. It is a very unique KMT, and the only one known to methylate the globular domain of histone proteins (Ng et al., 2002). Investigations into its SAM binding functionality revealed that it held SAM in a different conformation to other SET domain proteins, instead forming typical bonds characteristic of PRMTs. Further analysis of its structure reveals a characteristic Rossmann-fold-like domain, indicating that it likely evolved lysine specificity independently from the other KMTs. It is currently unknown why Rossmann-fold type methyltransferases show such a wide range of substrate specificities in comparison to other methyltransferase families.

In attempting to ensure that all known PRMT members were included on the tree, a number of other related proteins were also forced to be included. These included proteins from the METTL and NSUN families, as well as some individual proteins such as Bud23 and COQ3. While this may not be unexpected, given that they are all part of the same Rossmann-fold superfamily, they do not align perfectly into branches based off their substrate groups, but are instead partially interspersed. Whether this means that some proteins can methylate multiple substrates that have not yet been identified, or that the family has evolved different substrate specificities independently over time, or that the alignments are not accurate to the true evolutionary history, remains to be determined.

1.4 BUD23

BUD23 is a putative Rossmann-fold-like methyltransferase with two seemingly independent functions – its role in methylation and in ribosome maturation (Zorbas et al., 2015). It was originally identified in *S. cerevisiae* during a bioinformatical screen searching for genes involved in ribosome development (White et al., 2008). While BUD23 was not required for survival of budding yeast, knockdown was responsible for severely impaired growth and a significant reduction in levels of the small ribosomal subunit, indicating that it might serve an important purpose during small subunit biogenesis.

Its human ortholog, WBSCR22/MERM1, was originally characterised for its role in Williams-Beuren syndrome (Doll & Grzeschik, 2001). This is a rare developmental disorder that presents with a wide range of symptoms, including diabetes mellitus, stunted growth, congenital heart disease and premature aging (Morris et al., 1988; Pober, 2010). BUD23 was identified as one of approximately 27 genes that are deleted in this disorder, and subsequently was identified as a putative methyltransferase.

BUD23 shows a strong mRNA expression profile in tissues such as cardiac and skeletal muscle, the kidney, and bronchial epithelium (Doll & Grzeschik, 2001; Jagani et al., 2014).

1.4.1 Ribosomal Maturation

As knockdown of BUD23 creates a deficiency in levels of 40S ribosomal subunits in both yeast and human systems, it stands to reason that BUD23 may be implicated in ribosomal biogenesis (White et al., 2008; Õunap et al., 2013). This is further supported by the observation that early 40S precursors accumulate within the nucleus in cells lacking BUD23, indicating that they are failing to mature.

Biogenesis of the human ribosome begins with the RNA polymerase I-mediated transcription of the 47S precursor (Fig. 1.5; Henras et al., 2008). This is a primary

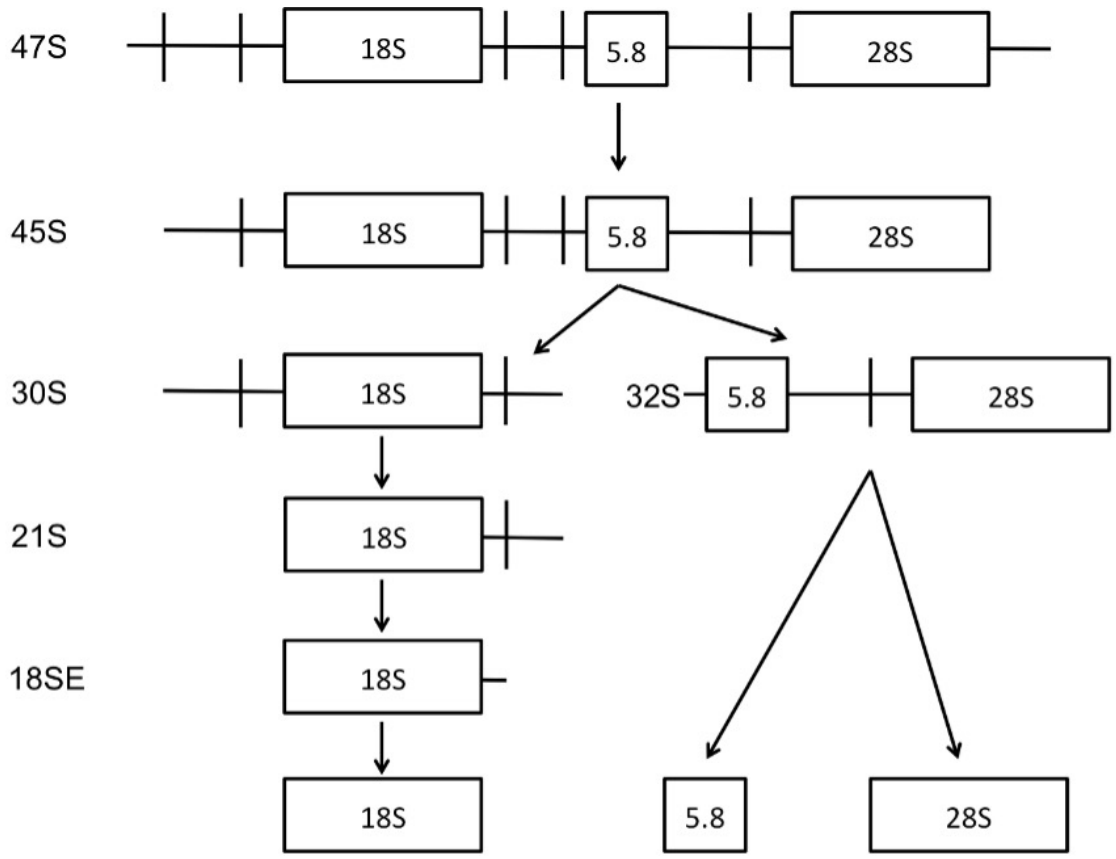

Figure 1.5: Human rRNA maturation stages. Vertical lines indicate cleavage events, while boxes represent mature rRNA sequences.

transcript that contains sequences for almost all of the ribosomal RNA, interspersed with internal and external spacers (Mullineux & Lafontaine, 2012). This transcript is initially trimmed to form the 45S precursor, before undergoing endonucleolytic cleavage at site 2. This breaks the transcript into two, of which one portion, the 32S pre-RNA, will go on to become the large 60S subunit, and the other, the 30S pre-RNA, will mature into the small 40S subunit. Maturation from this point on occurs independently, until the final assembly stage of the processed subunits.

The 30S pre-RNA is cleaved to form the 21S pre-RNA sequence via removal of its 5' external transcribed spacer. From here, the process begins to diverge from what is known to happen in yeast, as the 21S pre-RNA is further processed into 18SE pre-RNA (Preti et al., 2013). It then undergoes a final cleavage stage by NOB1 to form its mature 3' end (Pertschy et al., 2009), prior to export from the nucleus.

A study by Haag et al. (2015) managed to identify that knockdown of BUD23 specifically created an accumulation of 18SE pre-RNA within the nucleus. They hypothesised that the presence of BUD23 is essential for 18SE trimming, and that only mature 18S RNA can be successfully exported from the nucleus. Interestingly, this ribosomal maturation phenotype does not seem to be linked to BUD23's methyltransferase function, as mutation of key residues within its SAM binding site block methylation without disrupting protein structure, but did not disrupt 40S maturation, indicating that the presence of a structurally sound protein is sufficient to allow ribosomal biogenesis to proceed (Létoquart et al., 2014).

1.4.2 Function as a methyltransferase

In vivo studies have indicated that BUD23 is responsible for the m7G methylation of G1575 on 18S RNA in *S. cerevisiae* (White et al., 2008). This residue is strongly conserved and lies at the anticodon stem of the P-site tRNA, which is a functionally important region within the ribosome. Given the significance of this residue, and the strong conservation of the SAM site within Bud23, it is therefore highly likely that this modification should serve some important role.

Both this residue and the m7G modification are also conserved at the corresponding position in humans, at G1639 (Choi & Busch, 1978). One study used aniline cleavage assays followed by northern blot probing to investigate methylation of the small ribosomal subunit (Haag et al., 2015). Aniline is a potent drug that causes specific cleavage at m7G sites, of which only one exists on the small ribosomal subunit. This revealed that in wild-type cells, around 60% of all ribosomes contained the m7G mark, but in the absence of BUD23 this modification became undetectable. BUD23 is therefore somehow responsible for modifying this site, which is logical given that it also appears to interact with the 18S RNA during ribosomal maturation. Given BUD23's vital role in ribosomal maturation, the absence of a methyl mark on 40% of ribosomes is surprising, and the factors responsible for governing its penetrance remain undetermined.

However, *in vitro* biochemical assays failed to detect any effect of BUD23 on 18S RNA (Létoquart et al., 2014; Haag et al., 2015). Some studies postulate that this is because 18S RNA must undergo a conformation change in order to permit methylation, which is catalysed by additional cofactors that are yet unknown. It is also possible that other *in vivo* conditions can affect BUD23's function that have not been determined. Interestingly, the purpose of the m7G modification at G1639 remains unknown. Cells containing catalytically inactive Bud23 lack this mark, but appear to be phenotypically normal (Létoquart et al., 2014). This has led to the idea that it may be a non-essential modification, or part of a multi-site modification network where the effects of other modified residues compensate for its absence. It is also possible that it is imparted as a quality control marker, showing that the 18S RNA has undergone successful maturation. However, the high degree of conservation in BUD23's catalytic site points to the methyltransferase action being functionally important.

Other studies have also linked BUD23 to other methyl marks, including H3K9 and trimethylation of H3K4 (Nakazawa et al., 2011; Jangani et al., 2014). However, they also failed to prove any mechanism for its methyl action through biochemical assays. It is likely that these marks are imparted through downstream signalling that is perturbed upon loss of BUD23, though this has yet to be determined.

1.4.3 BUD23 in disease

Dysregulation of BUD23 has been linked to various disease states. It was initially described in Williams-Beuren syndrome (Doll & Grzeschik, 2001), where symptoms including cardiac abnormalities and stunted growth are attributed to a deletion of the BUD23 gene. As BUD23 is normally highly expressed within cardiac and skeletal muscle, its absence appears to create a severe phenotype in these tissues in particular.

Impaired BUD23 function has also been implicated in neoplastic and pulmonary inflammatory diseases (Jangani et al., 2014). High levels of IFNγ and TNFα, as can be found in pro-inflammatory conditions, cause degradation of BUD23 in a

ubiquitin-dependent manner, which causes prominent effects upon glucocorticoid receptor function.

Finally, upregulation of BUD23 has been identified in various forms of cancer. In colorectal cancer, it confers resistance to chemotherapeutic drugs such as oxaliplatin (Yan et al., 2017). Targeted treatments may then be a useful tool to re-sensitise cancer cells to drug therapies. Meanwhile, BUD23 has also been found to aid breast cancer in avoiding p53-dependent apoptosis through suppression of ZAC1 (Nakazawa et al., 2011).

1.4.4 Potential role of BUD23 in metabolism

Preliminary studies within the Ray group have revealed a potential novel role for BUD23 in translational homeostasis of metabolic transcripts (Baxter et al., 2020). siRNA mediated depletion of BUD23 in A549 cells, a human airway epithelial cell line, resulted in a slow growth phenotype, similar to that observed in yeast (White et al., 2008).

To analyse the effect of BUD23 knockdown on ribosomal function, polysome profiling was performed, which enabled the interrogation of altered translational efficiencies of individual transcripts. Approximately 650 transcripts were identified which showed a significant reduction in translational efficiency upon BUD23 depletion. These clustered into a tightly connected network of transcripts encoding proteins involved in many different metabolic processes, in addition to transcripts involved in RNA processing.

Surprisingly, all transcripts encoding mitochondrial proteins showed a strong reduction in translational efficiency, with the average transcript decreasing by approximately 50%. This highlighted a potential new function of BUD23, implicating it in metabolic transcript processing.

1.5 This project

BUD23, a putative methyltransferase with two known functions, has recently been implicated in the control of metabolic transcript homeostasis. One of its major roles is the deposition of a methyl mark on the small ribosomal subunit. However, little is known about the functional significance of rRNA modifications, although modifications in other contexts serve to provide cells with a dynamic system to facilitate rapid adaptation to changes.

This thesis seeks to explore the role of BUD23 in an *in vivo* context, with a particular focus on exploring a potential connection between rRNA modifications and their functional consequences. It primarily tests the hypothesis that **BUD23 is responsible for the selective control of metabolic mRNA translation**, potentially via its methylation activity.

The first results chapter, 'BUD23 as a determinant of mitochondrial function in cardiac tissue', explores the function of BUD23 in cardiomyocytes, a metabolically rich tissue that is heavily dependent on mitochondrial function. It tests the hypothesis that knockdown of BUD23 would cause a selective defect in translation of metabolic transcripts. In addition, it explores whether known functions of BUD23, which has primarily been studied in the context of yeast to date, are conserved across mammals. The data presented in this chapter was published in eLife in January 2020 (Baxter et al., 2020).

The second results chapter, 'BUD23's function in thermogenesis in adipose tissue', seeks to determine if the findings of the previous chapter are consistent in a second specialised tissue type. It tests the hypothesis that loss of BUD23 should cause a loss of thermogenic potential in brown adipose tissue, and goes on to explore the underlying mechanisms governing BUD23's role in translation of mitochondrial transcripts.

Finally, the last results chapter, 'The structure and function of BUD23', focuses on the development of an *in silico* model of human BUD23. It aims to offer

mechanistic insight into the role of BUD23 through analysis of its 3D structure, and to establish a way to delineate the two known functions of BUD23. In addition, it also explores a model of the ribosome to enable functional assessment of the methylation event catalysed by BUD23.

2
Materials and Methods

Contents

General methodology is described here. Methods specific to each chapter are provided where appropriate.

2.1 Animals and Reagents

All animals were routinely housed in 12:12 light/dark cycles with *ad libitum* access to food and water. Experiments were conducted in accordance with the UK Animals (Scientific Procedures) Act 1986. Animal cohorts were matched by age and sex, and littermates ($Cre^{-/-}$) were used as experimental controls.

All reagents are from Sigma unless otherwise stated.

2.2 Genotyping

Ear clips were taken from all experimental animals at approximately 2 weeks of age. DNA was extracted using the REDExtract-N-Amp Tissue PCR kit according to the manufacturer's protocol. In brief, the tissue was incubated in extraction solution supplemented with tissue preparation solution for 10 minutes at room temperature. The sample was then heated at 95°C for 3 minutes before the addition of neutralisation solution.

PCR reactions were set up by combining extracted genomic DNA (gDNA), Extract-N-Amp PCR Reaction Mix, nuclease-free water, and appropriate primers (IDT) before being run on a thermocycler. Full details of PCR reactions and cycling parameters for each mouse line are included in appendix A. PCR reaction products were resolved using 2% agarose (Appleton) gels in Tris-Borate–EDTA (TBE) buffer. SYBR Safe (Thermo Fisher) was added to the gel. Gel electrophoresis was carried out for approximately 40 minutes at a constant 110V. Gels were visualised on the Azure 600 using the EpiBlue channel.

All results were verified by a second round of genotyping using tail tips from the same animals.

2.3 Protein Extraction

Tissue was rapidly dissected out of animals and snap frozen in liquid nitrogen, before being transferred to -80°C for long term storage. Tissue was homogenised using a TissueRuptor (Qiagen) in sterile tris-buffered saline supplemented with protease inhibitor cocktail (Promega). Homogenate was transferred to a clean tube and 20% sodium dodecyl sulfate was added to a final concentration of 4%. Samples were sonicated briefly (<10 secs) to disrupt nuclear material. 1M DTT was then added to a final concentration of 100mM before heating for 10 mins at 85°C. Samples were then spun down at maximum speed using a benchtop centrifuge

for 15 mins, and the supernatant was transferred to a fresh tube. Protein content was determined by Bradford.

2.4 Western Blots

50μg of protein, as determined by Bradford assay, were added to NuPAGE LDS sample buffer (Invitrogen) supplemented with 100mM DTT. Samples were boiled at 85°C for 5 mins in order to denature them, prior to loading into the wells of a 4-20% Mini-PROTEAN TGX Precast Protein Gel (Bio-Rad). Gels were run until completion (approximately 45 mins) at 140V in 1x TGS buffer (Bio-Rad). Protein was transferred to nitrocellulose (Bio-Rad) using the TurboBlot system (Bio-Rad). The membrane was then blocked with LI-COR Odyssey Blocking Buffer (LI-COR Biosciences) before incubation with appropriate antibodies, per manufacturer's instructions.

2.5 Oroboros

Tissue homogenates were used for assessment of mitochondrial function. All measurements were carried out at 37°C. 20 mg of tissue was weighed and transferred to 1.5 ml of ice-cold MiRO5 medium (in mM: EGTA 0.5, MgCl2 1.4, taurine 20, KH2P04 10, HEPES 20, BSA 1%, K-MES 60 mM, sucrose 110 mM, pH 7.1, adjusted with 5 M KOH). Tissue was homogenized for 3s in 1s bursts with a tissue homogenizer and loaded immediately (40 µg/ml) into an Oroboros Oxygraph 2k high resolution respirometry system (Oroboros Instruments) for measurement of mitochondrial respiration. The O2k-Fluo LED2-Module was used for H2O2 measurement.

Two respiration chambers were run in parallel for each experimental run. H2O2 flux was measured simultaneously with respiration via the use of Amplex UltraRed (10 μM) with 1 U/mL horse radish peroxidase and 5 U/mL superoxide dismutase. Calibrations were performed with two sequential injections of H2O2 at 0.1 μM steps.

OXPHOS, LEAK and ETS were measured in the presence of pyruvate (5 mmol/l) and malate (0.25 mmol/l; Complex I substrates), or succinate (10 mmol/l; Complex

III). Tetramethyl-phenylene-diamine was used to measure flux through Complex IV. OXPHOS with Complex I substrates was measured by adding saturating levels of ADP (2 mM/l). Following steady-state conditions, succinate was added to achieve OXPHOS with CI+CII substrates. To uncouple respiration and achieve ETS with CI+CII substrates, carbonyl cyanide 4-trifluoromethoxyphenylhydrazone was carefully titrated to a maximum concentration of 0.25 μmol/l. Rotenone was then added to achieve ETS with CII substrates and antimycin A (5 μmol/l) was given to block Complex III and measure background non-mitochondrial residual oxygen consumption (ROX). OXPHOS through Complex IV alone was assessed by adding the electron donor TMPD (0.5 mmol/l). To avoid oxidation of TMPD, ascorbate (2 mMol/l) was added prior to TMPD injection.

2.6 Citrate synthase assay

Citrate synthase activity was measured from frozen homogenates. Maximal activity was determined using the Synergy HTX spectrophotometer (BioTek) at 412nm in 50 mM TRIS-HCl, pH 8.0 at 37°C. Homogenates were incubated in assay buffer containing 0.5 oxaloacetate, 0.3 mM acetyl-CoA, 0.15 mM 5,5-dithiobis-2-nitrobenzoic acid for 10 mins. Extinction coefficients were empirically determined to quantify V_{max} values. Activity was normalised to total protein content, as determined by Bradford.

2.7 Genomic DNA extractions

Genomic DNA (gDNA) was extracted using phenol-chloroform. Tissue homogenates were added to 1 volume of phenol:chloroform:isoamyl alcohol (25:24:1; Thermo Fisher) and vortexed for 20 seconds. Samples were transfered into phase lock tubes (Qiagen) prior to centrifugation at 16,000g for 5 mins. The aqueous phase was carefully removed and transferred to a fresh tube. 1 μl GlycoBlue, half a volume of 7.5M ammonium acetate, and 2.5 volumes of 100% ethanol were added. The sample was kept at -80°C for one hour to facilitate DNA precipitation. The sample was

then centrifuged at 16,000g at 4°C for 30 mins to pellet the DNA. The pellet was washed in ethanol once and left to air dry. Purified genomic DNA was resuspended in nuclease-free water for downstream applications.

2.8 Cell culture

A549 and HEK293T cells (ECACC) were routinely cultured in high glucose Dulbecco's Modified Eagle's Medium supplemented with L-glutamine, sodium bicarbonate, and sodium pyruvate (D6429) and 10% foetal calf serum. Cells were incubated at 37°C in 5% v/v CO_2 and regularly tested for mycoplasma contamination.

3

BUD23 as a determinant of mitochondrial function in cardiac tissue

Contents

An adapted version of this chapter was published in eLife in 2020 (see appendix 2).

3.1 Introduction

BUD23 was originally identified during a bioinformatical screen in *S. cerevisiae*, searching for genes involved in ribosomal biogenesis (White et al., 2008). While not essential for the survival of budding yeast, its loss results in severe growth impairment and a strong decline in levels of the small ribosomal subunit. Work done by Zorbas et al. (2015) revealed that BUD23 has two independent functions in budding yeast: to impart a m7G1575 methyl mark on the yeast 18S ribosomal RNA strand; and to assist with progression through the 18SE to 18S phase of ribosomal biogenesis. This methyl mark is highly conserved across all eukaryotes, and experimental evidence from human immortalised cell lines indicates that both functions are also present there.

However, it is widely reported that translation in multicellular organisms is a highly dynamic process that serves as a key regulator of protein expression across heterogeneous tissues. Translation is under tight spatiotemporal control, ensuring that appropriate quantities of proteins can be produced in the correct tissue types in response to demand. While translation is considered a robust, fundamental process, each tissue type is capable of responding in different ways to the same stimuli, permitting the appropriate control of their translatome in a heterogeneous manner.

BUD23 has previously predominantly been studied in the context of unicellular organisms. Whether its known functions are conserved within a complex mam-

malian system, and more so whether they vary throughout specialised tissues, is currently unknown.

3.1.1 Development of the global BUD23 knockout mouse

An attempt was made to generate a global BUD23 null mouse through the introduction of a frameshift deletion within a critical exon of the gene (Baxter et al., 2020). Unfortunately, no knockout animals could be obtained as deletion of BUD23 throughout the entire animal led to embryonic lethality. Examination of embryos at embryonic day E10.5 revealed no homozygous null allele mice, suggesting that they fail to develop at a very young stage.

In addition, analysis of offspring Mendelian ratios showed a secondary defect in numbers of heterozygote knockout animals. Only half the expected number of heterozygotes were born, with the rest failing to mature through the late stages of embryogenesis, indicating that even heterozygous deficiency is deleterious in mammals.

Surviving heterozygote animals did not appear to show any phenotypic discrepancies from the wild-type animals, indicating that in a subset of animals a single copy of the gene was sufficient to permit survival. It is likely these animals had additional compensatory mechanisms to facilitate survival despite haploinsufficiency. Unfortunately, the severe embryonic lethality of full knockouts and the apparent normal phenotype of surviving heterozygote animals means that this model is not suitable for studying the effects of BUD23 within a mammalian system.

3.1.2 Rationale for Cre targeting

To combat the issues seen with the global knockout BUD23 mouse, we proposed to create a floxed BUD23 model, which can be combined with various Cre alleles to drive knockdown in specific tissues. Preliminary work in our lab has shown that BUD23 may be implicated in the translation of metabolic transcripts *in vitro*. Polysome profiling of BUD23 siRNA treated A549 cells revealed a decrease in translational efficiency of mRNAs involved in various metabolic and catabolic

processes. A potential link between BUD23 and metabolism has not been identified before, and may indicate a novel role for BUD23 in mammalian organisms.

In order to interrogate whether this occurs *in vivo*, targeting tissues that have a high metabolic demand, such as the heart and skeletal muscle, for BUD23 knockout would provide an excellent model for studying its effects. In particular, the heart is rich in mitochondria and is under very high energetic demand. As such, we proposed that using a muscle creatine kinase (MCK) Cre driver, which would drive knockout in both the heart and skeletal muscle, would be a good initial target in which to detect a phenotype.

3.1.3 Post-natal cardiac development

Cardiac tissue undergoes extensive remodelling in the post-natal animal as it becomes subjected to different environmental pressures. Within the foetus, both ventricles function in parallel and are primarily used for systemic circulation (Rudolph & Heymann, 1967). Pulmonary circulation is reduced to approximately 10% of its typical flow as the foetal lungs are collapsed and blood is diverted away via a series of shunts in the vasculature (Heymann & Rudolph, 1975). However, in the immediate hours post-birth, alveolar expansion causes a corresponding decrease in pulmonary resistance as lung capacity increases. This results in the development of normal pulmonary circulation and the blocking of shunts to prevent diversion of blood flow (Hew & Keller, 2003).

Parallel to this process, the heart muscle mass begins to expand rapidly, initially undergoing hyperplasia and then, as the cardiomyocytes undergo terminal differentiation, progressing into hypertrophic expansion (Li et al., 1996; Hoerter et al., 1991). Upon completion of the cell cycle, some cardiomyocytes also fail to undergo karyokinesis, thus resulting in the typical binucleation phenotype observed in approximately 30% of all heart muscle cells (Clubb & Bishop, 1984). The exact timing of the switch from hyperplasia to hypertrophy appears to be species-specific. In humans the cardiomyocytes are already terminally differentiated prior

to birth (Mollova et al., 2013), while in rats onset of hypertrophy begins at 3 post-natal days (Shin et al., 2018).

Metabolic switching

To accompany these changes, the heart is forced to undergo a metabolic rewiring to meet new energetic demands as the organism enters a rapid growth phase (Piquereau et al., 2010). During early development, cardiomyocytes have a strong preference for glycolysis, which while low in energy efficiency has a very small requirement for oxygen. However, in the adult heart energy is generated almost exclusively via oxidative metabolism using fatty acids. This metabolic switch is controlled not only by the presence of the correct enzymes and transporters, but is also heavily dependent on substrate availability (Bartelds et al., 1998).

During foetal development, blood supplied to the embryo via the placenta is high in lactate, and low in fatty acids. This favours a glycolytic phenotype, with presence of lactate actively inhibiting fatty acid metabolism (Werner et al., 1989). Interestingly, through the conversion of lactate to pyruvate, a low level of oxidative metabolism is maintained (Warshaw, 1969), even though at this stage cardiomyocytes contain a very low mitochondrial mass. After birth, the consumption of breast milk provides a diet rich in fatty acids that alters the metabolic balance within the newborn animal, forcing a switch to oxidative metabolism. With the rapid expansion of the cardiac muscular mass, mitochondrial density also increases. This is driven in part by the binding of circulating fatty acids to PPARs, which activate and up-regulate genes involved in mitochondrial biogenesis (Xu et al., 1999). At the same time, fatty acids work to inhibit the uptake of glucose and lactate from circulation, while in the mature heart ATP blocks the action of PFK, a major regulator of glycolytic flux, facilitating maintenance of an oxidative phenotype (Bristow et al., 1987).

These are not the only changes that occur during cardiomyocyte development. The switch in metabolism permits development of the myofibrils, allowing them

to mature. As they develop, particularly between 7-21 days of age, they show a strong rise in active tension and alterations to their calcium binding characteristics (Piquereau et al., 2010). This permits stronger muscular contractions to provide sufficient blood flow to the body, which continues to grow even after the heart has reached adult size. Within the cells, mitochondria also continue to mature even after their rapid expansion in copy number during early post-natal development. In particular, complex II, which is responsible for metabolising fatty acids during oxidative respiration, increases from 54% of its adult value to 76% from between 3-7 days (Piquereau et al., 2010). Meanwhile, complex I, which matures at a slower rate, takes up to 21 days to mature to its adult capacity. The maximum respiratory capacity of mitochondria increases steadily throughout development until final adult maturity.

3.1.4 BUD23 in cardiac disease

While BUD23 has not been directly implicated in any cardiac diseases to date, it is known to contribute to the pathology of Williams-Beuren syndrome (WBS). This is a condition in which approximately 26-28 genes are deleted from chromosome 7, resulting in their haploinsufficiency, including BUD23. Typically, patients will present with distinct facial abnormalities, intellectual disability, stunted growth, and problems with their heart and vascular systems. Exactly which genes contribute to the different aspects of the pathology of WBS remain to the be determined, but one study hypothesised that BUD23 might be responsible in part for the observed cardiac defects (Grzeschik & Doll, 2001). If so, understanding the role that BUD23 plays in the heart could provide valuable insight into the progression of this disorder.

3.1.5 Hypothesis and aims

Overall, we intend to explore the role of BUD23 in a mammalian *in vivo* system. We seek to generate the first viable murine model in which BUD23 can be studied, permitting us to explore both whether its known functions are conserved within mammals, and whether its functions vary within different tissues. In addition, we

aim to see if we can identify a novel metabolic function for BUD23, as hinted at by siRNA screens. **We hypothesise that the knockdown of BUD23 in cardiac and skeletal muscle will result in a defect in translation of metabolic transcripts.**

Aim 1: Develop a viable *in vivo* model to study the effects of BUD23

By crossing BUD23$^{fl/fl}$ mice with mice carrying an MCK-Cre driver, we aim to generate a murine model in which BUD23 is disrupted specifically within cardiac and skeletal muscle. These tissues are rich in mitochondria, and under strong metabolic demand. We will then assess the viability of these animals, as well as any phenotypic effects caused by BUD23 knockdown, to determine if this is a suitable model for investigating the loss of BUD23 in specialised tissue.

Aim 2: Determine if BUD23 is responsible for small ribosomal subunit maturation in a mammalian system

BUD23 has been implicated in the development of the small ribosomal subunit in yeast. However, BUD23 is conserved throughout all eukaryotes, and it is unknown if its functions are the same throughout different organisms. Studies using human immortalised cell lines, such as HEK293 and HeLa cells, have indicated that BUD23 is still responsible for small subunit biogenesis in them. We will further validate this by investigating if the function is conserved within specialised tissues in our *in vivo* knockout system.

Aim 3: Establish if there is a link between BUD23 and metabolic protein production

While we have observed a potential connection between BUD23 and the translational efficiency of metabolic transcripts, this data came from a preliminary study temporarily silencing BUD23 in an immortalised cell culture model and has not previously been described in any yeast studies. We do not know if this is a common conserved function of BUD23 in mammals, or an artifact derived from this particular model. Therefore, we will interrogate whether any connection exists between BUD23 and the translation of metabolic proteins in our *in vivo* model.

3.2 Materials and Methods

Methods specific to this chapter are reported here. All reagents are from Sigma unless otherwise stated.

3.2.1 Cardiac Tissue Mass Spectrometry

Cardiac tissue lysates were prepared for label-free quantification using filter-aided sample precipitation (FASP) in accordance with published protocols (Hernandez-Valladares et al., 2016). In brief, 30 kDa centrifugal filters (Millipore) were prepared for use by the addition of FASP-Urea buffer (8M urea in 0.1M Tris-HCl, pH 8.5), followed by a 20 min centrifugation step at 12,000*g*. Samples were diluted in FASP-Urea buffer to reduce their final SDS concentration to 0.5% before being loaded onto the prepared columns. Samples were spun for 20 minutes, or until the entire sample had passed through the filter. The filter was then washed with a series of wash buffers, including FASP-Urea buffer, 50mM iodoacetamide in FASP-Urea buffer, and 50mM ammonium bicarbonate. Samples were then digested in the column by incubation with trypsin in 50mM ammonium bicarbonate overnight at 37°C. Peptides were eluted using 50mM ammonium bicarbonate before quantification using the Pierce Quantitative Colorimetric Peptide Assay (Thermo Scientific) and final desalting using Pierce C18 tips (Thermo Scientific).

Digested samples were analysed via liquid chromatography tandem-mass spectrometry using an UltiMate 3000 Rapid Separation System (Dionex) coupled to a Q Exactive HF mass spectrometer (Thermo Scientific). Peptide mixtures were separated using a multistep gradient of 0.1% formic acid in 5% acetonitrile for 1 min, up to 7% acetonitrile over 80.5 mins, 18% over 20.5 mins, 27% over 2 mins, 60% over 1 min, held at 60% for 1 min, and reduced to 5% over 14 mins, at a speed of 300 nL min^{-1} using a 75mm x 250µm i.d. 1.7µM CSH M-Class C- 18 analytical column. The final run time was 120 mins. The top twelve precursors were selected for fragmentation automatically by data dependant analysis during each cycle.

The stepped normalised collision energy was centred around 28, and an ionisation potential of 1,900V was used. The survey scan window was set to 300-1750 m/z. MS1 had a maximum injection time of 20ms, with a resolution of 120,000 and a target ion intensity of 3e6, using higher-energy collisional dissociation. MS2 had a maximum injection time of 110ms, with a resolution of 60,000 and a target ion intensity of 2e5. Peptides were dynamically excluded for 15s after one occurrence.

3.2.2 Mass Spectrometry Data Analysis

Mass spectra were analysed using MaxQuant version 1.6.0.16 (Cox & Mann, 2008). The native Andromeda engine was used to search against the Uniprot *Mus musculus* database (accessed 21/12/2017). At least 1 spectra was required for identification, and a minimum of 2 for quantification. Match between runs was selected to mitigate problems with missing values, with retention time set to 1 minute. Carbamidomethyl (C) was used for the fixed modifications parameter, while Oxidation (M) and Acetyl (Protein N-term) were used for the variable modifications. MS1 and MS2 had respective search tolerances of 20ppm and 4.5ppm. All other parameters were left as default.

Output data was further processed using R statistical software (R Core Team, 2017; Wickham, 2009) and Perseus version 1.6.0.7 (Tyanova et al., 2016). Proteins were filtered to remove any entries that were flagged as potential contaminants, part of the decoy reverse database, identified by site only, or belonging to the 'blood microparticle' GO term. Any protein that was only identified in less than half of the total number of samples was also removed. All label-free quantification values were $\log_2$ transformed. Missing values were imputated using a normal distribution (width = 0.3, downshift = 0.18 standard deviations; Lazar et al., 2016). Statistical significance was assessed through four different methods: t-test with a permutation based false discovery rate (s = 0.1), LIMMA, SAM and ROTS (all using FDR $<$ 0.05).

Copy numbers were estimated using the proteomic ruler plug-in (version 0.1.6; Wiśniewski et al., 2014). Proteins were mapped to subcellular localisations using the HeLa spatial proteome database as previously described for cardiac tissue (Doll et al., 2017; Itzhak et al., 2016). Proteins with no localisation data were manually annotated using the Uniprot database, and all proteins listed as 'actin-binding' were further sub-classified into either myofibril or cytoskeletal locations. Interaction networks were built using STRING version 10.5 (Szklarczyk et al., 2019) and exported into Cytoscape (Shannon et al., 2013) for visualisation. Seven data sources were used to determine networks: co-expression, databases, experiments, gene fusion co-occurrence, neighbourhood, and text-mining. PANTHER was used for enrichment analysis (Mi et al., 2017).

3.2.3 Echocardiogram

Mice were placed under light anaesthesia using 1-1.5% isoflurane delivered via a facemask. Heart rate was monitored and kept constant at approximately 450 beats/min. A Vevo 770 High-Resolution Imaging System (Visualsonics) with a 30MHz probe was used to take views for transthoracic echocardiography. M-mode tracings taken over three cardiac cycles were used to determine left ventricular end-diasatolic diameter (LVDD), left ventricular end-systolic diamater (LVSD), posterior wall thickness in diastole (LVPWD), posterior wall thickness in systole (LVPWS), interventricular septum thickness in diastole (IVSD) and interventricular septum thickness in systole (IVSS).

Left ventricular fractional shortening (FS) was calculated as follows:

$$FS = \frac{LVDD - LVSD}{LVDD} * 100$$

Relative wall thickness (RWT) was calculated as follows:

$$RWT = \frac{IVSD + LVPWD}{LVDD}$$

3.2.4 Electrocardiogram (ECG)

Mice were placed under light anaesthesia using 1-1.5% isoflurane delivered via a facemask. Body temperature was monitored and kept constant at approximately 37°C using a heating pad. Needle electrodes were inserted subcutaneously into the right hindlimb, and left and right forelimbs. The Power Lab/4SP system and Chart 7 software (Adinstruments) were used to record lead II ECGs for a period of 5 minutes. The recording was examined for any abnormal P, QRS or T wave shapes, as well as for any irregular variations in timing durations or abnormal beats. Heart rate, RR interval, P wave duration, PR interval, QRS duration, JT duration, and corrected QT duration (Bazett, 1997) were determined from a representative 15s recording segment.

3.2.5 Electron Microscopy

Mice were euthanised via cervical dislocation and their hearts were rapidly dissected out. Tissue was sliced into small cubes (<0.5mm thickness) and fixed overnight in 2.5% glutaraldehyde 2% paraformaldehyde in 100mM sodium cacodylate (pH 7.2). Staining was performed in accordance with published protocols with minor modifications (Holcomb et al., 2013). Briefly, samples were stained with the following, with three 10 min ddH_2O washes between each step: 2% osmium tetroxide 1.5% potassium ferrocyanide in 100mM sodium cacodylate for 1h; 1% thiocarbohydrazide for 20 mins; 2% osmium for 30 mins; 1% uranyl acetate for 16h; and Walton's lead aspartate for 30 mins at 60°C. Samples were then dehydrated through an ascending ethanol gradient from 50% to 100% prior to infiltration with TAAB 812 hard resin with propylene oxide for embedding. Resin blocks were then heated for 40h at 70°C before sectioning using a Leica UC6 ultramicrotome at a thickness of 80nm. Images were acquired using a FEI Tecnai12 Biotwin at 100kV. Computational analysis was performed using Fiji (Schindelin et al., 2012).

Gene Name	Company	Assay ID
Non-targeting control	Thermo Fisher	AM4611
BUD23	Thermo Fisher	s41530
RPS27A	Thermo Fisher	s12339
LTV1	Thermo Fisher	s39727
RIOK2	Thermo Fisher	s224387

Table 3.1: List of siRNAs used in this chapter.

3.2.6 siRNA Silencing

1 x 10^6 A549 cells were seeded in a 10cm cell culture dish. Cells were transfected with either control siRNA or targeted siRNA using DharmaFECT 1 (Horizon) according to the manufacturer's protocols. See table 3.1 for a list of all siRNA species used here.

3.3 Results

3.3.1 Characterisation of cardiac BUD23 deficient mice

$BUD23^{fl/fl}$ mice were generated that exhibited tissue-specific deletion of BUD23 in cardiac and skeletal muscle when coupled to a muscle creatine kinase (MCK) Cre driver. Briefly, the critical exon 7 was chosen for LoxP flanking as it had an uneven splicing phase and thus would generate a frameshift mutation, disrupting the BUD23 protein. Knockdown was confirmed at both the genomic DNA (gDNA) level and the protein level by PCR and western blotting respectively (Fig. 3.1). $BUD23^{fl/fl}$ MCK-$Cre^{-/-}$ littermates were used as wild-type controls. While wild-type bands are also present in the $BUD23^{fl/fl}$ MCK-$Cre^{+/-}$ knockout mice, this is because all analyses were done on whole hearts which contain a heterogeneous population of cells, of which only cardiomyocytes are BUD23 ablated. The significant reduction in BUD23 levels suggests that BUD23 has been disrupted in cardiac muscle but not in

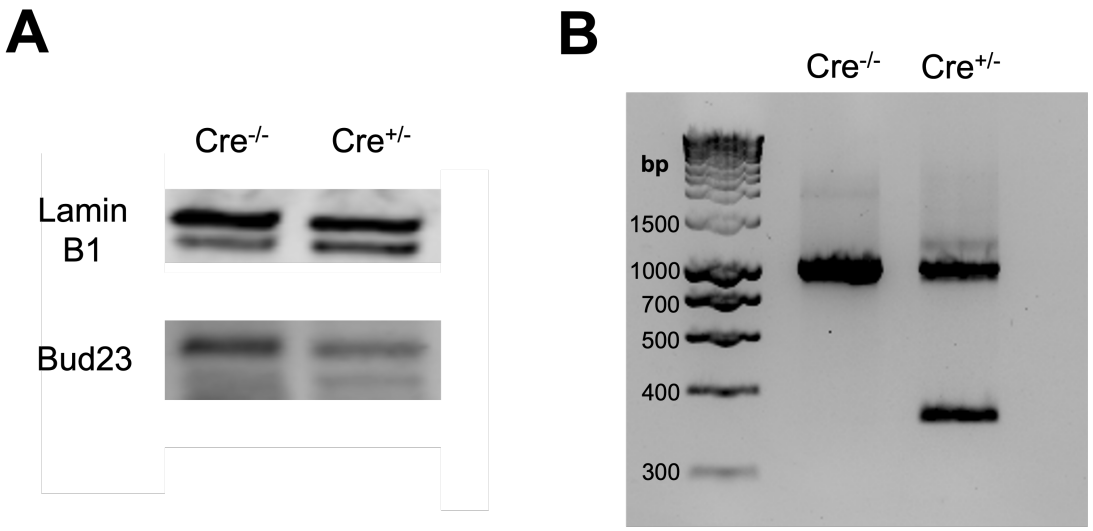

Figure 3.1: MCK-Cre mediated knockdown of BUD23. $BUD23^{fl/fl}$ animals were generated and co-expressed with MCK-Cre to drive recombination. Whole hearts were lysed and analysed to assess for Cre-LoxP excision. (A) Western blot showing a reduction in BUD23 protein levels. BUD23 primary antibody was used at 1:500 dilution. BUD23 is still present in some cell types within the heart as it contains heterogeneous tissue types. (B) PCR amplification of the excised region reveals a ~350bp band in $Cre^{+/-}$ animals, indicating successful recombination. Whole hearts contain a mixed population of cells, and so the ~1000bp wild-type band is also still present.

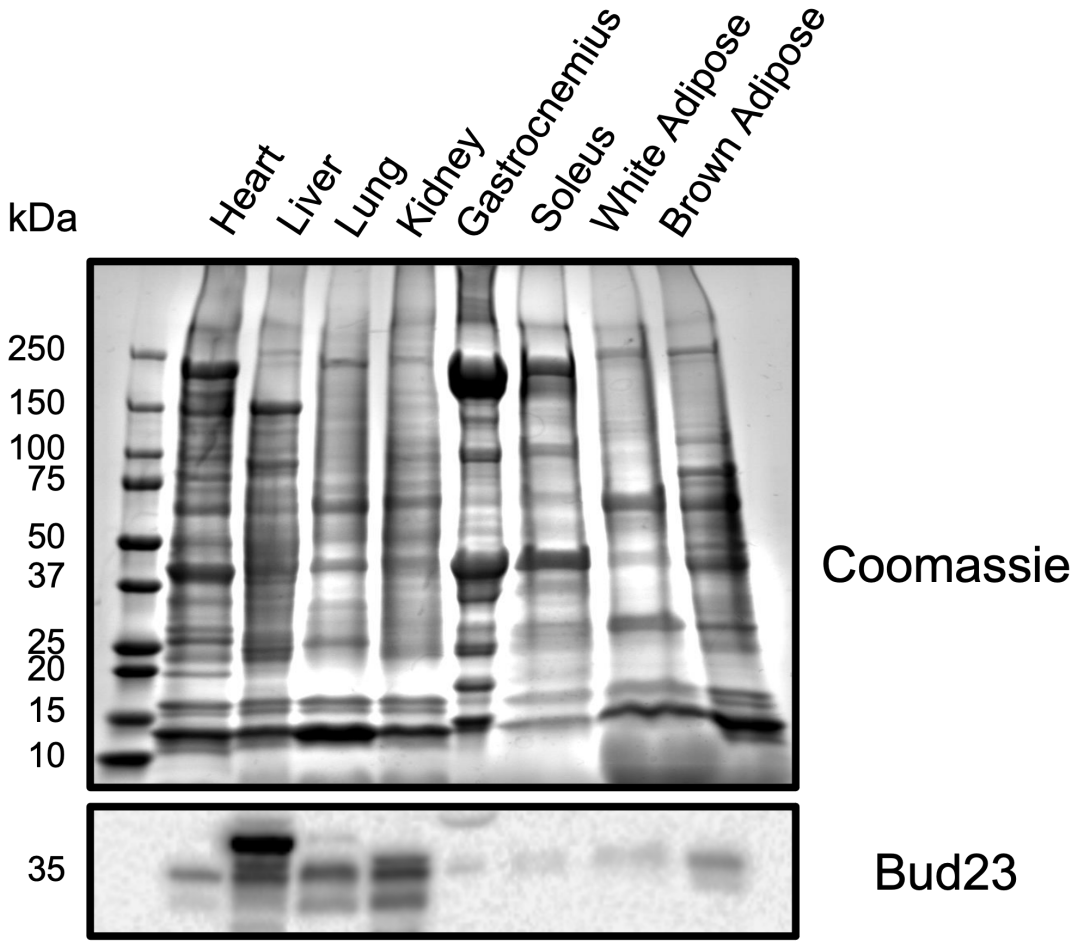

Figure 3.2: BUD23 expression across tissue types. BUD23 protein levels were assessed across a variety of different organs via western blot in wild-type mice. BUD23 primary antibody was used at 1:500 dilution. Coomassie blue staining was used as a control to detect total protein content in each tissue type.

other cardiac tissues. BUD23 protein could not be detected in either the soleus or the gastrocnemius, two different types of skeletal muscle, in wild-type animals (Fig. 3.2).

BUD23$^{fl/fl}$ MCK-Cre$^{+/-}$ mice were viable until the age of approximately 28-35 days, upon which they declined into terminal cardiac failure culminating in death with bilateral pleural effusions (Fig. 3.3A). BUD23$^{fl/fl}$ MCK-Cre$^{-/-}$ mice and BUD23$^{wt/wt}$ MCK-Cre$^{+/-}$ mice were viable and appeared healthy, indicating that the observed phenotype was due to Cre-mediated depletion of BUD23. Mice were taken at 26 days of age and their cardiac morphology examined to investigate

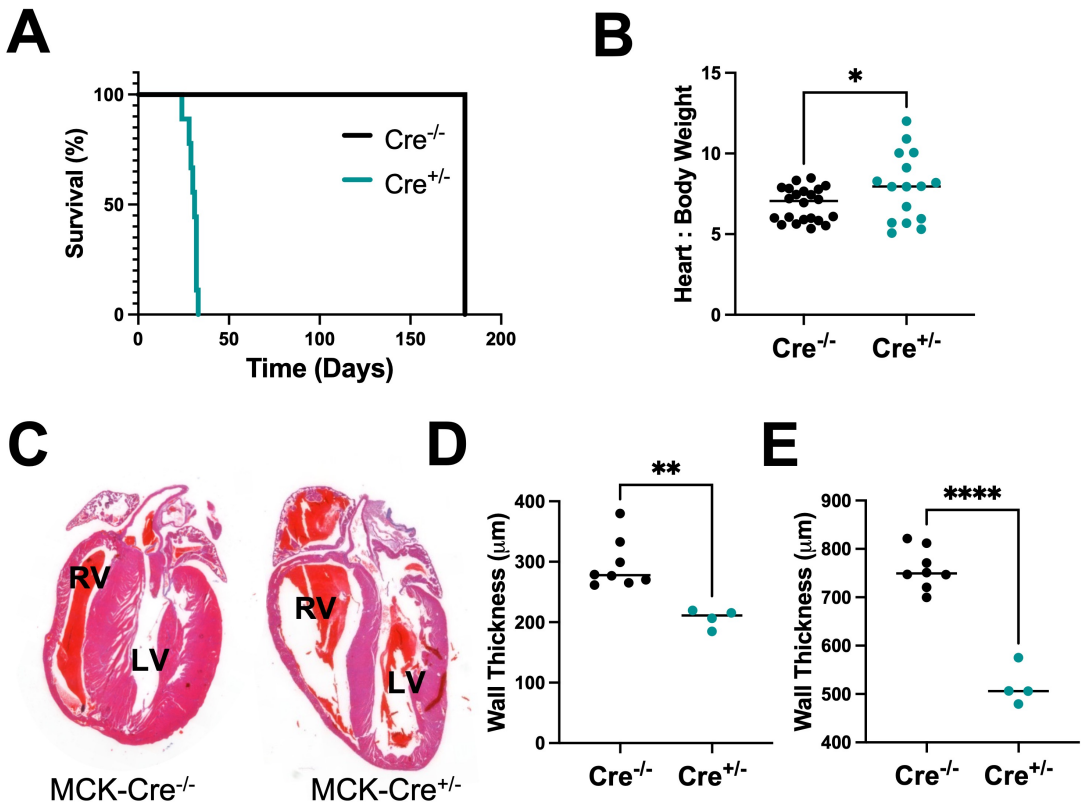

Figure 3.3: BUD23 knockout in cardiac tissue results in cardiac failure. (A) Survival curve comparing BUD23$^{fl/fl}$ MCK-Cre$^{-/-}$ (black) and BUD23$^{fl/fl}$ MCK-Cre$^{+/-}$ (green) (n=8 per genotype). (B) Ratio of heart to body weight (n=16-22 per genotype). (C) H & E staining of 26 day old hearts cut in the coronal plane. (D-E) Analysis of left (D) and right (E) ventricular wall thickness (n=4-8 per genotype). Student's T-test was used for statistical analysis. * indicates p-value $\leqslant 0.05$; ** $p \leqslant 0.01$; **** $p \leqslant 0.0001$

the cardiac failure phenotype prior to terminal decline. Initial observation of the hearts revealed that BUD23 ablation resulted in a significant increase in heart size (Fig. 3.3B), suggesting that cardiomyocytes are undergoing either hyperplasia or hypertrophy. This phenotype is only observed in a subset of BUD23$^{fl/fl}$ MCK-Cre$^{+/-}$ hearts, separating the population into a bimodal distribution, indicating that only some mice enter into cardiac failure at this time point. Histological staining (Fig. 3.3C-E) reveals ventricular dilation together with a concomitant decrease in septum and cardiac wall thickness in BUD23 knockout hearts.

Liver and lungs were taken from the BUD23 knockout animals and assessed for fluid accumulation to identify whether hearts were going into right or left ventricular

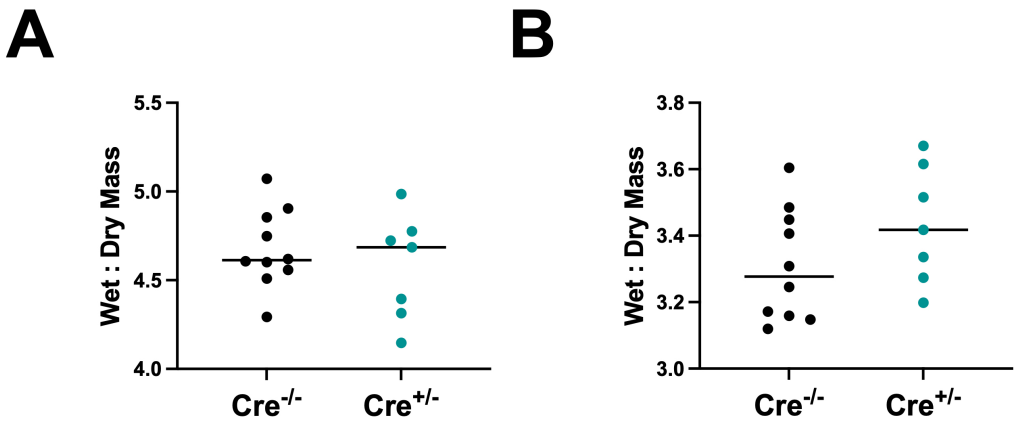

Figure 3.4: No evidence was found of either pulmonary or liver oedema. Wet to dry mass ratios in (A) liver and (B) lung were assessed to establish whether either organ showed signs of fluid accumulation. No statistical difference was observed (Student's T-test, n = 7-10).

failure (Fig. 3.4). However, no indication was found of either pulmonary or liver oedema. This indicates that knockout animals are still entering the early stages of cardiac failure at 26 days of age.

3.3.2 Loss of BUD23 in cardiomyocytes results in dilated cardiomyopathy

In order to assay the exact extent of the observed cardiac defects, we took echocardiograms of BUD23$^{fl/fl}$ MCK-Cre$^{+/-}$ and BUD23$^{fl/fl}$ MCK-Cre$^{-/-}$ mice between the ages of 26-28 days old (n=10; Fig. 3.5A). Loss of BUD23 in cardiac muscle resulted in increased diastolic and systolic diameters, but a decrease in relative wall thickness and fractional shortening in the hearts of knockout animals. Therefore, the loss of BUD23 in these animals results in systolic dysfunction, impairing the ability of the left ventricle to contract and causing a decreased stroke volume.

ECGs also showed abnormalities, with hearts presenting with narrow QRS complexes and significantly decreased corrected QT (QTc) intervals, with no alteration to heart rate (Fig. 3.5B-D). This revealed that signals are being relayed to the ventricles more rapidly than would be expected, a phenomenon that has been linked to various cardiac disorders including sudden cardiac arrest. This is likely a

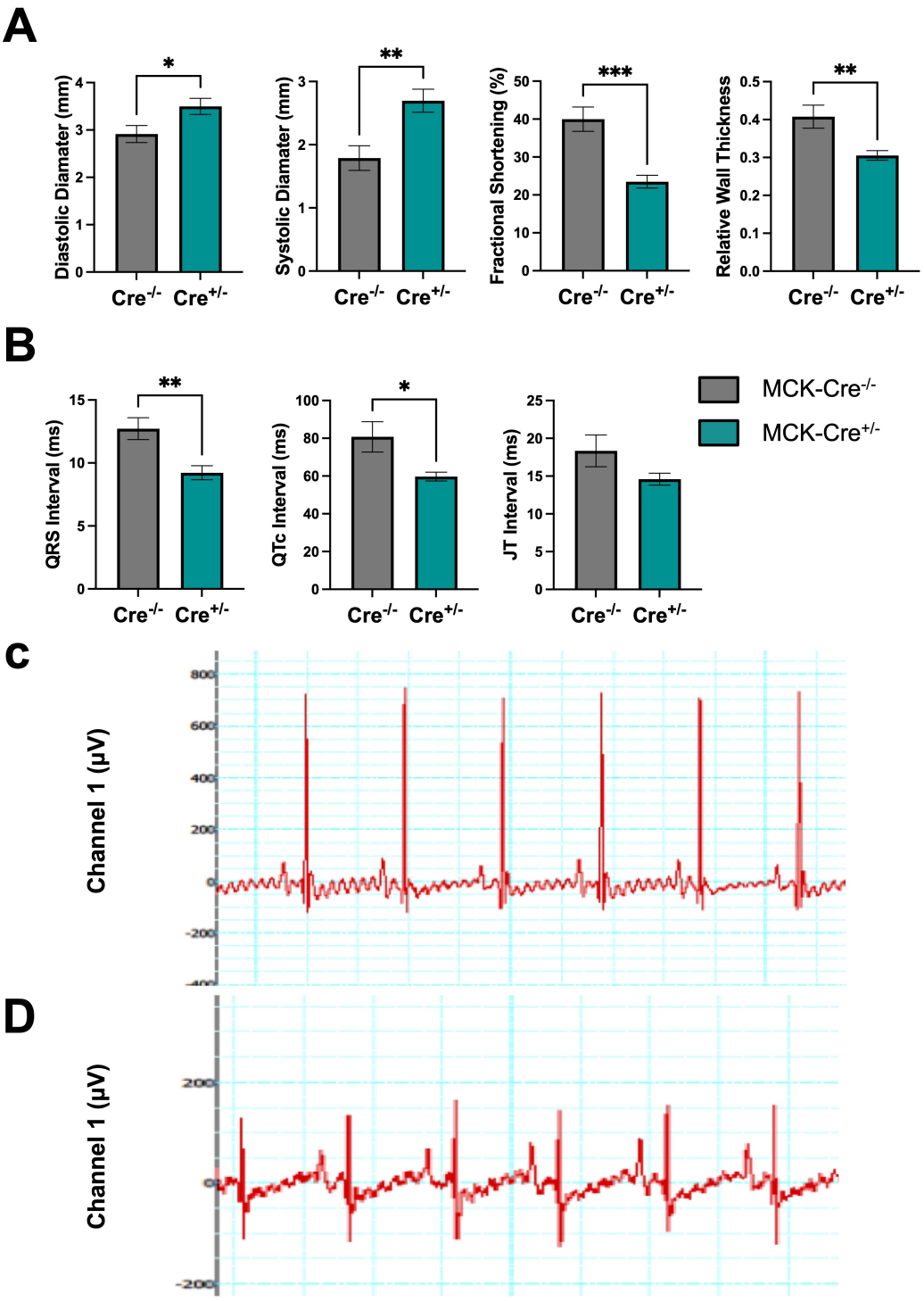

Figure 3.5: Loss of BUD23 in cardiomyocytes results in dilated cardiomyopathy. (A) Echocardiography and (B) electrocardiography were performed on 26-28 day old mice, using littermates as controls. Data is shown for diastolic and systolic diameter, fractional shortening, relative wall thickness, and QRS, QTc and JT interval durations (Student's T-test, n = 10). Values are shown as mean +/- SEM. (C & D) Example ECG traces for (C) MCK-Cre$^{-/-}$ and (D) MCK-Cre$^{+/-}$ animals. * indicates p-value $\leqslant 0.05$; ** $p \leqslant 0.01$; *** $p \leqslant 0.001$

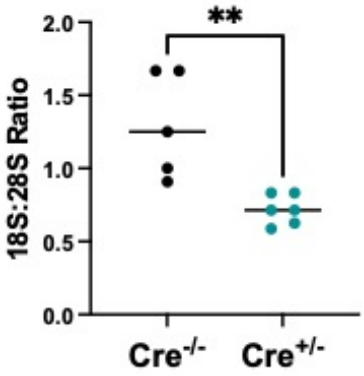

Figure 3.6: Loss of BUD23 results in ribosomal subunit imbalance. The ratio of small to large ribosomal subunit was measured via TapeStation to investigate for a ribosomal maturation defect (Student's T-test, n = 5-6). ** indicates p-value $\leqslant 0.01$

consequence of the observed structural defects. Overall, this indicates that mice have severely impaired cardiac function, resulting in systolic dysfunction, impairments in ventricular signalling, and ultimately culminating in early death in these animals.

3.3.3 Ribosomal maturation is disrupted in BUD23 deficient hearts

BUD23 has previously been implicated as a crucial element in ribosomal small subunit maturation. In order to determine whether ribosomal maturation was disrupted in BUD23-deficient and wild-type hearts, isolated RNA from whole heart lysates was run on a TapeStation, an automated electrophoresis system. Hearts from mice of mixed ages, ranging from 21 to 27 days old, were used. The 18S:28S subunit ratio was significantly disrupted in hearts lacking BUD23, consistent with our hypothesis that small ribosomal subunit maturation would be disrupted in the cardiac muscle of these animals (Fig. 3.6). No significant differences were found due to age in hearts of animals from the same genotype, an interesting finding that indicates that failures in ribosomal maturation occur at an early timepoint in these mice.

3.3.4 BUD23 is essential for correct regulation of translational and metabolic processes

To determine the underlying cause of the cardiac myopathy and how it is linked to the observed ribosomal defect, we decided to take a proteomic approach. Label-free quantification (LFQ) was performed on 26 day old knockout ($BUD23^{fl/fl}$ MCK-$Cre^{+/-}$) and control ($BUD23^{fl/fl}$ MCK-$Cre^{-/-}$) whole heart homogenates (n=3 per genotype). This point was chosen as it occurs just prior to terminal decline, in order to enable observation of the causal factors leading to cardiac decline, rather than the effects thereof. The two groups showed very strong separation via principal component analysis, with 54.32% of all variation explained by one component (Fig. 3.7A). Both groups clustered strongly and separately from each other. Although BUD23 deficient hearts were more dispersed, this can be explained by differing onset times of cardiac failure, and all show higher degrees of relation to each other than to controls.

Initially, a total of 2,995 proteins were identified, of which 2,047 were selected for further analysis after filtering to remove potential contaminants and proteins detected in less than half of all samples. In current literature, a variety of potential statistical methods are available for determining the significance of differentially expressed proteins. However, there is no singular consensus on which method should be used. We therefore tested four different statistical methods and assessed what proportion of proteins were deemed to be differentially expressed between knockout and control animals (Fig. 3.7B). We identified 658 proteins that were significantly different according to all four tests, which constituted the main bulk of differentially expressed proteins identified by any test. LIMMA was the most stringent test, excluding 129 proteins that were called as differentially expressed by the other three tests. SAM and ROTS were the least stringent, identifying another 70 proteins between them, and a further 131 just by SAM. We opted to use t-tests with a permutation based FDR (s0=0.1, FDR <0.05), as they were the most stringent

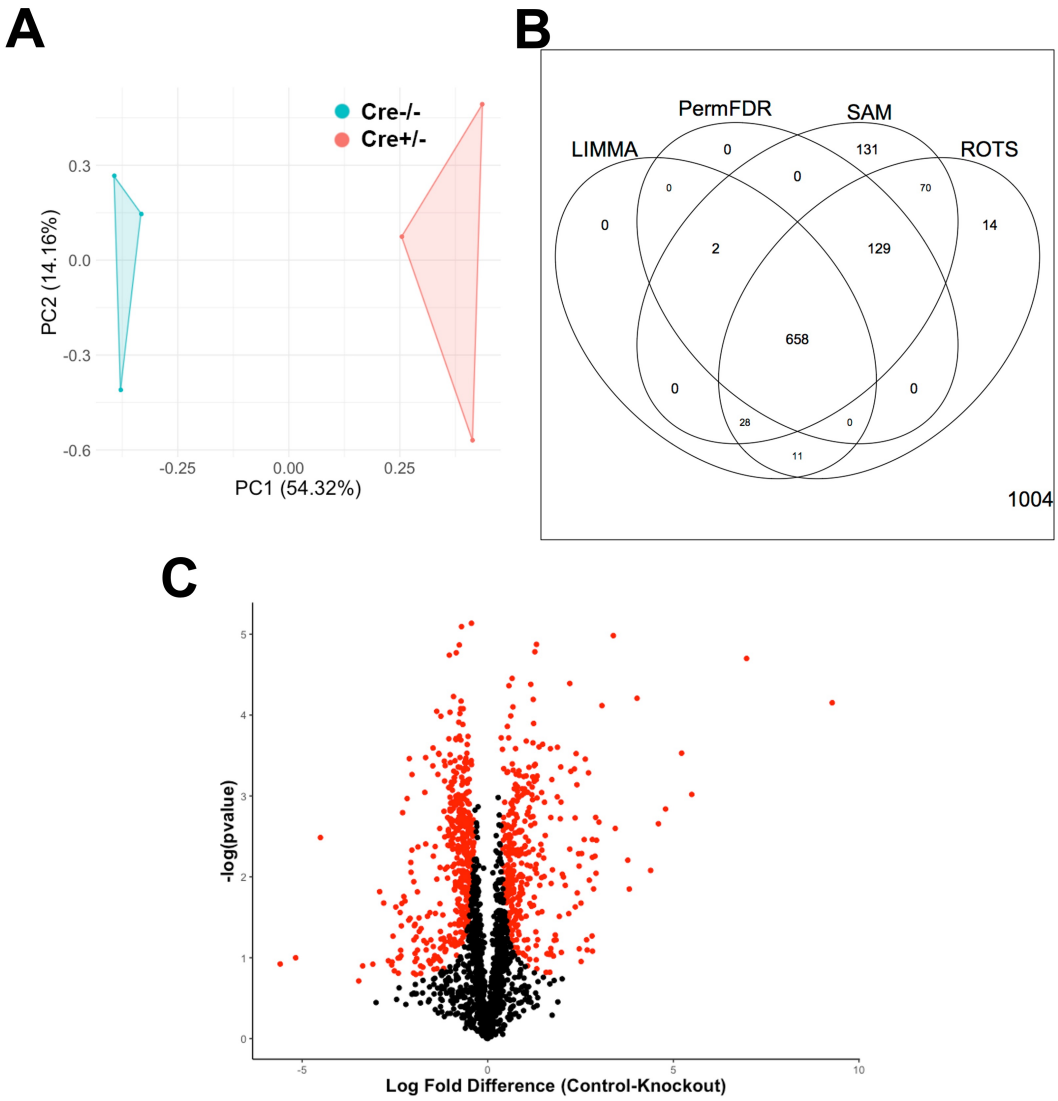

Figure 3.7: Proteomic analysis of BUD23 knockout cardiac tissue revealed a large translational shift. Label-free proteomics was performed on cardiac homogenates from 26 day old knockout ($BUD23^{fl/fl}$ MCK-$Cre^{+/-}$) and control ($BUD23^{fl/fl}$ MCK-$Cre^{-/-}$) animals (n=3 per genotype). (A) Principal component analysis shows a clear separation between wild-type and knockout hearts. (B) Number of proteins that were identified as differentially expressed by four different statistical algorithms. (C) Volcano plot showing significantly differentially expressed proteins between wild-type and knockout hearts (red; FDR < 0.05, s0 $= 0.2$).

algorithm apart from LIMMA, and otherwise only called proteins that were also identified by at least 3 tests total, which LIMMA would have excluded.

This statistical approach identified that 347 proteins were up-regulated in BUD23-knockout hearts relative to control wild-type hearts, and 442 proteins were

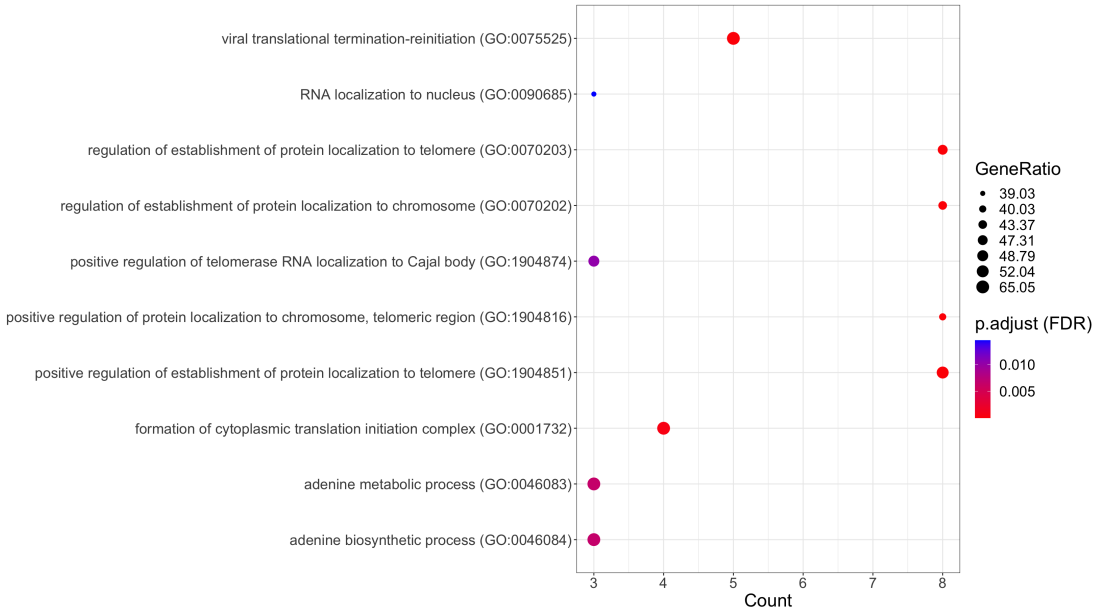

Figure 3.8: Over-representation analysis of upregulated proteins. Analysis of proteins that were significantly up-regulated in response to BUD23 knockdown in cardiac tissue was performed using Panther. The top 10 significantly over-represented biological process terms are shown.

down-regulated (Fig. 3.7C). Gene ontology analysis was performed on both groups of proteins to investigate pathway enrichment.

Up-regulated proteins were mapped to purine biosynthesis, nitrogen compound metabolism, mRNA binding, ribosomal transport, translation initiation, cajal body transport, and proteasomal pathways (Fig. 3.8). The heavy investment in translational equipment, taken together with the defect in the 18S:28S ribosomal ratio suggests that the cells are under heavy burden to produce more proteins, potentially as a consequence of faulty protein synthesis. However, as some terms relating to nucleic acid synthesis are up-regulated, cardiomyocytes may also be under heavy replicative stress, or be trying to up-regulate mRNA levels to compensate for a reduction in protein production.

Analysis of the down-regulated group revealed three tight clusters of protein groups – namely ones involved in carbon metabolism, mitochondria, and mitochondrial ribosomes (Fig. 3.9). Enrichment was also shown in myofibrillar proteins. This implies a strong metabolic defect coupled with a rise in translational demand,

leading to cardiovascular remodelling and death due to an impaired ability to meet cellular energy demands.

In addition, application of the proteomic ruler technique, which can be used to help quantify protein levels in label-free mass spectrometry by estimating levels of histone proteins within specific cell types, revealed that cells had less overall protein per cell (Fig. 3.10). This further points to a gross translational defect upon disruption of BUD23.

3.3.5 Loss of BUD23 strongly affects mitochondrial protein expression

Mitochondrial proteins were extremely susceptible to the effects of BUD23 ablation (Fig. 3.11A). Annotation of proteins by sub-cellular compartment revealed a 4.6% loss in mitochondrial mass as a proportion of total protein mass, which was the source of the main loss of protein content. Out of 481 total mitochondrial-associated proteins detected, 219 were down-regulated and only 20 up-regulated, with a further 242 showing no significant fold change difference (Fig. 3.11B). This corresponds to approximately half of the total down-regulated proteins.

While mitochondria encode their own genome, this is very limited and contains only 13 genes, leaving them dependent on genomically encoded accessory proteins to form the bulk of their proteome. Out of those 13, only 10 were identified at detectable levels in the proteomics dataset. However, only two, mt-ND1 and mt-CO2, were reduced, with the others showing no significant difference between knockout and control hearts. This indicates that the mitochondrial defect is particularly prevalent amongst genomically encoded mitochondrial proteins, and that mitochondrially encoded species are not as affected. This fits with the fact that BUD23 is known to have a role in nuclear encoded translation, and has no known effect on mitochondrial ribosomes. Mitochondrial ribosomes are very different from standard ribosomes, and have their own control mechanisms independent from those governing nuclear encoded translation.

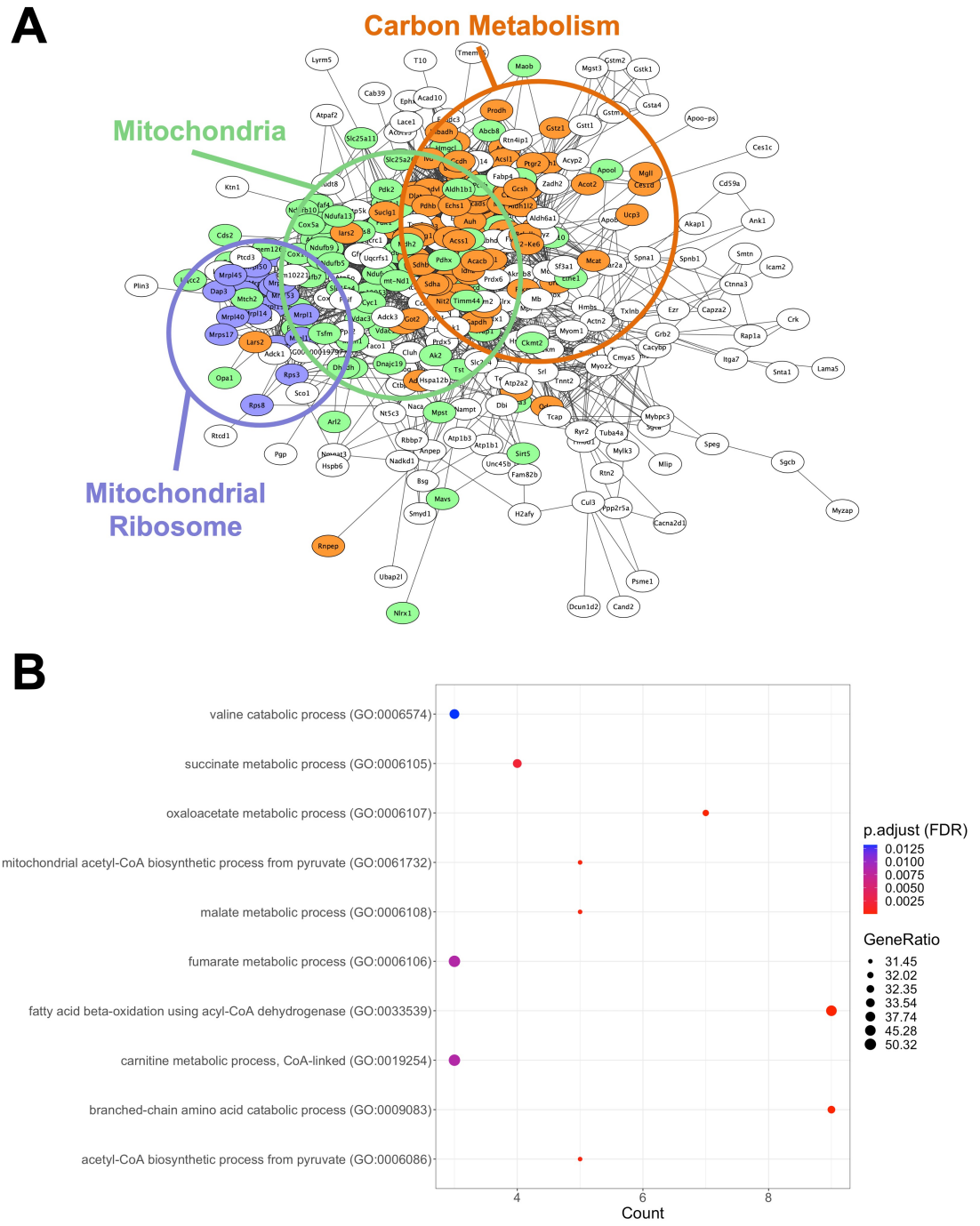

Figure 3.9: Evidence of a strong metabolic signature in down-regulated protein terms. Gene ontology analysis of proteins that were significantly down-regulated in response to BUD23 knockdown in cardiac tissue was performed using Panther. (A) Proteins clustered into three main groups, those involved in 'carbon metabolism', 'mitochondria' and 'mitochondrial ribosome'. (B) The top 10 significantly over-represented biological process terms are shown.

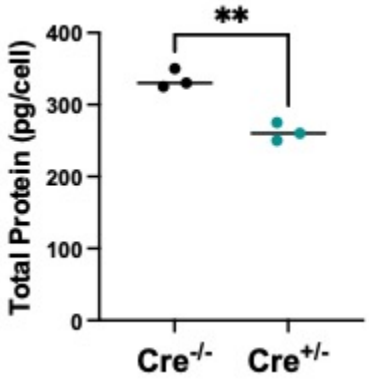

Figure 3.10: Cardiomyocytes lacking BUD23 show a reduction in overall protein content. Application of the proteomic ruler technique, which uses histone data from the proteomic data set to estimate protein content relative to cell number, revealed a potential difference in cellular protein content (Student's T-test). ** indicates p-value $\leqslant 0.01$

Analysis of the up-regulated mitochondrial proteins shows no significant enrichment, with proteins unable to cluster into a functional network. Gene ontology terms include various structural and envelope proteins. However, down-regulated proteins form a tight network containing proteins associated with oxidation-reduction, various metabolic processes, and mitochondrial ribosomes. The remaining unchanged proteins cluster neatly into two groups of mitochondrial ribosome-associated proteins

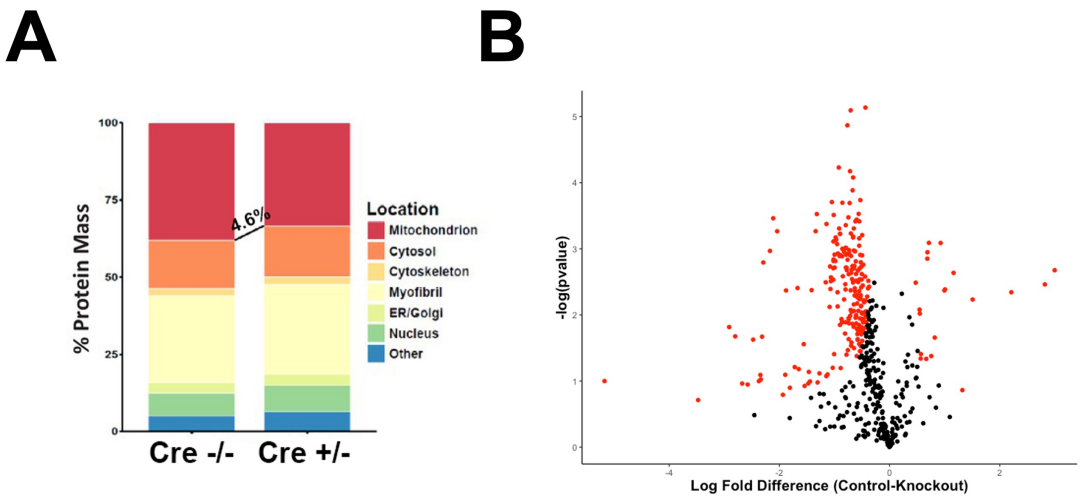

Figure 3.11: Mitochondrial proteins are particularly susceptible to loss of BUD23. (A) Annotation of proteins by subcellular location reveal a 4.6% decrease in relative mitochondrial mass. (B) Volcano plot showing significant up- and down-regulated mitochondrial proteins in red.

and the remaining oxidation-reduction proteins.

3.3.6 Mitochondrial function and density are reduced in BUD23 ablated cardiac tissue

Given the observed impact on mitochondrial protein expression, we wanted to examine whether loss of BUD23 constituted a loss of mitochondrial function. By using mitochondrial genome copy number as a proxy for number, we identified that BUD23 deficient cardiac tissue showed a significant reduction in mitochondrial content (Fig. 3.12A). Citrate synthase levels were also significantly lower in $Cre^{+/-}$ hearts, which is a secondary measure of mitochondrial density (Fig. 3.12B). Functional analysis was performed using the Oroboros microrespirometry system. Analysis of cardiac homogenates revealed that BUD23 knockout animals had reduced routine respiratory rates and lower maximal respiration rates, but had no change in LEAK respiration, which corresponds to the mitochondria's inactive state (Fig. 3.12C). As a result, their respiratory control ratios are also reduced, indicating that they are unable to produce energy as efficiently. Analysis was performed in two ways, in one normalising to protein content, and in one normalising to mitochondrial density. In both cases, mitochondria performed worse even when taking into account their reduced numbers, indicating that their function is compromised in addition to their density.

To investigate whether the effects of mitochondrial dysfunction caused any gross morphological differences, we used electron microscopy to study the mitochondria within BUD23 deficient cardiac tissue. Interestingly, despite their reduced number and apparent dysfunction, mitochondria appeared normal with no obvious differences in size, and presenting with intact membranes and folded cristae (Fig. 3.13). However, the overall architecture of the cardiomyocytes was disrupted. In wild-type tissue, mitochondria typically lie in strict arrangement against myofibrils to ensure efficient ATP transfer. Loss of BUD23 resulted in altered cellular architecture, with mitochondria forming disorganised clumps within the tissue. Furthermore, electron dense inclusion bodies were identified within mitochondria from BUD23 deficient

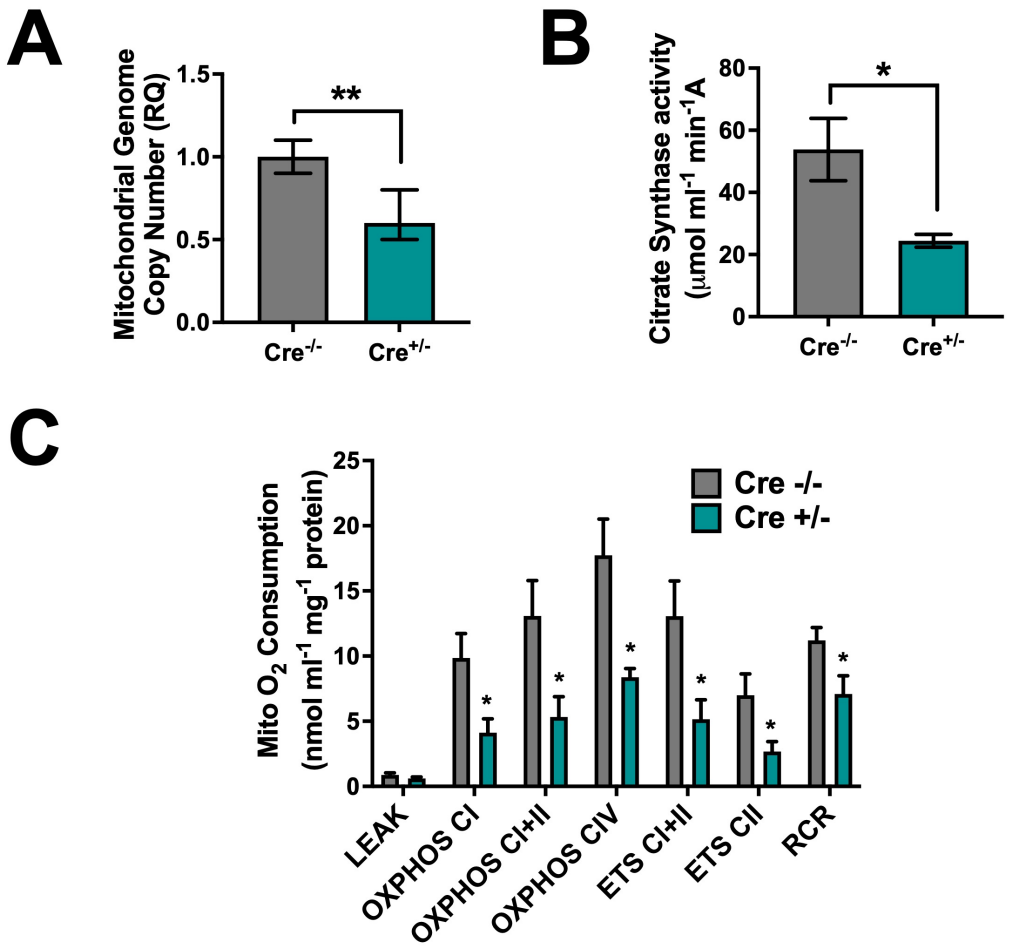

Figure 3.12: Mitochondrial number and function are reduced in BUD23 disrupted cardiac tissue. (A) Mitochondrial genome copy number was measured via qPCR, normalised against autosomal genome copy number (n=6). (B) Citrate synthase activity was measured in homogenised cardiac tissue as a secondary marker for mitochondrial density (n=6). (C) Functional analysis of mitochondrial respiration using the Oroboros system. LEAK respiration with Complex I substrates; oxidative phosphorylation in the presence of ADP (OXPHOS) through complex I, I + II, or IV; ETC maximal respiration rate through complex I + II or II; RCR respiratory control ratio. Values are shown as mean +/- SEM. * indicates p-value $\leqslant 0.05$; ** $p \leqslant 0.01$

tissue. Inclusion bodies in mitochondria are not a well described phenomena, but previous studies have hypothesised that they may be produced as a compensatory mechanism for increased bioenergetic demand (Jacob et al., 1994).

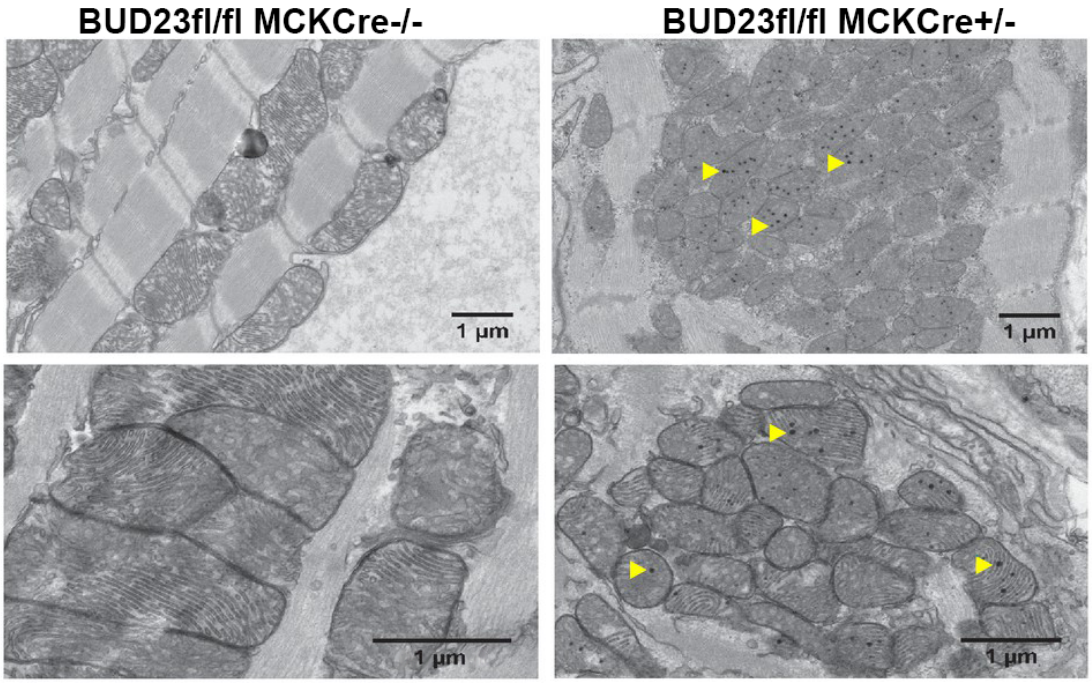

Figure 3.13: Mitochondrial morphology is not altered despite mitochondrial failure. Electron microscopy of wild-type (left) and knockout (right) cardiomyocytes. While overall mitochondrial morphology is not disturbed, the presence of electron dense inclusion bodies can be observed in BUD23$^{fl/fl}$ MCK-Cre$^{+/-}$ hearts (yellow arrows).

3.3.7 Metabolic gene transcription is induced under BUD23 knockdown

To assess the origin of the identified metabolic defect, qPCR analysis was performed on a panel of metabolic and mitochondrial-associated transcripts in hearts from 26 day old mice (Fig. 3.14). A significant induction was found in PGC1a and PGC1b in BUD23 knockout hearts, which are both strongly implicated in mitochondrial biogenesis, and have also been linked to glucose and fatty acid metabolism. In addition, mt-ND1 transcripts were significantly increased, but no change was found in levels of TFAM. As the mitochondrial genome is polycistronic, an increase in mt-ND1 transcripts, which is a mitochondrially encoded gene, implies that all mitochondrially encoded transcripts are up-regulated, as they are all transcribed together and later undergo auto-splicing into mature mitochondrial mRNA. TFAM is a transcription factor responsible for the initiation of mitochondrial genome transcription. The lack of induction in TFAM raises questions as to the mechanisms

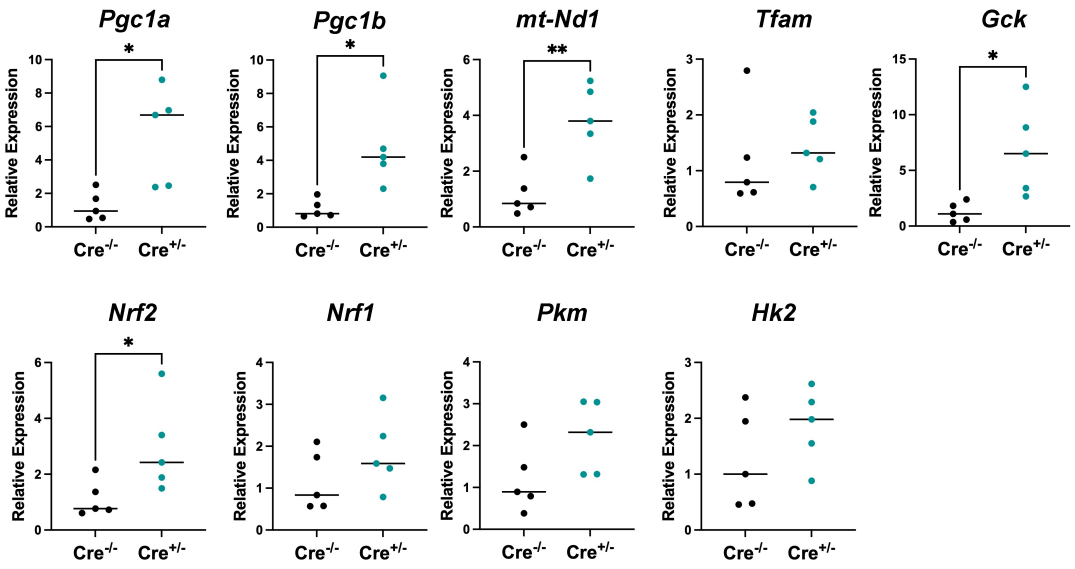

Figure 3.14: qPCR analysis of metabolic and mitochondrial mRNA transcripts in BUD23 knockout hearts. All data is shown as relative fold change expression (Student's T-test). * indicates p-value $\leqslant 0.05$; ** $p \leqslant 0.01$

contributing to increased levels of mitochondrial transcripts.

Induction of NRF2 was also found with BUD23 knockdown, which is an essential gene responsible for modulating signalling in response to oxidative stress. NRF1, a transcription factor implicated in mitochondrial biogenesis and regulation of metabolic processes, was also probed for but no significant difference was found in relative expression data. Finally, under the assumption that oxidative respiration was impaired in the BUD23 knockouts, genes involved in glycolysis were analysed to investigate if there was any shift in metabolic mechanisms utilised by the heart. GCK was found to be significantly elevated, while both PKM and HK2 appeared to show an upward trend by eye but produced no significant change between genotypes. This indicates that the cardiomyocytes may be trying to switch to glycolysis to compensate for a reduction in mitochondrial function.

3.3.8 Disruption of metabolic protein translation is not caused by alterations to ribosomal biogenesis

BUD23 has two independent functions: to impart the m7G methyl mark on the small ribosomal subunit, and to promote small subunit maturation - specifically through

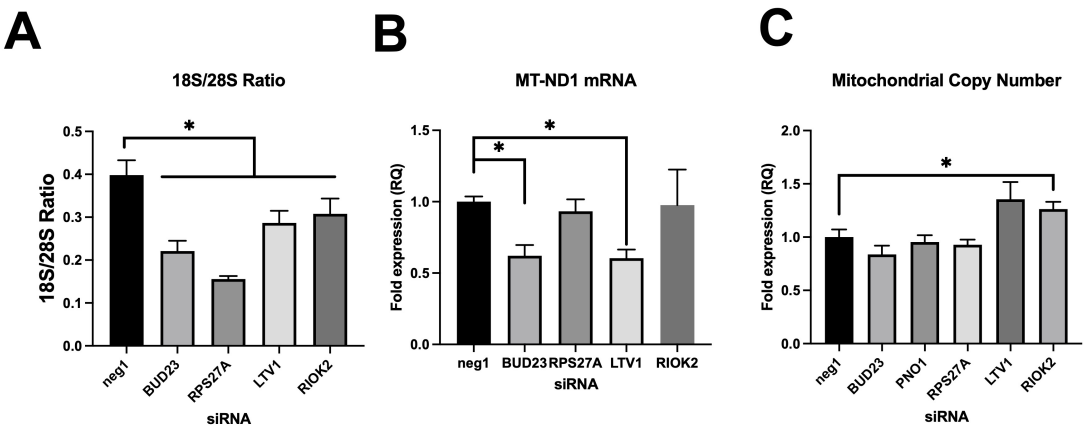

Figure 3.15: Alterations to ribosomal subunit biogenesis do not cause a metabolic phenotype. A549 cells were treated with either control siRNA (neg) or siRNA targeting ribosomal biogenesis genes. (A) 18S/28S ratio was measured to confirm ribsomal biogenesis defect. (B) mt-ND1 expression was assessed via qPCR to determine if there was an increased drive for mitochondrial transcription. (C) Mitochondrial copy number was used to determine the relative quantity of mitochondria. * indicates p-value $\leqslant 0.05$

the 18SE phase. To determine whether the observed defects in mitochondrial and metabolic protein translation where due to the specific actions of BUD23, and not a generic consequence of 18S:28S ribosomal subunit disruption, we screened other known small ribosomal biogenesis factors to see if their knockdown also resulted in mitochondrial disruption (Fig. 3.15).

We used siRNA to knock down the expression of LTV1, RIOK2 and RPS27A in A549 cells. The first two are known ribosome biogenesis factors, while the latter is a small ribosomal subunit associated protein that has been implicated in subunit balance (Sloan et al., 2019). Knockdown of all three resulting in a significant reduction in their 18S:28S ratios, indicating that all cause a subunit imbalance similar to BUD23 knockdown. While LTV1 showed a reduction in mitochondrial transcript levels, similar to BUD23 siRNA knockdown, the other two showed no significant differences. In addition, none showed a decrease in their mitochondrial copy numbers. However, it is important to note that in this model, BUD23 knockdown also does not cause a reduction in mitochondrial number, unlike in mice, which may be a reflection of the shorter duration of knockdown due to

siRNA's transient nature. Overall, we were unable to find a definitive link between small subunit biogenesis and a mitochondrial phenotype.

This implies that the observed defects in translation of proteins involved in carbon metabolism and mitochondrial function are not a common feature of small to large ribosomal subunit imbalance. They are instead a specific consequence of BUD23 knockdown.

3.4 Discussion

BUD23 is tightly conserved across all eukaryotes, yet whether its functions are equivalent in different organisms has yet to be determined. With the aim of exploring the physiological role of BUD23 *in vivo*, we generated a conditional BUD23 floxed mouse, that when co-expressed with a MCK-Cre driver resulted in selective ablation of BUD23 in cardiac muscle. Knockout animals showed a strong cardiac failure phenotype, but remained viable until approximately 30 days of age. By taking mice at 26 days of age, we were able to assess their phenotypic differences before they entered into terminal cardiac decline, constituting the first viable mammalian BUD23 knockout model. Unfortunately, while previous literature has suggested that BUD23 should be highly expressed in skeletal muscle, we were unable to detect BUD23 in either the soleus or the gastrocnemius, as evidenced by anti-BUD23 western blotting. As such, the bulk of our analysis was focused on the heart.

Previous studies in yeast have revealed that BUD23 serves two independent functions: for rRNA maturation and as a methyltransferase. Both have been shown to be conserved in immortalised human cell lines, where BUD23's presence is crucial for the m7G methylation of G1639 on the human small ribosomal subunit (Haag et al., 2015). Through analysis of the 18S:28S ribosomal subunit ratio, we have shown that BUD23 is also responsible for correct ribosomal biogenesis in our model, consistent with previous findings. This highlights that these core functions appear to be conserved across multiple organisms, including within mammals.

Mice lacking BUD23 in their cardiac muscle presented with cardiac dilation, a large increase in total heart weight, thinning of the ventricular wall, and systolic dysfunction. Death at this time-point is an interesting phenomenon, as while the heart undergoes heavy developmental remodelling in the postnatal animal, most of the cellular cytoarchitecture is fully organised by the age of 7 days (Piquereau et al., 2010). However, subtle changes continue to occur after this phase as the cardiac tissue continues to mature towards an adult phenotype. In particular, myofibrils show a rise in active tension and alter the characteristics of their calcium binding.

While calcium sensitivity is relatively stable at this developmental stage, the hill coefficient of the interaction increases, meaning that myofibrils have a much stronger affinity for subsequent calcium ion binding after binding of the first ligand (Piquereau et al., 2010). In addition, the maximum respiratory capacity of cardiac mitochondria continues to increase even after 21 days of age, and their binding affinity for ADP shows a concomitant rise. This is accompanied by a decrease in the heart weight to body weight ratio as the mouse continues to grow, demonstrating a strong metabolic burden on the cardiac system. Death at this late developmental stage indicates that BUD23 ablated mice may be unable to meet the required metabolic demands, resulting in gross structural abnormalities due to the underlying metabolic deficit. This leads to ventricular failure, and ultimately cardiac death.

Proteomic analysis of BUD23 ablated hearts supports this theory, revealing a major imbalance between translational machinery and metabolism, with a particularly strong mitochondrial defect. These two cellular processes are highly intertwined, with translation forming one of the highest bioenergetic demands of the cell, and thus rendering it dependent on correct mitochondrial function. In particular, the mammalian target of rapamycin (mTOR) has been implicated as a key regulator of metabolic and translational flux (Morita et al., 2013). mTOR acts by inhibiting eukaryotic translation initiation factor 4E binding proteins, thus inducing translation of genomically-encoded mitochondrial transcripts and ultimately driving ATP generation and mitochondrial biogenesis. It is also responsible for the regulation of various ribosomal kinases, and is susceptible to changes in nutrient levels, creating a malleable system by which it can alter these two key processes. However, mTOR was not expressed at a high enough level to cross the detection threshold for mass spectrometry, and so was not present in our dataset for analysis. Targeted methods may be more appropriate to investigate if mTOR signalling is implicated in BUD23 ablation.

Proteins assigned the GO term ‘translation’ were up-regulated in the BUD23 knockout hearts. However, the ratio of large to small ribosomal subunit was strongly

disrupted, showing a significant decrease in 18S rRNA levels. This implies that the absence of BUD23 is causing stalling of small ribosomal subunit maturation at the pre-18SE phase, and therefore does not permit correct ribosomal function. An up-regulation in translational proteins may be indicative of a compensatory mechanism, in which poor translational efficiency is compensated for by overproduction of ribosomal material. In addition, proteasomal proteins are also elevated. This indicates that many proteins are either being incorrectly translated, processed, or folded, and therefore are marked for degradation, further highlighting a translational defect. BUD23 plays two roles in the ribosome, not only to mature the small subunit, but also to impart a methyl mark near the tRNA P-site. While a reduction in global ribosome levels would explain the increase in translational proteins, it is insufficient to explain why the generated peptide sequences are being degraded by the proteasome. Therefore, we implicate that the methyl mark may be essential for correct processing and folding of the nascent polypeptide strands.

In further support of this, estimation of protein content per cardiac cell revealed a significant decrease in protein levels in BUD23 knockout hearts. However, it is important to note that the proteomic ruler technique applied bases its approximation on histone levels, which are consistent across cells with the same haplotype. However, approximately one third of all cardiomyocytes are binucleated, with more frequent multinucleation events being tied to some forms of cardiac failure (Kajstura et al., 1998). As such, this estimate may not be accurate. More importantly, the rate of binucleation in BUD23 ablated cardiomyocytes has not currently been investigated, so we cannot definitively conclude that protein content is reduced, but may instead be detecting a further karyokinetic defect. There is some evidence to support that this might be the case, as terms relating to proliferation such as 'purine biosynthesis' and 'cajal body trafficking' were also up-regulated in the proteomics dataset. However, it is currently unknown whether the cells are actively proliferating and have failed to terminally differentiate during earlier cardiac development, giving rise to our phenotype, or if this is a karyokinetic defect and it is causing multinucleation events. It is also possible that these terms are instead tied to a global increase

in transcription to compensate for the observed translational defect, and not an indication of a true proliferative phenotype.

As expression of translational machinery appears to be up-regulated, it would be expected that metabolic processes would also be heightened to meet the increased bioenergetic demands of the cells. However, mitochondrial protein mass is instead reduced by 4.6% in the BUD23 knockout hearts as a proportion of total protein mass. In addition, down-regulated proteins cluster strongly into three groups: carbon metabolism, mitochondrial proteins, and mitochondrial ribosomes. Around half of all the proteins down-regulated upon BUD23 knockdown are localised in the mitochondria. These all suggest a specific metabolic defect, which is further demonstrated by a reduction in mitochondrial number and function. Preliminary studies in human immortalised cell lines also support this theory, as a potential tentative link between BUD23 and metabolism was hinted at through siRNA studies. However, expression of various metabolic and mitochondrial genes is increased at the transcript level in the knockout mice, indicating that the disruption occurs during translation. The particular reduction in genomically encoded mitochondrial proteins reveals a highly selective defect impacting on specific sequences – although no consensus sequence or structure has yet been determined to explain this specificity. The mechanism linking BUD23 to this defect has not been identified, however we have shown that there does not appear to be a clear link between ribosomal subunit balance and mitochondrial dysfunction through the analysis of three other small ribosomal subunit associated proteins. As such, we conclude that mitochondrial and metabolic dysfunction are a specific consequence of BUD23 knockdown, and may be linked to BUD23's other function - deposition of a methyl mark. This modification may be essential for regulating the correct translation of metabolic proteins. However, more in depth work is required to fully delineate the two functions to verify this.

Overall, we have successfully generated the first viable *in vivo* BUD23 knockout model, where we selectively disrupted BUD23 expression within cardiac muscle. We hypothesise that BUD23 is serving a two-fold purpose within cardiac tissue.

Firstly, it is essential for the maturation of the small ribosomal subunit, and its absence promotes a strong, global translational defect within cardiomyocytes. This is consistent with previous findings from yeast, and indicates that this function is conserved across multiple organisms. However, it has a secondary action of selectively controlling metabolic translation, potentially via its impartment of the methyl mark. While the faulty translational equipment creates a strong metabolic burden on the heart in BUD23 knockouts, the mitochondrial system is failing in parallel and unable to produce sufficient ATP, ultimately resulting in death via systolic cardiac failure. As such, we have implicated BUD23 as a key regulator of metabolic gene translation, and have further substantiated the evidence that it is essential for ribosomal maturation. This is a novel function of BUD23 that has not been identified in yeast. Whether it is a specific function within cardiac tissue, or a more general finding, remains to be determined. Future work should focus on studying BUD23 in other specialised tissues - especially those heavily implicated in metabolic function.

3.5 Acknowledgements

Matthew Baxter, for initiating the project and providing good mentorship. Gina Galli, for assisting with the Oroboros analysis. Christian Pinali, for his expertise with electron microscopy. The University of Manchester Biological Mass Spectrometry Core Facility, for running the proteomics mass spectrometry. Toryn Poolman, for taking the time to teach me proteomics analysis pipelines.

4

BUD23's function in thermogenesis in adipose tissue

Contents

4.1 Introduction

The development of the floxed BUD23 cardiac knockout model (established in Chapter 3) has revealed novel insights into the workings of BUD23 within mammalian organisms. In particular, it revealed a novel functionality for BUD23 as a master controller of mitochondrial function through attenuation of translation. However, some large questions remain unanswered as to the exact mechanism of action of BUD23, and it is unclear if this mitochondrial phenotype is a specific consequence of the cardiac model, or if it is a more general, but previously unidentified, BUD23 phenotype.

Unfortunately, the severity of the cardiac phenotype shown by the MCK-Cre BUD23 knockout model makes it difficult to study the effects of BUD23 in a long-term manner. Mice go into the late stages of cardiac failure after approximately 28 days of age, providing a very narrow window in which to investigate the underlying mechanisms and to provide any interventions. This strongly limits the scope of any potential experiments, due to both the young age of the mice and the limited time-frame within which they can be completed. In addition, as mice descend into terminal cardiac failure they develop increasing levels of compensatory mechanisms that conceal the key functionality of BUD23, making it difficult to obtain any core mechanistic insights.

To counteract these issues, we proposed the generation of a second BUD23 knockout model, instead targeting BUD23 knockdown to adipose tissue.

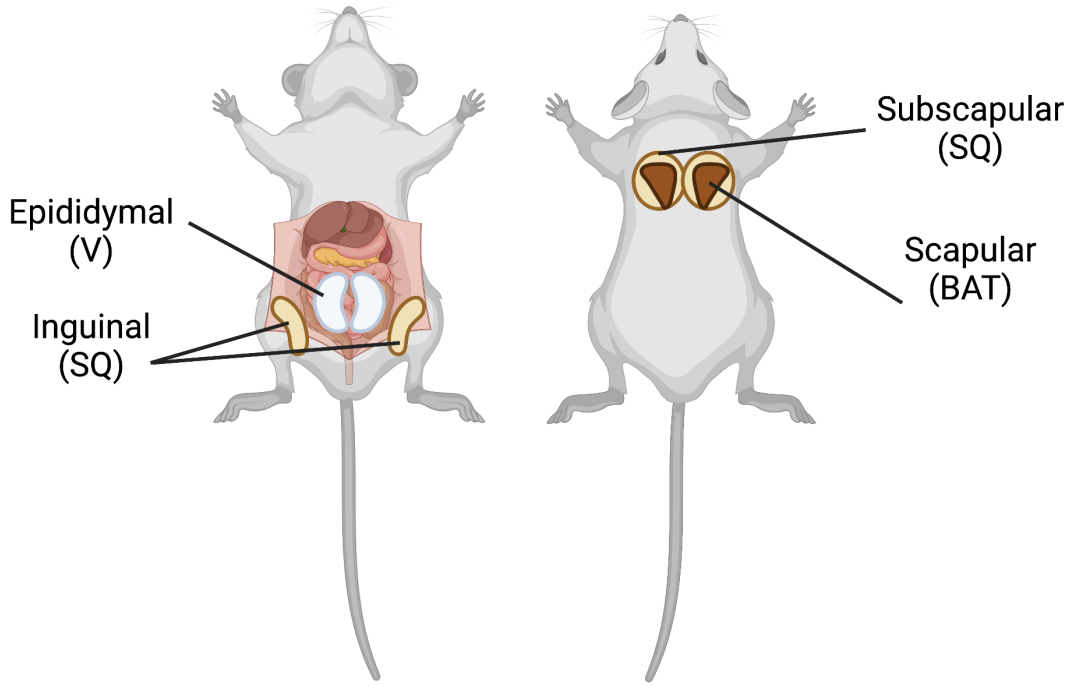

Figure 4.1: Simplified diagram of key adipose deposits within mice. V = Visceral White Adipose; SQ = Subcutaneous White Adipose; BAT = Brown Adipose Tissue.

4.1.1 The adipose organ

Mammalian adipose tissue is composed of two main distinct cellular lineages: white adipocytes and brown adipocytes (Cinti, 2005). White adipocytes are unilocular, storing dietary energy in the form of a single, large lipid droplet. When animals go into a negative calorie balance, stored triglycerides are liberated, undergoing hydrolysis and then secretion into the bloodstream for subsequent uptake by other organs. White adipose tissue (WAT) deposits can be further broadly categorised into two different divisions, varying both in terms of their anatomical location and their particular features (Fig. 4.1). Visceral depots, including perigonadal, retroperitoneal and mesenteric WAT, have a very uniform appearance, consisting primarily of stereotypical white adipocytes, and form later in development than subcutaneous depots (Tchernof et al., 2006; Tchkonia et al., 2007). Meanwhile, subcutaneous WAT, which includes inguinal and subscapular depots, has a more heterogeneous appearance, also containing multilocular adipocytes known as beige

adipocytes, which have a more brown-like appearance (Wu et al., 2012).

Brown adipocytes are multilocular, containing multiple, smaller triglyceride droplets. Unlike WAT, brown adipose tissue's (BAT's) main function is to burn fat to generate heat, a process known as thermogenesis (Enerbäck et al., 1997; Ellis et al., 2010). BAT is characterised by its rich mitochondrial presence and high UCP-1 expression, an uncoupling protein that serves as the primary mediator of thermogenesis. Originally, while BAT was known to be important during human neonatal development, it wasn't thought to be physiologically relevant in adults (Aherne & Hull, 1966; Heaton, 1972; Lean, 1989). Most studies therefore focused on BAT from a rodent-centric approach, where its function was known to be important throughout all life stages. However, while BAT had been described to be present in adult humans in various studies (Heaton, 1972; Huttunen et al., 1981; Bouillaud et al., 1983), it was the discovery of functionally active BAT in 2007 (Nedergaard et al.), and its subsequent characterisation in 2009 using ^{18}F-fluorodeoxyglucose positron emission tomography coupled with computer tomography (Cypess et al., 2009; van Marken Lichtenbelt et al., 2009; Virtanen et al., 2009; Zingaretti et al., 2009), that greatly increased research into BAT in humans. Now, BAT is studied in many different contexts, and in particular in studies concerning obesity and targeted weight loss strategies.

The evolutionary advantage of adipose tissue is evident through its primary function as an energy store, permitting the sequestering of energy when it's in abundance, and release during times of need. However, more recent work has identified adipose as not just a storage facility, but in fact as the body's largest endocrine signalling organ (Gesta et al., 2007). Through the secretion of various cytokines, adipokines, and other regulatory molecules, adipose is able to control various biological processes in a systemic manner, including glucose and insulin signalling, fertility, appetite, and thermoregulation (Nawrocki & Scherer, 2004).

4.1.2 Non-shivering thermogenesis and brown adipose

Thermogenesis is a taxing bodily process that accounts for approximately 20% of daily oxygen consumption (Rolfe & Brown, 1997). This equates to roughly 15% of total energy expenditure, demonstrating a significant metabolic burden on the body (van Marken Lichtenbelt & Schrauwen, 2011). While both shivering and non-shivering thermogenesis (NST) contribute to heat production, shivering is an uncomfortable and metabolically costly process and so is inefficient for chronic exposure to a low temperature environment. NST, defined as heat production that is independent from muscle contraction, is a much more effective strategy for mammals that are constantly exposed to cold, permitting them to ramp up their baseline aerobic capacity and oxygen consumption for thermoregulation.

The main site of NST in mammals is BAT. While most of the core mechanisms of NST have primarily been studied in rodents, it is believed that BAT's method of action is conserved within humans and is essentially the same. Upon exposure to a cold stimulus, transient receptor potential channels are activated, sending signals to the brain through the sensory nervous system (Dhaka et al., 2006). These are a group of cation permeable membrane proteins that serve to relay somatosensory information regarding environmental factors such as temperature, pain, pressure, osmotic concentration, and the presence of certain substances. This stimulates the release of noradrenaline from sympathetic nerve endings within BAT, which is detected locally by the β_3-adrenergic receptor (β_3-AR) on the surface of brown adipocytes (Emorine et al., 1989). Stimulation of the β_3-AR drives a cyclic adenosine monophasphate signalling cascade via the activation of PKA, p38 MAPK, and PGC-1α, resulting in triglyceride liberation, fatty acid oxidation, and the up-regulated expression of UCP-1 (Sears et al., 1996; Cao et al., 2001). The lipolysis of triglycerides releases long chain fatty acids which feed back into the TCA cycle. This triggers the activation of UCP-1 on the inner mitochondrial membrane, flooding protons down the electrochemical gradient and therefore releasing energy in the form of heat (Fedorenko et al., 2012).

4.1.3 Brown adipose metabolism

A range of metabolic substrates are utilised by brown adipose in order to correctly begin and maintain a thermogenic response, including intracellular triglycerides, circulating free fatty acids, and glucose. In particular, the role of intracellular triglycerides has been well described, as they form the primary source of energy for thermogenesis (Labbé et al., 2015). In models where triglyceride lipolysis is suppressed, the thermogenic potential of BAT is severely impaired, resulting in compensatory heat generation mechanisms such as shivering (Blondin et al., 2017).

The utilisation of glucose during thermogensis is less well characterised, though it is highly likely that glycolytic intermediates serve a key role. Glucose enters brown adipocytes through the glucose transporters GLUT1 and GLUT4, where it is converted into pyruvate through glycolysis. Approximately 50% of glucose uptake during cold exposure in BAT is released as lactate after conversion from pyruvate, corresponding to roughly four times the amount of lactate produced in WAT (Weir et al., 2018). In further support of this, expression of monocarboxylate 1 and 4, the lactate transporters, are very high in rodent BAT (Petersen et al., 2017). Some studies have also indicated that a proportion of the lactate is then converted into fatty acids within the BAT (Saggerson et al., 1988), or alternatively can also directly enter the tricarboxylic acid (TCA) cycle (Hui et al., 2017). Following entry into mitochondria, pyruvate can alternatively undergo conversion into acetyl coenzyme A (acetyl-CoA) via pyruvate dehydrogenase (Weir et al., 2018). Acetyl-CoA can then feed into the TCA cycle to drive oxidative phosphorylation, resulting in the production of citrate (Held et al., 2018). Citrate can be used to initiate *de novo* lipogenesis (DNL) for the formation of new fatty acids (Sanchez-Gurmaches et al., 2018). Interestingly, fatty acids obtained from citrate are not immediately oxidised for thermogenesis, but are instead used to replenish depleted triglyceride droplets (Irshad et al., 2017).

Free fatty acids, derived either directly from circulation or from hydrolysis of triglyceride rich lipoproteins (TRLs) via lipoprotein lipase (LPL), also form

an essential source of fatty acids for DNL (Weinstock et al., 1997; Ouellet et al., 2012). During exposure to cold, up to 50% of systemic TRL clearance can be attributed to uptake by BAT (Bartelt et al., 2011; Berbée et al., 2015; Khedoe et al., 2015). However, it is unknown whether free fatty acids obtained through this method are immediately used to fuel UCP-1 mediated thermogenesis, or are instead sequestered into triglyceride stores.

While traditionally glucose, free fatty acids and triglycerides were believed to be the main substrates for BAT function, more recent work has highlighted that BAT actually uses a much wider range of substrates than previously thought. In particular, significant uptake of glutamate, succinate and branched chain amino acids by BAT is observed in response to a cold stimulus (Weir et al., 2018; Mills et al., 2018; Yoneshiro et al., 2019). It is thought that these can also feed into the TCA cycle at various points, helping to drive thermogenesis. Knockdown of SLC25A4, the primary transporter of valine and leucine into mitochondria, causes impaired thermogenesis in mice, further evidencing the importance of branched chain amino acids as a thermogenic substrate (Yoneshiro et al., 2019).

4.1.4 Hypothesis and aims

Adipose tissue presents an attractive system in which to study the role of BUD23. While we obtained critical insights into BUD23's function using our previous MCK-Cre model, the early lethality and severity of the phenotype made it difficult to elucidate the core mechanisms in play. Brown adipose tissue is rich in mitochondria, which is necessary to drive a thermogenic response when exposed to cold. By knocking down BUD23 specifically within adipose tissue, we will then have a system in which we can introduce a cold challenge to drive mitochondrial function, enabling us to better study how BUD23 affects the translation of mitochondrial proteins. We will also be able to verify whether BUD23 is response for the same core phenotype observed in the heart in a second specialised tissue, verifying the findings of the previous chapter. Overall, **we hypothesise that the knockdown of BUD23**

in adipose tissue will result in mice that have an impaired thermogenic capacity, as a consequence of reduced mitochondrial density and function.

Aim 1: Generate a BUD23 knockout model that is viable into adulthood

By crossing BUD23$^{fl/fl}$ mice with mice carrying an Adiponectin-Cre driver, we aimed to generate a BUD23 knockout model with a milder phenotype than our previous MCK-Cre model. Brown adipose is rich in mitochondria and has an intricate metabolic profile, utilising a variety of substrates to drive thermogenesis. Other mouse models that cause severe impairment to their brown adipose are still viable (Kazak et al., 2017), so we predicted that these animals would be able to survive into adulthood, enabling us to carry out more intricate interventions.

Aim 2: Assess whether loss of BUD23 impacts non-shivering thermogenesis

Non-shivering thermogenesis is driven by UCP-1 mediated uncoupling of the TCA cycle in mitochondria, permitting protons to flood across the electrochemical gradient and therefore produce heat. BUD23 knockdown in the heart results in selective defects in mitochondrial function and density, with a strong impact on carbon metabolism. Therefore, we predicted that mitochondrial function would be similarly impaired in adipose tissue, and therefore mice would be unable to recover their body temperature in response to a cold challenge.

Aim 3: Establish the mechanisms underpinning BUD23's role in mitochondrial protein translation

Through the use of techniques such as proteomics and RNA-Seq, we aimed to determine the origin of defects caused by loss of BUD23 within adipose tissue. By comparing these results with those found in our previous BUD23 knockout model, we aimed to identify the core mechanisms through which BUD23 acts in order to build a working model of BUD23's function in mammalian organisms.

4.2 Materials and Methods

4.2.1 *In vivo* phenotyping

Body composition was measured from individually housed mice via the EchoMRI Body Composition Analyzer E26-258-MT. Accumulations were set to 3, and water stage was on. Energy expenditure was measured using the CLAMS Comprehensive Lab Animal Monitoring System (Columbus Instruments) via indirect calorimetry. All mice were permitted to acclimatise to their cages for at least 2 days. An average of 5 days of recordings were collected. Radiotelemetry devices (TA-F10; Data Sciences International) were surgically implanted for collection of body temperature data. Mice were anaesthetized using 2-5% isofluorane in oxygen for approximately 20 mins, after which the radiotelemetry device was inserted into the abdominal cavity. Mice were allowed 7-10 days recovery prior to individual housing and follow-up experiments.

4.2.2 Electron Microscopy

Mice were euthanised via cervical dislocation and their adipose tissue was rapidly dissected out. Tissue was cut into small cubes (1mm sides) and immediately placed into pre-warmed (37°C) fixative (2.5% glutaraldehyde and 4% formaldehyde in 0.1M sodium cacodylate buffer, pH 7.2) for 2 hours at room temperature. Samples were then transferred to 4°C overnight. For longer storage, tissue was transferred into 0.25% glutaraldehyde in 0.1M sodium cacodylate and kept at 4°C until further processing. Samples were then washed twice in 0.1M sodium cacodylate buffer (pH 7.2) for 45 mins with rotation, prior to transfer into carrier baskets. They were then processed for electron microscopy using a Leica AMW automated microwave processing unit (Table 4.1)

Samples were then transferred to 2ml tubes filled with fresh TAAB Hard Plus epoxy resin, centrifuged for 2 mins at 2,000g, and incubated at room temperature overnight with rotation. The following day, the resin was removed and replaced with fresh resin, and the samples were centrifuged as above and incubated at

room temperature with rotation for 3 hrs. This step was repeated and then tissue pieces were transferred to individual Beem capsules filled with fresh resin and polymerised for 48 hrs at 60°C.

Once polymerised, blocks were sectioned using a Diatome diamond knife on a Leica UC7 Ultramicrotome. Ultrathin (90nm) sections were transferred onto 200 mesh copper grids and then post-stained with lead citrate for 5 mins, washed and air dried. Grids were imaged with a Thermo Fisher Tecnai 12 TEM (operated at 120 kV) using a Gatan OneView camera.

4.2.3 Mass spectrometry preparation

To enable better recovery of proteins from fatty tissues, a modified methanol/chloroform protein extraction method was used. Following tissue lysis, proteins were digested in-solution. Briefly, DTT was added to adipose homogenates to a final concentration of 5mM and samples were incubated for 60 mins at room temperature. Iodoacetamide was added to a final concentration of 20mM prior to a second 60 min incubation step. Samples were then vortexed in 60% methanol 15% chloroform and diluted prior to centrifugation at max speed in a bench-top centrifuge for 1 minute. The aqueous phase was removed, and methanol was added to the organic phase. This was vortexed, and then centrifuged at maximum speed again for 2 minutes. The supernatant was then discarded. The protein pellet was resuspended in 6M urea buffer. Once dissolved, milliQ water was added to dilute the total urea concentration down to <1M. Protein concentratinon was determined via Bradford. Samples were trypsinised overnight at 37°C, using a 1:50 ratio of trypsin to protein. Peptides were desalted using Pierce C18 tips (Thermo Scientific). All further steps, including mass spectrometry settings and subsequent data analysis were describes as previously performed.

Steps	Reagent	Time (mins)	Temp (°C)	Power (W)	Mode
1-2	0.1M sodium cacodylate buffer pH 7.2	1	37	20	Slope
3	0.1M sodium cacodylate buffer pH 7.2 + 50mM glycine	1	37	20	Slope
4	0.1M sodium cacodylate buffer pH 7.2	1	37	20	Slope
5	0.1M sodium cacodylate buffer pH 7.2	1	37	15	Cont.
6	1% osmium tetroxide + 1.5% potassium ferricyanide in 0.1M sodium cacodylate buffer pH 7.2	12	37	20	Pulse
7-13	MilliQ water	1	37	15	Cont.
14	2% uranyl acetate in water	5	37	20	Cont.
		2	20	0	Cont.
		2	37	15	Cont.
15-16	MilliQ water	1	37	15	Cont.
17	30% Ethanol	1.5	37	15	Cont.
18	50% Ethanol	1.5	37	25	Cont.
19	70% Ethanol	1.5	37	25	Cont.
		1	37	25	Cont.
20	90% Ethanol	1.5	37	25	Cont.
21	95% Ethanol	1	37	25	Cont.
22-25	100% Ethanol	2	37	25	Cont.
26	25% TAAB Hard Plus epoxy resin in Ethanol	3	37	10	Cont.
27	50% TAAB Hard Plus epoxy resin in Ethanol	3	37	10	Cont.
28	50% TAAB Hard Plus epoxy resin in Ethanol	5	45	12	Cont.
29	75% TAAB Hard Plus epoxy resin in Ethanol	3	45	12	Cont.
30-31	100% TAAB Hard Plus epoxy resin	10	45	12	Cont.
32-33	100% TAAB Hard Plus epoxy resin	15	45	12	Cont.
34	100% TAAB Hard Plus epoxy resin	30	45	12	Cont.

Table 4.1: Leica AMW automated processing unit program.

4.2.4 RNA-Sequencing

RNA was extracted from adipose tissue using the SV Total RNA Isolation System (Promega) according to manufacturer's instructions. RNA yield was quantified by TapeStation (Agilent), to ensure it was of sufficient quality for sequencing. Library preparation and sequencing for the Illumina HiSeq 4000 platform were performed

by Novogene. Raw FASTQ files were processed through a standard pipeline by Novogene to generate a list of counts. I carried out subsequent data processing and analysis. Gene lists were analysed for differential expression using a combination of techniques, including edgeR (Robinson et al., 2010) as well as the methods described in Chapter 3 for differential protein analysis.

4.2.5 Serum metabolites

Mice were euthanised via pentobarbital overdose and blood serum was acquired via cardiac puncture using heparinised needles. Blood was allowed to clot at room temperature for 30 mins, before centrifugation at 2,000g for 10 mins. Serum was collected and the pellet discarded. Metabolites were assessed in both blood serum and liver homogenates via colorimetric assays per manufacturer's instructions (Cayman Chemical, BioAssay Systems).

4.2.6 Fatty Acid Profiling

Total lipids were extracted from extracted from white adipose tissue according to the Folch method (Folch et al., 1957) and prepared for analysis by a 6890N Network GC System (Agilent) according to previously published protocols (Burdge et al., 2000). A standard containing 31 known fatty acids was used to aid in identifying correct retention times.

4.3 Results

4.3.1 Adipose BUD23 deficient mice are viable but lean

BUD23$^{fl/fl}$ mice were crossed to an Adiponectin-Cre$^{+/-}$ line (AdipoCre), resulting in the tissue-specific disruption of BUD23 in both white and brown adipose tissue. All studies were performed on adult mice between the ages of 12-16 weeks old, using BUD23$^{fl/fl}$ AdipoCre$^{-/-}$ animals as control mice. Where possible, littermates were used for experimental cohorts. Otherwise, all cohorts were age and sex matched as closely as possible, unless otherwise indicated.

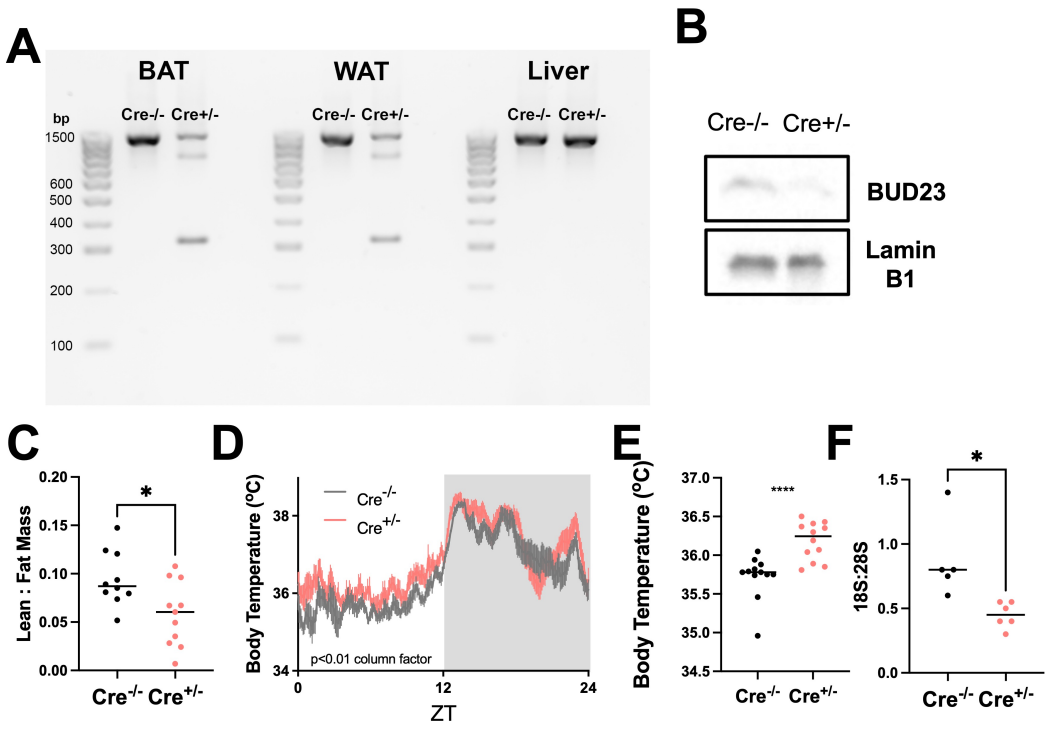

Figure 4.2: Basic profiling of adipose BUD23 knockout mice. BUD23$^{fl/fl}$ mice were crossed to an Adiponectin-Cre line. (A) Recombination was assessed via PCR to ensure knockdown in the correct target organs. Liver was included as a negative control, where recombination did not occur. The band at approximately 350bp in WAT and BAT of AdipoCre$^{+/-}$ animals indicated recombination was successful. (B) Knockdown at the protein level was assessed via western blot in BAT. BUD23 primary antibody was used at 1:500 dilution. (C) EchoMRI was performed to determine body composition of adipose BUD23 knockout animals, revealing that knockout animals were leaner. (D) Telemetry data showing body temperature throughout a 24h period. (E) Average daytime body temperature (two-way ANOVA; n=12 per genotype) (F) Analysis of 18S:28S ratio using the TapeStation system (Student's T-test). * indicates p-value $\leqslant 0.05$; **** $p \leqslant 0.0001$

Recombination was confirmed at the genomic DNA level in both white and brown adipose tissue from adult mice (Fig. 4.2A). While wild-type bands are also present in the knockout adipose tissue, the presence of the recombinant band indicates that recombination has successfully occurred, and that the presence of wild-type bands is due to contamination from other cell types present in the sample. Liver was used as a negative control, to show that recombination did not occur in off-target tissues. Knockdown was also confirmed at the protein level in BAT (Fig. 4.2B), however this was not possible in WAT due to the low expression level of BUD23 in white adipocytes.

Unlike the MCK-Cre model, AdipoCre$^{+/-}$ mice were fully viable through adulthood and lacked any obvious phenotypic differences. While mice did not show any statistically significant differences in body weight between genotypes, body composition analysis using EchoMRI revealed that BUD23$^{fl/fl}$ AdipoCre$^{+/-}$ animals had lower fat:lean mass body ratios, indicating that they are slightly leaner than their littermate controls (Fig. 4.2C), potentially due to a reduction in their adipose tissue depots.

We then measured mouse baseline body temperatures over a 24 hour period through the use of an implanted telemetry probe (Fig. 4.2D-E). Mice lacking BUD23 still showed normal circadian body temperature cycles, with higher body temperatures during their active phase at night, and lower body temperatures during their resting phase in the day. Interestingly, AdipoCre$^{+/-}$ individuals showed a gain in average daytime body temperatures when compared to their AdipoCre$^{-/-}$ littermates, suggesting a potential thermogenic phenotype.

Finally, we verified that BUD23 was also responsible for ribosomal biogenesis in adipose tissue (Fig. 4.2F). This is consistent with previous findings in yeast and also with our previous findings in cardiac tissue, solidifying the hypothesis that this is a core, conserved BUD23 function across multiple organisms and tissue types.

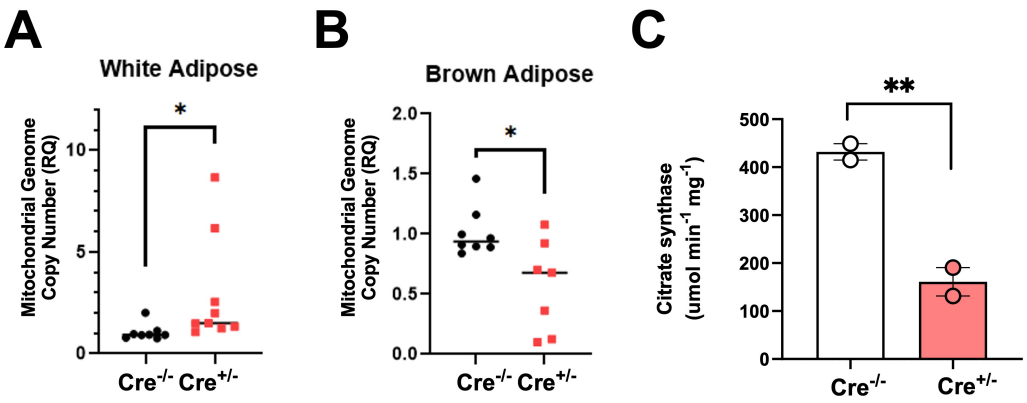

Figure 4.3: Mitochondrial number is reduced in BUD23 ablated BAT. Mitochondrial genome copy number was measured via qPCR and normalised against autosomal genome copy number for both (A) WAT and (B) BAT (n=7-9 per genotype). (C) Mitochondria were isolated from BUD23 knockout mice and their littermate controls (n=4). Each isolation contained BAT from 2-3 mice combined. Values are Mean, +/- SEM, and were normalised against mitochondrial protein. * indicates p-value $\leqslant 0.05$; ** $p \leqslant 0.01$

4.3.2 Mitochondrial number but not function is disrupted in brown adipose

While we have previously discovered that BUD23 is responsible for correct mitochondrial function in cardiac muscle, we wanted to verify if this was a conserved phenotype within BAT as well. Analysis of mitochondrial genome copy number, which acts as a proxy for mitochondrial number, revealed a significant reduction in mitochondrial density in BAT, consistent with previous findings from the heart (Fig. 4.3). Interestingly, we also tested mitochondrial count in WAT, but instead found the opposite, with some WAT samples showing vastly increased numbers of mitochondria. One potential explanation for this is that the WAT may be undergoing browning, recruiting beige adipocytes that are brown-like in function to compensate for loss of thermogenesis in BAT.

To determine if BAT mitochondria were functional despite their reduced number, we used the Oroboros microrespirometry system to assess for differences in respiratory rates (Fig. 4.4). While initial analysis of BAT homogenates suggested that their respiratory rates were impaired, normalisation to citrate synthase levels (a secondary marker for mitochondrial number) revealed that there was no significant

difference in respiratory function. While number was reduced, mitochondria were still fully functional and capable of oxidative phosphorylation.

We also performed electron microscopy to interrogate the morphology of the mitochondria, and to look for any obvious architectural differences within the cells (Fig. 4.5). Mitochondria from BUD23 ablated BAT appeared normal, large in size with intact membranes and many, fully formed, correctly folded cristae. They were interspersed through the intracellular space, filling most of the area between the lipid droplets, in the same way as the BAT from control animals did. We did not find any evidence of electron dense inclusion bodies in the BAT mitochondria, contrary to what was observed in the cardiac model. As inclusion bodies are thought to be a compensatory mechanism for severe bioenergetic demand, it is possible that mitochondria from BAT are not under the same level of demand in these mice.

These findings oppose those seen in the heart, indicating that there is still a mitochondrial phenotype, but that it does not affect the functionality of the mitochondria within the BAT. This points to an interesting delineation of the

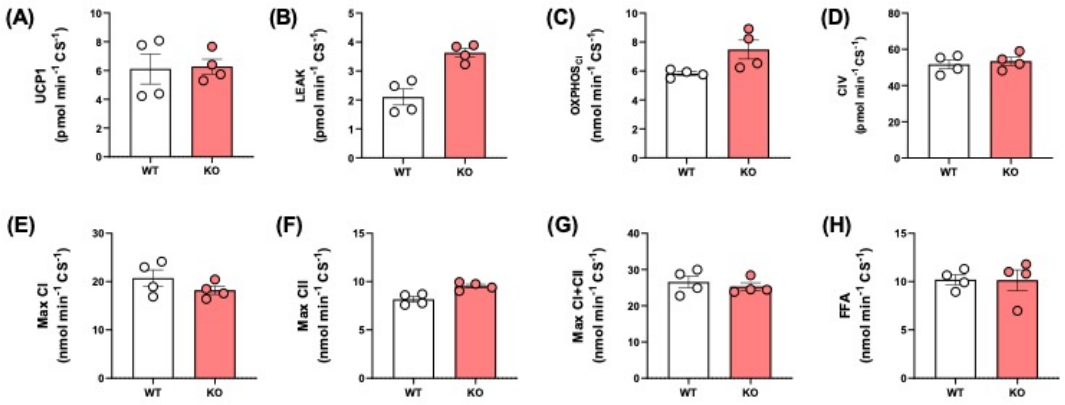

Figure 4.4: BAT mitochondrial respiration normalised to citrate synthase. Mitochondria were isolated from BUD23 knockout and control mice (n=2 isolations & 2 biological replicates per genotype). Each isolation contained BAT from 2-3 mice combined. (A) UCP1 GDP-dependent respiration. (B) Leak respiration rate with Complex I substrates. (C) Oxidative phosphorylation (OXPHOS) in the presence of ADP. (D) Respiration through Complex IV. (E-G) Maximal uncoupled respiration with substrates for Complex I, II, and I+II. (H) Respiration with free fatty acids (palmitoyl carnitine). Values are mean +/- SEM.

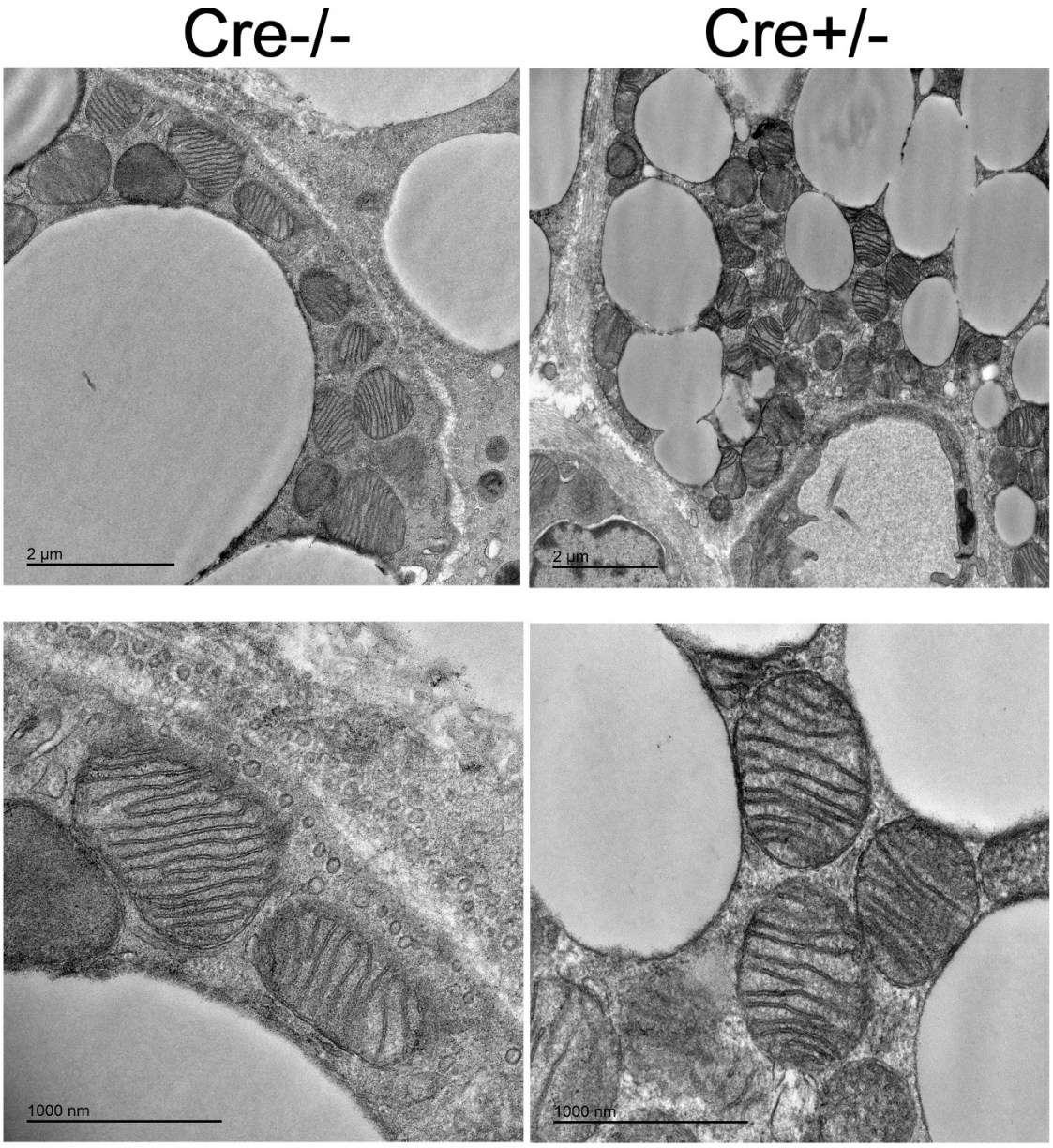

Figure 4.5: Mitochondria do not show any morphological abnormalities Electron microscopy images of mitochondria from wild-type BAT (left) and BUD23 knockout BAT (right). No electron dense inclusion bodies can be observed.

observed defects, and may indicate that the severity of the mitochondrial phenotype in the heart was due to the specific model and the heavy metabolic burden of the tissue. By observing which defects occur in the absence of BUD23 in both tissues, we may be able to better elucidate the core mechanism governing BUD23's control of mitochondrial translation.

4.3.3 BUD23 ablated brown adipose can still produce a thermogenic response

In order to test whether BUD23 ablated BAT could induce a thermogenic response, mice were implanted with telemetry probes and then exposed to an acute cold challenge (4°C for 6 hours). By exposing the animal to a low temperature, BAT tissue will be activated, inducing a mitochondrial response and enabling us to observe how well they can recover. While BUD23$^{fl/fl}$ AdipoCre$^{+/-}$ animals showed an initial strong decline in body temperature, they recovered quicker and better than their littermate controls (Fig. 4.6A), indicating that not only can they rescue their body temperature in response to acute cold, but are also quite efficient at it. This opposes our predicted findings, as we anticipated that they would be unable to protect their core body temperature against a cold challenge. It is possible that they have developed alternative compensatory mechanisms to permit heat generation, such as increased shivering or through non-BAT mediated thermogenesis. In addition to a seemingly normal response to a cold challenge, BUD23 knockout mice also showed a normal response to food withdrawal during a 24 hour fast (Fig. 4.6B).

To see if we could directly induce a targeted NST response, we injected mice with either saline or a known selective β3-agonist, CL316243 (1 mg/kg), and measured their core body temperature for five hours post-injection (Fig. 4.6C). Following administration of either the drug, or control vehicle, all mice had an initial spike in body temperature which can be attributed to a stress response following handling. Wild-type (AdipoCre$^{-/-}$) animals that were given saline returned back to their baseline body temperature after approximately 100 minutes. However, wild-type animals that were administered the drug showed an elevated body temperature of roughly 37°C for the entire duration of the recording, indicating that their BAT had been stimulated via the β3-AR and had triggered a thermogenic response. Interestingly, AdipoCre$^{+/-}$ animals failed to produce a NST response, behaving in an identical fashion to the mice given vehicle only. This indicates that they do not respond to sympathetic stimulation via the β3-AR.

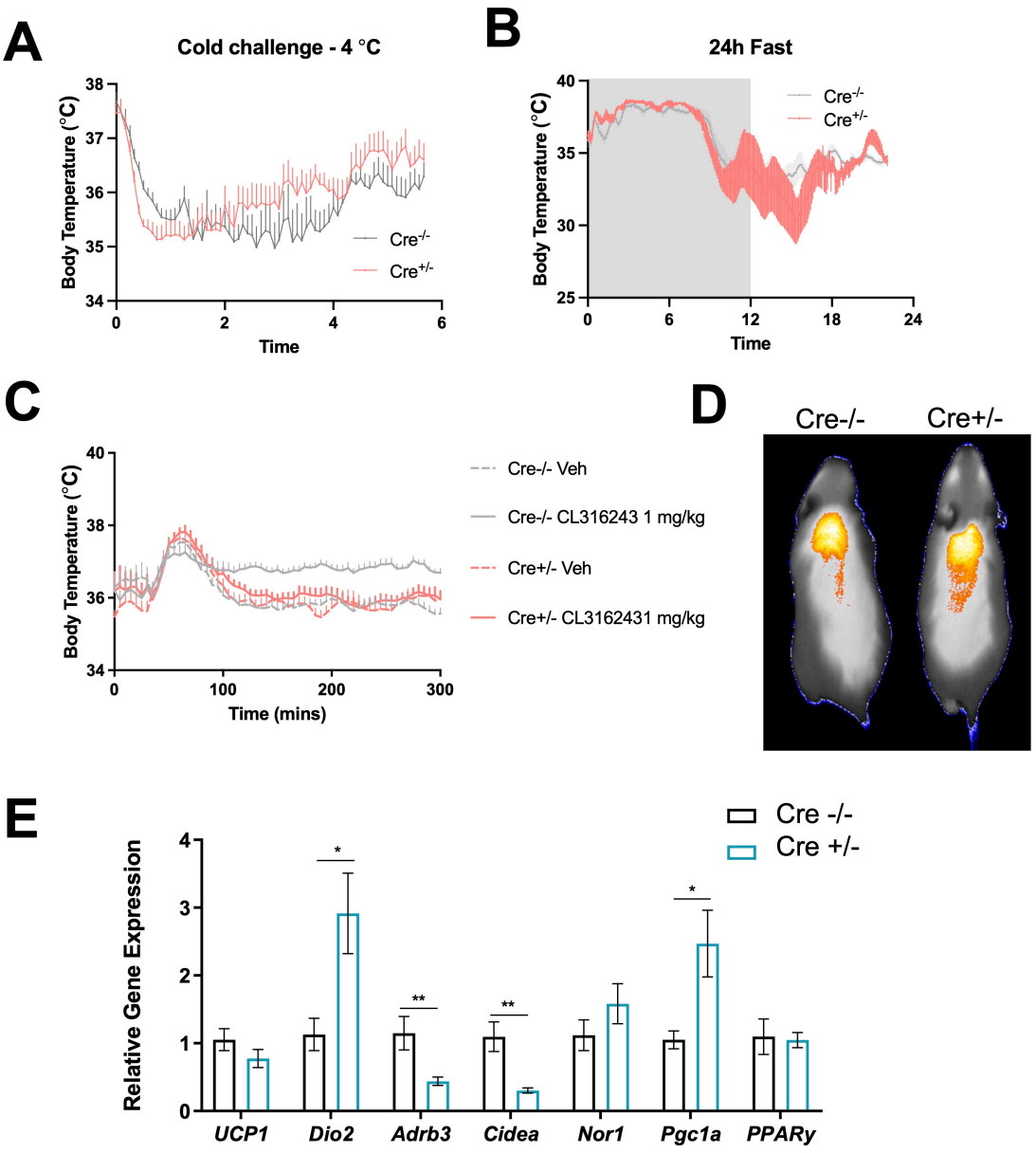

Figure 4.6: BUD23 knockout BAT can still undergo thermogenesis. Mice were implanted with telemetry probes to track core body temperature (n=11-12 per genotype). (A) Response to an acute cold challenge (n=11-12 per genotype). (B) Response to a 24h fast (n=11-12 per genotype). (C) Mice were injected with either CL316243, a selective β3-agonist, or a vehicle control to induce thermal production in BAT (n=12 per group). (D) Thermal imaging of scapular BAT. (E) qPCR analysis of thermogenic gene expression (n=5 per genotype; Student's T-test). * indicates p-value $\leqslant 0.05$; ** $p \leqslant 0.01$

Mice are routinely housed at 21°C, which is lower than their thermoneutral point. Therefore, animals are constitutively under a low level of thermal challenge,

having to expend energy for thermoregulation. We therefore took thermal images of mice to enable visualisation of their BAT, and to permit us to read whether they have a clear thermal signature as a result of NST (Fig. 4.6D). In control animals, there is a clear hot spot between the shoulder blades, corresponding to active BAT. Interestingly, despite the fact that BUD23 knockout BAT is incapable of mounting a thermal response to sympathetic stimulation, knockout animals still had a clear thermal signature behind their shoulder blades, indicating that they have active BAT that is producing heat.

To attempt to determine why BUD23 ablated BAT shows no response to sympathetic stimulation, but appears to be able to produce a thermogenic response, we quantified the relative gene expression levels of major genes involved in NST in BAT using qPCR (Fig. 4.6E). No change was identified in UCP-1 levels, indicating that mitochondria may still be capable of UCP-1 mediated heat generation. However, the expression of β3-AR was strongly reduced. Loss of β3-AR expression explains why the mice were unable to respond to a β3-agonist, and would indicate that they cannot respond to the canonical sympathetic stimulation pathway that generally drives NST.

4.3.4 BAT shows signs of whitening without BUD23

Visual inspection of brown adipose tissue deposits reveal several obvious phenotypic differences (Fig. 4.7A). In control animals, brown adipose tissue sits behind the shoulder blades under a white fat deposit. It forms two characteristic dark red pads that are clearly distinct from the surrounding white tissue. However, in knockout mice, the brown adipose deposits are much smaller and also fainter in colour, taking on a beige-like appearance. The boundary edges lose their distinct contrast, as they become very similar to the surrounding white adipose deposit. This appearance is typical of brown adipose tissue that is undergoing 'whitening', with loss of colour representing the loss of mitochondrial mass.

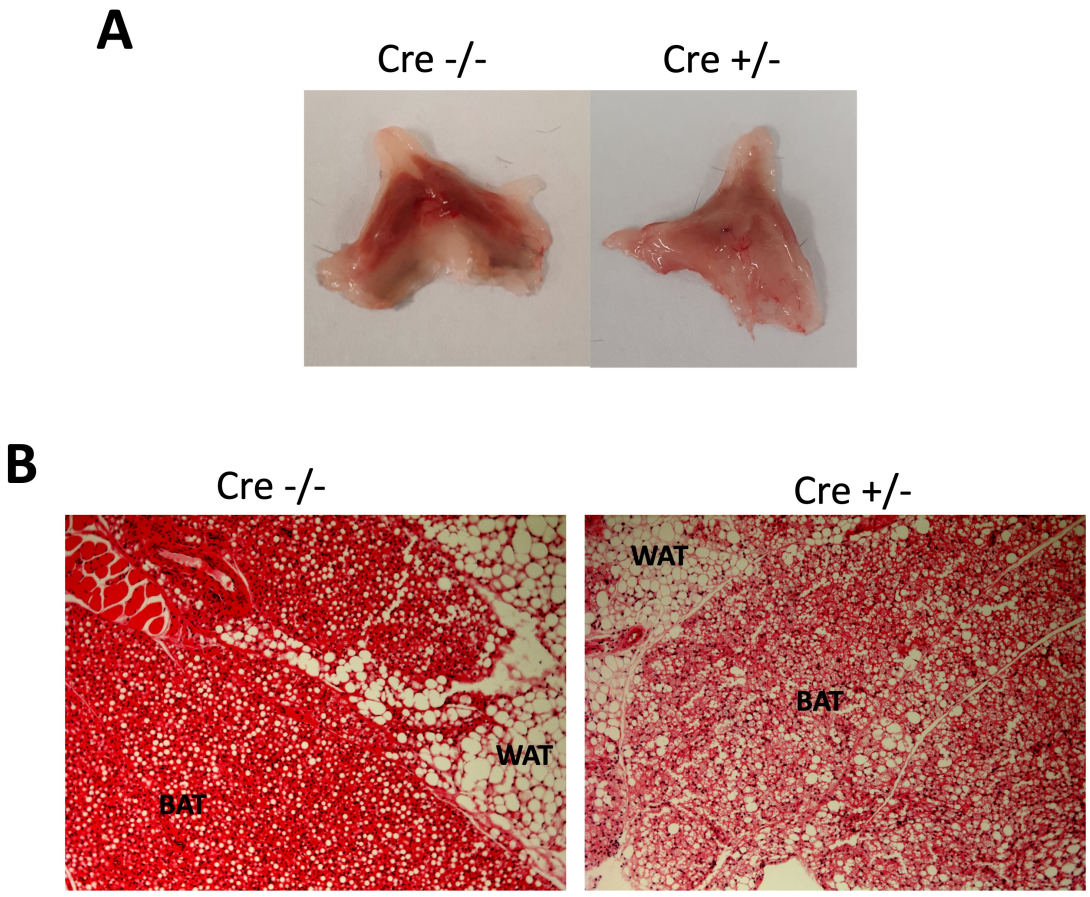

Figure 4.7: BUD23 knockout BAT appears to be whitening. (A) Image of freshly dissected BAT tissue from control (left) and knockout (right) animals. BUD23 knockout results in pale BAT morphology. (B) Haematoxylin-Eosin staining of BAT sections, revealing enlarged triglyceride droplets within knockout BAT.

Histological staining further confirms morphological disruption within the tissue (Fig. 4.7B). BAT from control animals shows heavy H&E staining, interspersed with multilocular triglyceride droplets of a relatively uniform size. However, in BAT from animals lacking BUD23, staining is much more diffuse, potentially as a result of protein mass due to mitochondrial loss. In addition, triglyceride droplets are no longer uniform in size, and some very large triglyceride droplets can be observed that are not present in the control BAT. On the tissue boundaries, AdipoCre$^{-/-}$ animals show a very distinct difference between the intrascapular BAT depot and the underlying subscapular WAT, which is lost in AdipoCre$^{+/-}$ BAT. It is unclear if the presence of large triglyceride stores in the BUD23 knockout BAT is due to increased triglyceride uptake and storage, a failure to deplete triglyceride stores due

to a loss of fatty acid oxidation resulting from reduced mitochondrial number, or due to infiltration of white adipocytes from the underlying WAT depot.

4.3.5 BUD23 regulates the translational control of metabolic processes in BAT

To investigate the underlying mechanisms governing BUD23's regulation of translation, we performed sample matched LFQ proteomics and RNA-Seq on BAT homogenates. A total of 16 adult mice were used for this study, all between the ages of 14-16 weeks (n=8 per genotype). Mice were matched as closely as possible across the experimental groups, both in terms of age and sex. 4 male and 4 female mice of each genotype were used, as females have previously been described to have a protected phenotype against mitochondrial defects relative to males (Ventura-Clapier et al., 2017), so we wanted to investigate any potential sexual dimorphisms.

For both sets of experiments, knockout animals ($BUD23^{fl/fl}$ $AdipoCre^{+/-}$) showed clear separation from wild-type animals ($BUD23^{fl/fl}$ $AdipoCre^{-/-}$) through principal component analysis (Fig. 4.8A). Unfortunately, one of the wild-type samples did not cluster well with either group in either the proteomics or the RNA-Seq datasets, which is likely due to a sample error introduced during tissue collection rather than a true result. Inspection of heat map data between the samples further confirms that this was an outlier (Fig. 4.8B). This sample was therefore excluded from further analysis in both datasets. In the proteomics data, 44.7% of variation was explained by component 1, and 15.2% by component 2, while in the RNA-Seq data, 25.7% was explained by component 1 and 12.2% by component 2. In the latter, component 1 appeared to separate samples based on genotype, and component 2 by sex.

Following filtering to remove potential contaminants and any proteins that were detected in less than half the total number of samples, a total of 2,525 proteins were identified. We then used t-tests, corrected by using a permutation based false discovery rate to compensate for the large dataset ($s0 = 0.2$, FDR < 0.05), to identify differentially expressed proteins between the two conditions. s0 is a

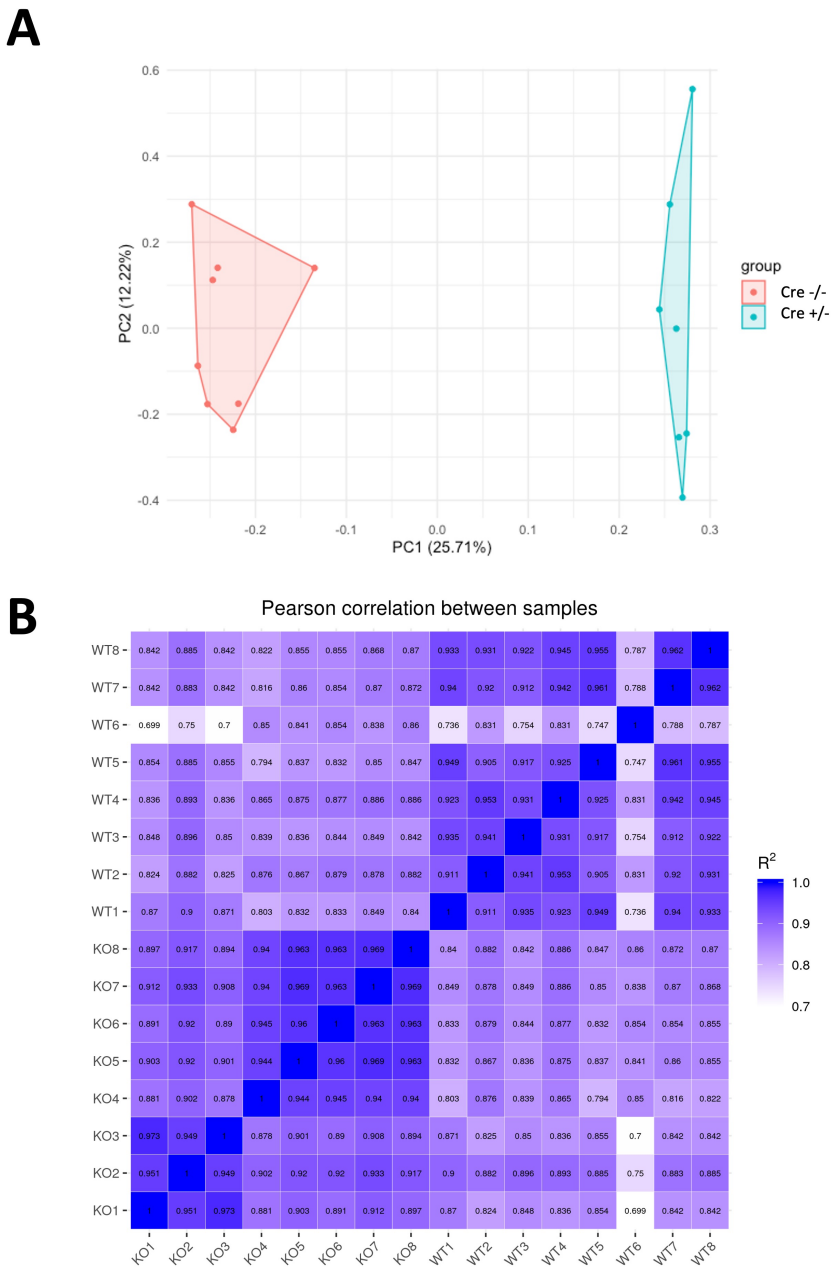

Figure 4.8: Clustering of animals by genotype. Matched RNA-Seq and proteomics were performed, using 4 animals of each sex per genotype. (A) Principal component analysis of RNA-Seq samples. Component 1 separated samples by genotype, and 2 by sex. (B) Pearson correlation plot further showing clustering into two groups. WT (control animals) and KO (knockouts) showed stronger correlation within groups than between. WT6 can be seen as an outlier here, which was removed from all subsequent analysis.

parameter that takes into account the relative fold change of each protein, meaning that proteins with a smaller difference in expression required a higher p-value in

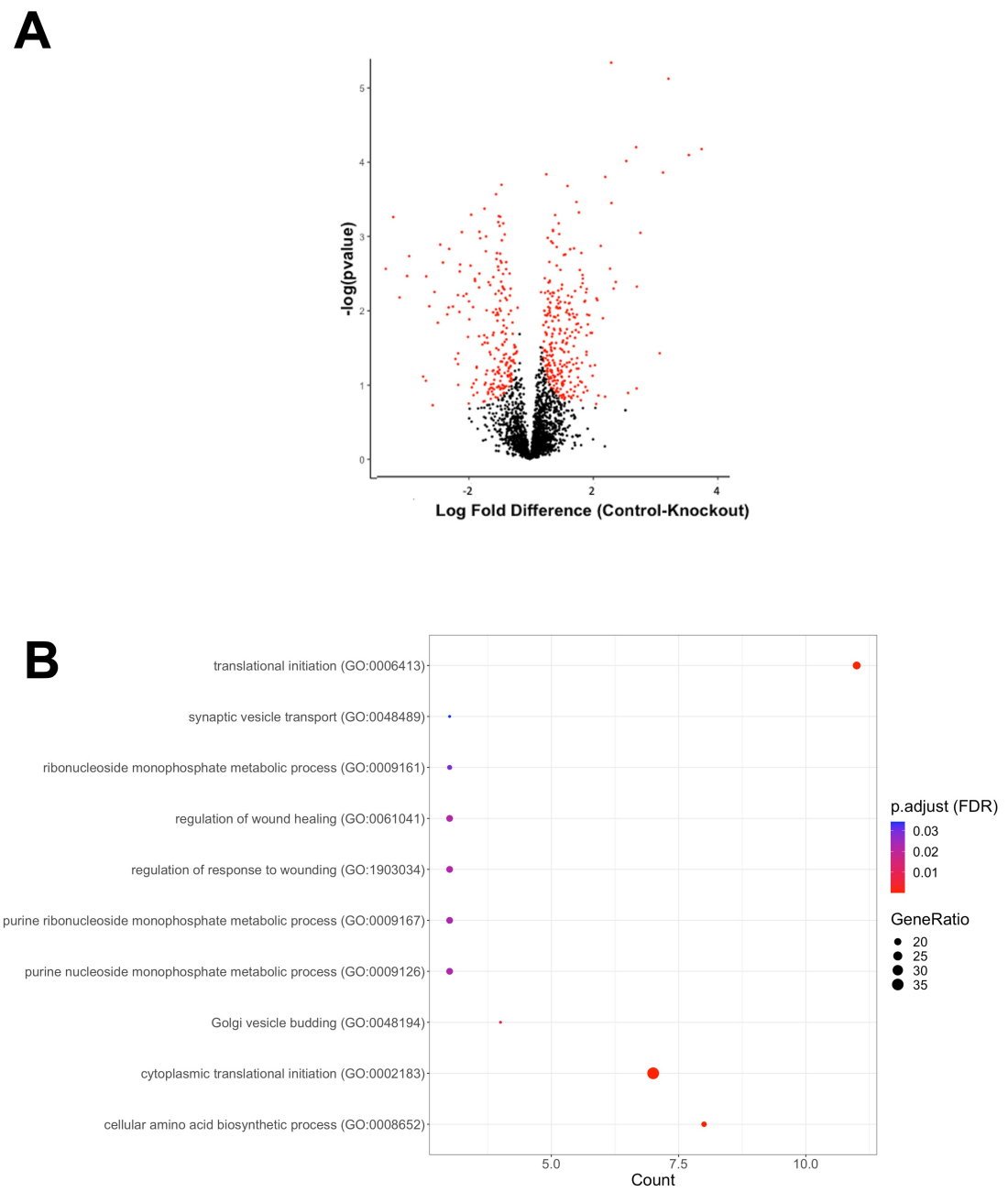

Figure 4.9: LFQ Proteomics of BUD23 knockout BAT. (A) Volcano plot showing differentially expressed proteins between BUD23 knockout and control BAT (red; FDR $<$ 0.05; s0 = 0.2) (B) Over-representation analysis of up-regulated biological processes was performed using Panther. The top 10 terms are shown here.

order to be identified as significantly different. 212 proteins were significantly down-regulated in BUD23 knockout BAT compared to control BAT, and 291 proteins were significantly up-regulated (Fig. 4.9A).

Gene ontology analysis was then performed on both groups of proteins to investigate pathway enrichment. Up-regulated terms included phagosome, RNA transport, protein processing in endoplasmic reticulum, aminoacyl-tRNA biosynthesis, and arginine and proline metabolism (Fig. 4.9B). Many of these terms correspond to a translational burden, potentially as a result of a global translational failure due to small:large ribosomal imbalance mediated by loss of BUD23. For example, tRNA biosynthesis pathways, increased protein processing and increased RNA transport indicate that cells are under stress to produce proteins. Arginine and proline metabolism is an interesting term, as this term covers glutamate uptake and processing, and glutamate uptake has been described to increase in BAT during cold exposure. This may point to an alternative metabolic pathway within BUD23 knockout BAT.

Down-regulated protein pathways mapped to ribosomal, metabolic pathways, pyruvate metabolism, and branched chain amino acid (BCAA) degradation (Fig. 4.10A). In addition, cell component analysis mapped loss of proteins primarily in mitochondria and the small ribosomal subunit. The specific defect in the small ribosomal subunit and mitochondria reflect changes that we were expecting to see, as we have previously established that BUD23 controls the correct development of the small ribosomal subunit and mitochondrial function in cardiac muscle. These appear to be a conserved phenotype in BAT, although here we observe a loss of mitochondrial density but not function instead. The alteration in BCAA catabolism also highlights a potential metabolic rewiring in these animals, as BCAAs have also been described as a thermogenic substrate in BAT.

No sex difference was observed on which pathways were identified, and so all data here is presented as a mixed sex summary.

We then compared differentially expressed proteins that were identified in our AdipoCre model proteomics (BAT) to those identified in our MCK-Cre model proteomics (cardiac muscle) to identify if any specific proteins overlapped between the two tissue types (Fig. 4.10B). 149 proteins were identified that were differentially

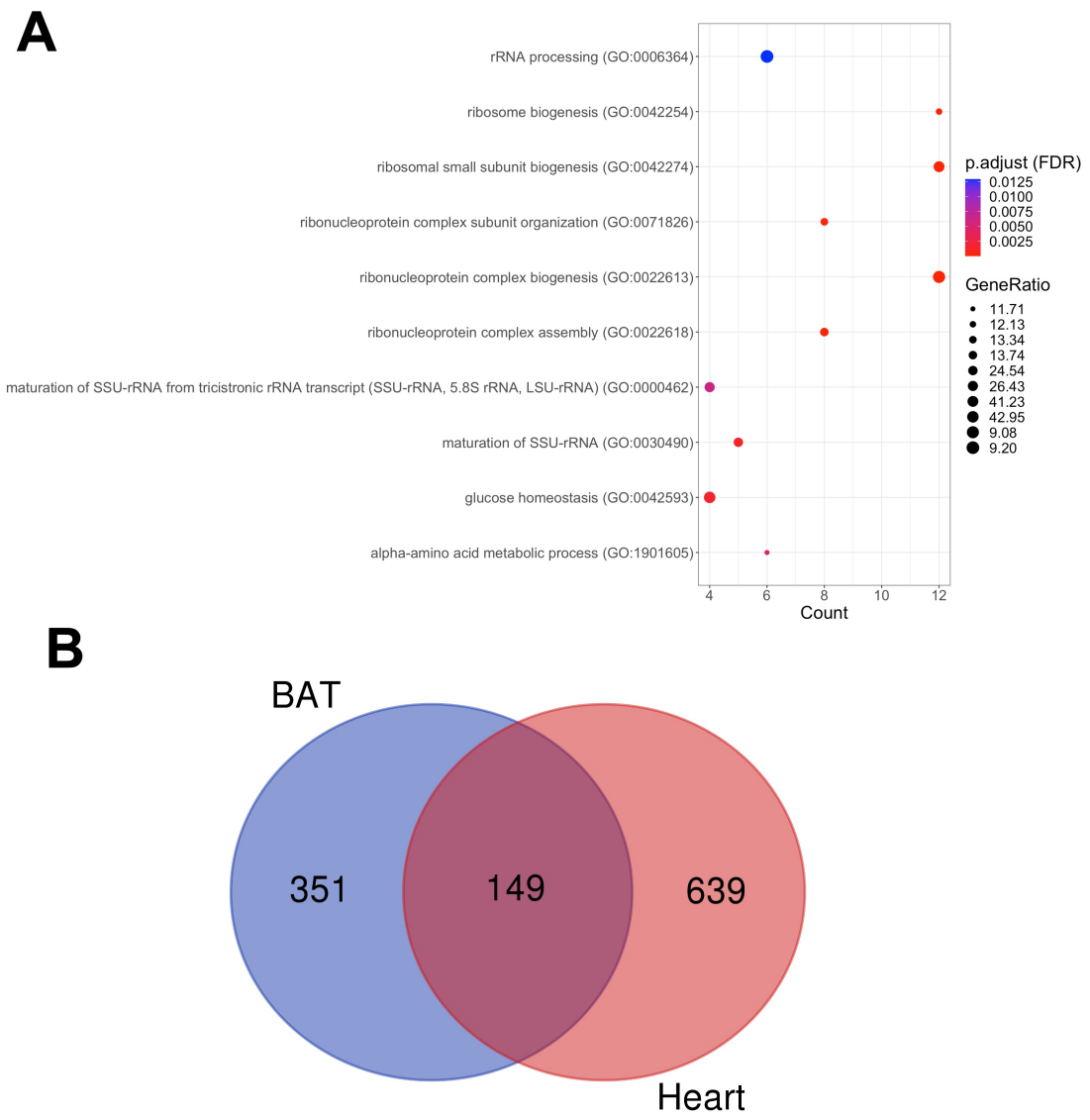

Figure 4.10: Down-regulated protein pathways in BUD23 knockout BAT. (A) Over-representation analysis of down-regulated biological processes was performed using Panther. The top 10 terms are shown here. (B) Comparison of proteins identified as significantly altered in the MCK BUD23 knockout proteome and the AdipoCre BUD23 knockout proteome.

expressed in both systems, which we then mapped to pathways to try to establish the core mechanism underlying BUD23's function. Up-regulated terms corresponded to translation, initiation of translation, protein folding, ribosomal biogenesis, and phagosomal proteins. Again, this highlights a strong drive within both models to drive protein biosynthesis, and likely reflects the change in ribosomal subunit ratio caused by BUD23's absence. Down-regulated terms map to mitochondria,

carbon metabolism, TCA cycle, and BCAA catabolism. This solidifies that changes in mitochondrial protein mass are a conserved phenotype across both models, but interestingly the loss of BCAA degradation pathways might highlight that BUD23 rewires metabolism in these tissues, which was not explored previously in the cardiac model.

RNA sequencing of the same samples identified 3,912 RNA species that were differentially up-regulated, and 3,763 that were down-regulated. Separating samples by sex did not alter any of the major findings, indicating a lack of sexual dimorphism in the BUD23 knockout phenotype. Therefore, all data is presented as mixed sex combined datasets. mRNA expression levels are generally weakly associated with protein expression, with mRNA quantity only acting as an approximately 40% strength predictor of protein abundance (Abreu et al., 2009). In our wild-type BAT, the correlation coefficient between mRNA and protein abundance was 0.528 (Spearman's rank test). If there was a major translational imbalance due to faulty ribosomal apparatus, mRNA abundance may be further disjointed from protein abundance, as failure to progress would stall in between the two phases. However, BAT lacking BUD23 still showed a correlation coefficient of 0.495 between mRNA and protein abundance, which while lower than the control BAT was not found to be significantly different ($p=0.06$, Fisher's Z-transformation). This would indicate that the effects of BUD23 are surprisingly selective, and that disruption of the small:large ribosomal subunit does not cause a gross failure of translation in our model.

Down-regulated mRNA species were associated with mitochondrial proteins, thermogenesis, oxidative phosphorylation, and carbon metabolism, in a similar fashion to the protoemics data (Fig. 4.11A). This is surprising, as our previous work in the cardiac model suggested that there was a drive to generate more mitochondrial proteins at the transcriptional level, but that it failed to progress through translation. Here, we show that mitochondrial transcripts are also down-regulated, perhaps suggesting that the reduction in mitochondrial density is as a result of downstream signalling resulting from BUD23 loss instead. However,

the up-regulated terms are surprising, as a strong immune phenotype can now be observed (Fig. 4.11B). In addition to pathways regarding rRNA processing, terms such as positive regulation of immune response, adaptive immune response, and defense response to virus are all strongly differentially up-regulated. Increased immune cell infiltration is a well described consequence of BAT whitening (Kotzbeck et al., 2018), and this finding further supports our view that BUD23 ablated BAT is undergoing this process. Unfortunately, none of the identified pathways can explain why BAT that is lacking BUD23 appears to have a whitened phenotype, which typically is incapable of a thermogenic response, yet is still able to produce heat, although not through canonical sympathetic stimulation.

4.3.6 BAT shows decreased *de novo* lipogenesis and β-oxidation in the absence of BUD23

To further investigate the mechanisms underlying BAT whitening and thermogenesis in the absence of BUD23, we investigated expression levels of panels of genes associated with key BAT functions (Fig. 4.12). Most genomically-encoded mitochondrial genes were significantly down-regulated, matching the pathway analysis results. However, *Pgc1a*, a major mitochondrial transcription factor, was up-regulated, which could be indicative of a potential compensatory pathway. Interestingly, *Elovl3* and *Cidea*, two genes heavily involved in thermogenesis were down, but *Dio2*, which is responsible for T4 thyroxine conversion into its active form, T3 3,5,3'-triiodothyronine, was up-regulated. Some studies have indicated that thyroid hormones are capable of driving thermogenesis through UCP-1 (Yau et al., 2018). This may point to a potential alternative pathway for initiation of thermogenesis, using thyroid hormones instead of sympathetic innervation to stimulate NST. Other studies have also implicated that G protein-coupled receptors may also be tied to NST function in BAT (Johansen et al., 2021). A subset of these are up-regulated in our model, however further work would be necessary to determine if these are truly capable of driving thermogenesis (Fig. 4.13).

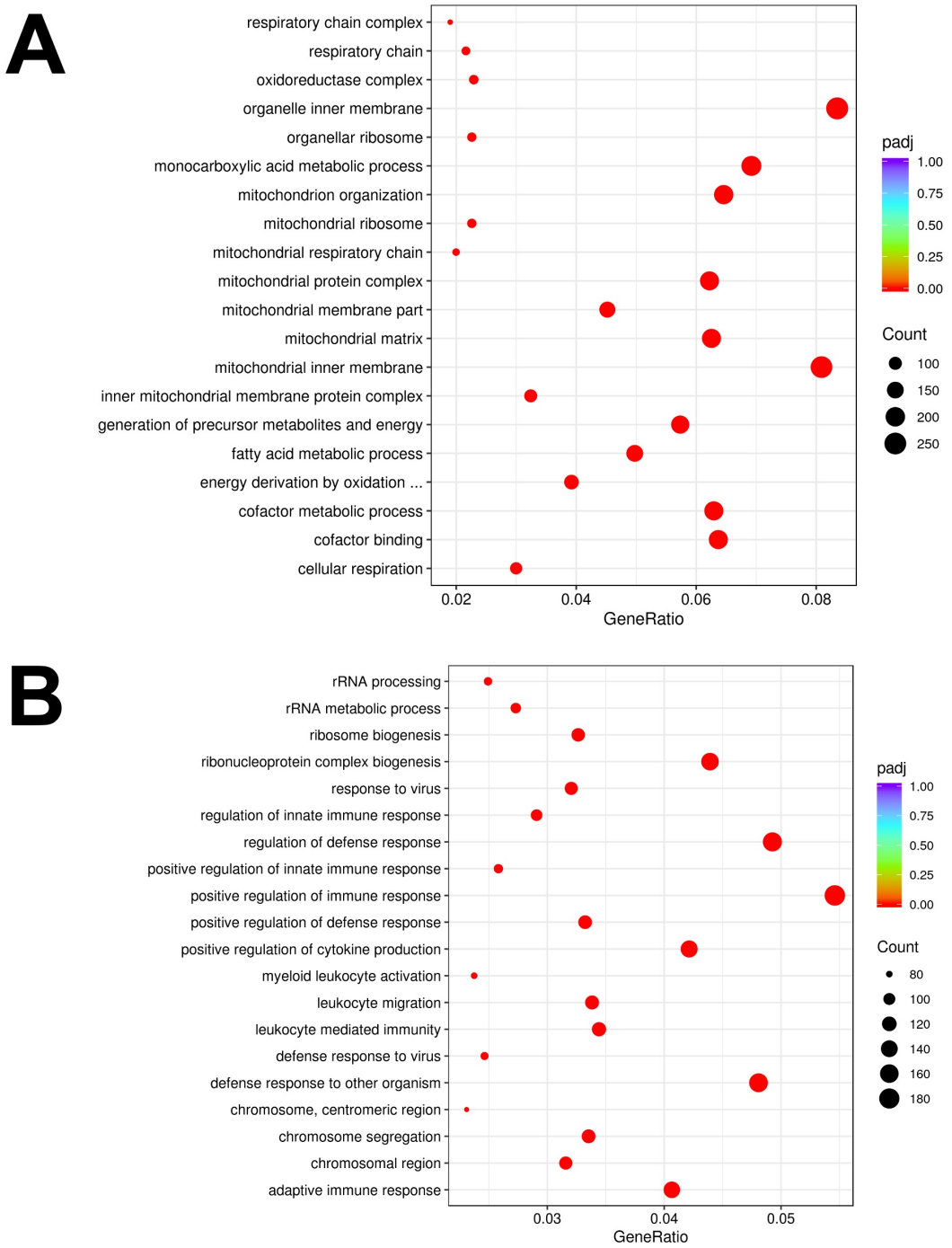

Figure 4.11: Over-representation analysis of BUD23 knockout BAT RNA-Seq. Over-representation analysis of (A) down-regulated and (B) up-regulated terms was performed on differentially expressed genes identified during RNA-Seq using Panther. The most significant terms are shown here.

Analysis of genes involved in fatty acid oxidation and *de novo* lipogenesis (DNL) show a strong decrease in expression in response to loss of BUD23 (Fig. 4.14). Fatty

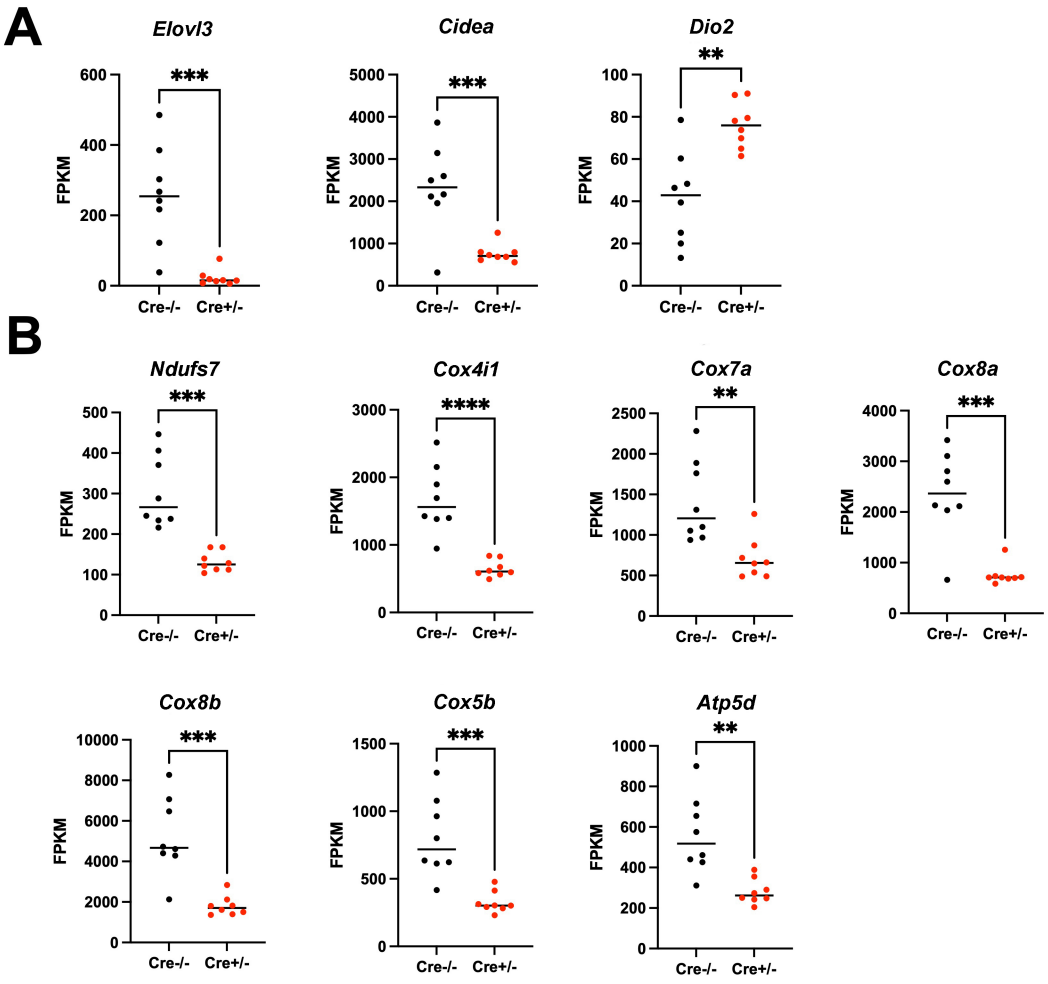

Figure 4.12: FPKM counts for key BAT function genes in BUD23 knockout BAT. A subset of expression counts for (A) thermogenic and (B) mitochondrial genes from RNA-Seq. ** indicates p-value $\leqslant 0.01$; *** $p \leqslant 0.001$; **** $p \leqslant 0.0001$

acids are the primary source of energy for BAT mitochondria, and a defect in the ability to correctly metabolise them could explain the mitochondrial phenotype observed upon loss of BUD23. The loss of DNL appears at odds with the apparent whitening phenotype of BUD23 knockout BAT, as adipocytes can be observed to have increased lipid loads. It is possible that triglycerides are not being utilised, as a result of loss of fatty acid oxidation, and thus the storage capacity of the brown adipocytes is maximised, resulting in a dampening of signals that would normally be used to replenish spent supplies. These changes indicate either a loss of β-oxidation, increased lipid synthesis, or increased lipoprotein lipase (LPL) driving fatty acid uptake from circulating VLDLs. However, analysis of LPL revealed

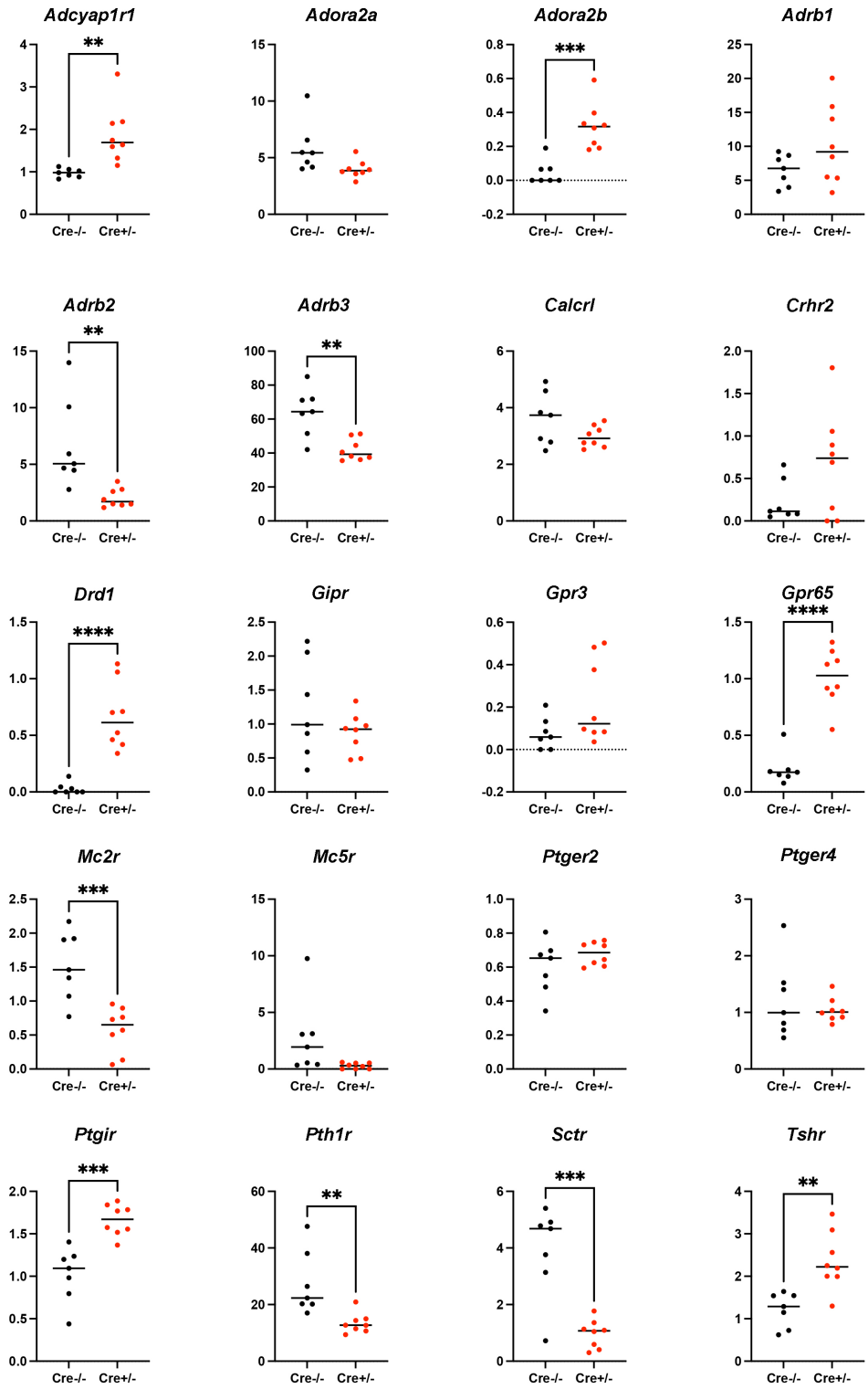

Figure 4.13: FPKM counts for G-protein coupled receptors in BUD23 knockout BAT. A subset of G-protein coupled receptor expression levels from RNA-Seq. GPCRs are expressed at too low of a level to be detected by proteomics. ** indicates p-value $\leqslant 0.01$; *** $p \leqslant 0.001$; **** $p \leqslant 0.0001$

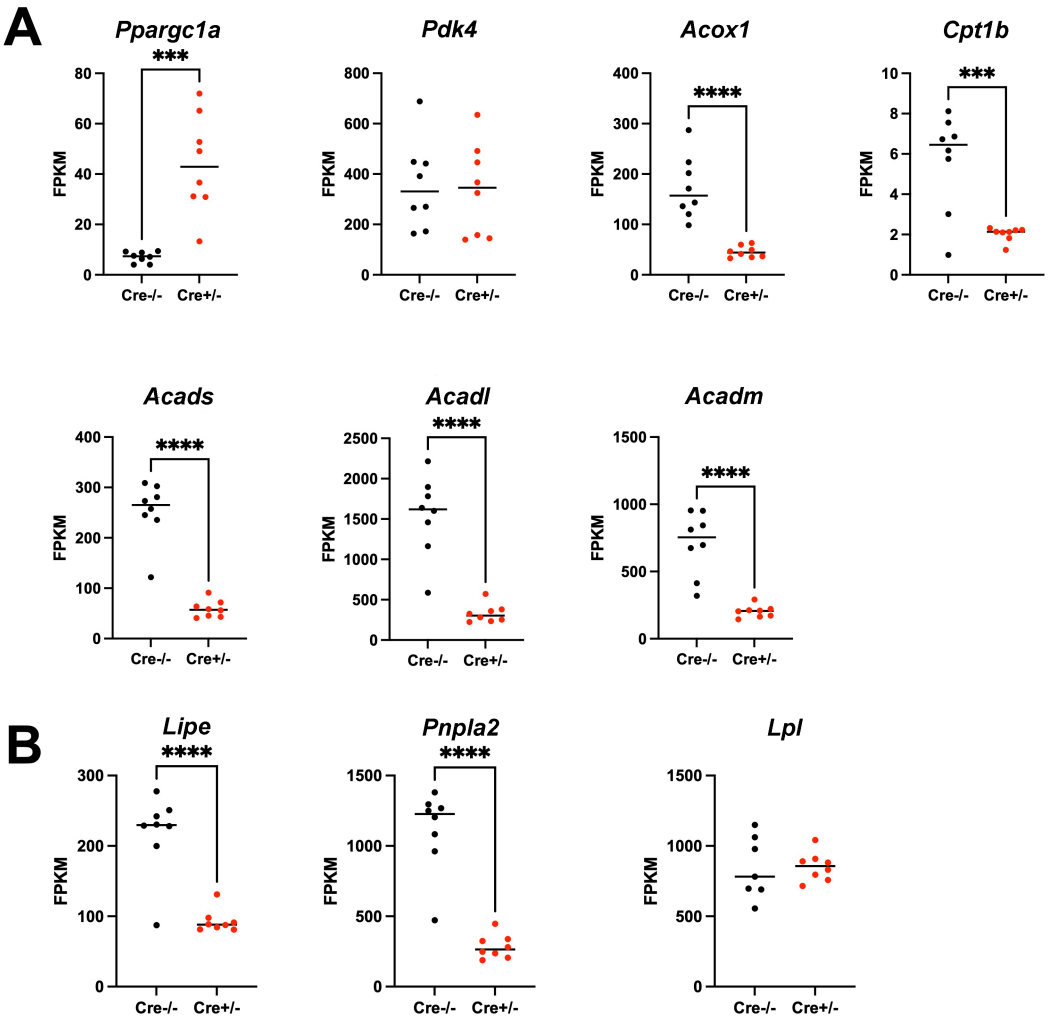

Figure 4.14: FPKM counts for fatty acid oxidation genes in BUD23 knockout BAT. A subset of expression counts for (A) fatty acid oxidation and (B) lipase genes from RNA-Seq. *** indicates p-value $\leqslant 0.001$; **** $p \leqslant 0.0001$

that its expression did not change, indicating that the observed changes are not likely to be due to increased uptake.

4.3.7 BUD23 deficient mice show signs of global metabolic rewiring

As pathway analysis from BUD23 knockout BAT suggested that certain metabolic pathways may be altered, adult mice were placed in a CLAMS Comprehensive Lab Animal Monitoring System to identify any obvious metabolic changes (Fig. 4.15A-B). Mice showed no genotype-dependent difference in their oxygen consumption

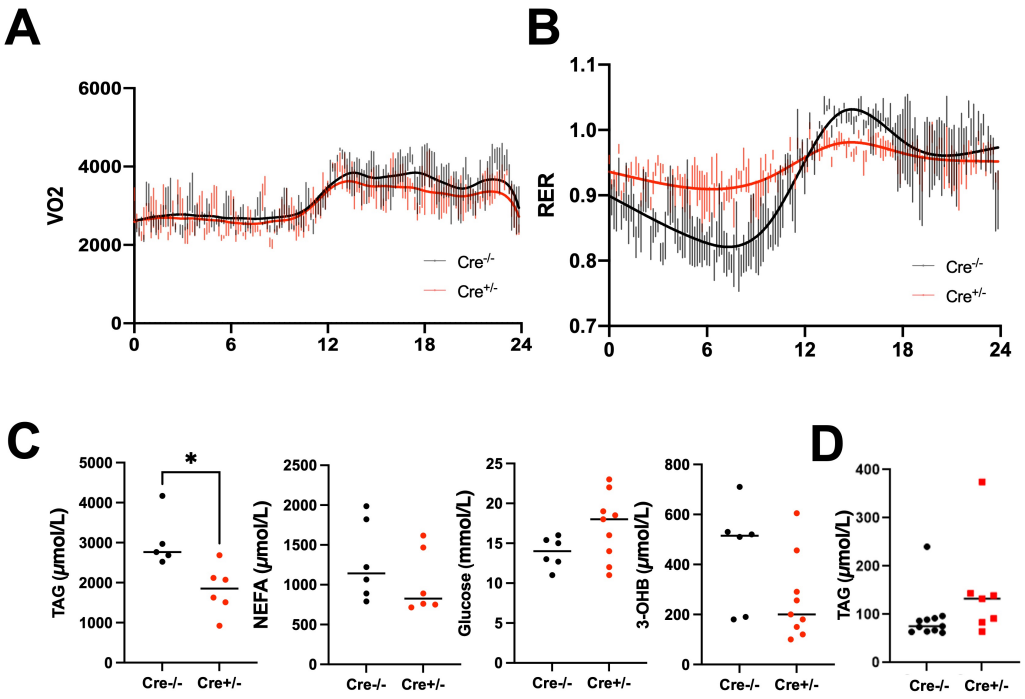

Figure 4.15: BUD23 deficient mice show global metabolic alterations. Individually housed mice were placed in a CLAMS metabolic cage to assess for (A) oxygen consumption, and (B) respiratory exchange ratio. (C) Circulating metabolites were assessed from blood serum. (D) Liver homogenate triglyceride content. * indicates p-value $\leqslant 0.05$

over a 24h period, with both AdipoCre$^{+/-}$ and AdipoCre$^{-/-}$ mice showing a clear circadian pattern. However, BUD23 adipose null mice showed a loss of diurnal rhythmicity in their respiratory exchange ratios (RERs) compared to wild-type mice. Wild-type mice had lower RER scores during their resting phase, indicating that they were burning fats as a primary energy substrate, and higher RER scores during their active phase, indicating they were using carbohydrates as fuel. Adipose null animals showed a flat, high RER for the full recording duration, indicating that they were constitutively burning carbohydrates and not utilising fats. This supports the theory that triglyceride accumulation in BAT may be due to impaired β-oxidation.

We then analysed blood serum from fasted mice for various metabolites to identify if there was any change in flux down certain metabolic pathways (Fig. 4.15C). No difference was observed in levels of circulating non-esterified fatty acids or 3-hydroxybutyrate in BUD23 adipose knockout animals. While glucose

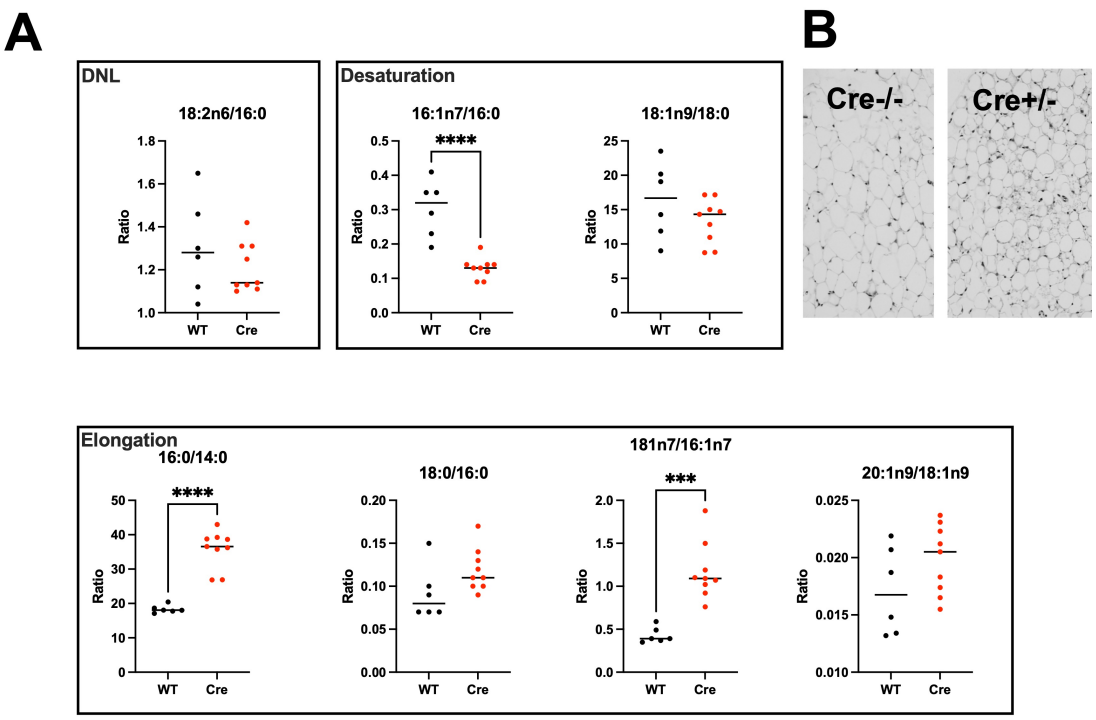

Figure 4.16: Assessment of WAT phenotype upon BUD23 knockdown. (A) Fatty acid ratios of species identified in WAT. Elongation of fatty acids appears to be increased, while desaturation is decreased (n=6 per genotype). (B) Histology of WAT sections, revealing smaller adipocytes in BUD23 knockout WAT. *** indicates p-value $\leqslant$ 0.001; **** $p \leqslant 0.0001$

appeared to be slightly elevated in knockouts, this was not found to be a significant change. Circulating triglycerides were decreased compared to wild-type animals, potentially as a result of metabolic inflexibility in the mice leading to preferred glucose utilisation. This indicates that the excess of triglycerides observed in BAT are not due to increased production and circulation by other organs. We also tested liver triglyceride levels to determine if mice had hepatic steatosis (Fig. 4.15D), but found no difference between the two genotypes, indicating the observed metabolic phenotype is not driven by liver pathology.

4.3.8 White adipocytes show altered fatty acid profiles

Histological analysis of epididymal WAT from BUD23 knockout mice revealed no major morphological alterations to their white adipocytes (Fig. 4.16), although they appeared to be slightly smaller in size than their control counterparts, potentially

indicating that they have smaller triglyceride stores. We then analysed the fatty acid profile of WAT in both BUD23 knockout and control mice, to investigate if there were any major metabolic changes (Fig. 4.16). By analysing the resulting ratios of fatty acid species, we could interrogate the separate pathways underlying WAT function. DNL appeared to be intact in white adipocytes, contrary to our findings in BAT, indicating that they can create triglycerides for storage. However, desaturation of fatty acids was reduced, while elongation of fatty acid chains was increased. One study hypothesised that elongation of fatty acids was a marker of insulin resistance, while increased desaturation correlated with increased body mass (Tan at al., 2015). We have not directly established whether animals lacking BUD23 in their adipose are insulin resistant, but this may explain some of the global metabolic changes observed throughout the mice. However, we have previously established that the protein expression of BUD23 in WAT is very low. We are therefore unable to determine if these effects are due to a loss of BUD23 function in WAT, or if the effects seen in WAT are as a result of a global metabolic rewiring driven by loss of BUD23 in BAT.

4.4 Discussion

Adipose tissue is metabolically rich, utilising a variety of substrates to carry out its various functions, which include energy storage, endocrine signalling, and heat generation (Nawrocki & Scherer, 2004; Gesta et al., 2007). In particular, brown adipose is the core site of NST in the body, which is facilitated by its rich mitochondrial presence and high UCP-1 expression (Enerbäck et al., 1997). This makes it an enticing model organ in which to study the biological consequences of BUD23 knockdown, and therefore infer the core mechanisms underlying BUD23's method of action. We have previously established that disruption of BUD23 within cardiomyocytes results in two major effects (Baxter et al., 2020) . Firstly, its absence promotes a global translational defect as a result of altered ribosomal biogenesis, driven by BUD23's role in small subunit maturation, and secondly, loss of BUD23 appears to cause a selective metabolic burden that ultimately drives cardiac failure in knockout animals. This was the first time an *in vivo* mammalian model of BUD23 was generated, revealing a potential novel function of BUD23 as a master controller of metabolic gene translation. However, this was only tested in one tissue type and so it was unclear if these findings reflected the nature of the model, or were a more generalised finding regarding the role of BUD23 in mammalian systems. We therefore generated a second conditional BUD23 knockout mouse, targeting knockdown specifically to adipose tissue through the use of an Adiponectin-Cre driver.

Adipose BUD23 knockout animals appeared to show a fairly mild phenotype as mice were viable through all stages of life. Interestingly, knockout adults were slightly leaner than their wild-type littermates and showed alterations to their average daytime body temperatures. This constituted the first hint of a thermogenic phenotype in these animals, consistent with our hypothesis that knockdown of BUD23 would alter the thermogenic capacity of BAT. There are several possible explanations for why knockout animals are lean. Firstly, it is possible that they are eating less and therefore have a smaller caloric intake. As adipose signalling

has been linked to appetite (Nawrocki & Scherer, 2004), it is possible that global endocrine signalling has been altered in these animals and is suppressing their urge to feed. Secondly, if we instead assume that feeding behaviour is not altered, it is possible that either mice are unable to metabolise their meal correctly and are excreting some of the nutrients from their food instead of absorbing them through their gut, or mice may have increased energy expenditure requirements and so are burning more of their triglyceride stores to maintain homeostasis. If mice are being forced to use less efficient thermogenic strategies, such as having a heavier reliance on shivering to maintain body temperature, an increase in energy expenditure would be expected. This can be investigated through the analysis of food intake over a 24 hour period in single-housed mice to determine if animals are consuming similar amounts of food. In addition, bomb calorimetry of their faecal pellets would permit us to look at the nutritional breakdown of their excrement.

One of the major findings in our previous cardiac muscle knockout model was that loss of BUD23 resulted in a specific mitochondrial defect. Here, we show that loss of BUD23 specifically in adipose tissue results in the loss of mitochondrial density, but not function, in brown adipose, contradicting the findings in the heart. In addition, electron microscopy of mitochondria from knockout animals revealed that they appear to be healthy and do not show any morphological abnormalities, such as fused mitochondria, incorrectly folded cristae, or disrupted membrane structures. In particular, mitochondria do not contain the electron dense inclusion bodies identified in MCK-Cre knockout mice. Inclusion bodies are a poorly studied phenomenon, however one study proposed that they were a compensatory response to a high metabolic burden (Jacob et al., 1994). As these animals have not undergone any interventions, it may be the case that their BAT is not under significant stress to drive heavy mitochondrial use. In order to confirm that inclusion bodies are a result of mitochondrial stress, it would be interesting to see if their presence can be detected in cold-challenged BAT tissue from BUD23 knockout animals. While the severity of the observed mitochondrial defects varies between the two models, both show a consistent failure in mitochondrial number, indicating that this is

a common feature resulting from loss of BUD23, and that it is consistent across multiple tissue types. The more severe loss of mitochondrial function observed in the cardiac knockout model may therefore be a consequence of subsequent cardiac failure, rather than driven directly by BUD23's absence.

As loss of BUD23 drives mitochondrial failure, we predicted that mice would not be able to produce heat when exposed to a cold challenge, as BAT driven thermogenesis relies on the uncoupling of the mitochondrial proton gradient to produce energy. Interestingly, mice were still capable of defending their body temperature in response to an acute cold challenge, despite the fact that they were unresponsive to sympathetic stimulation, the canonical driver of NST (Emorine et al., 1989). While this may be due to compensation in other organs, for example increased shivering in muscles, or browning of white adipose resulting in thermogenesis from subcutaneous white depots, thermal imaging of scapular BAT revealed a clear hot spot in knockout animals, indicating their brown adipose is still, at least partially, capable of thermogenesis. It is important to note that mice are typically housed at 21°C, and so are constantly under pressure to produce heat in order to maintain their body temperature. This low level drive may encourage the development of compensatory mechanisms in the case of failing, or partially failing, BAT. To eliminate these effects, BUD23 knockout mice could be raised in thermoneutral conditions and then exposed to a cold challenge to determine if their ability to produce heat is impaired. However, if BAT function is severely impaired due to BUD23 knockdown, it may atrophy in the absence of any cold stimulus and therefore when removed from thermoneutral conditions, the animals would not be able to thermoregulate, raising welfare concerns if we were to attempt a cold challenge.

Inspection of BUD23 knockout BAT reveals various typical characteristic changes often found in dysfunctional BAT, including enlarged triglycerides droplets, pale tissue morphology, and loss of mitochondrial density (Kotzbeck et al., 2018). This has been described in multiple models of BAT failure, and is commonly termed as BAT 'whitening', where brown adipocytes adopt a more unilocular, white-like

phenotype. Multiple factors have been described to initiate whitening, including high ambient temperatures (thermoneutrality), impairment of β_3-AR pathways, lipase deficiencies, and lipid accumulation resulting from a positive caloric balance, such as in obesity models (Kuipers et al., 2019). One study in *Atgl* knockout mice, a triglyceride lipase, showed a strong immune phenotype (Kotzbeck et al., 2018). When brown adipocytes reached a critical size, they were prone to death, encouraging the recruitment of MAC2 positive macrophages. This caused metabolic stress within the tissue, ultimately resulting in mitochondrial death via mitophagy. RNA-Seq in BUD23 knockout BAT revealed a clear immune signature, reflecting a potential inflammatory whitening phenotype that would match that seen in the *Atgl* knockout model. Further experiments should be carried out to confirm this, such as immunostaining of inflammatory markers within knockout BAT tissue. Another study linked vascular rarefaction to BAT whitening, primarily through the expression of VEGF (Shimizu et al., 2014), which promotes the growth of new blood vasculature. They found that obesity led to enlarged lipid droplet size, mitochondrial dysfunction, and decreased VEGF expression within BAT tissue. Targeted knockdown of VEGF in BAT was then shown to increase reactive oxygen species production, induce mitophagy, diminish β-adrenergic stimulation, and promote a hypoxic environment within BAT. Investigation of the RNA-Seq and proteomic data acquired from BUD23 knockout BAT also show a decrease in lipases, lipogenesis, VEGF, and mitochondrial proteins, consistent with published whitening models.

However, in all of these models the primary effect of BAT dysfunction is a complete loss of thermogenic capabilities, stemming from mitochondrial failure. Therefore, BUD23 knockout BAT constitutes a striking shift in the traditional paradigm of known whitening models, as while animals display all the characteristic changes of whitening, BAT tissue is still functional and capable of carrying out thermogenesis despite a reduced mitochondrial density. While BUD23 ablated BAT did not respond to canonical sympathetic stimulation, failure to produce heat in response to a β_3 agonist can be explained by the low expression of β_3-AR. However, BUD23 knockout BAT still showed normal UCP-1 expression, permitting

the uncoupling of mitochondrial oxidative phosphorylation via other putative, non-canonical pathways. *Dio2* was found to be up-regulated in BUD23 knockout BAT. This is a gene encoding type 2 iodothyronine deiodinase, which is responsible for the conversion of thyroxine (T4), a thyroid hormone, to its active form 3,5,3'-triiodothyronine (T3) within BAT tissue. *Dio2* has been identified as essential in order to mount a thermogenic response via standard adrenergic pathways, as it facilitates the cAMP signalling cascade that ultimately drives thermogenesis (de Jesus et al., 2001). While normally considered a synergistic pathway with canonical adrenergic signalling, it is possible that its over-activation permits downstream thermogenic signalling via cAMP and UCP-1, bypassing the requirement for an initial noradrenaline stimulus. A recent paper has also implicated that G protein-coupled receptors (GPCRs), and in particular GPR3, are capable of inducing thermogenesis in an adrenergic-independent manner (Johansen et al., 2021). While we cannot confirm if GPCRs are upregulated at the protein level due to their low abundance, we have shown that the expression of various GPCR mRNAs is induced upon loss of BUD23. We therefore propose that these may constitute an alternative thermogenic pathway in BUD23 knockout BAT, though further work would be required to confirm this.

Investigation into the underlying molecular causes of BAT dysfunction following BUD23 knockdown revealed a similar profile to that found in the heart: a strong mitochondrial signal, and evidence of a low-level drive for increased translation, although there did not appear to be a gross defect in translation overall. This further supports that the effects of BUD23 are conserved across multiple tissue types, and that these are therefore general findings and not limited to the cardiac model. Further analysis of proteins from key BAT pathways identified deregulation of lipogenesis, fatty acid uptake, and lipolysis (Fig. 4.17). On the other hand, glycolytic pathways showed an increased drive. In healthy BAT, intracellular triglycerides form the primary source of energy for thermogenesis (Blondin et al., 2017), and their loss corresponds to an impairment of BAT thermogenic function. This points to a metabolic rewiring within BUD23 knockout BAT, shifting away

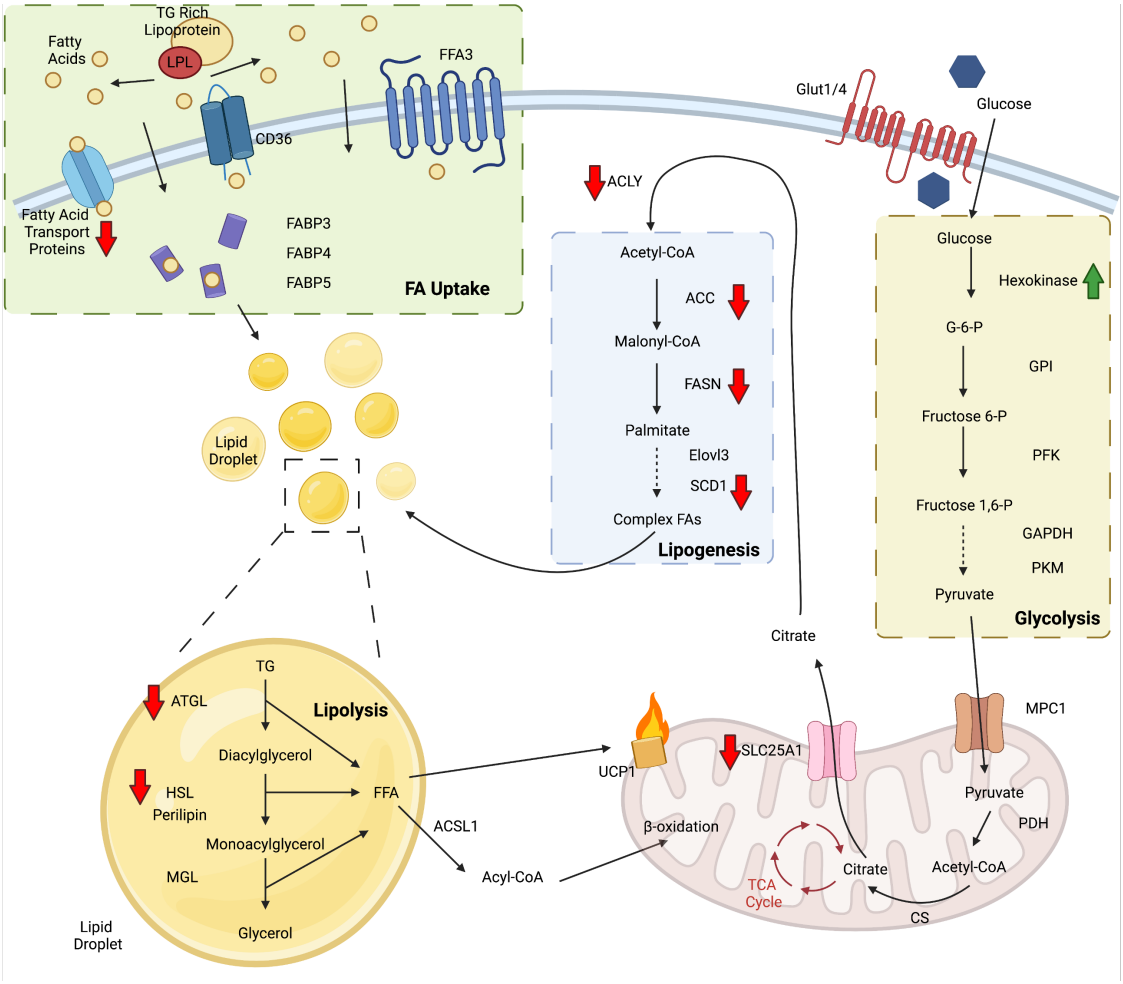

Figure 4.17: Summary figure of altered key BAT metabolic pathways. LFQ proteomics data was used to identify differentially regulated proteins in BUD23 knockout BAT. Figure was generated in BioRender.

from the traditional substrates and β-oxidation, but showing a heavier reliance on glucose pathways instead, although the origin of this switch remains to be determined. As brown adipocytes have enlarged triglyceride droplets, but decreased signalling for uptake and DNL, this appears to indicate that the failure to use triglycerides is repressing the standard pathways that would typically replenish spent triglyceride sources. The use of labelled triglyceride species and subsequent metabolomic analysis may constitute a method to explore the point of failure in triglyceride usage, and to elucidate if there is a key limiting step at which metabolic intermediates are accumulating.

Analysis of proteomic data also revealed a decrease in proteins associated

with branched chain amino acid (BCAA) catabolism in BUD23 knockout tissues. Increased BCAA uptake is observed in healthy BAT upon cold stimulation (Yoneshiro et al., 2019), and suppression of BCAA transporters results in impaired thermogenesis, pointing to its importance as a thermogenic substrate. Deregulation of BCAA pathways further highlights a potential metabolic rewiring in BUD23 knockout BAT.

In addition to an altered metabolic profile within BAT tissue, AdipoCre$^{+/-}$ BUD23$^{fl/fl}$ mice also showed altered global changes to their circadian metabolic rhythms. The most striking finding was a complete loss of their respiratory exchange ratio rhythm. In healthy animals, carbohydrates are used as a preferential energy source during their active period, where food is readily available, and fats are used during their resting period, when they do not feed. Knockout animals lose this pattern, instead utilising glucose as the primary source of energy at all times, resulting in a constitutively high respiratory exchange ratio. This indicates that knockout mice are metabolically inflexible, behaving in a similar fashion to patients with type 2 diabetes (T2D). T2D is characterised by a reduced capacity for fatty acid oxidation during fasting periods, impaired mitochondrial function, intracellular lipid accumulation, and insulin resistance (van de Weijer et al., 2013). While we have not tested if BUD23 knockout mice are insulin resistant, signalling from BAT has been implicated in insulin responses via various mechanisms, such as adiponectin secretion (Yamauchi et al., 2001; Lee et al., 2004). Any changes to key BAT pathways, such as the triglyceride accumulation and β-oxidation defects described from BUD23 knockdown, can then result in direct global metabolic rewiring throughout the entire mouse. This theory was supported by analysis of blood metabolites from BUD23 knockout mice, where we identified a decrease in circulating triglyceride levels, with no change to lactate, non-esterified fatty acids, or 3-hydroxybutyrate. While a decrease in circulating triglycerides may be initially surprising, as BAT tissue shows a defect in uptake and usage of triglycerides, so it might be expected that more triglycerides would be available in the blood stream, it is important to note that these are snapshot values, representing steady state levels of metabolites

within the blood stream. The decrease in triglycerides is likely a response to downstream metabolic signalling, directing the mouse to utilise glucose and not release triglycerides into the blood stream from other organs, such as the liver.

Overall, we have described a new *in vivo* knockout model of BUD23, targeting disruption specifically to adipose tissue. We have verified that the functions we identified in our previous cardiac model are consistent, including specific mitochondrial defects and a global translational defect, but have identified differences between the two that could aid in identifying the core changes that occur as a result of BUD23 knockdown. Here we present a model with a subtle but complex phenotype, where loss of BUD23 has metabolically rewritten brown adipose tissue in mice. We propose that removal of BUD23 results in an altered translational profile within the animals, initially altering the translational efficiency of a subset of transcripts that then results in further downstream signalling cascade alterations. While we have not identified the initiating set of proteins that are disrupted upon loss of BUD23, we have shown that their loss results in whitening of brown adipose, resulting in triglyceride accumulation, inflammation, mitochondrial loss, defects in β-oxidation, and a shift away from traditional substrate utilisation. We propose that signalling from brown adipose then acts on other organs, triggering the mouse to utilise glucose as an energy substrate globally and leading to metabolic inflexibility. One of the most striking findings within the adipose knockout model is that animals lacking BUD23 are still capable of thermogenesis, which is atypical for a whitened phenotype. Why BUD23 knockdown permits the escape from a canonical whitening phenotype is unknown, although we have proposed that the action of *Dio2* or G-protein coupled receptors could play a role in rescuing the thermogenic phenotype. However, this remains an intriguing question for future avenues of study, and further work should focus on what delineates the BUD23 knockout model from typical BAT whitening models.

4.5 Acknowledgements

Gina Galli and Kerri Smith, for assistance with the Oroboros data aquisition. Rebecca Northeast and Nichola Barron, for extensive help with the *in vivo* studies. Errin Johnson, for assisting with the electron microscopy. Elspeth Johnson, for carrying out the fatty acid profiling mass spectrometry. The Target Discovery Institute Mass Spectrometry group, for their assistance with the proteomic mass spectrometry.

5

The structure and function of BUD23

Contents

5.1 Introduction

Since its original identification as a ribosomal biogenesis factor (White et al., 2008), BUD23 has been primarily studied in the context of budding yeast, where its loss was described to cause a slow growth phenotype (Létoquart et al., 2014). However,

siRNA experiments in human immortalised cell lines revealed a novel phenotype, where knockdown of BUD23 resulted in a specific defect in translational efficiency of metabolic transcripts (Baxter et al., 2021). BUD23 is known to have two functions from previous work in yeast. Firstly, it is believed to catalyse the methylation of G1575 on the small ribosomal subunit (White et al., 2008), a modification present on roughly 60-100% of all ribosomes (Haag et al., 2015; Taoka et al., 2018). Secondly, it is essential for progression of small ribosomal subunit biogenesis, and its loss causes stalling at the 18SE stage (Haag et al., 2015). These functions have also been confirmed to be conserved in a human cell model, although the authors did not identify any metabolic phenotype at the time.

Modelling of protein structure can enable the deduction of a protein's function by assessing the molecular mechanisms underlying how it works. Unfortunately, crystallising proteins is a complex process, and is not possible for all types of proteins. However, if a good template is available, for example an ortholog from another species or a closely related protein, it is possible to carry out *in silico* homology-based modelling to build a theoretical model of a protein's structure.

5.1.1 Yeast structure

The crystal structure of the yeast Bud23 protein has been determined in complex with Trm112, which serves to stabilise the protein by hiding hydrophobic residues (Létoquart et al., 2014). Trm112 is a 15 kDa protein that has the capability to bind and stabilise a number of Rossmann-fold-like methyltransferases, including Mtq2, Trm9 and Trm11 (Purushothaman et al., 2005; Mazauric et al., 2010). All of its partners bind in a competitive manner, and an overexpression of any one methyltransferase will destabilise the equilibrium. For example, overexpression of Mtq2 creates a phenotype that mimics knockdown of Bud23, owing to the lost functionality of Bud23 as it is rapidly degraded *in vivo* without Trm112 (Figaro et al., 2012).

Yeast Bud23 has a characteristic Rossmann-fold-like structure, with a central sheet formed from seven β strands (Létoquart et al., 2014). However, instead of being sandwiched between three helices on either end, as is typical of most members of the Rossmann-fold-like family, the β sheet has four helices on one side and two on the other. Small fluctuations in the helix structures are fairly common within the family. Upon binding SAM, it undergoes a slight conformational change, with K21-G24 switching to extend one of the helices, whereas normally they would form an extended loop. In addition, A126-N131 and I12-H20 also reorganise themselves into a different configuration to permit correct SAM binding.

Létoquart et al. (2014) also devised a model to explain the mechanism behind methyltransfer from SAM to N7 on a guanine residue, such as would happen when Bud23 methylates the small ribosomal subunit via m7G. This permitted the identification of vital amino acids within the binding site, including E18, Y22, and S118. Mutation at E18 and Y22 sites generated structurally stable proteins that lacked methyltransferase activity, as determined by investigation of rRNA within the cells, while mutation at S118 appeared to result in misfolding of the protein and so disrupted both Bud23 functions. Targeted mutation of these key residues would be a useful tool for separating the two functions of Bud23 for further analysis, and would create a viable strategy to assess which function is responsible for the metabolic phenotype identified in human cell lines.

5.1.2 Hypothesis and aims

Overall, we hypothesised that by generating a working structural model of human BUD23, we could **assess its molecular mechanism of action and therefore permit us to to develop a targeted intervention to delineate its two functions**.

Aim 1: Build a suitable model of human BUD23 based off the yeast crystallised structure

Through the use of homology modelling tools, we aimed to generate a working model of human BUD23 structure using the published yeast structure generated by Létoquart et al. (2014). This enabled us to determine if human BUD23 used the same mechanisms as those observed in yeast in order to carry out its core functions.

Aim 2: Identify key residues essential to the methylation function of human BUD23

By investigating the SAM binding domain of our human BUD23 model, we aimed to identify the key amino acid residues necessary for its function as a methyltransferase. We could then selectively target these amino acids to try to disrupt methyl transfer, or SAM binding, without changing the overall structure of BUD23 and thereby preserve BUD23's secondary function in ribosomal biogenesis.

Aim 3: Create a cell line expressing methylation incompetent BUD23

We initially identified a potential metabolic defect in A549 human cells, which we wanted to interrogate further. As A549 cells are hypotriploid, targeted mutagenesis of the *Bud23* gene to alter the amino acid sequence of the BUD23 protein was not feasible. Instead, we knocked out endogenous BUD23 expression through the use of CRISPR, and then aimed to transfect cells with plasmids expressing the methylation incompetent forms of human BUD23, in order to separate the two known functions of BUD23 for further phenotypic profiling.

5.2 Materials and Methods

Methods specific to this chapter are reported here. All reagents are from Sigma unless otherwise stated.

5.2.1 *In silico* modelling

Homology modelling of human BUD23 was performed using C4XD software. The model was built using the template-based structure homology modelling tool, using the solved yeast BUD23 crystal structure (SAM bound form) as the base template. All 3D structures were accessed via the protein data bank (PDB; Table 5.1).

Multiple sequence alignment was performed using the structure alignment tool PROMALS3D (Pei et al., 2008).

5.2.2 CRISPR-Cas9 Transfection

All oligonucleotides used in this chapter can be found in Table 5.2

CRISPR-Cas9 delivery was performed through ribonucleoprotein transfection. Guide RNAs (gRNA) were supplied in two parts: crRNA, the custom targeting sequence; and tracrRNA, which binds with the crRNA and facilitates binding to

3D Structure	PDB Code	Citation
BUD23	4QTU	(Létoquart et al., 2014)
DOT1L	3QOW	(Richon et al., 2011)
NTMT1	5E2A	(Dong et al., 2015)
NTMT2	5UBB	(Dong et al., 2015)
METTL13	5WCJ	(Jakobsson et al., 2018)
PRMT3	2FYT	(Wu et al., 2006)
PRMT5	3UA3	(Sun et al., 2011)
PRMT6	5WCF	(Zeng et al., 2017)
PRMT8	5DST	(Toma-Fukai et al., 2016)
ASMT	4A6D	(Botros et al., 2013)
NSUN4	4FP9	(Spåhr et al., 2012)
NSUN6	5WWS	(Liu et al., 2017)
Ribosome	7O7Y	(Bhatt et al., 2021)

Table 5.1: Details of 3D structures used in this chapter.

Name	Type	Sequence
BUD23 TIDE F	PCR Primer	TGGGGTCACTTTCGAATGGT
BUD23 TIDE R	PCR Primer	GCTTCTCCACACCCATCAG
AAV TIDE F	PCR Primer	ACTAGGGACAGGATTGGTGACA
AAV TIDE R	PCR Primer	TGACGCACGGAGGAACAATA
BUD23 g909	crRNA	GGATGATTGATATCCAGACC
BUD23 g015	crRNA	CAGGATGGCTGGGCGAGCAT
BUD23 g916	crRNA	AGGTAACAGGGCTTATTCTC
gAAV	crRNA	CTCCCTCCCAGGATCCTCTC

Table 5.2: List of all oligonucleotides used in this chapter

Cas9. crRNA sequences and Alt-R CRISPR-Cas9 tracrRNA (IDT) were each re-suspended into 100μM stock concentrations in nuclease-free duplex buffer (IDT), before being mixed in equimolar concentrations to a final duplex concentration of 1μM and heated at 95°C for 5 mins to form the complexed gRNA.

In order to form the ribonucleoprotein complex, Engen Cas9 (New England Biolabs) was first diluted in OptiMEM media (Gibco) to a final working concentration of 1μM. The Lipofectamine CRISPRMAX kit (Invitrogen) was used to assemble the complex. In brief, complexed gRNA, Cas9, and Cas9 PLUS reagent (Invitrogen) were mixed together in OptiMEM media and incubated at room temperature for 5 mins.

The assembled ribonucleoprotein complex was then incubated with CRISPRMAX transfection reagent (Invitrogen) in OptiMEM media for 20 mins at room temperature to form the transfection complex according to manufacturer's instructions. A549 cells were washed with sterile PBS to remove all media and trypsinised. Cells were then diluted to 400,000 cells/mL in their standard media and plated into 6-well cell culture treated plates. Transfection complex was added to each well to a final concentration of 10nM. Plates were then incubated at 37°C in 5% CO_2 for 48h.

To generate a pure population of knockout cells, CRISPR-Cas9 transfected cells were diluted to a final concentration of 0.3 cells per well in a 96-well plate prior to monoclonal expansion. In brief, each well was investigated manually to determine how many cells were present within it. Any wells containing more than one cell were discarded. Single cell colonies were grown in the plate until they reached

approximately 70% confluency, prior to transfer into 12-well plates for expansion. Knockdown of BUD23 was confirmed via western blot for each resultant colony.

5.2.3 Tracking of Indels by Decomposition (TIDE) Analysis

In order to determine the cutting efficiency of each gRNA, TIDE analysis was performed. gDNA was extracted from transfected cells using the Wizard Genomic DNA Purification Kit (Promega), per manufacturer's instructions. In brief, cells were lysed in Nuclei Lysis Solution prior to incubation with RNase solution to break down any contaminant RNA sequences. Protein precipitation solution was then added, and purified DNA eluted using a column-based system into nuclease-free water. CRISPR-Cas9 targeted sequences were amplified using NEBNext High-Fidelity PCR Master Mix (New England Biolabs) with the primers listed in Table 5.2 according to the manufacturer's protocol. PCR products were then purified using the QIAquick PCR purification kit (Qiagen).

Purified PCR products were then submitted for Sanger Sequencing via the Genomic Technologies Core Facility at the University of Manchester. Resulting DNA chromatograms were analysed using the Tracking of Indels by DEcomposition (TIDE) tool (Brinkman et al., 2014).

5.3 Results

5.3.1 BUD23 is structurally conserved across multiple species

By using the published yeast Bud23 crystal structure as a template (Létoquart et al., 2014), we performed homology-based modelling to build a predicted structure of human BUD23 (Fig. 5.1). Yeast Bud23 is encoded by 275 amino acids, whereas human BUD23 is encoded by 281 amino acids, therefore the first six residues were trimmed where homology modelling was not possible due to a lack of template. The remaining residues showed a 46.9% match at the sequence level between human BUD23 and its yeast ortholog. These residues matched well in terms of structure and location, and therefore were modelled with high confidence. Only two small loops, located outside of the main body of the protein, had to be modelled *de novo* to facilitate structural prediction, corresponding to less than 5% of the total amino acid sequence. The remaining residues were modelled with medium confidence, with the software predicting that they would inhabit a similar location to the yeast equivalent residue, although the nature of the residues was not identical. This provided us with a suitable model of human BUD23, with very little *de novo* modelling, that appeared structurally very similar to the yeast protein despite more extensive divergence in sequence.

5.3.2 Identification of Rossmann-fold methyltransferase motifs

An alternative option for homology modelling is to instead use a closely related protein as a base template. We therefore compared our model to other closely related Rossmann-fold methyltransferases to identify similarities between the proteins, and to identify if there was a more suitable base structure that could be used (Fig. 5.2A-B). Models of BUD23, DOT1L, the closest protein to BUD23 according to the chemogenetic tree published by Richon et al. (2011), and NSUN6 were overlaid to look at the core structure of the proteins. By looking down into the SAM binding site, clear motifs common to the family were observed, including the six helices that frame the core beta sheet. While their exact positioning varied between

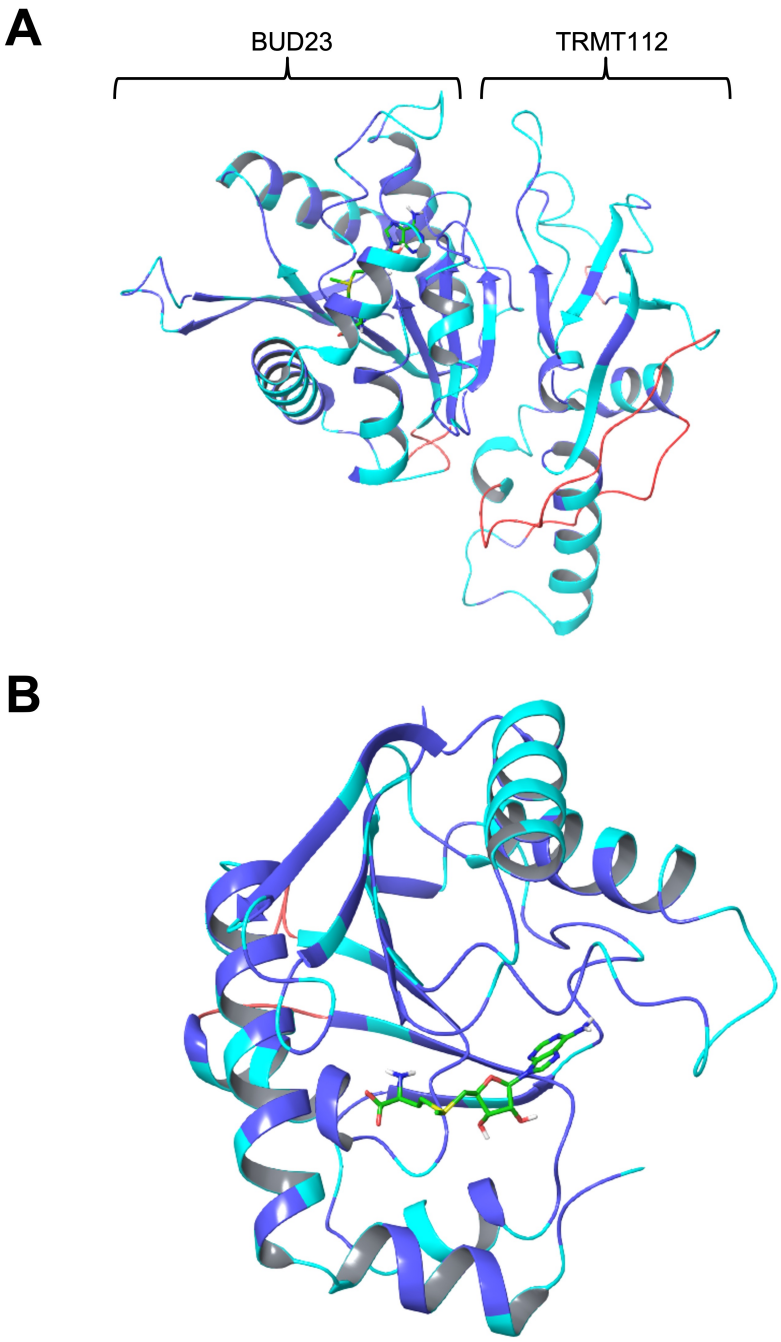

Figure 5.1: Homology model of human BUD23 in complex with TRMT112. A computer generated model of the structure of human BUD23 was built using the yeast crystalline structure as a template. Dark blue represents high confidence residues (identical to yeast structure), light blue represents medium confidence residues (not identical, but estimated to form a similar shape to the yeast model), and red represents low confidence residues (*de novo* modelling). SAM is indicated in green. Shown here is: (A) human BUD23 (left) in complex with TRMT112 (right) to show the interaction surface, and (B) the SAM binding site of human BUD23.

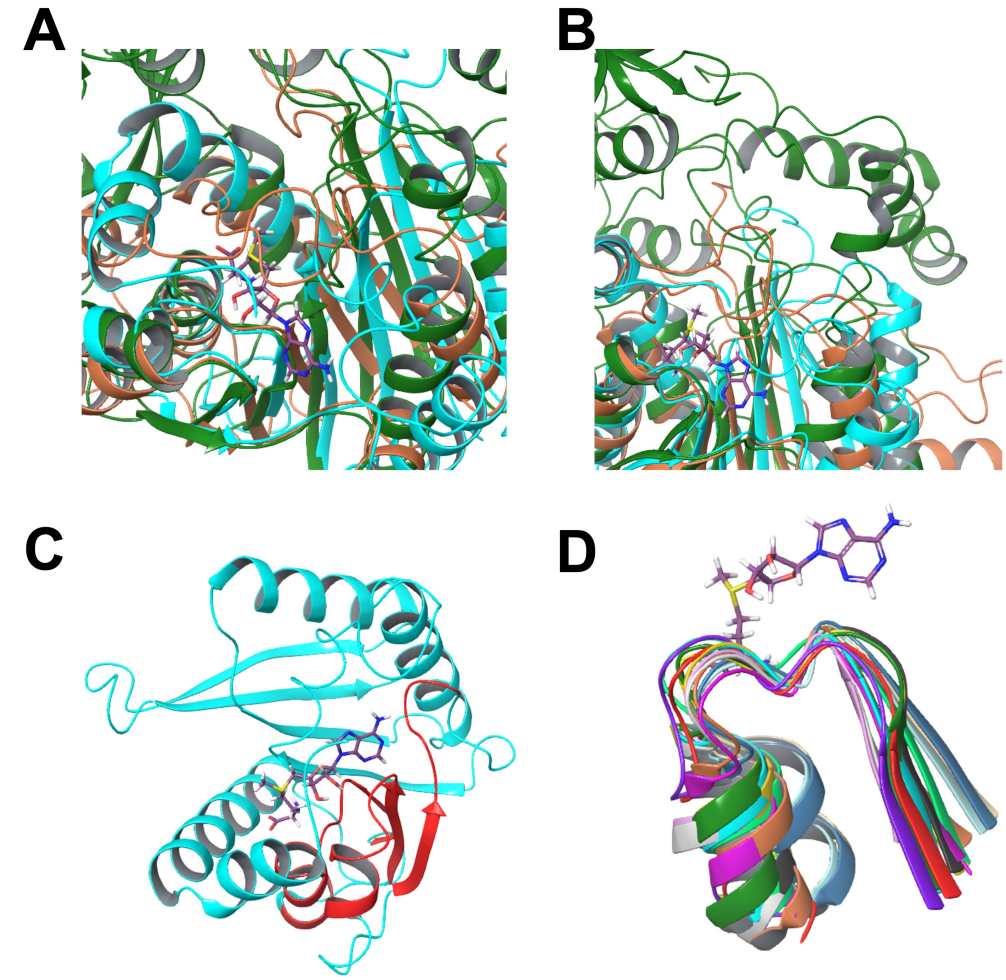

E

```
Conservation:                                                                                57 7 7 9
sp_O43709_BUD23_HUMAN_Pro    35  ----------------------IQTRMAG------RALELLYLPEN---KPCYLLDIGCGTGLSGSYLSD   73
3qow_chainA_p001            139  --------------------SFDL-----------VAQMIDEIKMT---DDDLFVDLGSGVGQVVLQVAA  174
5e2a_chainA_p002             36  ----GMLGGYGHISSIDINSSRKFL----------QRRFLREGPNKT-GTSSCALDCGAGIGRITKRLLL   90
5ubb_chainA_p003             27  ----GMMGNFIELSSPDIQASQKFL----------RKFVVGGPGRA---GTDCALDCGSGIGRVSKHVLL   79
5wcj_chainA_p004              7  ----AMI----------------AGLALL-----------RNPELLLEIPLALLLVVGLGGGSLPLFVHD   45
3ua3_chainA_p005            302  GVYNTFEQ--------DQIKYDVYGEAVV------GALKDLGADGR---KTVVIYLLGGGRGPIGTKILK  354
5wcf_chainA_p006             11  ----MMIA--------DRVRRTDAYR---------RLGILRNWAAL---RGKTVLDVGAGTGILSIFCAQ   56
2fyt_chainA_p007             12  ----EMLK--------DKIRTESYR-----------DFIYQNPHIF---KDKVVLDVGCGTGILSMFAAK   55
5dst_chainA_p008             10  ----EMLK--------DEVRTLTYR-----------NSMYHNKHVF---KDKVVLDVGSGTGILSMFAAK   53
4a6d_chainA_p009            146  ----AIYR--------SEGERLQFMQALQEVWSVNGRSVLTAFDLS---VFPLMCDLGGGAGALAKECMS  200
4fp9_chainA_p010            109  ----------------------YYLMDAA------SLLPVLALGLQ---PGDIVLDLCAAPGGKTLALLQ  147
5wws_chainA_p011            215  ----------------------LFLQNLP------SALVSHVLNPQ---PGEKILDLCAAPGGKTTHIAA  253
Consensus_aa:                        .....................h.............h.........s.hhlDlGtG.G..s..hh.
Consensus_ss:                           hh          hhhhhhhh  hh      hhhhhhhh         eeeee     hhhhhhhh
```

Figure 5.2: Alignment of Rossmann-fold methyltransferase family member structures. 3D structures of known Rossmann-fold methyltransferase members were overlaid, using the location of SAM to assist in correct alignment. (A) SAM binding site and (B) C-terminus of BUD23 (blue), DOT1L (green) and NSUN6 (brown). (C) BUD23 model showing conserved super-family SAM binding loops (red). (D) Overlay of key SAM binding loop from all known Rossmann-fold methyltransferase family 3D structures. (E) Multiple sequence alignment of Rossmann-fold methyltransferase proteins, showing a lack of amino acid consensus sequences (aa), but conserved secondary structures (ss). h = helix; e = beta sheet.

all three members, using the SAM molecule as an alignment tool revealed that the general structure appeared to be conserved across the family (Fig. 5.2A). However, the structure of the C-terminus of the proteins showed no homology between members (Fig. 5.2B), even between DOT1L and BUD23 - two supposedly closely related members of the family. This is the face of the protein responsible for conferring substrate recognition. Current literature describes that the Rossmann-fold methyltransferase family has very high substrate diversity compared to other methyltransferase families (Martin & McMillan, 2002), indicating that other related proteins are not suitable for homology modelling within this family.

Overlay of the protein structures did reveal some clear conserved loops that were common to the entire family. In particular, we identified three motifs that permitted SAM binding (Fig. 5.2C-D) that were highly structurally conserved. These loops all formed hydrogen bonds directly with the SAM molecule, and are therefore critical for the correct function of Rossmann-fold methyltransferases. Interestingly, alignment of the sequences revealed no common amino acid motifs or consensus sequences, although secondary structures were conserved (Fig. 5.2E), indicating that the family diverges heavily at the sequence level despite structural conservation.

5.3.3 Modelling of the SAM binding site revealed important amino acid residues

Analysis of the modelled human BUD23 SAM binding site revealed several key residues that facilitated ligand interactions (Fig. 5.3). D82 forms two hydrogen bonds with hydroxyl groups on the SAM ligand via side-chain interactions, forming part of one of the conserved family motif loops along with L81-M87. SAM also forms three hydrogen bonds via its amine group with S67, G61 and I122, in addition to others. These interactions serve to orientate SAM, facilitating access to the methyl group by the target substrate, 18S rRNA.

Surface modelling of human BUD23 highlights this functionality (Fig. 5.4), as a clear pocket can be seen on the C-terminus side of the protein where the methyl group

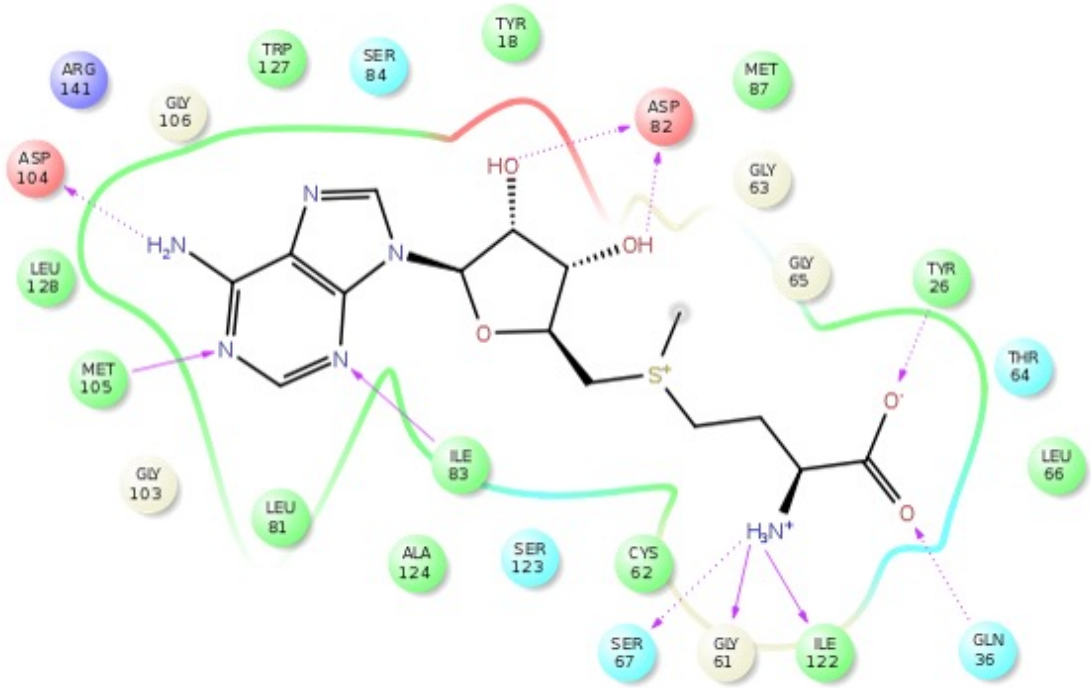

Figure 5.3: Predicted human BUD23 ligand interaction map. Amino acid residues that form the SAM binding pocket of human BUD23 are displayed, including all predicted hydrogen bonds between BUD23 and the SAM ligand. Red = negatively charged residue; dark blue = positively charged residue; white = glycine; green = hydrophobic residue; light blue = polar residue. Dashed lines represent side-chain hydrogen bonds, while solid lines represent backbone hydrogen bonds.

is accessible, giving insight to the mechanism by which BUD23 is capable of acting as a methyltransferase. In particular, we identify that residues Y26, which binds directly to SAM, and Y164, which enables the correct active site shape for SAM to bind, but does not directly form the binding pocket, would be good targets to disrupt methylation activity without changing the overall conformation of BUD23 structure.

5.3.4 Generation of constitutive knockdown cell lines

Preliminary siRNA knockdown work suggested that there was a metabolic phenotype in A549 cells upon loss of BUD23. To determine whether this was as a result of the loss of methylation activity of BUD23, or whether it was due to ribosomal subunit imbalance, we proposed that the generation of A549 cells expressing methylation incompetent BUD23 would be a suitable system to delineate the two functions. Unfortunately, A549 cells are hypotriploid, and so contain too many gene copies

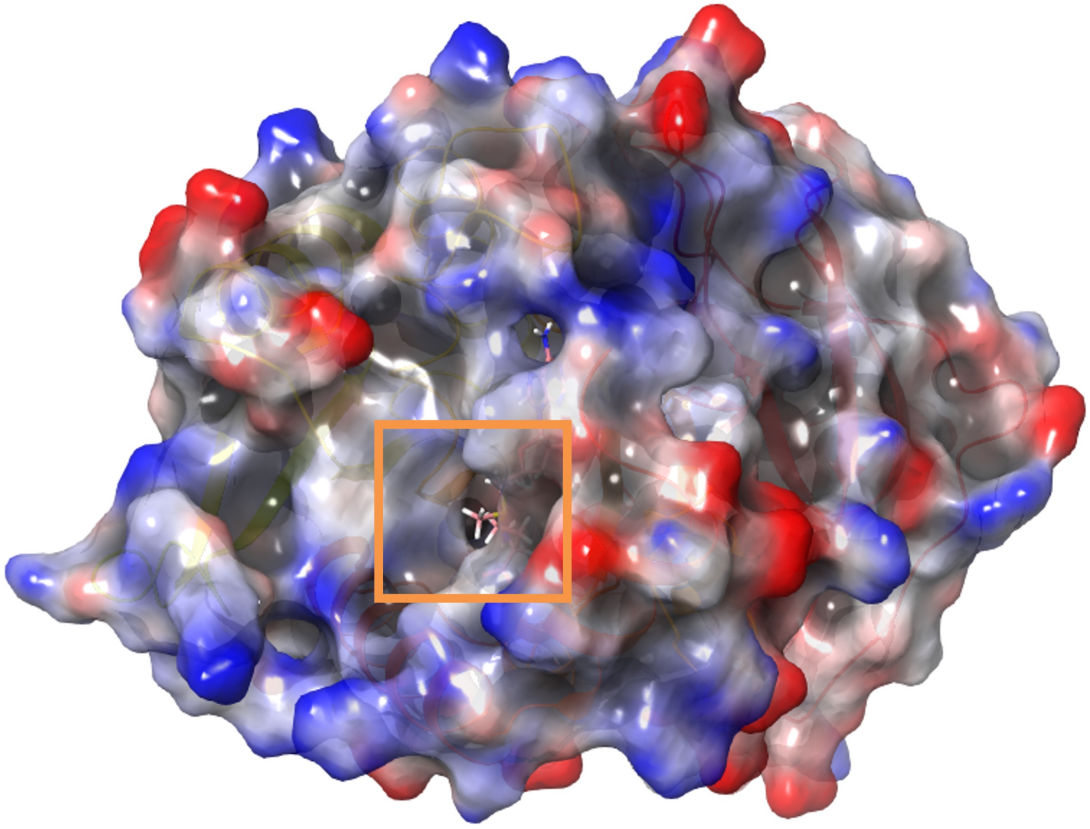

Figure 5.4: Surface modelling of human BUD23 in complex with TRMT112. The exposed methyl group of SAM can be seen extending from the surface of BUD23. Positively charged surface areas are indicated in blue. Negatively charged areas are indicated in red.

for targeted base substitution. Instead, we used CRISPR-Cas9 ribonucleoprotein complexes to generate constitutive BUD23 knockdown cell lines, with the aim of transfecting knockout cells with rescue plasmids expressing either wild-type BUD23, or methylation incompetent Y26A or Y164A BUD23. Three different gRNAs were created to drive knockdown of BUD23: g909, g015 and g916 (Fig. 5.5) and transfected into A549 cells using lipofection. A gRNA targeting AAV was used as a non-targeting control.

The area around the gRNA target sequence was then amplified and Sanger Sequenced for subsequent TIDE analysis to determine the cutting efficiency of the gRNAs (Fig. 5.5). Unfortunately, g015 failed to sequence, but g909 showed a 34.3% cutting efficiency, while g916 showed a 55.3% cutting efficiency. Both

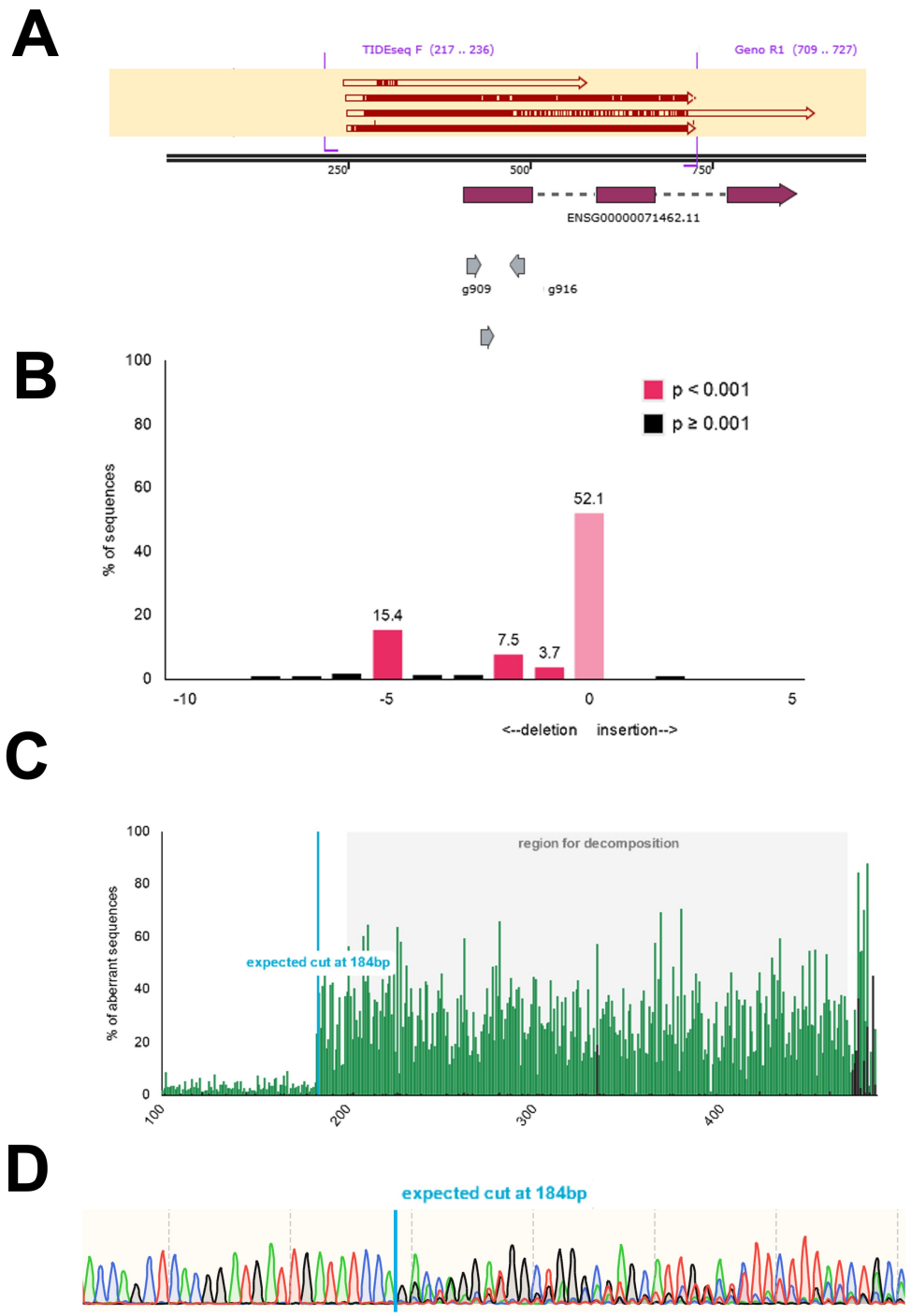

Figure 5.5: TIDE analysis of BUD23 gRNAs. Three separate guide RNAs were generated to guide CRISPR-Cas9 mediated BUD23 knockdown. (A) Map of BUD23 gRNA cutting locations and sequencing primers. (B) Insert-deletion analysis of g906. (C) Aberrant sequence presence after expected cut site of g906. (D) Sanger sequence trace showing aberrant trace after the expected cut site of g906.

of these were deemed suitable efficiencies to generate monoclonal populations for knockdown screening.

While we were able to produce single cell colonies that showed strong knockdown of BUD23 as determined by western blotting, unfortunately, we were unable to generate methylation incompetent BUD23 rescue plasmids during the duration of this project, and so this remains an ongoing experiment for future research.

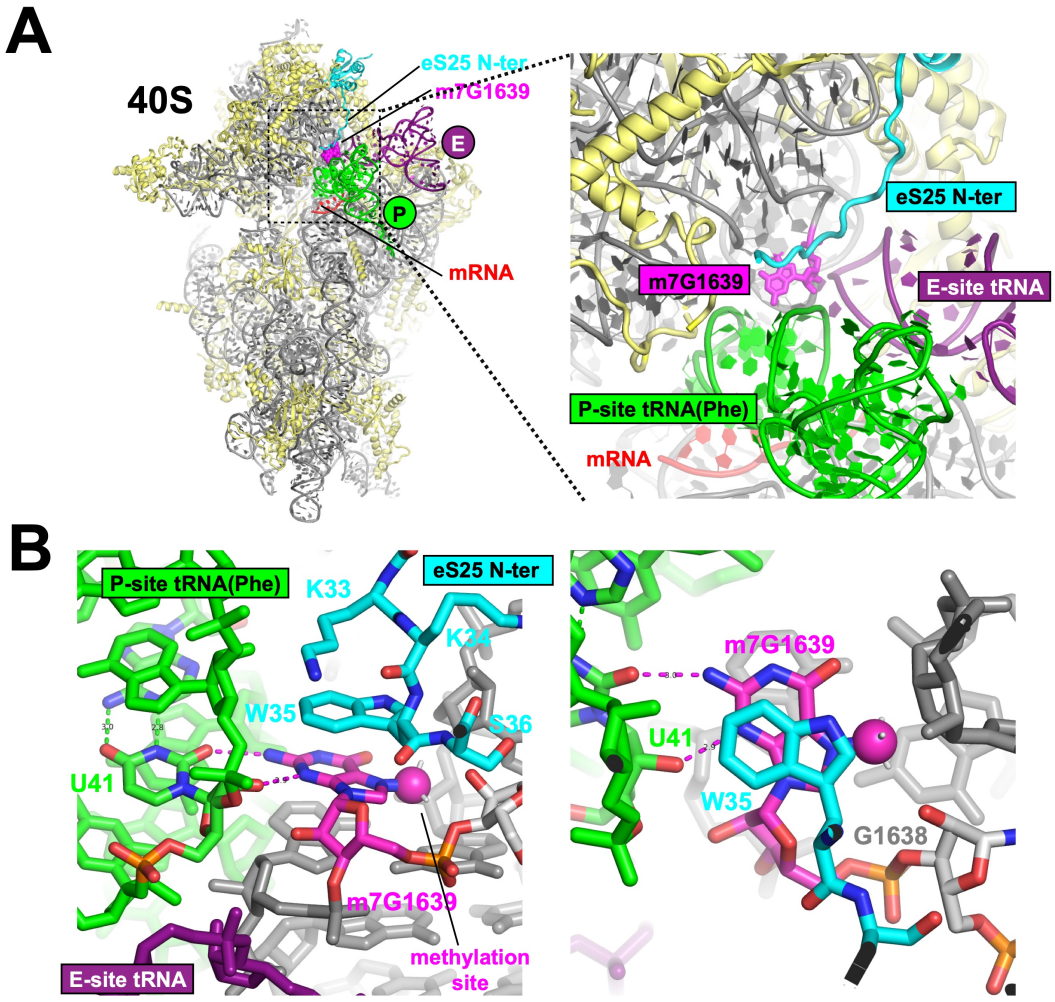

Figure 5.6: Ribosomal structure showing the functional impact of the m7G1639 methyl mark. Reconstruction of the ribosome showing (A) the location of the m7G1639 methyl mark on the small ribosomal subunit, and (B) two hydrogen bonds formed between U41 of the P-site tRNA and the m7G1639 methyl mark. Pink = m7G1639; green = P-site tRNA (phenylalanine); purple = E-site tRNA; red = mRNA; light blue = 40S ribosomal protein S25 (eS25).

5.3.5 Deposition of the m7G mark points G1639 towards the P-site tRNA

To assess the functional impact that methylation of m7G1639 would have on the mature ribosome, we looked at what effect presence and absence of the methyl mark had on tRNA binding by the ribosome (Fig. 5.6). The m7G methyl mark is located at the anticodon stem of the P-site tRNA, lying between A1640 of the 18S rRNA and W35 of the 40S ribosomal protein S25.

Analysis of the surrounding structure revealed that m7G1639 can form multiple hydrogen bonds with the P-site tRNA. For example, m7G1639 can form two hydrogen bonds with the oxygen groups in U41 of the phenylalanine tRNA (Fig. 5.6B). However, different tRNAs can have different amino acid residues in this position. If instead there was a carbon in these positions, the hydrogen bonding pattern would overall be the same, but if the amino acid was a purine then a nitrogen atom would instead fill this space, which would create weaker hydrogen bonding at this site.

In addition, the physical location of the methylation event works to hold G1639 in a more suitable conformation to stabilise the P-site tRNA on the other side by filling nearby empty space. Loss of the methyl mark would lead to a higher amount of flexibility for the G1639 position, and could potentially have an impact on translational kinetics. However, unmodified G1639 should hypothetically still be capable of adopting the same conformation as if it were methylated, as the m7G modification appears to serve mostly to aid in orientating the base towards the P-site tRNA, indicating that it is more mobile than methylated G1639. We predict that loss of the methyl mark should not grossly alter the conformation of the ribosome, but may therefore play a role in P-site tRNA processing, pointing to a potential functional role for the methylation event.

5.4 Discussion

While the human BUD23 ortholog was first identified in 2001 for its role in the pathology of Williams-Beuren syndrome (Doll & Grzeschik), the primary bulk of research concerning its function has been carried out in yeast. This means that little is known about how similar human BUD23 is in comparison, and whether it is responsible for carrying out the same identified functions. The crystalline structure of yeast Bud23 has been solved by Létoquart et al. (2014) and has provided information on how the protein catalyses its methylation reaction. We aimed to identify if human BUD23 worked in the same way, and to assess if we could infer conclusions about human BUD23 function from the previous yeast work. We therefore developed an *in silico* model of human BUD23, using the solved crystal structure of its yeast ortholog as a template to enable prediction of protein folding. Interestingly, while the amino acid sequence of human BUD23 only matched yeast Bud23 by 46.9%, structurally the two were very similar. Most of the model was predicted accurately using the shape of yeast Bud23, with only small loop sequences external to the primary bulk of the protein having to be modelled *de novo*. *De novo* modelling is notoriously poor, and is rarely able to accurately predict the tertiary shape of a protein from its coding sequence, so having roughly 95% of the model based on the previous template indicates a high degree of confidence. *In vivo* studies have identified that one of BUD23's functions is the deposition of the m7G methyl mark on a key residue of the small ribosomal subunit (White et al., 2008), and this modification is present and conserved throughout all eukaryotes. Therefore, it would be predicted that the structure of BUD23 would remain under similar conservative pressure to ensure it is still capable of carrying out this function, explaining why our model is so similar.

High sequence divergence is a common motif throughout the Rossmann-fold methyltransferase family, which BUD23 belongs to (Martin & McMillan, 2002). While the core structure around the SAM binding site is highly conserved across all species of the family, they diverge heavily at the sequence level. Comparison of our

model to other solved Rossmann-fold methyltransferase crystal structures revealed the presence of several core structural loops that facilitated SAM binding, but no consensus sequences when comparing sequence alignments. Study of the amino acid residues reveals that binding with SAM is carried out by the backbone of the amino acid, and thus while the amino acid needs to be positioned in the same orientation, the chemical structure of the molecule does not need to be conserved for functional preservation, consistent with current literature. A study by Richon et al. (2011) attempted to group Rossmann-fold methyltransferases into a chemogenetic tree through analysis of the structure of their catalytically active domains. The closest neighbour of BUD23 that had a confirmed crystallised structure was DOT1L, a known histone methyltransferase. We compared the structure of yeast BUD23, our model of human BUD23, and the published structure of DOT1L to identify if the nearest neighbour protein would be a better candidate for homology modeling than the yeast ortholog. However, we identified that even when looking at the closest related neighbour, the C-terminus of the proteins, which typically conveys substrate specificity, showed no homology between the two different proteins, and so was unsuitable for modeling of human BUD23. The Rossmann-fold methyltransferase family is strikingly different from other methyltransferase families in that it has a high variation in substrate specificities, even between the closest related proteins, though why it has evolved this way is currently unknown.

A novel computational method for determining protein structure from sequence, AlphaFold, has recently generated its own model for human BUD23 structure (Jumper et al., 2021). It does not use homology modeling, but instead uses a trained neural network based off multiple sequence alignments and an iterative residue pair algorithm to build highly accurate models of protein structure. Interestingly, their predicted structure closely resembles that of our homology modelling approach, further supporting that we can generate statements about the function of human BUD23 based on the findings observed in yeast.

In *S. cerevisiae*, Bud23 has been described to have two independent functions: as a methyltransferase and for small ribosomal subunit biogenesis (Zorbas et al., 2015). While the disruption to ribosomal biogenesis upon loss of BUD23 was identified to cause a slow growth phenotype in yeast (Létoquart et al., 2014), the function of the methyl mark is still heavily debated. Some studies have hypothesised that the G1575 methylation event is non-essential, or that it is part of a redundant modification network so the loss of any one individual modification does not have any overall effect on the ribosome (Haag et al., 2015). It has also been postulated that the methyl group could be imparted as a quality control marker, to indicate that the 18SE strand had successfully undergone maturation into 18S. However, preliminary work from our group has hinted that, at least in a human cell system, BUD23 may serve another function in the control of metabolic mRNA translation. Which of BUD23's primary functions results in this metabolic control phenotype is currently unknown, but developing a method to delineate the two functions would be a useful tool to identify the mechanism underlying human BUD23 function.

By assessing the SAM binding site in the *in silico* human BUD23 model, we were able to identify two key residues (Y26 and Y164) that we predicted were required for catalytic activity. Targeted mutagenesis of these key amino acids would hypothetically permit disruption of methyl function, but not of overall protein structure, thereby rendering a methylation incompetent form of human BUD23 that should still be able to permit correct ribosomal biogenesis. Analysis of the ribosomal structure with and without the methylation mark reveals that the m7G mark deposited by BUD23 may play a role in stabilising the potential conformations of the G1639 residue, and therefore could have a functional effect by conferring a translational advantage to certain transcripts that are enriched in tRNAs that better fit within that structure. It is therefore possible that methylation activity is linked to the metabolic effect of BUD23 loss identified in human cells, especially as other models of ribosomal subunit imbalance have not described a specific metabolic phenotype (Cheng et al., 2019).

Therefore, we suggest that using CRISPR to remove endogenous expression of BUD23 in human cell lines, and then rescuing the defect with plasmids expressing two different methylation incompetent forms of BUD23, Y26A and Y164A, would constitute a good model to delineate the two primary functions of BUD23 in a human model. Unfortunately, while we managed to develop multiple constitutive BUD23 knockout cell lines, we were unable to generate the rescue plasmids during the duration of this project. Future work should focus on generating rescue plasmids, transfecting them into the knockout lines, and then performing subsequent characterisation to determine what phenotypic differences occur as a result of loss of methylation activity. Using the Seahorse^{TM} system to assess for mitochondrial activity impairments would be of particular interest, as it could reveal defects in carbon metabolism pathways. In addition, using tools such as ribosomal profiling or polysome profiling would enable the assessment of translational efficiency of transcripts (Ingolia et al., 2009), permitting a direct readout of how well the ribosome can translate specific mRNA species with and without the methyl mark.

5.5 Acknowledgements

Martin Watson, for his assistance with generating the homology model. Marc Leibundgut, Ban Nenad, and David Gatfield for their work on the ribosome modelling.

6
General Discussion

The primary aim of this project was to investigate the functional role of BUD23, a putative ribosomal methyltransferase.

The human ribosome is extensively modified, containing at least 288 distinct modification sites (Taoka et al., 2018). This constitutes one of the most modified classes of RNA species, second only to tRNAs (Jackman & Alfonzo, 2013). Current literature suggests that most rRNA modifications serve to stabilise the tertiary structure of the ribosome (Polikanov et al., 2015), however this fails to explain why rRNA modifications tend to cluster in functionally important regions, in particular around the tRNA binding sites and the decoding site. Their spatial organisation and high level of conservation throughout all eukaryotes strongly suggest that rRNA modifications are instead responsible for the regulation of ribosomal function.

Recent studies have identified that the ribosomal modification landscape is not constitutively present, but that some modifications instead show heterogenous expression (Andersen et al., 2004; Birkedal et al., 2014; Taoka et al., 2016). While the role of rRNA modifications is generally poorly understood, modification heterogeneity in proteins and other nucleic acid species provides cells with the ability to rapidly respond to changes in their environment in a dynamic fashion (Morgan et al., 2005). Modifications have been described to be essential for a variety of

functions, including cell differentiation, chromatin remodelling, and kinase activation (Li, 2002; Ringrose & Paro, 2004; Reik, 2007). It is therefore plausible that rRNA modifications enable the ribosome to dynamically alter its translational profile, potentially via alteration of the translational efficiency of subsets of transcripts. This would permit the translation of specific groups of proteins in response to factors such as subcellular location, stress, or time of day, without the need for alterations in mRNA expression levels.

BUD23 is a putative methyltransferase that is responsible for the m7G methylation of G1575 on the yeast small ribosomal subunit (White et al., 2008). It also has a second independent function in small ribosomal subunit biogenesis, where its presence is essential for progression from the 18SE to 18S phase (Haag et al., 2015). While BUD23's role in small ribosomal subunit maturation has been well characterised, studies have failed to determine any functional consequences of its methylation activity. This has led to the idea that the methylation event may be non-essential, or is imparted simply as a quality control marker to indicate that 18S maturation has occurred (Létoquart et al., 2014). However, both functions have been found to be conserved within humans as well (Zorbas et al., 2015), where BUD23 instead imparts a methyl mark on G1639, and the high degree of preservation of BUD23's catalytic site indicates functional importance.

Preliminary work within our group highlighted a previously unidentified consequence resulting from BUD23 knockdown (Baxter et al., 2020). Polysome profiling of BUD23 siRNA treated cells revealed a selective decrease in the the translational efficiency of metabolic, catabolic, and mitochondrial mRNAs. Selective alterations to metabolism have not been described as a general consequence of ribosomal biogenesis disruption (Cheng et al., 2019), and therefore suggested that the G1639 methyl mark may be functionally implicated in assisting with metabolic transcript translation.

We therefore wanted to investigate the role of BUD23 in an *in vivo* system with the aim of interrogating for any metabolic defects caused by loss of BUD23. However, BUD23 is essential to life and therefore global deletion resulted in

embryonic lethality (Baxter et al., 2020), and was not a suitable model for our purposes. Instead, we opted to investigate BUD23 in two metabolically rich tissues: cardiac muscle and adipose.

The selective knockdown of BUD23 in cardiomyocytes led to an early death phenotype, as animals went into the late stages of cardiac failure at approximately 30 days of age, further highlighting the essential function of BUD23 *in vivo*. Consistent with previous studies from yeast, loss of BUD23 resulted in a disruption to ribosomal biogenesis, as evidenced by an imbalanced small:large ribosomal subunit ratio indicating a failure to produce sufficient mature 18S. This led to a general global translational defect, with proteomic analysis revealing an increased drive for ribosomal and proteasomal protein production in conjunction with a decreased total cellular protein level. However, we also identified a secondary defect whereby loss of BUD23 resulted in a selective loss of mitochondrial number and function in cardiac muscle. Mitochondria makes up approximately 30% of the total mass within the heart, as the heart is consistently under a strong metabolic burden and requires large amounts of ATP for normal function. Loss of BUD23 resulted in a reduction of roughly 1/6th of this total mitochondrial mass, in addition to further functional failure in the remaining mitochondria. Ultimately, this mitochondrial dysfunction combined with an increased metabolic burden resulting from faulty translation, led to animals being unable to meet energetic demands and resulting in systolic cardiac failure, finally culminating in death.

However, knockdown of BUD23 in adipose tissue caused a much more subtle phenotype. While a global translational defect was still observed, similar to that resulting from knockdown in the cardiac system, the nature of the mitochondrial phenotype was strikingly different between the two. Brown adipose tissue showed a loss of mitochondrial density, but not function, upon removal of BUD23. This potentially indicates that the severity of the mitochondrial phenotype in the cardiac knockout animal was a consequence of subsequent cardiac failure, and not driven directly by the absence of BUD23. Further profiling of brown adipose tissue revealed

that loss of BUD23 led to a canonical 'whitened' phenotype, which is typical of dysfunctional brown adipose. In particular, brown adipocytes showed increased lipid droplet size, impaired β_3 adrenergic signalling, and increased inflammation. Interestingly, one of the best characterised changes that results from brown adipose dysfunction is a complete loss of thermogenic potential (Grimpo et al., 2014; Shimizu et al., 2014; Kotzbeck et al., 2018). However, BUD23 knockout brown adipose, despite showing clear signs of whitening, is still capable of thermogenesis, and animals are able to defend their temperature in response to a cold challenge. While this may be in part due to compensatory mechanisms in other organs, thermal imaging revealed a clear heat signature in the scapular region corresponding to thermal production by brown adipose. This is a striking difference from the traditional whitening model, and we have proposed that the effects of DIO2 or G-protein coupled receptors may offer an explanation for why BUD23 knockout adipose is able to escape from a canonical whitening phenotype.

Further molecular characterisation of the effects of BUD23 knockout in brown adipose revealed a metabolic rewiring, with adipocytes shifting away from utilising traditional β-oxidation substrates. In addition to a failure to use triglycerides, branched chain amino acid catabolism was also impaired, which serves as a secondary fuel source for thermogenesis (Yoneshiro et al., 2019). These alterations led to global metabolic profile alterations throughout the animal, resulting in metabolic inflexibility similar to that observed in patients with type 2 diabetes (van de Weijer et al., 2013). We propose that BUD23 is acting as a regulator of systemic metabolism, and that it is capable of directing metabolic flux by reprogramming the ribosome and altering the translational efficiency of metabolic transcripts.

However, this still leaves the big question of how BUD23 is regulating ribosomal function in the context of metabolic changes. In order to attempt to delineate the two fundamental roles underlying BUD23 function, that is its methyltransferase activity and its control of ribosomal maturation, we performed siRNA mediated knock-down of other ribosomal biogenesis proteins and examined for obvious metabolic

phenotypes mimicking that of BUD23 knockdown to determine if this was simply a previously undetermined consequence of 18S:28S imbalance. Interestingly, no evidence was found that this was a common feature of small ribosomal subunit disruption, suggesting that the specific metabolic defects observed upon loss of BUD23 may be tied to its ribosomal modification capabilities.

To further interrogate if this was the case, an *in silico* model of human BUD23 was generated, using the solved yeast Bud23 3D structure as a template (Létoquart et al., 2014). This enabled the identification of key amino acid residues responsible for conferring methyltransferase function to human BUD23, and we proposed that by targeting these residues we could generate methylation incompetent BUD23 that would still be capable of correctly assisting in 18S maturation. This would permit the full delineation of its two functions, providing unequivocal proof of whether the m7G methylation event is responsible for the metabolic phenotype that has been observed. Unfortunately, this was not able to be completed during the scope of this project, but remains a fruitful avenue to pursue for future work.

Through investigation of the position of the m7G1639 modification, we were able to gain insight into a potential mechanism by which this rRNA modification may attenuate translation. Methylation of G1639 not only holds the ribosome in a more suitable conformation to stabilise its interaction with the P-site tRNA, but also has the potential to alter translational kinetics via differential hydrogen bonding with differing tRNA species. It would be interesting to study how this relates to metabolic transcripts, and whether they show any enrichment for certain amino acids.

One remaining major question underlying the observed BUD23 knockout phenotypes is which subset of transcripts initially loses their translational efficiency upon loss of BUD23, thereby driving the changes we observe and triggering downstream signalling cascades as tissues strive to rescue resulting defects. We propose that using a technique such as ribosome profiling may provide an answer. Ribosome profiling is a fairly new technology (Ingolia et al., 2009), in which ribosome protected mRNA fragments are sequenced to permit a direct readout of which

transcripts are being actively translated by ribosomal equipment within cells, and also facilitates identification of any ribosomal stalling on specific regions of transcripts. While a challenging approach, recent publications have indicated that ribosomal profiling can be performed in animal tissues (Arpat et al., 2020), and could therefore constitute a powerful tool to directly analyse the effect of loss of BUD23 specifically on the ribosome.

Finally, given that our hypothesis is that deposition of the m7G mark by BUD23 permits cells to respond to local stimuli in a rapid fashion, it would be interesting to see if the methyl mark is heterogeneously expressed in different conditions. For example, its presence could be evaluated across different tissue types, at different times of day, or in response to a high metabolic demand, such as during fasting. This would further provide evidence to support whether or not the m7G modification imparted by BUD23 is responsible for alteration of ribosomal function.

Overall, this thesis implicates that BUD23 is responsible for the regulation of tissue and organismal energy balance. We propose that this occurs as a result of ribosomal modification, and that presence of the m7G methyl mark alters ribosomal binding kinetics to facilitate the preferential translation of metabolic mRNAs. This constitutes a novel finding in the area of ribosomal function, as the effects of most rRNA modifications are generally poorly understood, and previous studies have failed to identify a functional effect resulting from loss of modifications.

Appendices

A
Appendix 1

Genotyping information can be found here.

ADCR (AdipoCre x Bud23 Flox) Genotyping

Primer sequences:
AdipoCre F: 5`-GGA TGT GCC ATG TGA GTC TG-3`
AdipoCre R: 5`-ACG GAC AGA AGC ATT TTC CA-3`
AdipoCre Int F: 5`-CTA GGC CAC AGA ATT GAA AGA TCT-3`
AdipoCre Int R: 5`-GTA GGT GGA AAT TCT AGC ATC ATC C-3`

Adiponectin Cre PCR

Primers: AdipoCre F, AdipoCre R, AdipoCre Int F, AdipoCre Int R

PCR Protocol:

94°C	2 min	
94°C	20 secs	10 cycles, -0.5°C per cycle**
65°C	15 secs	
68°C	10 secs	
94°C	15 secs	28 cycles
60°C	15 secs	
72°C	10 secs	
72°C	2 mins	
4°C	∞	

Run on 2% agarose gel.
Cre +ve mice give 2 bands; Cre –ve mice give 1 band

**touchdown PCR

MCAA (MCKCre x Bud23 Flox) Genotyping

Primer sequences:
MCK Cre F: 5'-GTG AAA CAG CAT TGC TGT CAC TT-3'
MCK Cre R: 5'-TAA GTC TGA ACC CGG TCT GC-3'
MCK Cre Int F: 5'-CAA ATG TTG CTT GTC TGG TG-3'
MCK Cre Int R: 5'-GTC AGT CGA GTG CAC AGT TT-3'
Bud23 DR01 geno2F: 5'- CCT GGC TGA TGT GTT GCT TT-3'
Bud23 DR01 LOA R: 5'-GCT CCC ATC CTA CCA GTT CA-3'

You'll need to set up 2x PCRs:

(1) **MCK Cre**
Primers: MCK Cre F, MCK Cre R, MCK Cre Int F, MCK Cre Int R

94°C	3 min	
94°C	30 secs	┐
60°C	30 secs	├ 35 cycles
72°C	30 secs	┘
72°C	2 mins	
4°C	∞	

Run on 1.5% agarose gel.
Cre +ve mice give 2 bands; Cre –ve mice give 1 band

Sizes: MCK Cre band at 450bp –either present or not; Internal positive control at 200bp – should always be present

(2) **Bud23 Flox**
Primers: Bud23 DR01 geno2F, Bud23 DR01 LOA R

94°C	3 min	
94°C	30 secs	┐
62°C	30 secs	├ 35 cycles
72°C	30 secs	┘
72°C	5 mins	
4°C	∞	

Run on 3% agarose gel.
Heterozygotes have two bands (334bp & 374bp), homozygous animals give one band (374bp only)

B
Appendix 2

eLIFE elifesciences.org

RESEARCH ARTICLE

Cardiac mitochondrial function depends on BUD23 mediated ribosome programming

Matthew Baxter[1,2,3]*, Maria Voronkov[1,2,3], Toryn Poolman[1,2,3], Gina Galli[1], Christian Pinali[4], Laurence Goosey[1], Abigail Knight[1], Karolina Krakowiak[1], Robert Maidstone[1,2,3], Mudassar Iqbal[4], Min Zi[4], Sukhpal Prehar[4], Elizabeth J Cartwright[4], Julie Gibbs[1], Laura C Matthews[5], Antony D Adamson[1], Neil E Humphreys[1], Pedro Rebelo-Guiomar[6,7], Michal Minczuk[7], David A Bechtold[1], Andrew Loudon[1], David Ray[1,2,3]*

[1]Faculty of Biology, Medicine and Health, University of Manchester, Manchester Academic Health Science Centre, Manchester, United Kingdom; [2]Oxford Centre for Diabetes, Endocrinology and Metabolism, University of Oxford, Oxford, United Kingdom; [3]NIHR Oxford Biomedical Research Centre, John Radcliffe Hospital, Oxford, United Kingdom; [4]Division of Cardiovascular Sciences, University of Manchester, Manchester Academic Health Science Centre, Manchester, United Kingdom; [5]Leeds Institute of Medical Research, Faculty of Medicine and Health, University of Leeds, Leeds, United Kingdom; [6]Graduate Program in Areas of Basic and Applied Biology (GABBA), University of Porto, Porto, Portugal; [7]Medical Research Council Mitochondrial Biology Unit, University of Cambridge, Cambridge, United Kingdom

***For correspondence:** matthew.baxter@ocdem.ox.ac.uk (MB); david.ray@ocdem.ox.ac.uk (DR)

Competing interests: The authors declare that no competing interests exist.

Funding: See page 22

Received: 30 July 2019
Accepted: 24 December 2019
Published: 15 January 2020

Reviewing editor: Ulrike Topf, Institute of Biochemistry and Biophysics Polish Academy of Sciences, Poland

Abstract Efficient mitochondrial function is required in tissues with high energy demand such as the heart, and mitochondrial dysfunction is associated with cardiovascular disease. Expression of mitochondrial proteins is tightly regulated in response to internal and external stimuli. Here we identify a novel mechanism regulating mitochondrial content and function, through BUD23-dependent ribosome generation. BUD23 was required for ribosome maturation, normal 18S/28S stoichiometry and modulated the translation of mitochondrial transcripts in human A549 cells. Deletion of *Bud23* in murine cardiomyocytes reduced mitochondrial content and function, leading to severe cardiomyopathy and death. We discovered that BUD23 selectively promotes ribosomal interaction with low GC-content 5'UTRs. Taken together we identify a critical role for BUD23 in bioenergetics gene expression, by promoting efficient translation of mRNA transcripts with low 5'UTR GC content. BUD23 emerges as essential to mouse development, and to postnatal cardiac function.

Introduction

Regulation of protein abundance within a cell is of fundamental importance to homeostasis, cell identity and responsiveness to changes in external environment. Many layers of regulatory control have evolved to fine-tune gene expression to meet cellular needs, including transcriptional regulation, cis-acting genomic elements, epigenetic structures, and translational efficiency. Selective control of mRNA translation at the level of the ribosome is emerging as important for protein dynamics within the cell; however, the regulatory mechanisms remain unclear (***Sonenberg and Hinnebusch,***

eLife digest Cells need to make proteins to survive, so they have protein-making machines called ribosomes. Ribosomes are themselves made out of proteins and RNA (a molecule similar to DNA), and they are assembled by other proteins that bring ribosomal components together and modify them until the ribosomes are functional.

Mitochondria are compartments in the cell that are in charge of providing it with energy. To do this they require several proteins produced by the ribosomes. If not enough mitochondrial proteins are made, mitochondria cannot provide enough energy for the cell to survive.

One of the proteins involved in modifying ribosomes so they are functional is called BUD23. People with certain diseases, such as Williams-Beuren syndrome, do not make enough BUD23; but it was unknown what specific effects resulted from a loss of BUD23.

To answer this question, Baxter et al. first genetically removed BUD23 from human cells, and then checked what happened to protein production. They found that ribosomes in human cells with no BUD23 were different than in normal cells, and that cells without BUD23 produced different proteins, which did not always perform their roles correctly. Proteins in the mitochondria are one of the main groups affected by the absence of BUD23. To determine what effects these modified mitochondrial proteins would have in an animal, Baxter et al. genetically modified mice so that they no longer produced BUD23. These mice developed heart problems caused by their mitochondria not working correctly and being unable to provide the energy the heart cells needed, eventually leading to heart failure. Heart problems are common in people with Williams-Beuren syndrome.

Many diseases arise when a person's mitochondria do not work properly, but it is often unclear why. These experiments suggest that low levels of BUD23 or faulty ribosomes may be causing mitochondria to work poorly in some of these diseases, which could lead to the development of new therapies.

2009). Protein synthesis is the most energetically-demanding process for a cell to perform and, therefore, mRNA translation is closely coupled to mitochondrial function (*Morita et al., 2013*).

Mitochondria are fundamental cellular components of eukaryotes, generating the majority of cellular ATP. The human mitochondrial genome contains only 37 genes, of which 13 are subunits of respiratory complexes, 22 encode mitochondrial tRNAs, and a further two encode rRNA. Whilst the mitochondrion translates the 13 protein-coding genes of its own genome using a bespoke mitochondrial apparatus, the majority of the genes required for a functional mitochondrion are encoded in the cell nuclear genome and are, therefore, dependent on the cytosolic translational apparatus. This relationship implies a fundamental role for the eukaryotic 80S ribosome in control of mitochondrial abundance and function. Indeed, mitochondrial content and function varies between tissues and cell-types, as well as within a tissue, in response to external and internal stimuli including energy demand, oxidative stress and cellular signals (*Palmer et al., 2011*). For example, red blood cells contain no mitochondria whereas in cardiomyocytes mitochondria occupy 30% of cell volume to meet the exceptionally high ATP demand (*Piquereau et al., 2013*). Mitochondrial dysfunction has been linked to a wide range of cardiac disorders, often due to the aberrant production of ROS, and attendant cell death (*Kanaan and Harper, 2017*; *Ott et al., 2007*).

BUD23 (previously known as WBSCR22) was initially identified as a putative methyltransferase implicated in tumour metastases (*Nakazawa et al., 2011*). Its expression is responsive to diverse inflammatory and cancer pathologies (*Jangani et al., 2014*), and reduction of BUD23 expression can affect cellular response to glucocorticoid and alter histone methylation (*Jangani et al., 2014*). However, BUD23 actions were diverse, and a unifying mechanism of action was elusive. More recent studies identified ribosomal RNA as the preferred substrate of BUD23 (*Haag et al., 2015*; *White et al., 2008*; *Zorbas et al., 2015*). There is little understanding of the physiological role of BUD23 in a mammalian context although it is one of the genes deleted in Williams-Beuren syndrome (WBS). WBS patients have a complex phenotype with prominent neurological and morphological features. In addition metabolic pathologies exist including diabetes and obesity (*Morris, 1993*). The contribution of individual genes within the 22-gene interval to the human phenotype has not been determined, but the neurological and metabolic features suggest a bioenergetic contribution.

BUD23 is a ribosomal RNA methyltransferase which imparts a methyl mark on a key guanosine residue (forming N7-methylguanosine) located between the E and P site of the small ribosomal subunit that has been mapped to residue G1575 of yeast 18S rRNA and G1639 of human 18S rRNA (**Haag et al., 2015**; **Õunap et al., 2013**; **White et al., 2008**; **Zorbas et al., 2015**). BUD23 protein is found in both the nucleus and the cytoplasm (**Õunap et al., 2015**), and its depletion leads to a nuclear accumulation of 18SE-pre-RNA (**Haag et al., 2015**). In both yeast and human cells the methyltransferase catalytic activity of BUD23 is not required for the processing of 18S pre-RNA, or the synthesis of 40S subunits, indicating that BUD23 has an additional role, distinct from its methyltransferase activity (**Haag et al., 2015**; **Zorbas et al., 2015**).

In human cell lines it has been suggested that some 18S rRNA lacks the m7-G1639 mark, which may indicate a selective role in ribosome function (**Haag et al., 2015**). BUD23 stability requires interaction with TRMT112 (TRM112 in yeast), an obligate binding partner, which is known to stabilise four client methyltransferase enzymes, all involved in the generation of the translational apparatus (**Bourgeois et al., 2017**; **Létoquart et al., 2014**). The binding of TRMT112 with these four methyltransferases is competitive, which results in tight regulation of BUD23 protein concentration and enzymatic function at the level of protein stability.

Here we identify a novel mechanism linking the energy-demanding process of protein translation to mitochondrial dynamics through BUD23. We examine the role of BUD23 in ribosome function and discover that BUD23 preferentially promotes the selection of mRNA species with low GC-content 5'UTRs. We also identify a role for BUD23 in mitochondrial transcript translation which impacts mitochondrial function in vitro. We go on to examine the role of BUD23 in a murine in vivo system and discover that the production of mitochondrial proteins is dependent on BUD23. Finally, we examine the role of BUD23 in the mitochondrially-rich and energetically-demanding cardiac tissue and discover a cardiomyopathy phenotype leading to premature death. These discoveries identify BUD23 as essential for mammalian mitochondrial function, with implications for human mitochondrial disease and cardiomyopathy.

Results

BUD23 plays a major role in translational homeostasis

We previously identified pleiotropic actions of BUD23 in airway epithelial cells, and attributed these to an epigenetic effect (**Jangani et al., 2014**). The discovery that BUD23 modifies ribosomal RNA rather than histone proteins prompted re-examination of the BUD23 role in physiology. To identify candidate pathways affected by BUD23 we depleted expression in human airway epithelial cells (**Figure 1A,B**). This intervention caused a small but statistically significant decrease in cell proliferation (**Figure 1C**), which is similar to the anti-proliferative effects caused by BUD23 deletion in yeast (**White et al., 2008**).

To investigate comprehensively the role of BUD23 in ribosome function we performed polysome profiling. The 48 hr knockdown of *BUD23* resulted in a reduction of the 40S subunit peak, and a concomitant increase in the 60/80S peak (**Figure 1D,E**). There was, however, little change in the profile of the polysome fractions at this early time-point following transient *BUD23* knockdown, allowing us to investigate the changes in mRNA substrate selection in the intact polysomes. To test the global efficiency of the translational apparatus in cells lacking BUD23, we used 35-S-methionine incorporation for 1 hr (**Figure 1—figure supplement 1**). This demonstrated little overall impact on global protein translation rate, confirming that the identified polysomes were essentially competent at this time-point, despite the impact on 40S maturation. In order to determine if BUD23-loss differentially impacted the translation of a specific subset of mRNAs, we profiled the translational efficiency (TE) of individual mRNA species within the polysome profiles.

To do this, the polysome fractions were divided into 'heavy' (more than three ribosomes) or 'light' (less than three ribosomes) and pooled, prior to RNA extraction and sequencing. This defined a total of 14,527 transcripts, from which the relative proportion of each individual transcript in the heavy compared to the light fraction was calculated to give a translation efficiency (TE) score. Average TE scores across the three replicates for each condition (+ /- BUD23) were then plotted against each other (**Figure 1F**). This revealed that the most efficiently translated transcripts in the control samples (more heavily loaded with ribosomes), were most significantly reduced in the *BUD23* knockdown

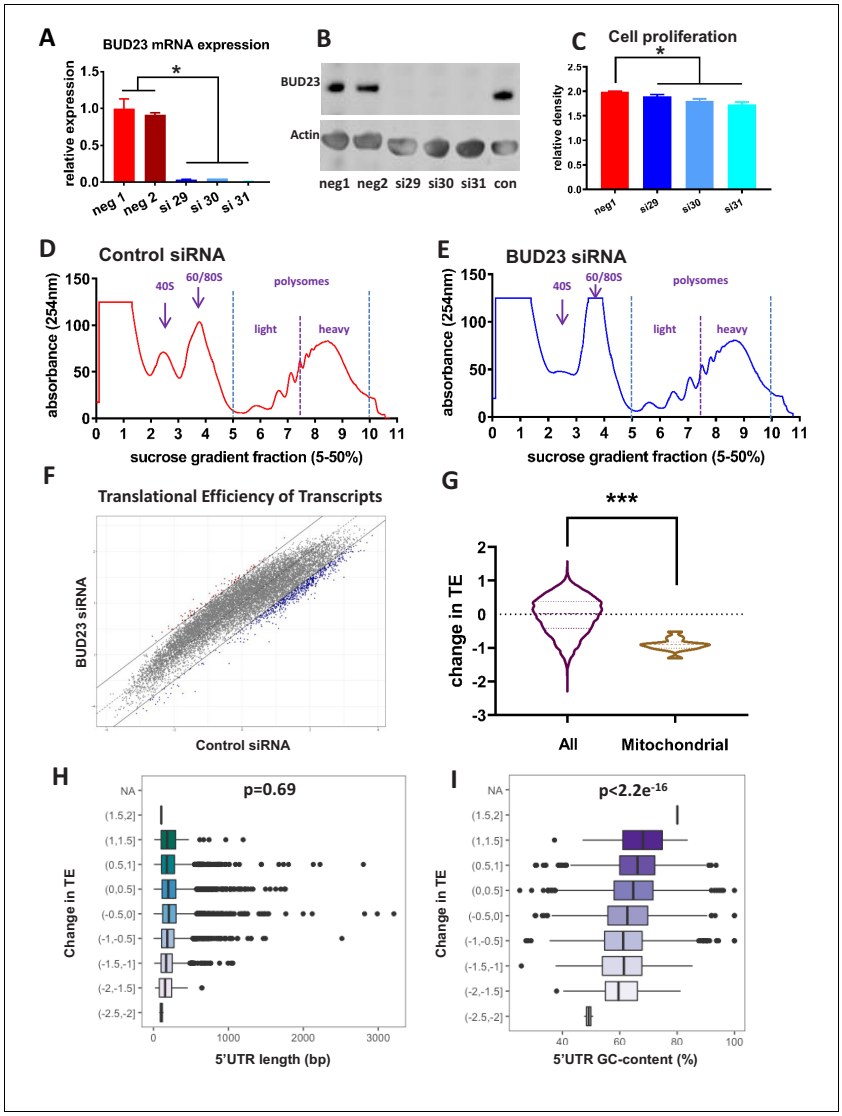

Figure 1. Analysis of BUD23-dependent ribosome function. (**A**) Relative mRNA expression levels of *BUD23*. A549 cells were transfected for 48 hr with either *BUD23* specific siRNA (si29, 30, 31) or non-targeting control (neg1, 2). Total RNA was extracted before reverse transcription to cDNA and qPCR (TaqMan). (**B**) Protein expression was determined by western blotting using antibody GTX105840. Actin was used as a loading control. (**C**) siRNA treated cells were plated into cell culture wells and allowed to grow in DMEM supplemented with 10% FBS for 48 hr. Total cell volume was then

Figure 1 continued on next page

Figure 1 continued

measured using SRB assay to indicate amount of proliferation. Polysome profiles were obtained from A549 cell lysates treated with (**D**) Control siRNA or (**E**) *BUD23* specific siRNA (si30) for 48 hr (n = 3). Changes in the ratio of the 40S peak to the 60/80S peak were observed between the two conditions. Polysome fractions were divided into heavy (more than three ribosomes) or light (three or less ribosomes) before RNA sequencing.. A translational efficiency (TE) score was derived by dividing the relative proportion of transcript abundance in the heavy fraction by that in the light fraction. (**F**) The TE scores in the two conditions derived from the samples in A and B are plotted against each other. (**G**) Violin plot showing the change in translational efficiency upon *BUD23* siRNA treatment ('change in TE score') for all detected transcripts (All) versus mitochondrially-encoded transcripts (Mitochondrial). (**H**) 5'UTR length of the transcripts was plotted against change in translational efficiency (TE, as defined in ***Figure 1G***). The data are plotted in bins with 'change in TE' (BUD23 TE/Control TE) windows of 0.5. (**I**) 5'UTR GC content was of the same transcripts was plotted against change in TE. The data are plotted in bins with TE windows of 0.5.

The online version of this article includes the following figure supplement(s) for figure 1:

Figure supplement 1. Further analysis of BUD23-dependent ribosome function in A549 cells.
Figure supplement 2. 5'UTR motif analysis.
Figure supplement 3. Further analysis of polysome profile dataset.

condition. To examine the identity of the most highly affected transcripts, a threshold of >1 or <-1 difference in the relative TE was set (i.e. TE doubled or halved), and applied to ***Figure 1F***, shown as trend lines. There were 650 transcripts with a TE ratio <-1 and 95 transcripts where the TE ratio >1 after BUD23 depletion; indicating the marked loss of high efficiency mRNA translation.

Analysis of BUD23 differentially translated mRNA species

The 650 transcripts for which TE was reduced (TE ratio <-1 after BUD23 depletion) constituted a highly connected network, with a significantly higher number of protein-protein interactions than would be expected from a random dataset of similar size, and an interaction analysis (PPI) enrichment p-value<$1e^{-16}$. Gene set analysis of these transcripts revealed enrichment for genes involved in RNA processing, metabolic processes and organelle organisation among other high energy demand processes (***Figure 1—figure supplement 1***).

Surprisingly, the TE of mitochondrially-encoded transcripts was observed to be particularly strongly down-regulated (***Figure 1G***). In fact, all mitochondrial transcripts had a negative change in TE after BUD23 loss, with approximately 50% reduction in TE.

BUD23 expression promotes ribosome interaction with low GC 5'UTRs

To investigate the mechanism underlying the BUD23 dependent selection of transcripts we examined specific mRNA features associated with translational efficiency. Given the known influence of 5'UTR features on translation efficiency, we reasoned that specific features of the 5'UTR may be particularly important for BUD23 action. A number of well-characterised 5'UTR features impact mRNA translation, including length, secondary structure, GC content, and specific motifs including the TOP sequence (***Gandin et al., 2016***; ***Meijer and Thomas, 2002***). We saw no enrichment for TOP sequence content in the differentially translated mRNA species (***Figure 1—figure supplement 2***), and no correlation between change in TE score and 5'UTR length was observed (***Figure 1H***). We also noted that transcripts with shorter total lengths were not more likely to shift from the heavy to the light fraction (***Figure 1—figure supplement 3***). There was, however, a highly significant correlation between change in TE score and GC content (Pearson's correlation value of −0.1337, p-value<$2.2e^{-16}$) (***Figure 1I***). This identifies an intersection between mRNA transcript 5'UTR GC content and BUD23 ribosome maturation. There was no difference in the distribution of 5'UTR GC in mitochondrial-related transcripts relative to all transcripts detected in the polysome analysis (***Figure 1—figure supplement 3***).

Loss of BUD23 causes changes in cellular protein homeostasis

Our studies reveal the consequences for the ribosome of BUD23 action and point to an impact on the cellular proteome. Therefore, to investigate the downstream consequences of BUD23 loss we examined the cellular proteome by LC-MS/MS. *BUD23* knockdown downregulated 83 proteins and upregulated 64, out of a total of 3255 identified (***Figure 2—source data 1***). When tested using PANTHER GO cellular component ontology analysis, upregulated proteins were over-represented for components of the large ribosomal subunit (14/64 proteins), whilst downregulated proteins were

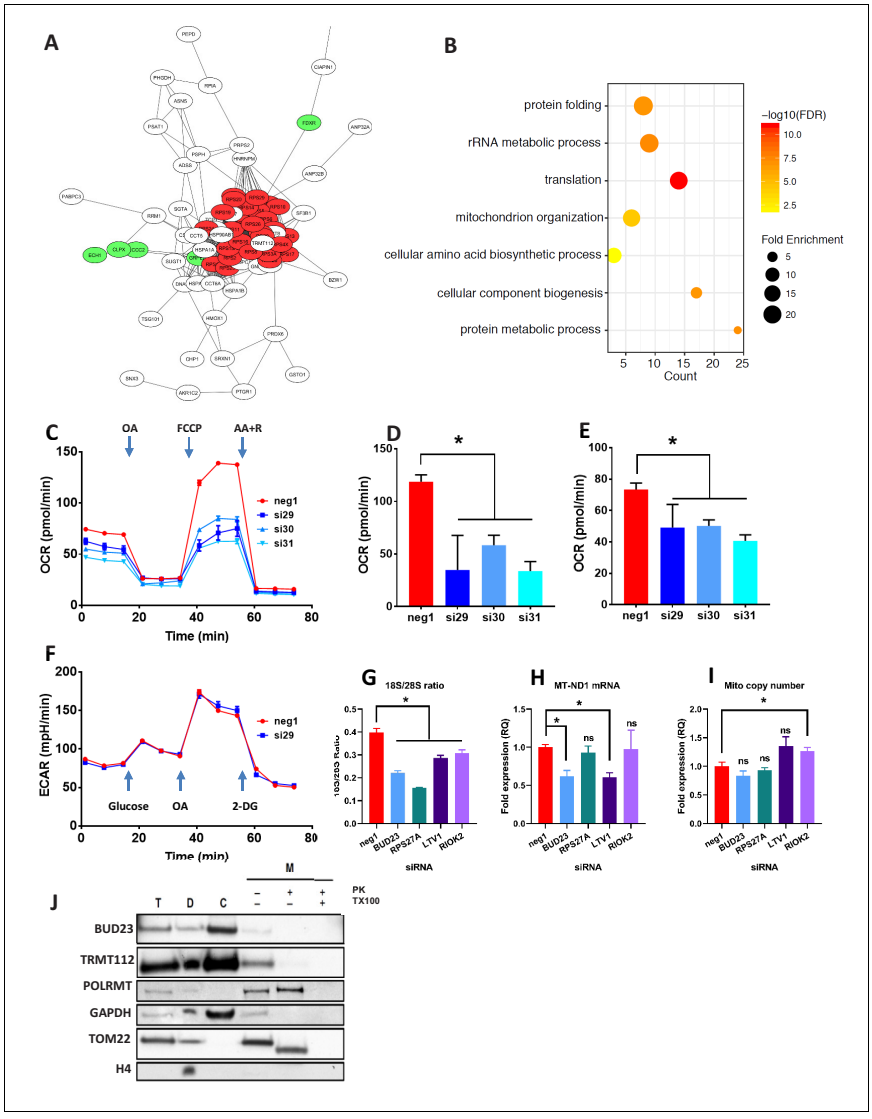

Figure 2. Proteomic analysis of BUD23 deficiency reveals mitochondrial phenotype Proteomics was performed on A549 cell lysates 48 hr after transfection with either *BUD23*-targeting siRNA or control siRNA. Significantly down-regulated and up-regulated proteins were defined using Welch's T-test with a permutation-based FDR < 0.05. (**A**) Significantly down-regulated proteins were visualised as a network using String 10 online software. Red nodes are 40S ribosomal proteins, Green nodes are mitochondrial proteins (**B**) Over-representation analysis of the significantly down-regulated protein

Figure 2 continued on next page

Figure 2 continued

dataset was performed using the PANTHER GO-Slim Biological Processes, and significantly over-represented terms were visualise using ggplot2. (**C**) Mitochondrial stress test was conducted on A549 cells treated with *BUD23*-targeting or non-targeting control siRNA (n = 3). Oxygen consumption rate (OCR) was measured over time to obtain mitochondrial respiration rates. Values for ETS (**D**) and OXPHOS (**E**) were derived from the OCR measurements after the addition of oligomycin A (OA), FCCP and antimycin A + rotenone (AA+R) in succession. (**F**) Glycolytic capacity was tested using a Seahorse glycolytic stress test and measuring extracellular acidification rate (ECAR). (**G**) A549 cells were treated with control siRNA (neg1) or siRNA specifically targeting *BUD23* (si30), RPS27A, LTV1 or RIOK2. 18S/28S ratio was measured using Tapestation to confirm ribosome subunit imbalance. (**H**) MT-ND1 mRNA was measured by qPCR as an indicator of mitochondrial transcript abundance (relative to control gene HPRT). (**I**) Mitochondrial copy number was measured relative to genomic copy number by qPCR. (**J**) Cellular fractionation into total 'T', cytosolic 'C', cellular debris 'D' and mitochondrial 'M' fractions. Protein was isolated from these fractions before SDS-PAGE and immuno-blotting for BUD23 and TRMT112. POLRMT was blotted as a control for mitochondrial proteins, TOM22 as a control for a mitochondrial membrane protein and GAPDH and Histone H4 as control non-mitochondrial proteins.

The online version of this article includes the following source data and figure supplement(s) for figure 2:

Source data 1. Proteomics data table.
Figure supplement 1. Network analysis of up-regulated proteins.
Figure supplement 2. Further analysis of ribosomal deficiency in A549 cells.

over-represented for components of the small ribosomal subunit (22/83 proteins), (***Figure 2A***, ***Figure 2—figure supplement 1***). This imbalance in the relative abundance of ribosomal proteins, recapitulates the observation in the polysome profiles and confirms a major role for BUD23 in the maturation of the protein translation apparatus of the cell. Interestingly, TRMT112 protein, an obligate partner for BUD23, was also significantly down-regulated with *BUD23* knock-down, which may indicate a reciprocal stabilising interaction.

Ontology analysis of the proteomics dataset was used to predict the functional consequences of BUD23 reduction (PANTHER GO biological processes). Over-representation analysis of the up-regulated proteins overlapped significantly with the 'protein translation'. Analysis of the down-regulated proteins again showed a statistically significant over-representation for proteins associated with GO biological terms including 'translation', as well as 'rRNA metabolic process' and 'protein metabolic process' which support a major effect on the translational apparatus (***Figure 2B***). Unexpectedly, there was also over-representation within the down-regulated proteins for the terms 'Mitochondrion organization' and 'Cellular component biogenesis', suggesting a consequential impact on mitochondrial function, a major destination for new protein synthesis in the cell.

BUD23 regulates mitochondrial function

Because the TE of mitochondrial transcripts was down-regulated and mitochondrial organisation emerged from the proteome analysis, specific assays of mitochondrial activity were performed. Depletion of BUD23 with any of three, independent siRNAs resulted in a > 50% reduction in oxidative phosphorylation (OXPHOS) and around a 25% reduction in Electron Transfer Capacity (ETC) (***Figure 2C,D,E***) but no observable difference in leak respiration (LEAK), relative to control (***Figure 2—figure supplement 2***). Moreover, no alteration in glycolytic capacity was observed indicating specificity for mitochondrial energetic pathways (***Figure 2F***). We also observed a reduction in mitochondrial mRNA abundance with *BUD23* knockdown, but no change in mitochondrial genome copy number, implying a functional defect, rather than loss of mitochondrial mass (***Figure 2G,H,I***), although these measurements were performed soon after siRNA knockdown, and so a later impact on mitochondrial mass resulting from prolonged BUD23 loss cannot be excluded.

To examine whether this mitochondrial transcription defect was specific to BUD23 deficiency, or part of a more general mechanism resulting from 40S/60S imbalance, we performed siRNA-mediated knockdowns of other known ribosome biogenesis factors, LTV1 and RIOK2, as well as the ribosomal small subunit protein RPS27A (also reported to result in ribosomal subunit imbalance) (***Sloan et al., 2019***). Depletion of *LTV1*, *RIOK2* and *RPS27A* all resulted in significant decrease in 18S/28S ratio relative to control siRNA, indicating a similar 40S/60S imbalance as observed with *BUD23* knockdown (***Figure 2G***, ***Figure 2—figure supplement 2***). *LTV1* knockdown resulted in a similar decrease in mitochondrial transcript expression as observed in *BUD23* knockdown (***Figure 2H***). However, *RPS27A* and *RIOK2* knockdown-induced ribosome imbalance did not affect mitochondrial

transcript expression (**Figure 2H**, **Figure 2—figure supplement 2**). This indicates that disruption of 40S subunit biogenesis is not by itself sufficient to result in mitochondrial dysfunction.

To check that BUD23 was not regulating mitochondria directly, we blotted for the protein after sub-cellular fractionation. BUD23 was found to be abundant in the cytosolic fraction but was not detected in the mitochondrial fraction after proteinase K digestion (**Figure 2J**). This suggests the mechanism of BUD23 action does not occur within the mitochondria. Furthermore, TRMT112, the obligate BUD23 binding partner, was also abundant in the cytosol, but barely detectable within mitochondria (**Figure 2J**). Together these data indicate that BUD23-dependent mitochondrial regulation is likely to be a downstream consequence of effects on ribosome composition, function, and cellular protein repertoire, rather than a direct effect of BUD23 protein within the mitochondria.

Homozygous deletion of *Bud23* results in embryo-lethality

To investigate the physiological impact of BUD23 we generated *Bud23* null mice. We introduced a frameshift deletion within the *Bud23* gene, which resulted in a null allele (**Figure 3A**). However, upon further breeding of heterozygous mice a clear deviation from the expected Mendelian ratio was observed in the resultant offspring. Out of 74 pups born, 39 were found to be wild-type for the *Bud23* gene, 35 were heterozygous, and zero were homozygous for the null allele (**Figure 3B**), indicating embryonic lethality in *Bud23*-null mice. This is in contrast to reports in yeast where BUD23 was shown to be non-essential for life (**White et al., 2008**). Furthermore, it is notable that approximately half the expected heterozygote birth rate was seen, implying an additional haplo-insufficiency developmental death rate. Accordingly, we analysed embryos at day E10.5 and detected Mendelian ratios of wild-type, and heterozygous animals, but again no homozygous null embryos were seen (**Figure 3B**), suggesting total *Bud23* loss is incompatible with embryogenesis, but haploinsufficiency results in fetal death later in development.

Surprisingly, surviving adult heterozygous mice showed no difference compared to wildtype littermate controls in body weight, lean body weight or body fat between 10 and 30 weeks of age (**Figure 3C**). There was also no significant change in energy expenditure or respiratory exchange ratio in $Bud23^{+/-}$ mice relative to WT littermate controls (**Figure 3—figure supplement 1**), suggesting compensatory mechanisms to permit survival.

To circumvent embryonic lethality, we generated a floxed *Bud23* allele mouse, allowing post-natal tissue-specific KO (**Figure 3A**). Mice homozygous for this floxed *Bud23* ($Bud23^{fl/fl}$) allele showed no observable differences from wild-type littermates. To confirm the embryonic lethality phenotype using an independent genetic approach, we crossed these mice with a Cre-deleter mouse line (*Hprt*-cre) (**Nichol et al., 2011**) to globally delete *Bud23* alleles. $Bud23^{+/-}$ heterozygous crosses also failed to generate any homozygous null offspring (0 out of 28 cre positive offspring), confirming the observation in the global knockout mouse line (**Figure 3D**).

We targeted *Bud23* disruption to skeletal and cardiac muscle using Muscle Creatine Kinase (*Mck*)-cre as the driver (**Whitnall et al., 2008**). Cardiac muscle relies heavily on mitochondrial production of ATP in post-natal life, but less so during development, so offering us the chance to analyse BUD23 impact on a highly mitochondrially-dependent tissue. $Bud23^{fl/fl}$ *Mck*-$Cre^{+/-}$ mice exhibited Cre-mediated deletion of exon 7 of the *Bud23* gene in cardiac tissue, with a consequent reduction in BUD23 protein levels (**Figure 3E,F**).

BUD23 deficiency drives preferential dysregulation of mitochondrial proteins

Loss of BUD23 in cardiac muscle resulted in sudden death between the age of 28–35 days (**Figure 4A**). Littermate control mice expressing $Bud23^{fl/fl}$*Mck*-$Cre^{-/-}$ or $Bud23^{fl/wt}$ *Mck*-$Cre^{+/-}$ (i.e. mice retaining at least one functional copy of the *Bud23* allele) were viable, fertile and did not die prematurely (**Figure 4A**). Mouse tissues from this line were therefore subsequently harvested at 26 days of age. A significant reduction in the 18S/28S RNA ratio, consistent with the in vitro data using siRNA knockdown was observed at this time point (**Figure 4B**).

Proteomic analysis of cardiac tissue recovered from 26 day old $Bud23^{fl/fl}$*Mck*-$Cre^{+/-}$ mice and littermate controls ($Bud23^{fl/fl}$*Mck*-$Cre^{-/-}$) revealed a significant decrease in protein content per cell with loss of BUD23 (**Figure 4C**), with clear separation by genotype (**Figure 4—figure supplement 1**). When detected proteins were annotated by sub-cellular compartment, mitochondria were found to

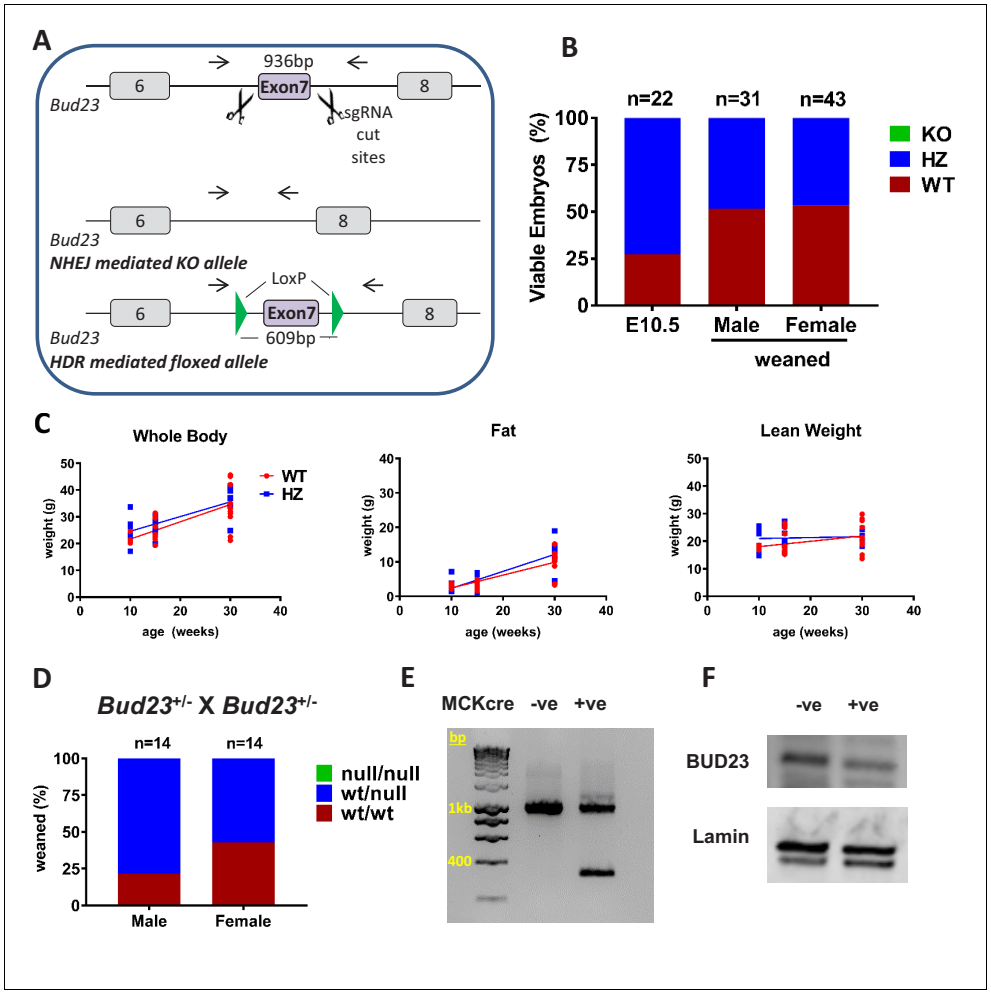

Figure 3. Generation and characterisation of murine *Bud23* null and floxed alleles. (**A**) Schematic of the targeting strategy used to create a murine *Bud23* knockout allele and a floxed allele were generated by CRISPR-Cas9. (**B**) Genotype analysis of day E10.5 embryos and the offspring from heterozygous breeding pairs. (**C**) *Bud23* Heterozygous (HZ) and wildtype (WT) mice (10–30 weeks old) were analysed over time for body composition by ECHO-MRI. (**D**) Genotype analysis of offspring from heterozygous recombined *Bud23* (*Bud23*$^{tm1c/wt}$) allele crosses. (**E**) PCR amplification of the *Bud23* genomic locus in *Bud23*$^{fl/fl}$ mice positive or negative for MCKcre expression in heart tissue, shows successful recombination of the mutant *Bud23* allele (bp = base pairs). (**F**) Disruption of BUD23 protein in the cre positive animals was confirmed by Western blot.
The online version of this article includes the following figure supplement(s) for figure 3:

Figure supplement 1. Metabolic analysis of BUD23 heterozygous mice.

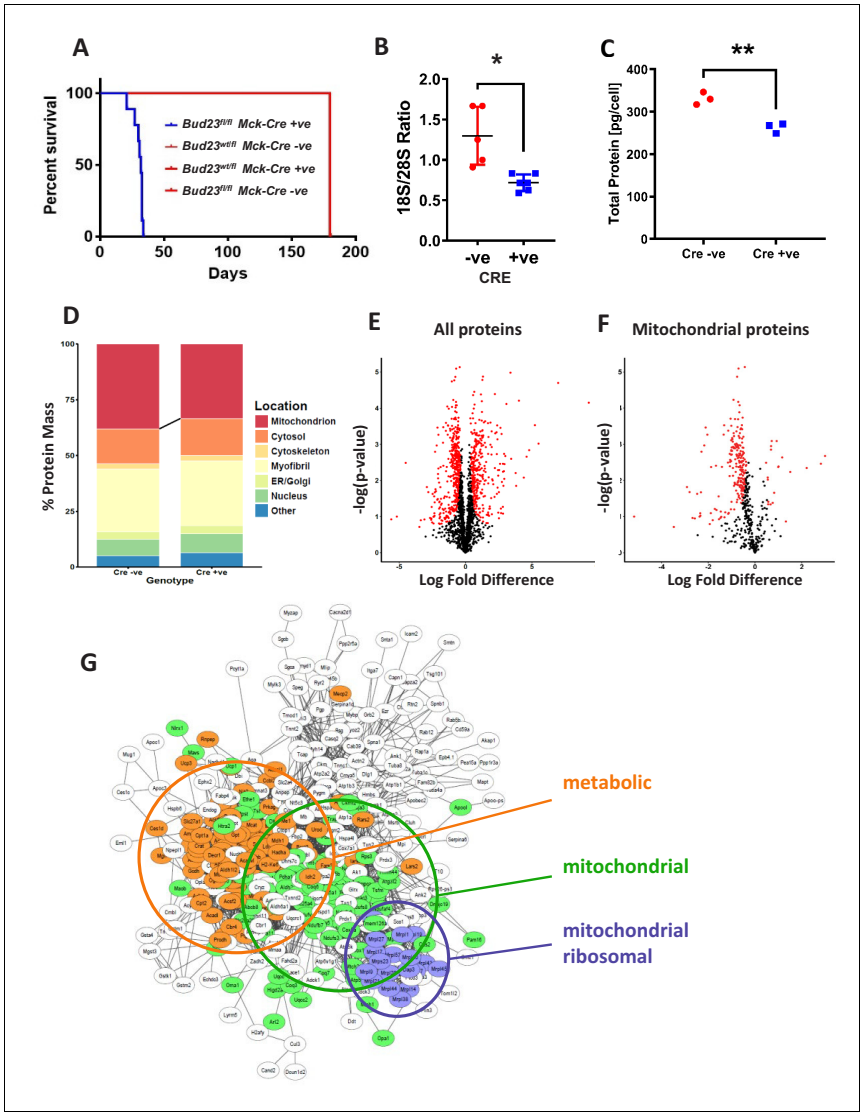

Figure 4. Proteomic analysis of BUD23 deficient heart tissue shows selective mitochondrial phenotype A murine *Bud23* knockout allele and a floxed allele were generated by CRISPR-Cas9. (**A**) Survival curve for *Bud23*$^{fl/fl}$ *Mck-Cre*$^{+/-}$ (*Bud23* knock-out targeted to heart and muscle) shown in blue, compared to littermate controls (*Bud23*$^{wt/fl}$ *Mck-Cre*$^{-/-}$, *Bud23*$^{wt/fl}$ *Mck-Cre*$^{+/-}$, *Bud23*$^{fl/fl}$ *Mck-Cre*$^{-/-}$), all shown in red. For subsequent analyses, hearts were collected from 26 day old *Bud23*$^{fl/fl}$ *Mck-Cre*$^{+/-}$, and *Bud23*$^{fl/fl}$ *Mck-Cre*$^{-/-}$ littermate controls. (**B**) 18S/28S ratio analysis of RNA extracted from

Figure 4 continued on next page

Figure 4 continued

BUD23 positive or negative mouse hearts using TapeStation. (**C**) Proteomics was performed on heart tissue from Cre +ve and Cre -ve littermates (n = 3). Total protein concentration per cell is shown, as determined via the proteomic ruler approach. (**D**) Relative contribution levels of each organelle to total protein mass based on ontology. The decrease in mitochondrial mass observed in Cre positive hearts is indicated. (**E and F**) Volcano plots of either total protein or mitochondrial protein fold change differences in Cre positive hearts relative to Cre negative hearts. Significantly up- and down-regulated proteins are indicated in red (FDR < 0.05, s0 = 0.2). (**G**) Functional enrichment network of total down-regulated proteins. The network was built using String 10 online software prior to export into Cytoscape.

The online version of this article includes the following source data and figure supplement(s) for figure 4:

Source data 1. Proteomics data table.
Figure supplement 1. Proteomic analysis of BUD23 deficient mouse hearts.
Figure supplement 2. Change in TE correlates poorly with change in protein abundance.
Figure supplement 3. Network analysis of down-regulated proteins in BUD23 deficient mouse hearts.

be subject to the largest loss of protein content, with small reciprocal increases in the other compartments (***Figure 4D***), again identifying mitochondria as especially sensitive to BUD23 action. Of the 2047 proteins identified by mass spectroscopy, 347 were found to be significantly up-regulated and 442 were found to be significantly down-regulated in the BUD23 deficient condition (***Figure 4E***, ***Figure 4—source data 1***). Whilst an approximately equivalent number of down and up regulated proteins was identified globally, when this list was refined to mitochondrial proteins only 20 were up-regulated compared to 220 down-regulated (50% of all down-regulated proteins) (***Figure 4F***). By contrast, the up-regulated dataset was enriched for translational (60S proteins) and proteasomal proteins (***Figure 4—figure supplement 1***). Whilst correlation between change in protein abundance in BUD23-deficient heart tissue and change in mRNA TE of the corresponding transcripts in the *BUD23* siRNA treated A549 cells was poor overall (***Figure 4—figure supplement 2***), it is striking that mitochondria are affected to a great extent in both models. These observations show a strong selectivity for impaired expression of mitochondrial proteins as a result of BUD23 deficiency.

Within the set of mitochondrial proteins, we found that electron transport chain complexes I, IV and V (ATP synthase) were most strongly reduced in response to loss of BUD23 (***Figure 4—figure supplement 3***). Furthermore, ontology analysis of all the significantly down-regulated proteins identified three main clusters of proteins: mitochondrial proteins, mitochondrial ribosomal proteins and proteins involved in energy metabolism, indicating a functional mechanism linking between the BUD23 dependent ribosomal defect, through reduced mitochondrial protein expression to result in disruption of energy metabolic pathways (***Figure 4G***). Therefore, BUD23 actions on the ribosome result in down-regulation of core mitochondrial proteins involved in ATP synthesis.

BUD23 deficiency causes mitochondrial dysfunction in cardiomyocytes

Given the observation of preferential dysregulation of mitochondrial proteins, we hypothesised that mitochondrial function was likely to be compromised in BUD23-deficient cardiac tissue. Mitochondrial DNA copy number was reduced in BUD23 deficient cardiac tissue (***Figure 5A***). Functional analysis of mitochondrial function in cardiac homogenates using the Oroboros microrespirometer system revealed that mitochondrial OXPHOS and ETC were both significantly reduced in mice deficient for BUD23, while LEAK respiration was unaffected (***Figure 5B***). The reduction in OXPHOS led to a lower respiratory control ratio (RCR) indicating that mitochondria from mice deficient for BUD23 were less efficient at producing ATP. These effects were apparent regardless of which substrate was used for electron donation. In addition to reduced mitochondrial capacity, mice deficient for BUD23 had lower citrate synthase activity, indicating a reduction in cardiac mitochondrial density (***Figure 5C***), which accords with the measured loss of mitochondrial genome copy number (***Figure 5A***).

To test whether haplo-insufficiency of BUD23 protein was enough to impair mitochondrial function we also tested heart homogenates from *Bud23*$^{+/-}$ mice. These were found to have no significant difference in mitochondrial respiratory capacity across any mitochondrial state (LEAK, OXPHOS, ETS), whether normalised to citrate synthase activity or protein content (***Figure 5—figure supplement 1***). It was, however, noted that, compared to wild-types, *Bud23*$^{+/-}$ mice did exhibit significantly higher citrate synthase activities, indicating greater mitochondrial density. This may result from increased mitochondrial biogenesis to compensate for defective oxidative phosphorylation function and may partly explain the reduced viability in *Bud23*$^{+/-}$ mice. Interestingly, the impact of BUD23

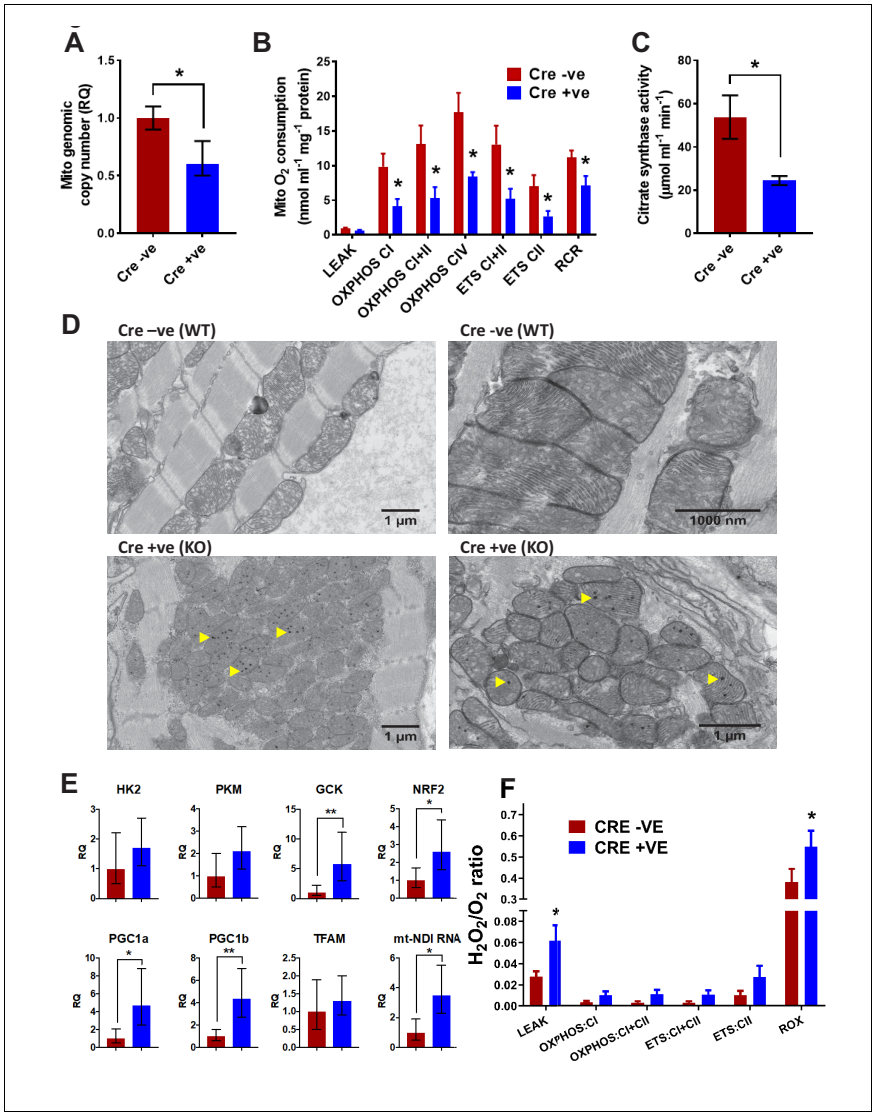

Figure 5. Analysis of mitochondrial structure and function in BUD23 depleted heart. Mouse tissues were collected at 26 days old. (**A**) Mitochondrial genome copy number measured in the heart tissue by qPCR, relative to autosomal genome copy number (n = 6). (**B**) Mitochondrial respiration was measured in heart homogenates (n = 5–6). Oxygen consumption was measured under various mitochondrial states and normalised to protein content: LEAK conditions (malate, pyruvate and glutamate as substrates); OXPHOS (routine respiration rate) through Complex I, I+II or IV; ETC (maximal

Figure 5 continued on next page

Figure 5 continued

respiration rate) through Complex I+II and II; Respiratory Control Ratio (RCR, measure of mitochondrial efficiency). (**C**) Citrate Synthase activity was measured in the heart homogenates as a marker of mitochondrial content. (**D**) Electron microscopy images of mitochondria in cardiomyocytes from either *Bud23*$^{fl/fl}$ (WT) hearts, or *Bud23*$^{fl/fl}$ *Mck*-Cre +ve (KO) hearts. Accumulation of electron dense granules is visible in *Bud23*$^{fl/fl}$ *Mck*-Cre +ve (KO) hearts, denoted by arrows. (**E**) These hearts were further analysed for expression of mitochondrial biogenesis genes, markers of glycolysis, mitochondrial biogenesis, oxidative stress and indicators of mitochondrial transcription using qPCR. (**F**) ROS was measured simultaneously with O_2 consumption (see ***Figures 1–3***) under various mitochondrial states and normalised to citrate synthase activity: LEAK conditions (malate, pyruvate and glutamate as substrates); OXPHOS (routine respiration rate) through Complex I or I+II; ETS (maximal respiration rate) through Complex I+II and II, and in the presence of antimycin-A (residual oxygen consumption, ROX)(n = 5–6).
The online version of this article includes the following figure supplement(s) for figure 5:

Figure supplement 1. Oroboros analysis of mitochondrial function in cardiac homogenates from HZ mice and WT littermate controls.

loss on mitochondrial function appears to be sexually-dimorphic. When mitochondrial respiration was normalised to citrate synthase, male heterozygous (HZ) mice exhibited a deficiency in OXPHOS and ETS relative to wildtype, whereas female mice did not (***Figure 5—figure supplement 1***). This observation indicates a more severe phenotype in BUD23 deficient males, with further derangement of individual components of the electron transport chain.

Analysis of mitochondrial morphology, and operation of compensatory circuits in targeted cardiac muscle

Electron microscopy (EM) analysis revealed that despite decreased mitochondrial protein abundance and reduced mitochondrial function in the BUD23 cardiac tissue, the individual mitochondria appear to be formed normally with an equivalent number of cristae compared to the wildtype. The inter-myofibrillar mitochondria were typically arranged in a highly ordered pattern in the wildtype cardiac tissue, however, there was marked disorganisation in the BUD23-deficient cardiac tissue (***Figure 5D***). In addition, we identified the presence of numerous spherical electron dense inclusion bodies within the mitochondria of BUD23 deficient cardiac cells (***Figure 5D***, yellow arrows). Similar electron dense structures have been previously reported in myocardial mitochondria, which may accumulate in response to increased cellular bioenergetic demand (***Jacob et al., 1994***). The observation of these structures here may be consistent with attempted mitochondrial adaptation to energetic-demand challenge.

A frequent cellular adaptation to impaired oxidative phosphorylation is a switch to glycolytic ATP generation, and so we measured rate-limiting glycolytic gene expression (***Figure 5E***). We identified a significant induction of glucokinase (GCK), and a trend to induction of phosphofructokinase (PKM) and hexokinase (HK2) supporting such an adaptive switch to glycolysis. A further adaptation predicted was an induction in mitochondrial biogenesis programmes. We identified a significant induction in PGC1a and PGC1b, but no change in TFAM1 expression (***Figure 5E***). Taken together these results point to some of the expected cellular responses to loss of oxidative phosphorylation, but it was surprising that the changes were so few. This implies that additional cellular injury may be proceeding, which acts to limit successful adaptation.

Impaired mitochondrial function may result in overproduction of reactive oxygen species, which can trigger the apoptotic cascade and lead to cell death. Such a progression may explain the distorted and thinned ventricular walls observed in the cardiac *Bud23*-null mice. We found induction of NRF2 (***Figure 5E***), a key sentinel gene controlling cellular responses to reactive oxygen species stress, which led us to measure reactive oxygen species directly, and found that these were significantly higher in hearts lacking BUD23 expression (***Figure 5F***), identifying a burden of increased reactive oxygen species in BUD23 deficient cardiomyocytes resulting from the action of deranged mitochondria.

BUD23 deficiency in cardiac muscle leads to dilated cardiomyopathy

Deficient mitochondrial generation of ATP in cardiac tissue is a key cause of cardiomyopathy. Given the strong mitochondrial deficiencies observed in BUD23-deficient cardiac tissue, we predicted that the cardiomyopathy was the likely cause of sudden death. Histological examination of hearts from *Bud23*$^{fl/fl}$ *Mck*-Cre$^{+/-}$ (BUD23-deficient) mice showed significant enlargement, ventricle dilatation and decreased ventricle wall thickness compared to littermate controls at 26 days old (***Figure 6A–D***).

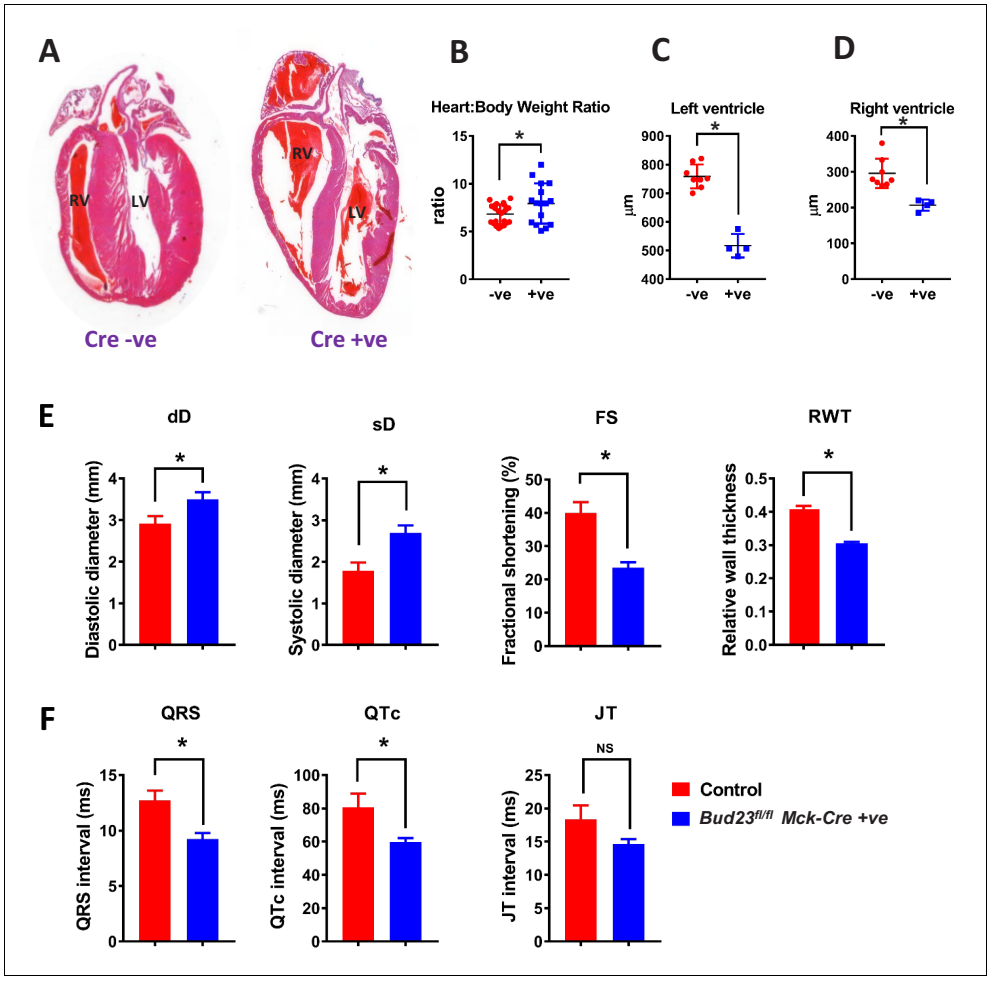

Figure 6. Targeted disruption of *Bud23* in cardiac tissue results in dilated cardiomyopathy. (**A**) Heart sections cut in the coronal plane and stained with haematoxylin and eosin from day 26 mice. Representative images are shown. (**B**) Heart weight measured as a ratio to total bodyweight. (**C and D**) Analysis of heart ventricle wall thickness in **H** and **E** stained heart sections. (**E**) Echocardiography of *Bud23*$^{fl/fl}$*Mck*-Cre$^{+/-}$ mice and littermate controls at 26–28 days of age (n = 9–10). Mice were lightly anesthetized maintaining the heart rate at approximately 450 beats/min. Data for diastolic diameter (dD), systolic diameter (sD), fractional shortening (FS) and relative wall thickness (RWT) are shown; full parameter measurements are shown in supplementary. (**F**) Electrocardiography of *Bud23*$^{fl/fl}$*Mck*-Cre$^{+/-}$ mice and littermate controls at 26–28 days of age (n = 9–10). Data for QRS, QTc and JT intervals are shown. Full parameter measurements are shown in supplementary. * denotes statistical significance (p<0.05) using Student's T-test.
The online version of this article includes the following source data and figure supplement(s) for figure 6:

Source data 1. Data table of echocardiogram analysis results and electrocardiogram analysis results.
Figure supplement 1. Fibrosis markers are up-regulated in BUD23 deficient mouse hearts.

Littermate control mice expressing *Bud23*$^{fl/fl}$*Mck*-Cre$^{-/-}$ or *Bud23*$^{fl/wt}$ *Mck*-Cre$^{+/-}$ (i.e. mice retaining at least one functional copy of the *Bud23* allele) were viable, fertile and did not die prematurely (***Figure 3A***).

Echocardiogram analysis of *Bud23*$^{fl/fl}$ *Mck*-Cre$^{+/-}$mice at 26–28 days old showed that cardiac BUD23-deficiency resulted in systolic dysfunction indicated by significantly dilated left ventricle (sD), as well as significantly decreased fractional shortening and relative wall thickness (***Figure 6E***, ***Figure 6—source data 1***).). There was, however, no observed pulmonary oedema or liver oedema (***Figure 6—figure supplement 1***,). Further analysis of the heart proteomics data from ***Figure 4*** showed an increase in a number of markers of fibrosis, including Col4a2, CTGF, Galectin-3 and others (***Figure 6—figure supplement 1***). Taken together, these observations indicate that *Bud23*$^{fl/fl}$ *Mck*-Cre$^{+/-}$ mice exhibit the early stages of heart failure around 26–28 days of age. Electrocardiogram analysis of the same mice at the same age revealed significantly shorter QRS and corrected QT (QTc) intervals but no change in heart rate (***Figure 6F***; ***Figure 6—source data 1***).).

Discussion

BUD23 is tightly conserved through evolution and has recently emerged as a ribosomal RNA methyltransferase, although its physiological role in mammals is unexplored. It is one of the genes deleted in Williams-Beuren Syndrome, a complex multi-gene deletion syndrome with neurological, and energy homeostatic features, although themediating role of individual genes to the phenotype has not been determined (***Morris, 1993***). We now identify BUD23 as playing a major role in regulating the translational efficiency of specific transcripts through its role in ribosome maturation. Indeed, translation of low 5'UTR GC-content mRNA species were particularly dependent on BUD23 expression, in contrast to the picture seen with simple ribosome deficiency in which transcripts with short/unstructured 5'UTRs were seen to be most affected (***Khajuria et al., 2018***). Furthermore, we identified a surprising role for BUD23 in maintaining mitochondrial oxidative phosphorylation capacity. As protein translation is tightly coupled to ATP demand this raised the possibility that BUD23-dependent ribosomal maturation is critical to link the two processes in living cells and tissues (***Morita et al., 2013***). Indeed, BUD23 loss greatly impaired mitochondrial ATP generation, both in vitro and in vivo. In mice, cardiomyocyte loss of BUD23 greatly impaired mitochondrial ATP generation leading to dilated cardiomyopathy and premature death, and global loss of BUD23 resulted in embryo-lethality.

BUD23 is thought to perform two functions in the generation of the translational apparatus: firstly, in the processing of pre-18S RNA into its mature form, and secondly imparting a m7-G methyl mark on a key residue. As the catalytic activity of BUD23 is not required for efficient pre-18S RNA processing, these two functions appear to be independent of each other (***Haag et al., 2015***; ***Zorbas et al., 2015***). It is notable that both the BUD23 imparted m7-G methyl mark and structurally complex 5'UTRs are characteristic features of translation specific to Eukaryotes. We speculate the co-evolution of this regulatory 18S methyl mark with the need for more complex regulation of differential translation. Further work should focus on delineating the effect of BUD23-dependent 18S maturation, from the role of the methylation mark.

We used proteomics to examine the relative changes in protein abundance which result from targeted loss of BUD23 in cardiomyocytes. This revealed a selective loss of mitochondrial proteins, explaining the observed reduction in mitochondrial capacity. As BUD23 appears to have no direct role within mitochondria we propose that the mitochondrial phenotype results from impaired translation of nuclear-encoded genes with a role in mitochondrial homeostasis. Indeed, we found that the translational efficiency of a number of mitochondria-targeted as well as mitochondrial regulating proteins were BUD23-dependent. There are many potential candidates linking the change of translational efficiency to the mitochondrial phenotype. Mammalian target of rapamycin (mTOR), for example, is known to regulate mitochondrial activity and biogenesis by regulation of translation (***Morita et al., 2013***) and, interestingly, BUD23 loss resulted in impaired translation of mTOR itself. We also observed a marked decrease in the translational efficiency of mitochondrially-encoded transcripts.

We initially generated and characterised a frame shift-generating null allele mouse. The homozygote null animals were all lost prior to embryonic day e10.5 and we were unable to identify a cause but considered that a major defect in a mitochondrially–dependent organ such as heart may be a

plausible mechanism. We moved, therefore, to a conditional allele mouse, using which we confirmed the developmental lethality of the null allele by crossing with a global deleter-cre strain (Hprt-cre). Using the conditional allele mice with a muscle Cre driver we were able to profile the impact of BUD23 in a physiological role. Loss of BUD23 in heart and skeletal muscle resulted in early death from cardiac failure. This striking phenotype was accompanied by morphological changes including cardiac dilatation, ventricular wall thinning, and impaired ventricular contractility. There was evidence for an attempted switch to glycolytic ATP generation in the hearts, with induction of rate-limiting glycolytic enzyme genes; and also adaptation to conditions of oxidative stress with induction of NRF2. Mitochondrial dysfunction frequently imposes a burden of oxidative stress on affected cells, which can result in apoptosis, thereby explaining the loss of cardiac muscle seen. Detailed ultrastructure analysis of cardiac mitochondria revealed no major loss of mitochondrial volume, but there was a striking additional feature seen within the mitochondria: electron-dense, spheroid inclusions. These were not observed in control hearts, and are not typically seen in mitochondria from individuals with mitochondrial myopathies, but have been reported before under conditions of extreme ATP demand, and to result from bilayer budding from the inner cristae, to generate additional ATP generating surface area (***Jacob et al., 1994***; ***Somlyo et al., 1974***). Therefore, we propose this may be a further adaptation to the impaired oxidative phosphorylation function within the mitochondria.

There is a growing recognition that transcriptional control mechanisms are insufficient to explain differentiated cell function. Recent advances have identified differential translation of mRNA species dependent on 5'UTR features as an important control mechanism, potentially coupling global changes in protein translation with appropriate upregulation of mitochondrial ATP generation to meet demand [2]. BUD23, a highly conserved ribosomal RNA methyltransferase which lies within a multigene interval, deleted as a cause of Williams-Beuren syndrome, plays a specific role in highly ATP-hungry cells, promoting translation of mitochondrial proteins, and impacting on oxidative phosphorylation. This function likely contributes to aspects of the human phenotype, in particular neurological dysfunction, glucose intolerance and obesity. Complete global loss of *Bud23* is embryonic lethal, and early post-natal death follows deletion of *Bud23* in the heart. The cardiac phenotype is severe, with marked mitochondrial dysfunction, and evidence of compensatory changes towards glycolytic ATP generation, and adaptation to oxidative stress. Therefore, BUD23 plays a critical role in coupling protein translation to mitochondrial function, with implications for mitochondrial diseases, and cardiomyopathies.

Materials and methods

Key resources table

Reagent type (species) or resource	Designation	Source or reference	Identifiers	Additional information
Gene (*Homo sapiens*)	BUD23		Gene ID: 114049	Aliases: WBSCR22, MERM1
Genetic reagent (*Mus musculus*)	*Bud23*^{null}	This paper	*Bud23*^{null}	Mutant allele: deleted exon 7 of BUD23 gene
Genetic reagent (*Mus musculus*)	*BUD23*$^{fl/fl}$	This paper	*BUD23*$^{fl/fl}$	Mutant allele: floxed exon 7 of BUD23 gene
Genetic reagent (*Mus musculus*)	*Mck*-Cre	***Whitnall et al., 2008***	B6.FVB(129S4)-Tg (Ckmm-cre)5Khn/J	Heart and muscle specific Cre-driver
Cell line (*Homo-sapiens*)	A549	ATCC	CCL-185	Airway epithelial adenocarcinoma
Antibody	anti-BUD23 (Rabbit polyclonal)	GeneTex	Cat# GTX105840	WB (1:500)
Sequence-based reagent	BUD23_F	This paper	Genotyping primers	5'-CCTGGCTGATGTGTTGCTTT-3' Annealing temperature: 62˚C
Sequenced-based reagent	BUD23_R	This paper	Genotyping primers	5'-GCTGCACATCTCTCCTCACT-3' Annealing temperature: 62˚C
Sequence-based reagent	MT-ND1_F	This paper	qPCR primers	5'-GAAGTCACCCTAGCCATCATTC-3'

Continued on next page

Continued

Reagent type (species) or resource	Designation	Source or reference	Identifiers	Additional information
Sequenced-based reagent	MT-ND1_R	This paper	qPCR primers	5'GCAGGAGTAATCAGAGGTGTTC-3'
Sequenced-based reagent	siRNA: nontargeting control 1	Thermo Fisher	AM4611	Silencer Select
Sequenced-based reagent	siRNA: nontargeting control 2	Thermo Fisher	4390847	Silencer Select
Sequenced-based reagent	siRNA: BUD23	Thermo Fisher	41529	Silencer Select
Sequenced-based reagent	siRNA: BUD23	Thermo Fisher	41530	Silencer Select
Sequenced-based reagent	siRNA: BUD23	Thermo Fisher	41531	Silencer Select
Software, algorithm	R	www.r-project.org		Key packages: -EDGER -BIOCONDUCTOR -EDASEQ
Commercial assay or kit	Seahorse XF Mito stress test	Agilent	103015–100	
Commercial assay or kit	Seahorse XF Glyco stress test	Agilent	103020–100	

Animals

All mice were routinely housed in 12:12 light/dark (L:D) cycles with ad libitum access to food and water. All experiments were carried out in accordance with the Animals (Scientific Procedures) Act 1986 (UK) under Home Office protocol number 70/8768 and P3A97F3D1. In studies utilizing conditional targeted mice, littermate controls (floxed/floxed) were used as control; these mice carried no copies of the Cre or iCre. Genotyping was performed on all experimental animals.

Physiological monitoring

To assess body composition, whole body, fat mass and lean body mass was assessed using the EchoMRI system (Echo Medical Systems). To assess metabolic gas exchange, mice were individually housed in indirect calorimetry cages (CLAMS, Columbus Instruments). Mice were acclimatised to the cages for 48 hr prior to recording data. Measurements of O_2 consumption and CO_2 production were recorded every 10 min for >72 hr. RER was derived from these measures (VCO_2/VO_2), as was energy expenditure ($3.815^{*}VO_2 + 1.232^{*}VCO_2$).

Generation of *Bud23* conditional KO mice

In order to conditionally KO the *Bud23* gene by Cre recombinase expression we generated a transgenic mouse line with the critical exon seven flanked by LoxP sites. Exon seven has an unequal splicing phase, meaning its Cre mediated excision would lead to a frame shift and KO of the *Bud23* gene. This exon is also flanked by large introns giving sufficient space to insert LoxP sites without perturbing normal gene splicing and regulation. We used CRISPR (clustered regularly interspaced short palindromic repeats)-Cas9 in the mouse zygote to integrate these LoxP sites.

Briefly, sgRNA targeting this genomic region, and with minimal off target potential, were identified (sgRNA-1 GGCATTGGGCCTACTTAAAG-GGG, sgRNA-2 AGTTGAAGGGTTCCATAATG-AGG, sgRNA-3 CTTTACAGCCCAAGACCACT-TGG) and selected for use. sgRNA was synthesised in vitro, using protocols developed by ***Bassett et al. (2013)***. Forward primers of the form GAAATTAATACGACTCACTATA $GGN_{18\text{-}20}$GTTTTAGAGCTAGAAATAGC (where $GGN_{18\text{-}20}$ is the sgRNA sequence) for each guide were combined with the universal reverse primer, AAAAGCACCGACTCGGTGCCACTTTTTCAAGTTGATAACGGACTAGCCTTATTTTAACTTGCTATTTCTAGCTCTAAAAC and used in a PCR reaction with high fidelity polymerase (Phusion, NEB). 200 ng of the resulting amplicon were used overnight in an in vitro transcription reaction (HiScribe, NEB, as per manufacturer's instructions), before purification (Megaclear, Ambion) and quantification by nanodrop.

A double stranded DNA (dsDNA) repair template was designed to (i) incorporate loxP sites, with unique restriction sites for screening purposes, 300 bp upstream and 200 bp downstream of exon seven respectively and (ii) integrate silent shield mutations for all three sgRNA to prevent cutting of the repair template and (iii) contain 1000 bp 5′ and 3′ homology arms to the target region. The above template was synthesised in a pUC57 vector (Genscript, US), the linear 5′homology-loxP-exon7-loxP-3′homology fragment excised from the vector by restriction digest, gel extracted (Bioline) and further cleaned prior to microinjection (Monarch PCR purification kit, NEB).

An injection mix of the three sgRNA (40 ng/ul each), Cas9 mRNA (100 ng/ul) and the dsDNA repair template (10 ng/ul) was prepared and directly microinjected into B6D2F1 (Envigo) zygote pronuclei using standard protocols. Zygotes were cultured overnight and the resulting 2 cell embryos surgically implanted into the oviduct of day 0.5 post-coitum pseudopregnant mice.

Potential founder mice were screened by PCR and digest. Animals positive for both 5′ and 3′ LoxP integration had the region fully verified by pCR-Blunt cloning followed by Sanger sequencing. two founder mice were identified and then back-crossed to C57BL/6J wild-type mice to assess germline penetrance. Additionally, the described CRISPR targeting strategy resulted in deletion of critical exon 7, a global *Bud23* KO line was generated from this founder animal.

Genotyping

DNA was extracted from ear snip or tail tip using REDExtract-N-Amp tissue PCR kit (Sigma). Primer sequences and PCR reaction conditions are listed in the key resources table and the primer sequences supplementary file. PCR products were resolved on 1.5% agarose gels.

Cells

STR authenticated A549 cells were obtained from the European Collection of Cell Cultures (ECACC Cat no: 86012804) and maintained in culture, incubated at 37˚C in humidified air, 5% v/v CO2. Cultured cells were tested regularly for mycoplasma contamination. A549 cells were cultured in DMEM growth medium (Sigma, D6546), supplemented with 2 mM L-Glutamine (Sigma, G7513), 10% foetal calf serum (FCS) (Sigma, F96665).

Depletion of *BUD23* with siRNA

A549 cells were plated at 1 × 106 cells in a 10 cm cell culture dish and transfected with *BUD23* specific or non-targeting control siRNA (S41529, S41530, S41531, negative control 1, negative control 2, Ambion Silencer Select) using Dharmafect DF-1 according to the manufacturer's guidelines.

Mass spectrometry

A549 cell pellets were lysed in M-PER mammalian protein extraction reagent (Thermo Scientific). Whole mouse hearts were dissected, quartered and washed in ice cold PBS to remove blood before disruption of the tissue in 1x TBS supplemented with protease inhibitor cocktail using a TissueRuptor (Qiagen). SDS was added to a final concentration of 4% (w/v) prior to sonication. Samples were then reduced with 100 mM DTT and heated for 3 min at 95˚C. Samples were prepared for label-free quantification in accordance with published protocols (***Hernandez-Valladares et al., 2016***). Digested samples were analysed by LC-MS/MS using an UltiMate 3000 Rapid Separation LC (RSLC, Dionex Corporation, Sunnyvale, CA) coupled to a Q Exactive HF (Thermo Fisher Scientific, Waltham, MA) mass spectrometer using a stepped normalized collision energy centered at 28.

A549 peptide mixtures were separated using a multistep gradient from 95% A (0.1% FA in water) and 5% B (0.1% FA in acetonitrile) to 7% B at 1 min, 18% B at 58 min, 27% B in 72 min and 60% B at 74 min at 300 nL min^{-1}, using a 75 mm x 250 µm i.d. 1.7 µM CSH M-Class C18, analytical column (Waters), for a final run time of 90 min. Cardiac samples were separated using a gradient from 5% B to 7% B at 1 min, 18% B at 81.5 min, 27% B at 102 min and 60% B at 104 min, with a final run time of 120 min. The top 12 precursors were selected for fragmentation automatically by data dependant analysis during each cycle.

Ionization potential was set at 1900V with a survey scan window of 300–1750 m/z. MS1 used a resolution of 120,000 with a target ion intensity of 3e6. Higher-energy collisional dissociation was used. MS2 was set at a resolution of 60,000 with a target ion intensity of 2e5. Maximum injection

times for MS1 and MS2 were 20 ms and 110 ms respectively. Peptides were dynamically excluded for 15 s after one occurrence.

Mass spectrometry data analysis

Mass spectra were analysed using MaxQuant version 1.6.0.16 (**Cox and Mann, 2008**), searching against either the Uniprot *Mus musculus* database (accessed 21/12/2017) or *Homo sapiens* database (accessed 12/03/2017) using the native Andromeda search engine. Match between runs was selected with a retention time of 1 min, using default parameters for all other settings. MS1 search tolerance was set at 20ppm, and MS2 at 4.5ppm. Modifications were set as Carbamidomethyl (C) for fixed, and Oxidation (M) and Acetyl (Protein N-term) variable. A minimum of 1 spectra was required for identification, while a minimum of 2 spectra were required for quantification. Resulting data was processed using Perseus version 1.6.0.7 (**Tyanova et al., 2016**) and R statistical software (**Wickham, 2009**; **R Development Core Team, 2017**). All proteins identified by site only, as a potential contaminant, or in the decoy reverse database were excluded. Data was then filtered to exclude proteins with more than 3 'zero-values' across all groups. All proteins assigned to the GO term 'blood microparticle' were removed as well. LFQ values were log(2) transformed and missing values imputated in Perseus using a normal distribution (**Lazar et al., 2016**). The width of the new distribution was 0.3 standard deviations of the data, and was shifted downwards by 1.8 standard deviations of the data. A total of 6.68% of values were imputated. Significance was determined using a T-test with a permutation based FDR (FDR < 0.05, s0 = 0.1). s0 represents the relative importance of the difference between the means, with non-zero s0 values taking fold change, and not only p-value, into account. Estimations of copy numbers were performed using the proteomic ruler plug-in version 0.1.6 (**Wiśniewski et al., 2014**). Proteins were then mapped to subcellular localisations to determine percentage protein mass by organelle according to published protocols using the HeLa spatial proteome database (**Doll et al., 2017**; **Itzhak et al., 2016**). Interaction networks were built using String 10 online software (**Szklarczyk et al., 2017**) using seven data sources (textmining, experiments, databases, co-expression, neighborhood, gene fusion co-occurrence) and imported into Cytoscape (**Shannon et al., 2003**). Network edges represent confidence. A minimum interaction score of 0.4 (medium confidence) was required for network inclusion. Enrichment analysis was performed using PANTHER (**Mi et al., 2017**). Lists of proteins were exported for the identified GO terms and then manually coloured using Cytoscape for visualization.

Echocardiogram

Transthoracic echocardiography (TTE) was performed using a Vevo 770 High-Resolution Imaging System (Visualsonics Inc, Toronto, Canada) and a 30MHz probe. Mice were lightly anesthetized with 1–1.5% isoflurane via facemask, maintaining the heart rate at approximately 450 beats/min. Views were taken in planes that approximated the parasternal short-axis view and the apical long-axis view. M-mode tracings were used to determine left ventricular end-diastolic diameter (LVDD) and end-systolic diameter (LVSD), posterior wall thickness in diastole (LVPWD) and systole (LVPWS), and interventricular septum thickness in diastole (IVSD) and systole (IVSS) over three cardiac cycles. The analysis was performed blinded to animal details. LV fractional shortening (FS) was calculated using the formula FS = [(LVDD - LVSD)/(LVDD)] x 100. Relative wall thickness (RWT) was calculated using the equation RWT = (IVDD + LVPWD)/LVDD.

Electrocardiogram (ECG)

Mice were lightly anesthetized with 1–1.5% isoflurane via facemask. The body temperature was maintained around 37˚C using a heat pad. The lead II ECG was recorded using Power Lab/4SP system (Adinstruments) from needle electrodes inserted subcutaneously into the left and right forelimbs and the right hindlimb. The signal was acquired for about 5 min using Chart 7 software (Adinstruments). During offline analysis, the 5 min recording was examined for unusually shaped P, QRS, or 'T' waves and for time-varying phenomenon (e.g. irregularities in interval durations). Ectopic or abnormal beats are noted. A representative 10–15 s segment of the recording was averaged to obtain the signal averaged ECG to calculate Heart rate, RR interval, P wave duration, PR interval, QRS, JT and QT durations. QT duration was corrected (QTc) using the Bazett's formula (**Bazett, 1997**).

Polysome profiling

Polysome profiles were prepared according to the protocols previously published in: (**Gandin et al., 2014**). Two conditions were profiled, *BUD23* siRNA and Control siRNA, with an n of 3 samples per condition. Fractions were collected from each sample and RNA was purified using the Trizol extraction method. RNA from fractions containing three or less ribosomes were pooled ('Low translational efficiency) and RNA from fractions containing more than three ribosomes ('high efficiency') were pooled. Sub-polysomal fractions were similarly pooled. RNA sequencing was used to quantify the expression of RNA species in each of the pooled samples. Translational efficiency (TE) was defined as the relative abundance of a transcript in the high and low efficiency pooled fractions. A TE score for each transcript was calculated by averaging the ratio derived from each of the three replicates in each condition. TE was plotted for the two conditions using R software.

Translational efficiency (TE) was then compared to both the length and GC content of the 5' UTR region. 5' UTRs were defined using the TxDb.Hsapiens.UCSC.hg38.knownGene (Bioconductor Core Team and Bioconductor Package Maintainer, 2016) and org.Hs.eg.db (**Carlson, 2018**) R packages. Sequences of the regions were extracted using the twoBitToFa program from the BLAT suite (**Kent, 2002**) and then GC content was calculated using the seqinr R package (**Charif and Lobry, 2007**). The Pearson correlation coefficients, and their relative significances, were calculated using cor.test function from the stats R package (**R Development Core Team, 2017**).

Assessment of mitochondrial function using seahorse

Live cell metabolic assays were performed on A549 cells pre-treated with either *BUD23* siRNA or control siRNA using a Seahorse XFe 96 analyser (Agilent). Mitochondrial stress tests was performed according to the manufacturer's instructions (Agilent). 2M Oligomycin (OA), 1M FCCP and 0.5M rotenone/antimycin A (AA+R) were used for all conditions. A549 cells were plated into Seahorse XF96 plates at 160,000 cells per well, utilising 16 wells per condition. Cell density was normalised using SRB assay. Experiments were performed in triplicate.

Assessment of mitochondrial function using oroboros

Of the three distinct experimental preparations available (isolated mitochondria, permeabilized fibers, and tissue homogenates), we utilized cardiac homogenates for mitochondrial assessment (see **Goo et al., 2013** for advantages of this method). Ventricular tissue (~20 mg) was weighed and transferred to 1.5 ml of ice-cold MiRO5 medium (in mM: EGTA 0.5, $MgCl_2$ 1.4, taurine 20, KH_2P0_4 10, HEPES 20, BSA 1%, K-MES 60 mM, sucrose 110 mM, pH 7.1, adjusted with 5 N KOH). Tissue was homogenized for 3 s in 1 s bursts with a tissue homogenizer and loaded immediately (40 µg/ml) into an Oroboros Oxygraph 2 k high resolution respirometry system (Oroboros Instruments, Innsbruck, Austria) for measurement of mitochondrial respiration combined with the Fluorescence-Sensor Green of the O2k-Fluo LED2-Module for H_2O_2 measurement (see **Makrecka-Kuka et al., 2015** for full details).

Two identical respiration chambers (chamber A and chamber B) held at the same temperature were run in parallel for each experimental run. All measurements of respiration rates were carried out at 37˚C. Oxygen electrodes were calibrated daily with air-saturated respiration solution Zero calibrations were achieved by injecting yeast into the experimental chambers. Oxygen solubility in the assay medium was calculated as described previously (**Lienig and Forstner, 1984**). H_2O_2 flux was measured simultaneously with respiration in the O2k-Fluorometer using the H_2O_2-sensitive probe Amplex UltraRed (10 µM) with 1 U/mL horse radish peroxidase (HRP) and 5 U/mL superoxide dismutase (SOD). AmR in the presence of H_2O_2 is catalysed by HRP to the fluorescent product resorufin. Calibrations were performed with two sequential injections of H_2O_2 at 0.1 µM steps.

Three parameters are commonly used to assess mitochondrial function (for reviews, see **Brand and Nicholls, 2011**; **Pesta and Gnaiger, 2012**). Firstly, the capacity for oxidative phosphorylation (OXPHOS) is the respiratory capacity of mitochondria in the ADP-activated state of oxidative phosphorylation (saturating concentrations of ADP, inorganic phosphate, oxygen, and defined substrates). Secondly, LEAK respiration rate represents mitochondrial respiration that occurs in the absence of ATP generation, mainly to compensate for proton leak across the mitochondrial inner membrane. Lastly, the respiratory electron transfer-pathway capacity (ETC) is mitochondrial respiration in the noncoupled state in the presence an uncoupler; this induces maximum oxygen flux

through the electron transport chain. The Respiratory Control Ratio (RCR, calculated here as OXPHOS/LEAK) provides a measure of the degree of coupling between oxidation and phosphorylation, or in other words, the efficiency of mitochondrial ATP production.

OXPHOS, LEAK and ETS were measured in the presence of Complex I substrates pyruvate and malate (electron transfer through Complexes I-IV) or Complex I+II substrates (addition of succinate). Additionally, respiratory flux with electron transfer through Complex IV alone was measured via the addition of the electron donor tetramethyl-phenylene-diamine (TMPD). The protocol used to measure these parameters was adapted from ***Pesta and Gnaiger (2012)***. Briefly, pyruvate (5 mmol l^{-1}), malate (0.25 mmol l^{-1}) and glutamate (10 mmol l^{-1}) are added as carbon substrates and to spark the citric acid cycle. Under these conditions, mitochondria are in LEAK respiration with CI substrates in the absence of adenylates. OXPHOS with CI substrates was achieved through addition of saturating levels of ADP (2 mM l^{-1}). Following steady-state conditions, succinate (10 mmol l^{-1}) was added to achieve OXPHOS with CI+CII substrates. To uncouple respiration and achieve ETS with CI+CII substrates, carbonyl cyanide 4-trifluoromethoxyphenylhydrazone (FCCP) was carefully titrated to a maximum concentration of 0.25 µmol l^{-1}. Rotenone was then added to achieve ETS with CII substrates and antimycin A (5 µmol l^{-1}) was given to block Complex III and measure background non-mitochondrial residual oxygen consumption (ROX). OXPHOS through Complex IV alone was assessed by adding the electron donor TMPD (0.5 mmol l^{-1}). To avoid oxidation of TMPD, ascorbate (2 mMol l^{-}1) was added prior to TMPD injection.

Citrate synthase assay

The citrate synthase activity of cardiac homogenates were measured in frozen homogenates. Briefly, maximal activity (Vmax) was determined with a spectrophotometer at 37˚C with a Synergy HTX spectrophotometer (BioTek, UK) in assay buffer; 50 mM TRIS-HCl, pH 8.0. Citrate synthase activity was monitored in the presence or absence of oxaloacetate by the appearance of 5-thio-2-nitrobenzoic acid as a result of the reaction of free acetyl-CoA with 5,5'-dithiobis(2-nitrobenzoic acid) at 412 nm over a 10 min incubation period (assay buffer with 0.5 oxaloacetate, 0.3 mM acetyl-CoA, 0.15 mM 5,5-dithiobis-2-nitrobenzoic acid). Extinction coefficients were empirically determined to quantify Vmax values. Enzyme activities were normalised to total soluble protein, which was quantified according to Bradford (***Bradford, 1976***).

Western blots

Total cell protein was isolated from cells using protein extraction buffer (50 mM Tris, 150 mM NaCl, 1% TritonX-100, supplemented with protease inhibitors). Total protein was isolated from snap-frozen tissue using RIPA buffer supplemented with protease inhibitor cocktail after disruption using Lysing Matrix D tubes (MP Bio).

Electron Microscopy

All experiments were performed according to current UK Home Office regulations and under approval of the relevant University of Manchester (Manchester, UK) local ethics committee.

Six mice were used for this study (n = 3 control, n = 3 Bud 23 KO). Immediately after euthanasia, hearts were harvested and small portions (cubes with sides smaller than 0.5 mm) of right and left ventricle were immersion fixed in 2.5% glutaraldehyde and 2% paraformaldehyde in 100 mM sodium cacodylate buffer (pH 7.2) overnight. Specimen preparation was performed, with small modifications, according to the Ellisman protocol (***Holcomb et al., 2013***). Briefly, after washings in sodium cacodylate, samples were sequentially stained in: 2% osmium tetroxide and 1.5% potassium ferrocyanide in 100 mM sodium cacodylate for 1 hr; 1% aqueous thiocarbohydrazide for 20 min; 2% aqueous osmium for 30 min; 1% aqueous uranyl acetate overnight and Walton's lead aspartate for 30 min the following morning at 60˚C. Samples were washed 3 times for 10 min in double distilled water after each staining step. Staining was followed by dehydration in ethanol ascending series (50%, 70%, 90%, 100%) and infiltration with TAAB 812 hard resin mixed with propylene oxide. After embedding, resin blocks were cured at 70˚ C for 40 hr. Plastic blocks were sectioned at 80 nm thickness using a Leica UC6 ultramicrotome and sections were imaged using a FEI Tecnai12 Biotwin operated at 100kV. Images were analysed using Fiji (***Schindelin et al., 2012***).

Cell fractionation

Fractionation experiments were performed by differential centrifugation as previously described previously (**Rorbach et al., 2014**).

Data analysis and statistics

Unless otherwise stated in the figure legend, parametric data was analysed by ANOVA with a Dunnett's multiple comparisons test. Non-parametric data was analysed using a Mann-Whitney test. RNAseq data was analysed using edgeR (**Robinson et al., 2010**). For Mass Spectrometry data analysis please refer to the dedicated section.

Acknowledgements

We would like to acknowledge the University of Manchester Genomics technology facility; Michael Smiga, Leo Zeef, and Andy Hayes. The Biological Mass Spectrometry Core Research Facility for technical support. Carolyn Jones for technical support with polysome profiling. The University of Manchester electron microscopy core facility. DWR and ASL are Wellcome Investigators, Wellcome Trust (107849/Z/15/Z, 107851/Z/15/2).

Additional information

Funding

Funder	Grant reference number	Author
Medical Research Council	MR/L010240/1	David Ray

The funders had no role in study design, data collection and interpretation, or the decision to submit the work for publication.

Author contributions

Matthew Baxter, Conceptualization, Data curation, Formal analysis, Investigation, Visualization, Methodology, Writing - original draft, Writing - review and editing; Maria Voronkov, Data curation, Formal analysis, Investigation, Visualization, Methodology, Writing - original draft, Writing - review and editing; Toryn Poolman, Conceptualization, Data curation, Formal analysis, Methodology, Writing - review and editing; Gina Galli, Data curation, Formal analysis, Methodology, Writing - original draft; Christian Pinali, Data curation, Formal analysis, Methodology; Laurence Goosey, Data curation, Investigation; Abigail Knight, Karolina Krakowiak, Investigation; Robert Maidstone, Mudassar Iqbal, Formal analysis, Methodology; Min Zi, Formal analysis, Investigation, Methodology, Writing - original draft; Sukhpal Prehar, Formal analysis, Investigation, Methodology; Elizabeth J Cartwright, Formal analysis, Supervision, Methodology; Julie Gibbs, Conceptualization, Resources, Investigation, Project administration; Laura C Matthews, Conceptualization, Investigation; Antony D Adamson, Neil E Humphreys, Resources, Investigation, Methodology; Pedro Rebelo-Guiomar, Investigation, Methodology; Michal Minczuk, Supervision, Methodology; David A Bechtold, Supervision, Writing - original draft; Andrew Loudon, Conceptualization, Supervision, Funding acquisition, Writing - review and editing; David Ray, Conceptualization, Supervision, Funding acquisition, Writing - original draft, Project administration, Writing - review and editing

Author ORCIDs

Matthew Baxter https://orcid.org/0000-0002-3612-2574
Maria Voronkov https://orcid.org/0000-0001-5636-9892
Michal Minczuk http://orcid.org/0000-0001-8242-1420

Ethics

Animal experimentation: All experiments were carried out in strict accordance with the Animals (Scientific Procedures) Act 1986 (UK) and protocols were approved by an internal ethics committee at

the University of Manchester. Every effort was made to minimize suffering. Home office project licence 70/8768 and P3A97F3D1.

Decision letter and Author response
Decision letter https://doi.org/10.7554/eLife.50705.sa1
Author response https://doi.org/10.7554/eLife.50705.sa2

Additional files

Supplementary files

- Supplementary file 1. Primer sequences.

Data availability

RNAseq data have been deposited to ArrayExpress, under the accession code E-MTAB-8673. All proteomics data is included in the supporting files, and raw data have been deposited to PRIDE under the accession code PXD017019.

The following datasets were generated:

Author(s)	Year	Dataset title	Dataset URL	Database and Identifier
Maria Voronkov, Toryn Poolman, Gina Galli, Christian Pinali, Laurence Goosey, Abigail Knight, Karolina Krakowiak, Robert Maidstone, Mudassar Iqbal, Min Zi, Sukhpal Prehar, Elizabeth J Cartwright, Julie Gibbs, Laura C Matthews, Antony D Adamson, Neil E Humphreys, Pedro Rebelo-Guiomar, Michal Minczuk, David A Bechtold, Andrew Loudon, David Ray, Matthew Baxter	2020	Data from: Cardiac mitochondrial function depends on BUD23 mediated ribosome programming	https://www.ebi.ac.uk/arrayexpress/experiments/E-MTAB-8673/	ArrayExpress, E-MTAB-8673
Maria Voronkov, Toryn Poolman, Gina Galli, Christian Pinali, Laurence Goosey, Abigail Knight, Karolina Krakowiak, Robert Maidstone, Mudassar Iqbal, Min Zi, Sukhpal Prehar, Elizabeth J Cartwright, Julie Gibbs, Laura C Matthews, Antony D Adamson, Neil E Humphreys, Pedro Rebelo-Guiomar, Michal Minczuk, David A Bechtold, Andrew Loudon, David Ray, Matthew Baxter	2020	The role of Bud23 in mouse heart tissue	https://www.ebi.ac.uk/pride/archive/projects/PXD017019	PRIDE, PXD017019

References

Bassett AR, Tibbit C, Ponting CP, Liu JL. 2013. Highly efficient targeted mutagenesis of Drosophila with the CRISPR/Cas9 system. *Cell Reports* **4**:220–228. DOI: https://doi.org/10.1016/j.celrep.2013.06.020, PMID: 23827738

Bazett HC. 1997. An analysis of the time-relations of electrocardiograms. *Annals of Noninvasive Electrocardiology* **2**:177–194. DOI: https://doi.org/10.1111/j.1542-474X.1997.tb00325.x

Bourgeois G, Létoquart J, van Tran N, Graille M. 2017. Trm112, a protein activator of methyltransferases modifying actors of the eukaryotic translational apparatus. *Biomolecules* **7**:7. DOI: https://doi.org/10.3390/biom7010007

Bradford MM. 1976. A rapid and sensitive method for the quantitation of microgram quantities of protein utilizing the principle of protein-dye binding. *Analytical Biochemistry* **72**:248–254. DOI: https://doi.org/10.1016/0003-2697(76)90527-3, PMID: 942051

Brand MD, Nicholls DG. 2011. Assessing mitochondrial dysfunction in cells. *Biochemical Journal* **435**:297–312. DOI: https://doi.org/10.1042/BJ20110162

Carlson M. 2018. org.Hs.eg.db: Genome wide annotation for Human. *R Package*. 3.6.0.

Charif D, Lobry JR. 2007. *SeqinR 1.0-2: A Contributed Package to the R Project for Statistical Computing Devoted to Biological Sequences Retrieval and Analysis*. Springer. DOI: https://doi.org/10.1007/978-3-540-35306-5_10

Cox J, Mann M. 2008. MaxQuant enables high peptide identification rates, individualized p.p.b.-range mass accuracies and proteome-wide protein quantification. *Nature Biotechnology* **26**:1367–1372. DOI: https://doi.org/10.1038/nbt.1511, PMID: 19029910

Doll S, Dreßen M, Geyer PE, Itzhak DN, Braun C, Doppler SA, Meier F, Deutsch MA, Lahm H, Lange R, Krane M, Mann M. 2017. Region and cell-type resolved quantitative proteomic map of the human heart. *Nature Communications* **8**:1469. DOI: https://doi.org/10.1038/s41467-017-01747-2, PMID: 29133944

Gandin V, Sikström K, Alain T, Morita M, McLaughlan S, Larsson O, Topisirovic I. 2014. Polysome fractionation and analysis of mammalian translatomes on a genome-wide scale. *Journal of Visualized Experiments*. DOI: https://doi.org/10.3791/51455, PMID: 24893926

Gandin V, Masvidal L, Hulea L, Gravel SP, Cargnello M, McLaughlan S, Cai Y, Balanathan P, Morita M, Rajakumar A, Furic L, Pollak M, Porco JA, St-Pierre J, Pelletier J, Larsson O, Topisirovic I. 2016. nanoCAGE reveals 5′ UTR features that define specific modes of translation of functionally related MTOR-sensitive mRNAs. *Genome Research* **26**:636–648. DOI: https://doi.org/10.1101/gr.197566.115, PMID: 26984228

Goo S, Pham T, Han JC, Nielsen P, Taberner A, Hickey A, Loiselle D. 2013. Multiscale measurement of cardiac energetics. *Clinical and Experimental Pharmacology and Physiology* **40**:671–681. DOI: https://doi.org/10.1111/1440-1681.12139, PMID: 23745944

Haag S, Kretschmer J, Bohnsack MT. 2015. WBSCR22/Merm1 is required for late nuclear pre-ribosomal RNA processing and mediates N 7 -methylation of G1639 in human 18S rRNA . *RNA* **21**:180–187. DOI: https://doi.org/10.1261/rna.047910.114

Hernandez-Valladares M, Aasebø E, Mjaavatten O, Vaudel M, Bruserud Ø, Berven F, Selheim F. 2016. Reliable FASP-based procedures for optimal quantitative proteomic and phosphoproteomic analysis on samples from acute myeloid leukemia patients. *Biological Procedures Online* **18**:13. DOI: https://doi.org/10.1186/s12575-016-0043-0, PMID: 27330413

Holcomb PS, Hoffpauir BK, Hoyson MC, Jackson DR, Deerinck TJ, Marrs GS, Dehoff M, Wu J, Ellisman MH, Spirou GA. 2013. Synaptic inputs compete during rapid formation of the Calyx of held: a new model system for neural development. *Journal of Neuroscience* **33**:12954–12969. DOI: https://doi.org/10.1523/JNEUROSCI.1087-13.2013, PMID: 23926251

Itzhak DN, Tyanova S, Cox J, Borner GH. 2016. Global, quantitative and dynamic mapping of protein subcellular localization. *eLife* **5**:e16950. DOI: https://doi.org/10.7554/eLife.16950, PMID: 27278775

Jacob WA, Bakker A, Hertsens RC, Biermans W. 1994. Mitochondrial matrix granules: their behavior during changing metabolic situations and their relationship to contact sites between inner and outer mitochondrial membranes. *Microscopy Research and Technique* **27**:307–318. DOI: https://doi.org/10.1002/jemt.1070270406, PMID: 8186449

Jangani M, Poolman TM, Matthews L, Yang N, Farrow SN, Berry A, Hanley N, Williamson AJK, Whetton AD, Donn R, Ray DW. 2014. The methyltransferase WBSCR22/Merm1 enhances glucocorticoid receptor function and is regulated in lung inflammation and Cancer. *Journal of Biological Chemistry* **289**:8931–8946. DOI: https://doi.org/10.1074/jbc.M113.540906

Kanaan GN, Harper M-E. 2017. Cellular redox dysfunction in the development of cardiovascular diseases. *Biochimica Et Biophysica Acta (BBA) - General Subjects* **1861**:2822–2829. DOI: https://doi.org/10.1016/j.bbagen.2017.07.027

Kent WJ. 2002. BLAT—the BLAST-Like alignment tool. *Genome Research* **12**:656–664. DOI: https://doi.org/10.1101/gr.229202

Khajuria RK, Munschauer M, Ulirsch JC, Fiorini C, Ludwig LS, McFarland SK, Abdulhay NJ, Specht H, Keshishian H, Mani DR, Jovanovic M, Ellis SR, Fulco CP, Engreitz JM, Schütz S, Lian J, Gripp KW, Weinberg OK, Pinkus GS, Gehrke L, et al. 2018. Ribosome levels selectively regulate translation and lineage commitment in human hematopoiesis. *Cell* **173**:90–103. DOI: https://doi.org/10.1016/j.cell.2018.02.036, PMID: 29551269

Lazar C, Gatto L, Ferro M, Bruley C, Burger T. 2016. Accounting for the multiple natures of missing values in Label-Free quantitative proteomics data sets to compare imputation strategies. *Journal of Proteome Research* **15**:1116–1125. DOI: https://doi.org/10.1021/acs.jproteome.5b00981, PMID: 26906401

Létoquart J, Huvelle E, Wacheul L, Bourgeois G, Zorbas C, Graille M, Heurgué-Hamard V, Lafontaine DL. 2014. Structural and functional studies of Bud23-Trm112 reveal 18S rRNA N7-G1575 methylation occurs on late 40S precursor ribosomes. *PNAS* **111**:E5518–E5526. DOI: https://doi.org/10.1073/pnas.1413089111, PMID: 25489090

Lienig D, Forstner H. 1984. Aquatic and Physiological Applications. In: Gnaiger E (Ed). *Polarographic Oxygen Sensor*. **12** Heidelberg, Berlin: Springer Verlag. DOI: https://doi.org/10.1002/aheh.19840120411

Makrecka-Kuka M, Krumschnabel G, Gnaiger E. 2015. High-Resolution respirometry for simultaneous measurement of oxygen and hydrogen peroxide fluxes in permeabilized cells, tissue homogenate and isolated mitochondria. *Biomolecules* **5**:1319–1338. DOI: https://doi.org/10.3390/biom5031319, PMID: 26131977

Meijer HA, Thomas AA. 2002. Control of eukaryotic protein synthesis by upstream open reading frames in the 5'-untranslated region of an mRNA. *Biochemical Journal* **367**:1–11. DOI: https://doi.org/10.1042/bj20011706, PMID: 12117416

Mi H, Huang X, Muruganujan A, Tang H, Mills C, Kang D, Thomas PD. 2017. PANTHER version 11: expanded annotation data from gene ontology and reactome pathways, and data analysis tool enhancements. *Nucleic Acids Research* **45**:D183–D189. DOI: https://doi.org/10.1093/nar/gkw1138, PMID: 27899595

Morita M, Gravel SP, Chénard V, Sikström K, Zheng L, Alain T, Gandin V, Avizonis D, Arguello M, Zakaria C, McLaughlan S, Nouet Y, Pause A, Pollak M, Gottlieb E, Larsson O, St-Pierre J, Topisirovic I, Sonenberg N. 2013. mTORC1 controls mitochondrial activity and biogenesis through 4E-BP-dependent translational regulation. *Cell Metabolism* **18**:698–711. DOI: https://doi.org/10.1016/j.cmet.2013.10.001, PMID: 24206664

Morris CA. 1993. Williams syndrome. *GeneReviews*. https://www.ncbi.nlm.nih.gov/books/NBK1249/ [Accessed May 15, 2019].

Nakazawa Y, Arai H, Fujita N. 2011. The novel metastasis promoter Merm1/Wbscr22 enhances tumor cell survival in the vasculature by suppressing Zac1/p53-dependent apoptosis. *Cancer Research* **71**:1146–1155. DOI: https://doi.org/10.1158/0008-5472.CAN-10-2695, PMID: 21148752

Nichol PF, Botham R, Saijoh Y, Reeder AL, Zaremba KM. 2011. A more efficient method to generate null mutants using Hprt-Cre with floxed alleles. *Journal of Pediatric Surgery* **46**:1711–1719. DOI: https://doi.org/10.1016/j.jpedsurg.2011.01.023

Ott M, Gogvadze V, Orrenius S, Zhivotovsky B. 2007. Mitochondria, oxidative stress and cell death. *Apoptosis* **12**:913–922. DOI: https://doi.org/10.1007/s10495-007-0756-2, PMID: 17453160

Õunap K, Käsper L, Kurg A, Kurg R. 2013. The human WBSCR22 protein is involved in the biogenesis of the 40S ribosomal subunits in mammalian cells. *PLOS ONE* **8**:e75686. DOI: https://doi.org/10.1371/journal.pone.0075686, PMID: 24086612

Õunap K, Leetsi L, Matsoo M, Kurg R. 2015. The Stability of Ribosome Biogenesis Factor WBSCR22 Is Regulated by Interaction with TRMT112 via Ubiquitin-Proteasome Pathway. *PLOS ONE* **10**:e0133841. DOI: https://doi.org/10.1371/journal.pone.0133841

Palmer CS, Osellame LD, Stojanovski D, Ryan MT. 2011. The regulation of mitochondrial morphology: intricate mechanisms and dynamic machinery. *Cellular Signalling* **23**:1534–1545. DOI: https://doi.org/10.1016/j.cellsig.2011.05.021, PMID: 21683788

Pesta D, Gnaiger E. 2012. High-resolution respirometry: oxphos protocols for human cells and permeabilized fibers from small biopsies of human muscle. *Methods in Molecular Biology* **810**:25–58. DOI: https://doi.org/10.1007/978-1-61779-382-0_3, PMID: 22057559

Piquereau J, Caffin F, Novotova M, Lemaire C, Veksler V, Garnier A, Ventura-Clapier R, Joubert F. 2013. Mitochondrial dynamics in the adult cardiomyocytes: which roles for a highly specialized cell? *Frontiers in Physiology* **4**:102. DOI: https://doi.org/10.3389/fphys.2013.00102, PMID: 23675354

R Development Core Team. 2017. R: a language and environment for statistical computing. Vienna, Austria, https://www.R-project.org

Robinson MD, McCarthy DJ, Smyth GK. 2010. edgeR: a bioconductor package for differential expression analysis of digital gene expression data. *Bioinformatics* **26**:139–140. DOI: https://doi.org/10.1093/bioinformatics/btp616

Rorbach J, Boesch P, Gammage PA, Nicholls TJ, Pearce SF, Patel D, Hauser A, Perocchi F, Minczuk M. 2014. MRM2 and MRM3 are involved in biogenesis of the large subunit of the mitochondrial ribosome. *Molecular Biology of the Cell* **25**:2542–2555. DOI: https://doi.org/10.1091/mbc.e14-01-0014, PMID: 25009282

Schindelin J, Arganda-Carreras I, Frise E, Kaynig V, Longair M, Pietzsch T, Preibisch S, Rueden C, Saalfeld S, Schmid B, Tinevez JY, White DJ, Hartenstein V, Eliceiri K, Tomancak P, Cardona A. 2012. Fiji: an open-source platform for biological-image analysis. *Nature Methods* **9**:676–682. DOI: https://doi.org/10.1038/nmeth.2019, PMID: 22743772

Shannon P, Markiel A, Ozier O, Baliga NS, Wang JT, Ramage D, Amin N, Schwikowski B, Ideker T. 2003. Cytoscape: a software environment for integrated models of biomolecular interaction networks. *Genome Research* **13**:2498–2504. DOI: https://doi.org/10.1101/gr.1239303, PMID: 14597658

Sloan KE, Knox AA, Wells GR, Schneider C, Watkins NJ. 2019. Interactions and activities of factors involved in the late stages of human 18S rRNA maturation. *RNA Biology* **16**:196–210. DOI: https://doi.org/10.1080/15476286.2018.1564467

Somlyo AP, Somlyo AV, Devine CE, Peters PD, Hall TA. 1974. Electron microscopy and electron probe analysis of mitochondrial cation accumulation in smooth muscle. *The Journal of Cell Biology* **61**:723–742. DOI: https://doi.org/10.1083/jcb.61.3.723

Sonenberg N, Hinnebusch AG. 2009. Regulation of translation initiation in eukaryotes: mechanisms and biological targets. *Cell* **136**:731–745. DOI: https://doi.org/10.1016/j.cell.2009.01.042, PMID: 19239892

Szklarczyk D, Morris JH, Cook H, Kuhn M, Wyder S, Simonovic M, Santos A, Doncheva NT, Roth A, Bork P, Jensen LJ, von Mering C. 2017. The STRING database in 2017: quality-controlled protein-protein association networks, made broadly accessible. *Nucleic Acids Research* **45**:D362–D368. DOI: https://doi.org/10.1093/nar/gkw937, PMID: 27924014

Tyanova S, Temu T, Sinitcyn P, Carlson A, Hein MY, Geiger T, Mann M, Cox J. 2016. The perseus computational platform for comprehensive analysis of (prote)omics data. *Nature Methods* **13**:731–740. DOI: https://doi.org/10.1038/nmeth.3901

White J, Li Z, Sardana R, Bujnicki JM, Marcotte EM, Johnson AW. 2008. Bud23 methylates G1575 of 18S rRNA and is required for efficient nuclear export of pre-40S subunits. *Molecular and Cellular Biology* **28**:3151–3161. DOI: https://doi.org/10.1128/MCB.01674-07, PMID: 18332120

Whitnall M, Suryo Rahmanto Y, Sutak R, Xu X, Becker EM, Mikhael MR, Ponka P, Richardson DR. 2008. The MCK mouse heart model of friedreich's ataxia: Alterations in iron-regulated proteins and cardiac hypertrophy are limited by iron chelation. *PNAS* **105**:9757–9762. DOI: https://doi.org/10.1073/pnas.0804261105, PMID: 18621680

Wickham H. 2009. *Ggplot2 : Elegant Graphics for Data Analysis*. New York: Springer.

Wiśniewski JR, Hein MY, Cox J, Mann M. 2014. A "proteomic ruler" for protein copy number and concentration estimation without spike-in standards. *Molecular & Cellular Proteomics* **13**:3497–3506. DOI: https://doi.org/10.1074/mcp.M113.037309, PMID: 25225357

Zorbas C, Nicolas E, Wacheul L, Huvelle E, Heurgué-Hamard V, Lafontaine DL. 2015. The human 18S rRNA base methyltransferases DIMT1L and WBSCR22-TRMT112 but not rRNA modification are required for ribosome biogenesis. *Molecular Biology of the Cell* **26**:2080–2095. DOI: https://doi.org/10.1091/mbc.E15-02-0073, PMID: 25851604

References

Abreu, R. de S., Penalva, L. O., Marcotte, E. M., & Vogel, C. (2009). Global signatures of protein and mRNA expression levels. *Molecular BioSystems*. 5(12), 1512.

Aherne, W., Hull, D. (1966). Brown adipose tissue and heat production in the newborn infant. *The Journal of Pathology and Bacteriology*. 91(1), 223–234.

Anantharaman, V., Koonin, E. V., Aravind, L. (2002) SPOUT: a class of methyltransferases that includes spoU and trmD RNA methylase superfamilies, and novel superfamilies of predicted prokaryotic RNA methylases. *Journal of Molecular Microbiology and Biotechnology.* 4, 71-5.

Andersen, T. E., Porse, B. O. T., & Kirpekar, F. (2004). A novel partial modification at C2501 in Escherichia coli 23S ribosomal RNA. *RNA*. 10(6), 907.

Anderson, J., Phan, L., Cuesta, R., Carlson, B. A., Pak, M., Asano, K., Björk, G. R., Tamame, M., Hinnebusch, A. G. (1998) The essential Gcd10p-Gcd14p nuclear complex is required for 1-methyladenosine modification and maturation of initiator methionyl-tRNA. *Genes & Development.* 12, 3650-62.

Anglin, J. L., Song, Y. (2013) A medicinal chemistry perspective for targeting histone H3 lysine-79 methyltransferase DOT1L. *Journal of Medicinal Chemistry.* 56, 8972-83.

Apweiler, R., Hermjakob, H., Sharon, N. (1999) On the frequency of protein glycosylation, as deduced from analysis of the SWISS-PROT database. *Biochimica et Biophysica Acta.* 1473, 4-8.

Aravind, L., Abhiman, S., Iyer, L. M. (2011) Natural history of the eukaryotic chromatin protein methylation system. *Progress in Molecular Biology and Translational Science.* 101, 105-76.

Aravind, L., Iyer, L. M. (2003) Provenance of SET-domain histone methyltransferases through duplication of a simple structural unit. *Cell Cycle.* 2, 369-76.

Arena, S., Benvenuti, S., Bardelli, A. (2005) Genetic analysis of the kinome and phosphatome in cancer. *Cellular and Molecular Life Sciences.* 62, 2092-9.

Arpat, A. B., Liechti, A., Matos, M. De, Dreos, R., Janich, P., Gatfield, D. (2020). Transcriptome-wide sites of collided ribosomes reveal principles of translational pausing. *Genome Research*. 30(7), 985–999.

Bartelds, B., Gratama, J. W., Knoester, H., Takens, J., Smid, G. B., Aarnoudse, J. G., Heymans, H. S., Kuipers, J. R. (1998) Perinatal changes in myocardial supply and flux of fatty acids, carbohydrates, and ketone bodies in lambs. *American Journal of Physiology.* 274, H1962-9.

Bartelt, A., Bruns, O. T., Reimer, R., Hohenberg, H., Ittrich, H., Peldschus, K., Kaul, M. G., Tromsdorf, U. I., Weller, H., Waurisch, C., Eychmüller, A., Gordts, P. L., Rinninger, F., Bruegelmann, K., Freund, B., Nielsen, P., Merkel, M., Heeren, J. (2011). Brown adipose tissue activity controls triglyceride clearance. *Nature Medicine*. 17(2), 200–206.

Batista, P. J., Molinie, B., Wang, J., Qu, K., Zhang, J., Li, L., Bouley, D. M., Lujan, E., Haddad, B., Daneshvar, K., Carter, A. C., Flynn, R. A., Zhou, C., Lim, K. S., Dedon, P., Wernig, M., Mullen, A. C., Xing, Y., Giallourakis, C. C., Chang, H. Y. (2014) m(6)A RNA modification controls cell fate transition in mammalian embryonic stem cells. *Cell Stem Cell.* 15, 707-19.

Baxter, M., Voronkov, M., Poolman, T., Galli, G., Pinali, C., Goosey, L., Knight, A., Krakowiak, K., Maidstone, R., Iqbal, M., Zi, M., Prehar, S., Cartwright, E. J., Gibbs, J., Matthews, L. C., Adamson, A. D., Humphreys, N. E., Rebelo-Guiomar, P., Minczuk, M., Bechtold, B., Loudon, A., Ray, D. (2020). Cardiac mitochondrial function depends on BUD23 mediated ribosome programming. *ELife*, 9.

Bazett, H. C. (1997) An analysis of the time-relations of electrocardiograms. *Annals of Noninvasive Electrocardiology*. 2, 177-194.

Berbée, J. F., Boon, M. R., Khedoe, P. P., Bartelt, A., Schlein, C., Worthmann, A., Kooijman, S., Hoeke, G., Mol, I. M., John, C., Jung, C., Vazirpanah, N., Brouwers, L. P., Gordts, P. L., Esko, J. D., Hiemstra, P. S., Havekes, L. M., Scheja, L., Heeren, J., Rensen, P. C. (2015) Brown fat activation reduces hypercholesterolaemia and protects from atherosclerosis development. *Nature Communications*. 6.

Bhatt, P. R., Scaiola, A., Loughran, G., Leibundgut, M., Kratzel, A., Meurs, R., Dreos, R., O'Connor, K. M., McMillan, A., Bode, J. W., Thiel, V., Gatfield, D., Atkins, J. F., & Ban, N. (2021). Structural basis of ribosomal frameshifting during translation of the SARS-CoV-2 RNA genome. *Science*. 372(6548), 1306–1313.

Bickle, T. A., Krüger, D. H. (1993) Biology of DNA restriction. *Microbiological Reviews.* 57, 434-50.

Bidlingmaier, S., Liu, B. (2015) Identification of posttranslational modification-dependent protein interactions using yeast surface displayed human proteome libraries. *Methods in Molecular Biology.* 1319, 193-202.

Biggar, K. K., Li, S. S. (2015) Non-histone protein methylation as a regulator of cellular signalling and function. *Nature Reviews Molecular Cell Biology.* 16, 5-17.

Birkedal, U., Christensen-Dalsgaard, M., Krogh, N., Sabarinathan, R., Gorodkin, J., Nielsen, H. (2015). Profiling of ribose methylations in RNA by high-throughput sequencing. *Angewandte Chemie International Edition*. 54(2), 451–455.

Blondin, D. P., Frisch, F., Phoenix, S., Guérin, B., Turcotte, É. E., Haman, F., Richard, D., Carpentier, A. C. (2017). Inhibition of intracellular triglyceride lipolysis suppresses cold-induced brown adipose tissue metabolism and increases shivering in humans. *Cell Metabolism*. 25(2), 438–447.

Botros, H. G., Legrand, P., Pagan, C., Bondet, V., Weber, P., Ben-Abdallah, M., Lemière, N., Huguet, G., Bellalou, J., Maronde, E., Beguin, P., Haouz, A., Shepard, W., & Bourgeron, T. (2013). Crystal structure and functional mapping of human ASMT, the last enzyme of the melatonin synthesis pathway. *Journal of Pineal Research*. 54(1), 46–57.

Bouillaud, F., Combes-George, M., Ricquier, D. (1983) Mitochondria of adult human brown adipose tissue contain a 32 000-Mr uncoupling protein. *Bioscience Reports.* 3(8):775-80.

Boye, E., Løbner-Olesen, A. (1990) The role of dam methyltransferase in the control of DNA replication in E. coli. *Cell.* 62, 981-9.

Brinkman, E. K., Chen, T., Amendola, M., & van Steensel, B. (2014). Easy quantitative assessment of genome editing by sequence trace decomposition. *Nucleic Acids Research*. 42(22), e168–e168.

Bristow, J., Bier, D. M., Lange, L. G. (1987) Regulation of adult and fetal myocardial phosphofructokinase. Relief of cooperativity and competition between fructose 2,6-bisphosphate, ATP, and citrate. *Journal of Biological Chemistry.* 262, 2171-5.

Bujnicki, J. M. (1999) Comparison of protein structures reveals monophyletic origin of the AdoMet-dependent methyltransferase family and mechanistic convergence rather than recent differentiation of N4-cytosine and N6-adenine DNA methylation. *In Silico Biology.* 1, 175-82.

Burdge, G. C., Wright, P., Jones, A. E., & Wootton, S. A. (2000). A method for separation of phosphatidylcholine, triacylglycerol, non-esterified fatty acids and cholesterol esters from plasma by solid-phase extraction. *British Journal of Nutrition*. 84(5), 781–787.

Cai, L., Sutter, B. M., Li, B., Tu, B. P. (2011) Acetyl-CoA induces cell growth and proliferation by promoting the acetylation of histones at growth genes. *Molecular Cell*. 42, 426-37.

Campaner, S., Spreafico, F., Burgold, T., Doni, M., Rosato, U., Amati, B., Testa, G. (2011) The methyltransferase Set7/9 (Setd7) is dispensable for the p53-mediated DNA damage response in vivo. *Molecular Cell.* 43, 681-8.

Cantara, W., Crain, P., Rozenski, J., McCloskey, J., Harris, K., Zhang, X., Vendeix, F., Fabris, D., Agris, P. (2011). The RNA Modification Database, RNAMDB: 2011 update. *Nucleic Acids Research*. 39.

Cao, W., Medvedev, A. V., Daniel, K. W., & Collins, S. (2001). β-Adrenergic activation of p38 MAP kinase in adipocytes: cAMP induction of the uncoupling protein 1 (UCP1) gene requires p38 map kinase. *Journal of Biological Chemistry*. 276(29), 27077–27082.

Cao, X. J., Arnaudo, A. M., Garcia, B. A. (2013) Large-scale global identification of protein lysine methylation in vivo. *Epigenetics*. 8, 477-85.

Chau, V., Tobias, J. W., Bachmair, A., Marriott, D., Ecker, D. J., Gonda, D. K., Varshavsky, A. (1989) A multiubiquitin chain is confined to specific lysine in a targeted short-lived protein. *Science*. 243, 1576-83.

Chawla, M., Oliva, R., Bujnicki, J. M., Cavallo, L. (2015) An atlas of RNA base pairs involving modified nucleobases with optimal geometries and accurate energies. *Nucleic Acids Research.* 43, 6714-29.

Chen, L., Chen, K., Lavery, L. A., Baker, S. A., Shaw, C. A., Li, W., Zoghbi, H. Y. (2015) MeCP2 binds to non-CG methylated DNA as neurons mature, influencing transcription and the timing of onset for Rett syndrome. *Proceedings of the National Academy of Sciences of the United States of America.* 112, 5509-14.

Chen, D., Meng, L., Pei, F., Zheng, Y., Leng, J. (2017) A review of DNA methylation in depression. *Journal of Clinical Neuroscience.* 43, 39-46.

Cheng, Z., Mugler, C. F., Keskin, A., Hodapp, S., Chan, L. Y. L., Weis, K., Mertins, P., Regev, A., Jovanovic, M., & Brar, G. A. (2019). Small and large ribosomal subunit deficiencies lead to distinct gene expression signatures that reflect cellular growth rate. *Molecular Cell*. 73(1), 36-47.e10.

Choi, Y. C., Busch, H. (1978) Modified nucleotides in T1 RNase oligonucleotides of 18S ribosomal RNA of the Novikoff hepatoma. *Biochemistry.* 17, 2551-60.

Christiansen, M. N., Chik, J., Lee, L., Anugraham, M., Abrahams, J. L., Packer, N. H. (2014) Cell surface protein glycosylation in cancer. *Proteomics*. 14, 525-46.

Cinti, S. (2005). The adipose organ. *Prostaglandins, Leukotrienes and Essential Fatty Acids*. 73(1), 9–15.

Clubb, F.J. Jr, Bishop, S.P. (1984) Formation of binucleated myocardial cells in the neonatal rat. An index for growth hypertrophy*. Laboratory Investigation.* May;50(5):571-7.

Cohen, P. (2000) The regulation of protein function by multisite phosphorylation - a 25 year update. *Trends in Biochemical Sciences.* 25, 596-601.

Coulondre, C., Miller, J. H., Farabaugh, P. J., Gilbert, W. (1978) Molecular basis of base substitution hotspots in Escherichia coli. *Nature.* 274, 775-80.

Cox, J., Mann., M. (2008) MaxQuant enables high peptide identification rates, individualized p.p.b.-range mass accuracies and proteome-wide protein quantification. *Nature Biotechnology.* 26, 1367-1372.

Cui, K., Yao, Q., Li, S., Ding, X., Lu, Q., Mao, H., Liu, L., Zheng, N., Chen, S., Shao, F. (2010) Glutamine deamidation and dysfunction of ubiquitin/NEDD8 induced by a bacterial effector family. *Science*. 329, 1215-8.

Cypess, A. M., Lehman, S., Williams, G., Tal, I., Rodman, D., Goldfine, A. B., Kuo, F. C., Palmer, E. L., Tseng, Y.-H., Doria, A., Kolodny, G. M., & Kahn, C. R. (2009). Identification and importance of brown adipose tissue in adult humans. *New England Journal of Medicine*. 360(15), 1509–1517.

Daigle, S. R., Olhava, E. J., Therkelsen, C. A., Basavapathruni, A., Jin, L., Boriack-Sjodin, P. A., Allain, C. J., Klaus, C. R., Raimondi, A., Scott, M. P., Waters, N. J., Chesworth, R., Moyer, M. P., Copeland, R. A., Richon, V. M., Pollock, R. M. (2013) Potent inhibition of DOT1L as treatment of MLL-fusion leukemia. *Blood.* 122, 1017-25.

Daigle, S. R., Olhava, E. J., Therkelsen, C. A., Majer, C. R., Sneeringer, C. J., Song, J., Johnston, L. D., Scott, M. P., Smith, J. J., Xiao, Y., Jin, L., Kuntz, K. W., Chesworth, R., Moyer, M. P., Bernt, K. M., Tseng, J. C., Kung, A. L., Armstrong, S. A., Copeland, R. A., Richon, V. M., Pollock, R. M. (2011) Selective killing of mixed lineage leukemia cells by a potent small-molecule DOT1L inhibitor. *Cancer Cell.* 20, 53-65.

Das, K., Acton, T., Chiang, Y., Shih, L., Arnold, E., Montelione, G. T. (2004) Crystal structure of RlmAI: implications for understanding the 23S rRNA G745/G748-methylation at the macrolide antibiotic-binding site. *Proceedings of the National Academy of Sciences of the United States of America.* 101, 4041-6.

de Jesus, L. A., Carvalho, S. D., Ribeiro, M. O., Schneider, M., Kim, S.-W., Harney, J. W., Larsen, P. R., & Bianco, A. C. (2001). The type 2 iodothyronine deiodinase is essential for adaptive thermogenesis in brown adipose tissue. *Journal of Clinical Investigation*. 108(9), 1379.

De Smet, C., Lurquin, C., Lethé, B., Martelange, V., Boon, T. (1999) DNA methylation is the primary silencing mechanism for a set of germ line- and tumor-specific genes with a CpG-rich promoter. *Molecular and Cellular Biology.* 19, 7327-35.

Deaton, A. M., Bird, A. (2011) CpG islands and the regulation of transcription. *Genes & Development.* 25, 1010-22.

Dhaka, A., Viswanath, V., Patapoutian, A. (2006) Trp ion channels and temperature sensation. *Annual Review of Neuroscience*. 29, 135–161.

Dhami, G. K., Liu, H., Galka, M., Voss, C., Wei, R., Muranko, K., Kaneko, T., Cregan, S. P., Li, L., Li, S. S. (2013) Dynamic methylation of Numb by Set8 regulates its binding to p53 and apoptosis. *Molecular Cell.* 50, 565-76.

Dillon, S. C., Zhang, X., Trievel, R. C., Cheng, X. (2005) The SET-domain protein superfamily: protein lysine methyltransferases. *Genome Biology.* 6, 227.

Doi, A., Park, I. H., Wen, B., Murakami, P., Aryee, M. J., Irizarry, R., Herb, B., Ladd-Acosta, C., Rho, J., Loewer, S., Miller, J., Schlaeger, T., Daley, G. Q., Feinberg, A. P. (2009) Differential methylation of tissue- and cancer-specific CpG island shores distinguishes human induced pluripotent stem cells, embryonic stem cells and fibroblasts. *Nature Genetics.* 41, 1350-3.

Doll, S., Burlingame, A. L. (2015) Mass spectrometry-based detection and assignment of protein posttranslational modifications. *ACS Chemical Biology*. 10, 63-71.

Doll, S., Dreßen, M., Geyer, P. E., Itzhak, D. N., Braun, C., Doppler, S. A., Meier, F., Deutsch, M.-A., Lahm, H., Lange, R., Krane, M., & Mann, M. (2017). Region and cell-type resolved quantitative proteomic map of the human heart. *Nature Communications*. 8(1), 1469.

Dominissini, D., Moshitch-Moshkovitz, S., Schwartz, S., Salmon-Divon, M., Ungar, L., Osenberg, S., Cesarkas, K., Jacob-Hirsch, J., Amariglio, N., Kupiec, M., Sorek, R., Rechavi, G. (2012) Topology of the human and mouse m6A RNA methylomes revealed by m6A-seq. *Nature.* 485, 201-6.

Dong, C., Mao, Y., Tempel, W., Qin, S., Li, L., Loppnau, P., Huang, R., & Min, J. (2015). Structural basis for substrate recognition by the human N-terminal methyltransferase 1. *Genes & Development*. 29(22), 2343–2348.

Eichler, J., Adams, M. W. (2005) Posttranslational protein modification in Archaea. *Microbiology and Molecular Biology Reviews.* 69, 393-425.

Ellis, J. M., Li, L. O., Wu, P.-C., Koves, T. R., Ilkayeva, O., Stevens, R. D., Watkins, S. M., Muoio, D. M., & Coleman, R. A. (2010). Adipose acyl-CoA synthetase-1 directs fatty acids toward β-oxidation and is required for cold thermogenesis. *Cell Metabolism*. 12(1), 53–64.

Emorine, L. J., Marullo, S., Briend-Sutren, M. M., Patey, G., Tate, K., Delavier-Klutchko, C., & Strosberg, A. D. (1989). Molecular characterization of the human β3-adrenergic receptor. *Science*. 245(4922), 1118–1121.

Enerbäck, S., Jacobsson, A., Simpson, E. M., Guerra, C., Yamashita, H., Harper, M. E., Kozak, L. P. (1997). Mice lacking mitochondrial uncoupling protein are cold-sensitive but not obese. *Nature*. 387(6628), 90–94.

Ernst, J., Kellis, M. (2010) Discovery and characterization of chromatin states for systematic annotation of the human genome. *Nature Biotechnology.* 28, 817-25.

Esteller, M. (2007) Epigenetic gene silencing in cancer: the DNA hypermethylome. *Human Molecular Genetics.* 16, R50-9.

Fedorenko, A., Lishko, P. V., & Kirichok, Y. (2012). Mechanism of fatty-acid-dependent UCP1 uncoupling in brown fat mitochondria. *Cell*. 151(2), 400

Feng, Q., Wang, H., Ng, H. H., Erdjument-Bromage, H., Tempst, P. Struhl, K., Zhang, Y. (2002) Methylation of H3-lysine 79 is mediated by a new family of HMTases without a SET domain. *Current Biology.* 12, 1052-8.

Ferrell, J. E. Jr. (1996) Tripping the switch fantastic: how a protein kinase cascade can convert graded inputs into switch-like outputs. *Trends in Biochemical Sciences.* 21, 460-6.

Figaro, S., Wacheul, L., Schillewaert, S., Graille, M., Huvelle, E., Mongeard, R., Zorbas, C., Lafontaine, D. L., Heurdué-Hamard, V. (2012) Trm112 is required for Bud23-mediated methylation of the 18S rRNA at position G1575. *Molecular and Cellular Biology.* 32, 2254-67.

Fischle, W., Tseng, B. S., Dormann, H. L., Ueberheide, B. M., Garcia, B. A., Shabanowitz, J., Hunt, D. F., Funabiki, H., Allis, C. D. (2005) Regulation of HP1-chromatin binding by histone H3 methylation and phosphorylation. *Nature*. 438, 1116-22.

Folch, J., Lees, M., Sloane Stanley, G. H. (1957) A simple method for the isolation and purification of total lipides from animal tissues. *Journal of Biological Chemistry.* 226(1):497-509

Fraga, M. F., Ballestar, E., Villar-Garea, A., Boix-Chornet, M., Espada, J., Schotta, G., Bonaldi, T., Haydon, C., Ropero, S., Petrie, K., Iyer, N. G., Pérez-Rosado, A., Calvo, E., Lopez, J. A., Cano, A., Calasanz, M. J. Colomer, D., Piris, M. A., Ahn, N., Imhof, A., Caldas, C., Jenuwein, T., Esteller, M. (2005) Loss of acetylation at Lys16 and trimethylation at Lys20 of histone H4 is a common hallmark of human cancer. *Nature Genetics.* 37, 391-400.

Fujiki, K., Kano, F., Shiota, K., Murata, M. (2009) Expression of the peroxisome proliferator activated receptor gamma gene is repressed by DNA methylation in visceral adipose tissue of mouse models of diabetes. *BMC Biology.* 7, 38.

Fustin, J. M., Doi, M., Yamaguchi, Y., Hida, H., Nishimura, S., Yoshida, M., Isagawa, T., Morioka, M. S., Kakeya, H., Manabe, I., Okamura, H. (2013)

RNA-methylation-dependent RNA processing controls the speed of the circadian clock. *Cell.* 155, 793-806.

Gesta, S., Tseng, Y., Kahn, C. (2007) Developmental origin of fat: tracking obesity to its source. *Cell*. 131(2), 242–256.

Goelz, S. E., Vogelstein, B., Hamilton, S. R., Feinberg, A. P. (1985) Hypomethylation of DNA from benign and malignant human colon neoplasms. *Science*. 228, 187-90.

Greer, E. L., Beese-Sims, S. E., Brookes, E., Spadafora, R., Zhu, Y., Rothbart, S. B., Aristizábal-Corrales, D., Chen, S., Badeaux, A. I., Jin, Q., Wang, W., Strahl, B. D., Colaiácovo, M. P., Shi, Y. (2014) A histone methylation network regulates transgenerational epigenetic memory in C. elegans. *Cell Reports.* 7, 113-26.

Grimpo, K., Völker, M. N., Heppe, E. N., Braun, S., Heverhagen, J. T., & Heldmaier, G. (2014). Brown adipose tissue dynamics in wild-type and UCP1-knockout mice: in vivo insights with magnetic resonance. *Journal of Lipid Research*. 55(3), 398.

Grzeschik, K. H., Doll, A. (2001) Characterization of two novel genes, WBSCR20 and WBSCR22, deleted in Williams-Beuren syndrome. *Cytogenetic and Genome Research.* 95, 20-7.

Gunawardena, J. (2005) Multisite protein phosphorylation makes a good threshold but can be a poor switch. *Proceedings of the National Academy of Sciences of the United States of America*. 102, 14617-22.

Haag, S., Warda, A. S., Kretschmer, J., Günnigmann, M. A., Höbartner, C., Bohnsack, M. T. (2015) NSUN6 is a human RNA methyltransferase that catalyzes formation of m5C72 in specific tRNAs. *RNA.* 21, 1532-43.

Heaton, J. M. (1972). The distribution of brown adipose tissue in the human. *Journal of Anatomy*. 112(Pt 1), 35.

Held, N. M., Kuipers, E. N., van Weeghel, M., van Klinken, J. B., Denis, S. W., Lombès, M., Wanders, R. J., Vaz, F. M., Rensen, P. C. N., Verhoeven, A. J., Boon, M. R., Houtkooper, R. H. (2018). Pyruvate dehydrogenase complex plays a central role in brown adipocyte energy expenditure and fuel utilization during short-term beta-adrenergic activation. *Scientific Reports*. 8(1).

Hellman, A., Chess, A. (2007) Gene body-specific methylation on the active X chromosome. *Science*. 315, 1141-3.

Henras, A. K., Soudet, J., Gérus, M., Lebaron, S., Caizergues-Ferrer, M., Mougin, A., Henry, Y. (2008) The post-transcriptional steps of eukaryotic ribosome biogenesis. *Cellular and Molecular Life Sciences.* 65, 2334-59.

Hernandez-Valladares, M., Aasebø, E., Mjaavatten, O., Vaudel, M., Bruserus, Ø, Berven, F., Selheim, F. (2016) Reliable FASP-based procedures for optimal quantitative proteomic and phosphoproteomic analysis on samples from acute myeloid leukemia patients. *Biological Procedures Online.* 18, 13.

Hew, K. W., Keller, K. A. (2003) Postnatal anatomical and functional development of the heart: a species comparison. *Birth Defects Research Part B: Developmental and Reproductive Toxicology.* 68, 309-20.

Heymann, M. A., Rudolph, A. M. (1975) Control of the ductus arteriosus. *Physiological Reviews.* 55, 62-78.

Hoerter, J. A., Kuznetsov, A., Ventura-Clapier, R. (1991) Functional development of the creatine kinase system in perinatal rabbit heart. *Circulation Research.* 69, 665-76.

Horwich, M. D., Li, C., Matranga, C., Vagin, V., Farley, G., Wang, P., Zamore, P. D. (2007) The Drosophila RNA methyltransferase, DmHen1, modifies germline piRNAs and single-stranded siRNAs in RISC. *Current Biology.* 17, 1265-72.

Huang, J., Dorsey, J., Chuikov, S., Pérez-Burgos, L., Zhang, X., Jenuwein, T., Reinberg, D., Berger, S. L. (2010) G9a and Glp methylate lysine 373 in the tumor suppressor p53. *Journal of Biological Chemistry.* 285, 9636-41.

Huang, J., Perez-Burgos, L., Placek, B. J., Sengupta, R., Richter, M., Dorsey, J. A., Kubicek, S., Opravil, S., Jenuwein, T., Berger, S. L. (2006) Repression of p53 activity by Smyd2-mediated methylation. *Nature.* 444, 629-32.

Hui, S., Ghergurovich, J. M., Morscher, R. J., Jang, C., Teng, X., Lu, W., Esparza, L. A., Reya, T., Le Zhan, Yanxiang Guo, J., White, E., Rabinowitz, J. D. (2017). Glucose feeds the TCA cycle via circulating lactate. *Nature*. 551(7678), 115–118.

Huttunen, P., Hirvonen, J., Kinnula, V. (1981) The occurrence of brown adipose tissue in outdoor workers. *European Journal of Applied Physiology and Occupational Physiology.* 46(4):339-45.

Irizarry, R. A., Ladd-Acosta, C., Wen, B., Wu, Z., Montano, C., Onyango, P., Cui, H., Gabo, K., Rongione, M., Webster, M., Ji, H., Potash, J., Sabunciyan, S., Feinberg, A. P. (2009) The human colon cancer methylome shows similar hypo- and hypermethylation at conserved tissue-specific CpG island shores. *Nature Genetics.* 41, 178-86.

Ingolia, N. T., Ghaemmaghami, S., Newman, J. R. S., & Weissman, J. S. (2009). Genome-wide analysis in vivo of translation with nucleotide resolution using ribosome profiling. *Science*. 324(5924), 218–223.

Irshad, Z., Dimitri, F., Christian, M., Zammit, V. A. (2017) Diacylglycerol acyltransferase 2 links glucose utilization to fatty acid oxidation in the brown adipocytes. *Journal of Lipid Research*. 58(1), 15–30.

Ito, Y., Koessler, T., Ibrahim, A. E., Rai, S., Vowler, S. L., Abu-Amero, S., Silva, A. L., Maia, A. T., Huddleston, J. E., Uribe-Lewis, S., Woodfine, K., Jagodic, M., Nativio, R., Dunning, A., Moore, G., Klenova, E., Bingham, S., Pharoah, P. D., Brenton, J. D., Beck, S., Sandhu, M. S., Murrell, A. (2008) Somatically acquired hypomethylation of IGF2 in breast and colorectal cancer. *Human Molecular Genetics*. 17, 2633-43.

Itzhak, D., Tyanova, S., Cox, J., Borner, G. (2016) Global, quantitative and dynamic mapping of protein subcellular localization. *eLife.* 5:e16950

Jackman, J. E., Alfonzo, J. D. (2013). Transfer RNA modifications: Nature's combinatorial chemistry playground. *Wiley Interdisciplinary Reviews. RNA*. 4(1), 35.

Jacob, W., Bakker, A., Hertsens, R., Biermans, W. (1994) Mitochondrial matrix granules: Their behavior during changing metabolic situations and their relationship to contact sites between inner and outer mitochondrial membranes. *Microscopy Research & Technique.* 27:307–318.

Jakobsson, M. E., Małecki, J. M., Halabelian, L., Nilges, B. S., Pinto, R., Kudithipudi, S., Munk, S., Davydova, E., Zuhairi, F. R., Arrowsmith, C. H., Jeltsch, A., Leidel, S. A., Olsen, J. V., & Falnes, P. Ø. (2018). The dual methyltransferase METTL13 targets N terminus and Lys55 of eEF1A and modulates codon-specific translation rates. *Nature Communications.* 9*:1*, *9*(1), 1–15.

Jangani, M., Poolman, T. M., Matthews, L., Yang, N., Farrow, S. N., Berry, A., Hanley, N., Williamson, A. J., Whetton, A. D., Donn, R., Ray, D. W. (2014) The methyltransferase WBSCR22/Merm1 enhances glucocorticoid receptor function and is regulated in lung inflammation and cancer. *Journal of Biological Chemistry*. 289, 8931-46.

Jensen, O. N. (2006) Interpreting the protein language using proteomics. *Nature Reviews Molecular Cell Biology.* 7, 391-403.

Jin, L., Pahuja, K. B., Wickliffe, K. E., Gorur, A., Baumgärtel, C., Schekman, R., Rape, M. (2012) Ubiquitin-dependent regulation of COPII coat size and function. *Nature*. 482, 495-500.

Jin, L., Williamson, A., Banerjee, S., Philipp, I., Rape, M. (2008) Mechanism of ubiquitin-chain formation by the human anaphase-promoting complex. *Cell*. 16, 653-65.

Johansen, O., Ma, T., Hansen, J. B., Markussen, L. K., Schreiber, R., Reverte-Salisa, L., Dong, H., Christensen, D. P., Sun, W., Gnad, T., Karavaeva, I., Nielsen, T. S., Kooijman, S., Cero, C., Dmytriyeva, O., Shen,

Y., Razzoli, M., O'Brien, S. L., Kuipers, E. N., … Gerhart-Hines, Z. (2021). Lipolysis drives expression of the constitutively active receptor GPR3 to induce adipose thermogenesis. *Cell*. 184(13), 3502–3518.

Jumper, J., Evans, R., Pritzel, A., Green, T., Figurnov, M., Ronneberger, O., Tunyasuvunakool, K., Bates, R., Žídek, A., Potapenko, A., Bridgland, A., Meyer, C., Kohl, S. A. A., Ballard, A. J., Cowie, A., Romera-Paredes, B., Nikolov, S., Jain, R., Adler, J., Back, T., Petersen, S., Reiman, D., Clancy, E., Zielinski, M., Steinegger, M., Pacholska, M., Berghammer, T., Silver, D., Vinyals, O., Senior, A. W., Kavukcuoglu, K., Kohli, P., Hassabis, D. (2021) Applying and improving AlphaFold at CASP14. *Proteins.* Oct 2. doi: 10.1002/prot.26257.

Jurianz, K., Ziegler, S., Garcia-Schüler, H., Kraus, S., Bohana-Kashtan, O., Fishelson, Z., Kirschfink, M. (1999) Complement resistance of tumor cells: basal and induced mechanisms. *Molecular Immunology.* 36, 929-39.

Kacem, S., Feil, R. (2009) Chromatin mechanisms in genomic imprinting. *Mammalian Genome.* 20, 544-56.

Kaelin, W. G. Jr., McKnight, S. L. (2013) Influence of metabolism on epigenetics and disease. *Cell.* 153, 56-69.

Kajstura, J., Leri, A., Finato, N., Di Loreto, C., Beltrami, C. A., Anversa, P. (1998) Myocyte proliferation in end-stage cardiac failure in humans. *Proceedings of the National Academy of Sciences of the United States of America*. 95, 8801-5.

Kaniskan, H. Ü., Konze, K. D., Jin, J. (2015) Selective inhibitors of protein methyltransferases. *Journal of Medicinal Chemistry.* 58, 1596-629.

Katoh, Y., Ikura, T., Hoshikawa, Y., Tashiro, S., Ito, T., Ohta, M., Kera, Y., Noda, T., Igarashi, K. (2011) Methionine adenosyltransferase II serves as a transcriptional corepressor of Maf oncoprotein. *Molecular Cell.* 41, 554-66.

Kazak, L., Chouchani, E. T., Stavrovskaya, I. G., Lu, G. Z., Jedrychowski, M. P., Egan, D. F., Kumari, M., Kong, X., Erickson, B. K., Szpyt, J., Rosen, E. D., Murphy, M. P., Kristal, B. S., Gygi, S. P., Spiegelman, B. M. (2017) UCP1 deficiency causes brown fat respiratory chain depletion and sensitizes mitochondria to calcium overload-induced dysfunction. *Proceedings of the National Academy of Sciences of the United States of America.* 114(30):7981-7986.

Keown, C. L., Berletch, J. B., Castanon, R., Nery, J. R., Disteche, C. M., Ecker, J. R., Mukamel, E. A. (2017) Allele-specific non-CG DNA methylation marks domains of active chromatin in female mouse brain. *Proceedings of the National Academy of Sciences of the United States of America.* 114, E2882-90.

Khaitovich, P., Tenson, T., Kloss, P., Mankin, A. S. (1999) Reconstitution of functionally active Thermus aquaticus large ribosomal subunits with in vitro-transcribed rRNA. *Biochemistry.* 38, 1780-8.

Khedoe, P. P., Hoeke, G., Kooijman, S., Dijk, W., Buijs, J. T., Kersten, S., Havekes, L. M., Hiemstra, P. S., Berbée, J. F., Boon, M. R., Rensen, P. C. (2015). Brown adipose tissue takes up plasma triglycerides mostly after lipolysis. *Journal of Lipid Research*. 56(1), 51–59.

Khoury, G. A., Baliban, R. C., Floudas, C. A. (2011) Proteome-wide post-translational modification statistics: frequency analysis and curation of the swiss-prot database. *Scientific Reports.* 1:90, 1-5.

Kim, E., Kim, M., Woo, D. H., Shin, Y., Shin, J., Chang, N., Oh, Y. T., Kim, H., Rheey, J., Nakano, I., Lee, C., Joo, K. M., Rich, J. N., Nam, D. H., Lee, J. (2013) Phosphorylation of EZH2 activates STAT3 signaling via STAT3 methylation and promotes tumorigenicity of glioblastoma stem-like cells. *Cancer Cell.* 23, 839-52.

Klevecz, R. R., Bolen, J., Forrest, G., Murray, D. B. (2004) A genomewide oscillation in transcription gates DNA replication and cell cycle. *Proceedings of the National Academy of Sciences of the United States of America.* 101, 1200-5.

Koeth, R. A., Kalantar-Zadeh, K., Wang, Z., Fu, X., Tang, W. H., Hazen, S. L. (2013) Protein carbamylation predicts mortality in ESRD. *Journal of the American Society of Nephrology.* 24, 853-61.

Kornblihht, A. R. (2006) Chromatin, transcript elongation and alternative splicing. *Nature Structural & Molecular Biology.* 13, 5-7.

Kotzbeck, P., Giordano, A., Mondini, E., Murano, I., Severi, I., Venema, W., Cecchini, M. P., Kershaw, E. E., Barbatelli, G., Haemmerle, G., Zechner, R., & Cinti, S. (2018). Brown adipose tissue whitening leads to brown adipocyte death and adipose tissue inflammation. *Journal of Lipid Research*. 59(5), 784.

Kouzarides, T. (2007) Chromatin modifications and their function. *Cell.* 128, 693-705.

Koyano, F., Okatsu, K., Kosako, H., Tamura, Y., Go, E., Kimura, M., Kimura, Y., Tsuchiya, H., Yoshihara, H., Hirokawa, T., Endo, T., Fon, E. A., Trempe, J. F., Saeki, Y., Tanaka, K., Matsuda, N. (2014) Ubiquitin is phosphorylated by PINK1 to activate parkin. *Nature.* 510, 162-6.

Koziol, M. J., Bradshaw, C. R., Allen, G. E., Costa, A. S. H., Frezza, C., Gurdon, J. B. (2016) Identification of methylated deoxyadenosines in vertebrates reveals diversity in DNA modifications. *Nature Structural & Molecular Biology.* 23, 24-30.

Kriaucionis, S., Heintz, N. (2009) The nuclear DNA base 5-hydroxymethylcytosine is present in Purkinje neurons and the brain. *Science*. 324, 929-30.

Krishna, R. G., Wold, F. (1993) Post-translational modification of proteins. *Advances in Enzymology and Related Areas of Molecular Biology.* 67, 265-98.

Kuipers, E. N., Held, N. M., In Het Panhuis, W., Modder, M., Ruppert, P. M. M., Kersten, S., Kooijman, S., Guigas, B., Houtkooper, R. H., Rensen, P. C. N., Boon, M. R. (2019). A single day of high-fat diet feeding induces lipid accumulation and insulin resistance in brown adipose tissue in mice. *American Journal of Physiology. Endocrinology and Metabolism*. 317(5), E820–E830.

Labbé, S., Caron, A., Bakan, I., Laplante, M., Carpentier, A., Lecomte, R., Richard, D. (2015). In vivo measurement of energy substrate contribution to cold-induced brown adipose tissue thermogenesis. *The FASEB Journal*. 29(5), 2046–2058.

Larsen, F., Gundersen, G., Lopez, R., Prydz, H. (1992) CpG islands as gene markers in the human genome. *Genomics.* 13, 1095-107.

Lapko, V. N., Smith, D. L., Smith, J. B. (2001) In vivo carbamylation and acetylation of water-soluble human lens alphaB-crystallin lysine 92. *Protein Science.* 10, 1130-6.

Lazar, C., Gatto, L., Ferro, M., Bruley, C., Burger, T. (2016) Accounting for the multiple natures of missing values in label-free quantitative proteomics data sets to compare imputation strategies. *Journal of Proteome Research.* 15, 116-25

Lean, M. E.. (1989). Brown adipose tissue in humans. *The Proceedings of the Nutrition Society*. 48(2), 243–257.

Lee, P., Smith, S., Linderman, J., Courville, A. B., Brychta, R. J., Dieckmann, W., Werner, C. D., Chen, K. Y., & Celi, F. S. (2014). Temperature-acclimated brown adipose tissue modulates insulin sensitivity in humans. *Diabetes*. 63(11), 3686–3698.

Létoquart, J., Huvelle, E., Wacheul, L., Bourgeois, G., Zorbas, C., Graille, M., Heurgué-Hamard, V., Lafontaine, D. L. (2014) Structural and functional studies of Bud23-Trm112 reveal 18S rRNA N7-G1575 methylation occurs on late 40S precursor ribosomes. *Proceedings of the National Academy of Sciences of the United States of America.* 111, E5518-26.

Li, B., Carey, M., Workman, J. L. (2007) The role of chromatin during transcription. *Cell.* 128, 707-19.

Li, E. (2002) Chromatin modification and epigenetic reprogramming in mammalian development. *Nature Reviews Genetics.* 3, 662–73.

Li, F., Wang, X., Capasso, J. M., Gerdes, A. M. (1996) Rapid transition of cardiac myocytes from hyperplasia to hypertrophy during postnatal development. *Journal of Molecular and Cellular Cardiology.* 28, 1737-46.

Li, H. B., Tong, J., Zhu, S., Batista, P. J., Duffy, E. E., Zhao, J., Bailis, W., Cao, G., Kroehling, L., Chen, Y., Wang, G., Broughton, J. P., Chen, Y. G., Kluger, Y., Simon, M. D., Chang, H. Y., Yin, Z., Flavell, R. A. (2017) m6A mRNA methylation controls T cell homeostasis by targeting the IL-7/STAT5/SOCS pathways. *Nature*. 548, 338-42.

Liu, J., Yue, Y., Han, D., Wang, X., Fu, Y., Zhang, L., Jia, G., Yu, M., Lu, Z., Deng, X., Dai, Q., Chen, W., He, C. (2014) A METTL3-METTL14 complex mediates mammalian nuclear RNA N6-adenosine methylation. *Nature Chemical Biology.* 10, 93-5.

Liu, J., Zhu, Y., Luo, G. Z., Wang, X., Yue, Y., Wang, X., Zong, X., Chen, K., Yin, H., Fu, Y., Han, D., Wang, Y., Chen, D., He, C. (2016) Abundant DNA 6mA methylation during early embryogenesis of zebrafish and pig. *Nature Communications.* 7, 13052.

Liu, R. J., Long, T., Li, J., Li, H., & Wang, E. D. (2017). Structural basis for substrate binding and catalytic mechanism of a human RNA:m5C methyltransferase NSun6. *Nucleic Acids Research*. 45(11), 6684–6697.

Lövgren, J. M., Wikström, P. M. (2001) The rlmB gene is essential for formation of Gm2251 in 23S rRNA but not for ribosome maturation in Escherichia coli. *Journal of Bacteriology.* 183, 6957-60.

Manning, G., Plowman, G. D., Hunter, T., Sudarsanam, S. (2002) Evolution of protein kinase signaling from yeast to man. *Trends in Biochemical Sciences. Sci.* 27, 514-20.

Martin, J. L., McMillan, F. M. (2002) SAM (dependent) I AM: the S-adenosylmethionine-dependent methyltransferase fold. *Current Opinion in Structural Biology.* 12, 783-93.

Mazauric, M. H., Dirick, L., Purushothaman, S. K., Björk, G. R., Lapeyre, B. (2010) Trm112p is a 15-kDa zinc finger protein essential for the activity of two tRNA and one protein methyltransferases in yeast. *Journal of Biological Chemistry.* 285, 18505-15.

Mazur, P. K., Reynoird, N., Khatri, P., Jansen, P. W., Wilkinson, A. W., Liu, S., Barbash, O., Van Aller, G. S., Huddleston, M., Dhanak, D., Tummino, P. J., Kruger, R. G., Garcia, B. A., Butte, A. J., Vermeulen, M., Sage, J., Gozani, O. (2014) SMYD3 links lysine methylation of MAP3K2 to Ras-driven cancer. *Nature.* 510, 283-7.

Meyer, K. D., Saletore, Y., Zumbo, P., Elemento, O., Mason, C. E., Jaffrey, S. R. (2012) Comprehensive analysis of mRNA methylation reveals enrichment in 3' UTRs and near stop codons. *Cell.* 149, 1635-46.

Mi, H., Huang, X., Muruganujan, A., Tang, H., Mills, C., Kang, D., Thomas, P. D. (2017) PANTHER version 11: expanded annotation data from Gene Ontology and Reactome pathways, and data analysis tool enhancements. *Nucleic Acids Research.* 45, D183-9.

Michel, G., Sauvé, V., Larocque, R., Li, Y., Matte, A., Cygler, M. (2002) The structure of the RlmB 23S rRNA methyltransferase reveals a new methyltransferase fold with a unique knot. *Structure.* 10, 1303-15.

Mills, E. L., Pierce, K. A., Jedrychowski, M. P., Garrity, R., Winther, S., Vidoni, S., Yoneshiro, T., Spinelli, J. B., Lu, G. Z., Kazak, L., Banks, A. S., Haigis, M. C., Kajimura, S., Murphy, M. P., Gygi, S. P., Clish, C. B., Chouchani, E. T. (2018). Accumulation of succinate controls activation of adipose tissue thermogenesis. *Nature*. 560(7716), 102–106.

Miranda-Morales, E., Meier, K., Sandoval-Carrillo, A., Salas-Pacheco, J., Vázquez-Cárdenas, P., Arias-Carrión, O. (2017) Implications of DNA methylation in Parkinson's disease. *Frontiers in Molecular Neuroscience.* 10, 225.

Mohn, F., Weber, M., Rebhan, M., Roloff, T. C., Richter, J., Stadler, M. B., Bibel, M., Schubeler, D. (2008) Lineage-specific polycomb targets and de novo DNA methylation define restriction and potential of neuronal progenitors. *Molecular Cell.* 30, 755-66.

Mollova, M., Bersell, K., Walsh, S. Savla, J., Das, L. T., Park, S., Silberstein, L. E., dos Remedios, C. G., Graham, D., Colan, S., Kühn, B. (2013) Cardiomyocyte proliferation contributes to heart growth in young humans. *Proceedings of the National Academy of Sciences of the United States of America.* 110, 1446-1451.

Morgan, H. D., Santos, F., Green K., Dean, W., Reik, W. (2005) Epigenetic reprogramming in mammals. *Human Molecular Genetics.* 14, R47-58.

Morita, M., Gravel, S. P., Chénard, V., Sikström, K., Zheng, L., Alain, T., Gandin, V., Avizonis, D., Arguello, M., Zakaria, C., McLaughlan, S., Nouet, Y. Pause, A., Pollak, M., Gottlieb, E., Larsson, O., St-Pierre, J., Topisirovic, I., Sonenberg, N. (2013) mTORC1 controls mitochondrial activity and bioegenesis through 4E-BP-dependent translational regulation. *Cell Metabolism.* 19, 698-711.

Morris, C. A., Demsey, S. A., Leonard, C. O., Dilts, C., Blackburn, B. L. (1988) Natural history of Williams syndrome: physical characteristics. *The Journal of Pediatrics.* 113, 318-26.

Mullineux, S. T., Lafontaine, D. L. (2012) Mapping the cleavage sites on mammalian pre-rRNAs: where do we stand? *Biochimie.* 94, 1521-32.

Muto, A., Hoshino, H., Madisen, L., Yanai, N., Obinata, M., Karasuyama, H., Hayashi, N., Nakauchi, H., Yamamoto, M., Groudine, M., Igarashi, K. (1998) Identification of Bach2 as a B-cell-specific partner for small maf proteins that negatively regulate the immunoglobulin heavy chain gene 3' enhancer. *The EMBO Journal.* 17, 5734-43.

Nakanishi, S., Lee, J. S., Gardner, K. E., Gardner, J. M., Takahashi, Y. H., Chandrasekharan, M. B., Sun, Z. W., Osley, M. A., Strahl, B.D., Jaspersen, S. L., Shilatifard, A. (2009) Histone H2BK123 monoubiquitination is the critical determinant for H3K4 and H3K79 trimethylation by COMPASS and Dot1. *Journal of Cell Biology.* 186, 371-7.

Nakazawa, Y., Arai, H., Fujita, N. (2011) The novel metastasis promoter Merm1/Wbscr22 enhances tumor cell survival in the vasculature by suppressing Zac1/p53-dependent apoptosis. *Cancer Research.* 71, 1146-55.

Nash, P., Tang, X., Orlicky, S., Chen, Q., Gertler, F. B., Mendenhall, M. D., Sicheri, F., Pawson, T., Tyers, M. (2001) Multisite phosphorylation of a CDK inhibitor sets a threshold for the onset of DNA replication. *Nature*. 414, 514-21.

Nawrocki, A. R., Scherer, P. E. (2004) The delicate balance between fat and muscle: adipokines in metabolic disease and musculoskeletal inflammation. *Current Opinion in Pharmacology*. 4(3), 281–289.

Nedergaard, J., Bengtsson, T., Cannon, B. (2007) Unexpected evidence for active brown adipose tissue in adult humans. *American Journal of Physiology-Endocrinology and Metabolism.* 293(2).

Ng, H. H., Feng, Q., Wang, H., Erdjument-Bromage, H., Tempst, P., Zhang, Y., Struhl, K. (2002) Lysine methylation within the globular domain of histone H3 by Dot1 is important for telomeric silencing and Sir protein association. *Genes & Development.* 16, 1518-27.

Niu, Y., Xia, Y., Wang, S., Li, J., Niu, C., Li, X., Zhao, Y., Xiong, H., Li, Z., Lou, H., Cao, Q. (2013) A prototypic lysine methyltransferase 4 from archaea with degenerate sequence specificity methylates chromatin proteins Sul7d and Cren7 in different patterns. *Journal of Biological Chemistry.* 288, 13728-40.

Noonan, E. J., Place, R. F., Pookot, D., Basak, S., Whitson, J. M., Hirata, H., Giardina, C., Dahiya, R. (2009) miR-449a targets HDAC-1 and induces growth arrest in prostate cancer. *Oncogene.* 28, 1714-24.

Nureki, O., Watanabe, K., Fukai, S., Ishii, R., Endo, Y., Hori, H., Yokoyama, S. (2004) Deep knot structure for construction of active site and cofactor binding site of tRNA modification enzyme. *Structure.* 13, 593-602.

Ohtake, F., Saeki, Y., Sakamoto, K. Ohtake, K., Nishikawa, H., Tsuchiya, H., Ohta, T., Tanaka, K., Kanno, J. (2015) Ubiquitin acetylation inhibits polyubiquitin chain elongation. *EMBO Reports.* 16, 192-201.

Ohtsubo, K., Marth, J. (2006) Glycosylation in cellular mechanisms of health and disease. *Cell.* 126, 855-67.

Okano, M., Bell, D. W., Haber, D. A., Li, E. (1999) DNA methyltransferases Dnmt3a and Dnmt3b are essential for de novo methylation and mammalian development. *Cell.* 99, 147-57.

Oudhoff, M. J., Freeman, S. A., Couzens, A. L., Antignano, F., Kuznetsova, E., Min, P. H., Northrop, J. P., Lehnertz, B., Barsyte-Lovejoy, D., Vedadi, M., Arrowsmith, C. H., Nishina, H., Gold, M. R., Rossi, F. M., Gingras, A. C., Zaph, C. (2013) Control of the hippo pathway by Set7-dependent methylation of Yap. *Developmental Cell.* 26, 188-94.

Ouellet, V., Labbé, S. M., Blondin, D. P., Phoenix, S., Guérin, B., Haman, F., Turcotte, E. E., Richard, D., & Carpentier, A. C. (2012). Brown adipose tissue oxidative metabolism contributes to energy expenditure during acute cold exposure in humans. *The Journal of Clinical Investigation*. 122(2), 545–552.

Õunap, K., Käsper, L., Kurg, A., Kurg, R. (2013) The human WBSCR22 protein is involved in the biogenesis of the 40S ribosomal subunits in mammalian cells. *PLOS One.* 8, e75686.

Pei, J., Kim, B. H., Grishin, N. V. (2008). PROMALS3D: a tool for multiple protein sequence and structure alignments. *Nucleic Acids Research*. 36(7), 2295–2300.

Pertschy, B., Schneider, C., Gnädig, M., Schäfer, T., Tollervey, D., Hurt, E. (2009) RNA helicase Prp43 and its co-factor Pfa1 promote 20 to 18 S rRNA processing catalyzed by the endonuclease Nob1. *Journal of Biological Chemistry*. 284, 35079-91.

Petersen, C., Nielsen, M. D., Andersen, E. S., Basse, A. L., Isidor, M.S., Markussen, L.K., Viuff, B.M., Lambert, I.H., Hansen, J.B., Pedersen, S.F. (2017) MCT1 and MCT4 expression and lactate flux activity increase during white and brown adipogenesis and impact adipocyte metabolism. *Scientific Reports*. *7*(1).

Petrossian, T., Clarke, S. (2009) Bioinformatic identification of novel methyltransferases. *Epigenomics.* 1, 163-75.

Piekna-Przybylska, D., Decatur, W. A., Fournier, M. J. (2008) The 3D rRNA modification maps database: with interactive tools for ribosome analysis. *Nucleic Acids Research.* 26, D178-83.

Piquereau, J., Novotova, M., Fortin, D., Garnier, A., Ventura-Clapier, R., Veksler, R., Joubert, F. (2010) Postnatal development of mouse heart:

formation of energetic microdomains. *The Journal of Physiology.* 588: 2443-54.

Pober, B. R. (2010) Williams-Beuren syndrome. *The New England Journal of Medicine.* 362, 239-52.

Pokholok, D. K., Harbison, C. T., Levine, S., Cole, M., Hannett, N. M., Lee, T. I., Bell, G. W., Walker, K., Rolfe, P. A., Herbolsheimer, E., Zeitlinger, J., Lewitter, F., Gifford, D. K., Young, R. A. (2005) Genome-wide map of nucleosome acetylation and methylation in yeast. *Cell.* 122, 517-27.

Polikanov, Y. S., Melnikov, S. V, Söll, D., & Steitz, T. A. (2015). Structural insights into the role of rRNA modifications in protein synthesis and ribosome assembly. *Nature Structural & Molecular Biology*. 22(4), 342.

Portela, A., Esteller, M. (2010) Epigenetic modifications and human disease. *Nature Biotechnology.* 28, 1057-68.

Prabakaran, S., Lippens, G., Steen, H., Gunawardena, J. (2012) Post-translational modification: nature's escape from genetic imprisonment and the basis for dynamic information encoding. *Wiley Interdisciplinary Reviews: Systems Biology and Medicine.* 4, 565-83.

Preti, M., O'Donohue, M. F., Montel-Lehry, N., Bortolin-Cavaillé, M. L., Choesmel, V., Gleizes, P. E. (2013) Gradual processing of the ITS1 from the nucleolus to the cytoplasm during synthesis of the human 18S rRNA. *Nucleic Acids Research.* 41, 4709-23.

Pruijn, G. J. (2015) Citrullination and carbamylation in the pathophysiology of rheumatoid arthritis. *Frontiers in Immunology.* 6, 192.

Purushothaman, S. K., Bujnicki, J. M., Grosjean, H., Lapeyre, B. (2005) Trm11p and Trm112p are both required for the formation of 2-methylguanosine at position 10 in yeast tRNA. *Molecular and Cellular Biology.* 25, 4359-70.

R Core Team (2021). R: A language and environment for statistical computing. R Foundation for Statistical Computing, Vienna, Austria. URL https://www.R-project.org

Ramsahoye, B. H., Biniszkiewicz, D., Lyko, F., Clark, V., Bird, A. P., Jaenisch, R. (2000) Non-CpG methylation is prevalent in embryonic stem cells and may be mediated by DNA methyltransferase 3a. *Proceedings of the National Academy of Sciences of the United States of America.* 97, 5237-42.

Rape, M. (2018) Ubiquitylation at the crossroads of development and disease. *Nature Reviews Molecular Cell Biology.* 19, 59-70.

Reik, W. (2007) Stability and flexibility of epigenetic gene regulation in mammalian development. *Nature*. 447, 425-32.

Richon, V. M., Johnston, D., Sneeringer, C. J., Jin, L., Majer, C. R., Elliston, K., Jerva, L. F., Scott, M. P., Copeland, R. A. (2011) Chemogenetic analysis of human protein methyltransferases. *Chemical Biology & Drug Design.* 78, 199-210.

Ringrose, L., Paro, R. (2004) Epigenetic regulation of cellular memory by the Polycomb and Trithorax group proteins. *Annual Review of Genetics.* 38, 413–43.

Robertson, K. D. (2005) DNA methylation and human disease. *Nature Reviews Genetics.* 6, 597-610.

Robinson, M. D., McCarthy, D. J., Smyth, G. K. (2010) edgeR: a Bioconductor package for differential expression analysis of digital gene expression data. *Bioinformatics*. 26(1):139-40.

Rolfe, D. F., Brown, G. C. (1997) Cellular energy utilization and molecular origin of standard metabolic rate in mammals. *Physiological reviews*. [Online] 77 (3), 731–758.

Roy, S., Musselman, C. A., Kachirskaia, I., Hayashi, R., Glass, K. C., Nix, J. C., Gozani, O., Appella, E., Kutateladze, T. G. (2010) Structural insight into p53 recognition by the 53BP1 tandem Tudor domain. *Journal of Molecular Biology.* 398, 489-96.

Rudolph, A. M., Heymann, M. A. (1967) The circulation of the fetus in utero. Methods for studying distribution of blood flow, cardiac output and organ blood flow. *Circulation Research.* 21, 163-84.

Sado, T., Fenner, M. H., Tan, S. S., Tam, P., Shioda, T., Li, E. (2000) X inactivation in the mouse embryo deficient for Dnmt1: distinct effect of hypomethylation on imprinted and random X inactivation. *Developmental Biology.* 15, 294-303.

Saggerson, E. D., McAllister, T. W., Baht, H. S. (1988). Lipogenesis in rat brown adipocytes. Effects of insulin and noradrenaline, contributions from glucose and lactate as precursors and comparisons with white adipocytes. *The Biochemical Journal*. 251(3), 701–709.

Sakata, S. F., Shelly, L. L., Ruppert, S., Schutz, G., Chou, J. Y. (1993) Cloning and expression of murine S-adenosylmethionine synthetase. *Journal of Biological Chemistry.* 268, 13978-86.

Sanchez-Gurmaches, J., Tang, Y., Jespersen, N. Z., Wallace, M., Martinez Calejman, C., Gujja, S., Li, H., Edwards, Y. J. K., Wolfrum, C., Metallo, C. M., Nielsen, S., Scheele, C., Guertin, D. A. (2018). Brown fat AKT2 is a cold-induced kinase that stimulates ChREBP-mediated de novo lipogenesis to optimize fuel storage and thermogenesis. *Cell Metabolism*. 27(1), 195-209.e6.

Sánchez-Romero, M. A., Cota, I., Casadesús, J. (2015) DNA methylation in bacteria: from the methyl group to the methylome. *Current Opinion in Microbiology.* 25, 9-16.

Schindelin, J., Arganda-Carreras, I., Frise, E., Kaynig, V., Longair, M., Pietzsch, T., Preibisch, S., Rueden, C., Saalfeld, S., Schmid, B., Tinevez, J., White, D., Hartenstein, V., Eliceiri, K., Tomancak, P., Cardona, A. (2012) Fiji: an open-source platform for biological-image analysis. *Nature Methods.* 9, 676-682.

Sears, I. B., MacGinnitie, M. A., Kovacs, L. G., & Graves, R. A. (1996). Differentiation-dependent expression of the brown adipocyte uncoupling protein gene: regulation by peroxisome proliferator-activated receptor gamma. *Molecular and Cellular Biology*. 16(7), 3410–3419.

Shannon, P., Markiel, A., Ozier, O., Baliga, N. S., Wang, J. T., Ramage, D., Amin, N., Schwikowski, B., Ideker, T. (2003) Cytoscape: a software environment for integrated models of biomolecular interaction networks. *Genome Research.* 13, 2498-504.

Shi, X., Kachirskaia, I., Yamaguchi, H., West, L. E., Wen, H., Wang, E. W., Dutta, S., Appella, E., Gozani, O. (2007) Modulation of p53 function by SET8-mediated methylation at lysine 382. *Molecular Cell.* 27, 636-46.

Shi, Y. (2007) Histone lysine demethylases: emerging roles in development, physiology and disease. *Nature Reviews Genetics.* 8, 829-33.

Shi, Y., Lan, F., Matson, C., Mulligan, P., Whetstine, J. R., Cole, P. A., Casero, R. A., Shi, Y. (2004) Histone demethylation mediated by the nuclear amine oxidase homolog LSD1. *Cell.* 119, 941-53.

Shimizu, I., Aprahamian, T., Kikuchi, R., Shimizu, A., Papanicolaou, K. N., MacLauchlan, S., Maruyama, S., Walsh, K. (2014). Vascular rarefaction mediates whitening of brown fat in obesity. *The Journal of Clinical Investigation*. 124(5), 2099–2112.

Shin, A. N., Han, L., Dasgupta, C., Huang, L., Yang, S., Zhang, L. (2018) SIRT1 increases cardiomyocytes binucleation in the heart development. *Oncotarget.* 9, 7996-8010.

Sloan, K., Knox, A., Wells, G., Schneider, C. (2018) Interactions and activities of factors involved in the late stages of human 18S rRNA maturation. *RNA Biology*. 16, 196-210.

Smith, B. C., Denu, J. M. (2008) Chemical mechanisms of histone lysine and arginine modifications. *Biochimica et Biophysica Acta.* 1789, 45-57.

Spåhr, H., Habermann, B., Gustafsson, C. M., Larsson, N.-G., & Hallberg, B. M. (2012). Structure of the human MTERF4–NSUN4 protein complex that regulates mitochondrial ribosome biogenesis. *Proceedings of the National*

Academy of Sciences of the United States of America. 109(38), 15253–15258.

Straussman, R., Nejman, D., Roberts, D., Steinfeld, I., Blum, B., Benvenisty, N., Simon, I., Yakhini, Z., Cedar, H. (2009) Developmental programming of CpG island methylation profiles in the human genome. *Nature Structural & Molecular Biology.* 16, 564-71.

Steinberg, S., Cedergren, R. (1995) A correlation between N2-dimethylguanosine presence and alternate tRNA conformers. *RNA*. 1, 886-91.

Sun, J. T., Yang, K., Lu, L., Zhu, Z. B., Zhu, J. Z., Ni, J. W., Han, H., Chen, N., Zhang, R. Y. (2016) Increased carbamylation level of HDL in end-stage renal disease: carbamylated-HDL attenuated endothelial cell function. *The American Journal of Physiology-Renal Physiology.* 310, F511-7.

Sun, L., Wang, M., Lv, Z., Yang, N., Liu, Y., Bao, S., Gong, W., & Xu, R.-M. (2011). Structural insights into protein arginine symmetric dimethylation by PRMT5. *Proceedings of the National Academy of Sciences of the United States of America*. *108*(51), 20538–20543.

Szklarczyk, D., Gable, A., Lyon, D., Junge, A., Wyder, S., Huerta-Cepas, J., Simonovic, M., Doncheva, N., Morris, J., Bork, P., Jensen, L., von Mering, C. (2018) STRING v11: protein–protein association networks with increased coverage, supporting functional discovery in genome-wide experimental datasets. *Nucleic Acids Research*. 47, D607–D613.

Tan, C., Virtue, S., Murfitt, S., Roberts, L. D., Phua, Y. H., Dale, M., Griffin, J. L., Tinahones, F., Scherer, P. E., & Vidal-Puig, A. (2015). Adipose tissue fatty acid chain length and mono-unsaturation increases with obesity and insulin resistance. *Scientific Reports. 5*(1), 1–11.

Taoka, M., Nobe, Y., Yamaki, Y., Sato, K., Ishikawa, H., Izumikawa, K., Yamauchi, Y., Hirota, K., Nakayama, H., Takahashi, N., & Isobe, T. (2018). Landscape of the complete RNA chemical modifications in the human 80S ribosome. *Nucleic Acids Research*. 46(18), 9289–9298.

Taoka, M., Nobe, Y., Yamaki, Y., Yamauchi, Y., Ishikawa, H., Takahashi, N., Nakayama, H., & Isobe, T. (2016). The complete chemical structure of *Saccharomyces cerevisiae* rRNA: partial pseudouridylation of U2345 in 25S rRNA by snoRNA snR9. *Nucleic Acids Research*. 44(18), 8951–8961.

Tchernof, A., Bélanger, C., Morisset, A., Richard, C., Mailloux, J., Laberge, P., Dupont, P. (2006) Regional differences in adipose tissue metabolism in women: minor effect of obesity and body fat distribution. *Diabetes*. 55(5):1353-60

Tchkonia, T., Lenburg, M., Thomou, T., Giorgadze, N., Frampton, G., Pirtskhalava, T., Cartwright, A., Cartwright, M., Flanagan, J., Karagiannides, I., Gerry, N., Forse, R. Tchoukalova, Y., Jensen, M., Pothoulakis, C., Kirkland,

J. (2007) Identification of depot-specific human fat cell progenitors through distinct expression profiles and developmental gene patterns. *American Journal of Physiology-Endocrinology and Metabolism.* 292, E298-307.

Tkaczuk, K. L., Dunin-Horkawicz, S., Purta, E., Bujnicki, J. M. (2007) Structural and evolutionary bioinformatics of the SPOUT superfamily of methyltransferases. *BMC Bioinformatics.* 8, 73.

Tokunaga, F., Sakata, S., Saeki, Y., Satomi, Y., Kirisako, T., Kamei, K., Nakagawa, T., Kato, M., Murata, S., Yamaoka, S., Akira, S., Takao, T., Tanaka, K., Iwai, K. (2009) Involvement of linear polyubiquitylation of NEMO in NF-kappaB activation. *Nature Cell Biology.* 11, 123-32.

Toma-Fukai, S., Kim, J. D., Park, K. E., Kuwabara, N., Shimizu, N., Krayukhina, E., Uchiyama, S., Fukamizu, A., & Shimizu, T. (2016). Novel helical assembly in arginine methyltransferase 8. *Journal of Molecular Biology*. 428(6), 1197–1208.

Trievel, R. C., Beach, B. M., Dirk, L. M., Houtz, R. L., Hurley, J. H. (2002) Structure and catalytic mechanism of a SET domain protein methyltransferase. *Cell.* 111, 91-103.

Tu, B. P, McKnight, S. L. (2009) Evidence of carbon monoxide-mediated phase advancement of the yeast metabolic cycle. *Proceedings of the National Academy of Sciences of the United States of America.* 106, 14293-6.

Tyanova, S., Temu, T., Sinitcyn, P., Carlson, A., Hein, M., Geiger, T., Mann, M., Cox, J. (2016) The Perseus computational platform for comprehensive analysis of (prote)omics data. *Nature Methods*. 13, 731-740.

Ubersax, J. A., Ferrell, J. E. Jr. (2007) Mechanisms of specificity in protein phosphorylation. *Nature Reviews Molecular Cell Biology.* 8, 530-41.

Valekunja, U. K., Edgar, R. S., Oklejewicz, M., van der Horst, G. T., O'Neill, J. S., Tamanini, F., Turner, D. J., Reddy, A. B. (2013) Histone methyltransferase MLL3 contributes to genome-scale circadian transcription. *Proceedings of the National Academy of Sciences of the United States of America.* 110, 1554-9.

van de Weijer, T., Sparks, L. M., Phielix, E., Meex, R. C., Herpen, N. A. van, Hesselink, M. K. C., Schrauwen, P., & Schrauwen-Hinderling, V. B. (2013). Relationships between mitochondrial function and metabolic flexibility in type 2 diabetes mellitus. *PLOS ONE*, 8(2), e51648.

van Marken Lichtenbelt, W., Schrauwen, P. (2011) Implications of nonshivering thermogenesis for energy balance regulation in humans. *The American Journal of Physiology - Regulatory, Integrative and Comparative Physiology.* 301(2):R285-96.

van Marken Lichtenbelt, W., Vanhommerig, J., Smulders, N., Drossaerts, J., Kemerink, G., Bouvy, N., Schrauwen, P. (2009). Cold-activated brown

adipose tissue in healthy men. *The New England Journal of Medicine*. 360(15), 1500–1508.

Varambally, S., Cao, Q., Mani, R. S., Shankar, S., Wang, X., Ateeg, B., Laxman, B., Cao, X., Jing, X., Ramnarayanan, K., Brenner, J. C., Yu, J., Kim, J. H., Han, B., Tan, P., Kumar-Sinha, C., Lonigro, R. J., Palanisamy, N., Maher, C. A., Chinnaiyan, A. M. (2008) Genomic loss of microRNA-101 leads to overexpression of histone methyltransferase EZH2 in cancer. *Science.* 322, 1695-9.

Ventura-Clapier, R., Moulin, M., Piquereau, J., Lemaire, C., Mericskay, M., Veksler, V., & Garnier, A. (2017). Mitochondria: a central target for sex differences in pathologies. *Clinical Science*. 131(9), 803–822.

Virtanen, K., Lidell, M., Orava, J., Heglind, M., Westergren, R., Niemi, T., Taittonen, M., Laine, J., Savisto, N., Enerbäck, Nuutila, P. (2009). Functional brown adipose tissue in healthy adults. *The New England Journal of Medicine*. 360(15), 1518–1525.

Waddington, C. H. (1956) The genetic assimilation of the bithorax phenotype. *Evolution.* 10, 1-13.

Walport, L. J., Hopkinson, R. J., Chowdhury, R., Schiller, R., Ge, W., Kawamura, A., Schofield, C. J. (2016) Arginine demethylation is catalysed by a subset of JmjC histone lysine demethylases. *Nature Communications.* 23, 11974.

Wang, H., Cao, R., Xia, L., Erdjument-Bromage, H., Borchers, C., Tempst, P., Zhang, Y. (2001a) Purification and functional characterization of a histone H3-lysine 4-specific methyltransferase. *Molecular Cell.* 8, 1207-17.

Wang, H., Huang, Z. Q., Xia, L., Feng, Q., Erdjument-Bromage, H., Strahl, B. D., Briggs, S. D., Allis, C. D., Wong, J., Tempst, P., Zhang, Y. (2001) Methylation of histone H4 at arginine 3 facilitating transcriptional activation by nuclear hormone receptor. *Science*. 293, 853-7.

Wang, J., Alexander, P., Wu, L., Hammer, R., Cleaver, O., McKnight, S. L. (2009) Dependence of mouse embryonic stem cells on threonine catabolism. *Science*. 325, 435-9.

Wang, Y.C., Peterson, S. E., Loring, J. F. (2014) Protein post-translational modifications and regulation of pluripotency in human stem cells. *Cell Research.* 24, 143-60

Warshaw, J. B. (1969) Cellular energy metabolism during fetal development. I. Oxidative phosphorylation in the fetal heart. *Journal of Cell Biology.* 41, 651-7.

Waterborg, J. H. (2002) Dynamics of histone acetylation in vivo. A function for acetylation turnover? *Biochemistry and Cell Biology.* 80, 363-78.

Weinstock, P. H., Levak-Frank, S., Hudgins, L. C., Radner, H., Friedman, J. M., Zechner, R., Breslow, J. L. (1997) Lipoprotein lipase controls fatty acid entry into adipose tissue, but fat mass is preserved by endogenous synthesis in mice deficient in adipose tissue lipoprotein lipase. *Proceedings of the National Academy of Sciences of the United States of America*. 94(19), 10261–10266.

Weir, G., Ramage, L. E., Akyol, M., Rhodes, J. K., Kyle, C. J., Fletcher, A. M., Craven, T. H., Wakelin, S. J., Drake, A. J., Gregoriades, M.-L., Ashton, C., Weir, N., van Beek, E. J. R., Karpe, F., Walker, B. R., & Stimson, R. H. (2018). Substantial metabolic activity of human brown adipose tissue during warm conditions and cold-induced lipolysis of local triglycerides. *Cell Metabolism*. 27(6), 1348–1355.

Welcker, M., Singer, J., Loeb, K. R., Grim, J., Bloecher, A., Gurien-West, M., Clurman, B. E., Roberts, J. M. (2003) Multisite phosphorylation by Cdk2 and GSK3 controls cyclin E degradation. *Molecular Cell.* 12, 381-92.

Werner, A., Iwasaki, S., McGourty, C. A., Medina-Ruiz, S., Teerikorpi, N., Fedrigo, I., Ingolia, N. T., Rape, M. (2015) Cell-fate determination by ubiquitin-dependent regulation of translation. *Nature*. 525, 523-7.

Werner, J. C., Sicard, R. E., Schuler, H. G. (1989) Palmitate oxidation by isolated working fetal and newborn pig hearts. *American Journal of Physiology.* 256, E315-21.

White, J., Li, Z., Sardana, R., Bujnicki, J. M., Marcotte, E. M., Johnson, A. W. (2008) Bud23 methylates G1575 of 18S rRNA and is required for efficient nuclear export of pre-40S subunits. *Molecular and Cellular Biology.* 28, 3151-61.

Wickham, H. (2009) Ggplot2: elegant graphics for data analysis. 2nd Edition, Springer, New York.

Wilson, A. S., Power, B. E., Molloy, P. L. (2007) DNA hypomethylation and human diseases. *Biochimica et Biophysica Acta.* 1775, 138-62.

Wiśniewski, J., Hein, M., Cox, J., Mann, M. (2014) A "proteomic ruler" for protein copy number and concentration estimation without spike-in standards. *Molecular & Cellular Proteomics.* 13, 3497-506.

Wu, J., Boström, P., Sparks, L. M., Ye, L., Choi, J. H., Giang, A.-H., Khandekar, M., Nuutila, P., Schaart, G., Huang, K., Tu, H., Lichtenbelt, W. D. van M., Hoeks, J., Enerbäck, S., Schrauwen, P., & Spiegelman, B. M. (2012). Beige adipocytes are a distinct type of thermogenic fat cell in mouse and human. *Cell*, 150(2), 366.

Wu, H., Min, J.R., Zeng, H., Loppnau, P., Sundstrom, M., Arrowsmith, C.H., Edwards, A.M., Bochkarev, A., Plotnikov, A. N. (2006). The crystal structure of human HMT1 hnRNP methyltransferase-like 3 in complex with SAH. *PDB*.

Xu, H. E., Lambert, M. H., Montana, V. G., Parks, D. J., Blanchard, S. G., Brown, P. J., Sternbach, D. D., Lehmann, J. M., Wisely, G. B., Willson, T. M., Kliewer, S. A., Milburn, M. V. (1999) Molecular recognition of fatty acids by peroxisome proliferator-activated receptors. *Molecular Cell.* 3(3):397-403.

Yamauchi, T., Kamon, J., Waki, H., Terauchi, Y., Kubota, N., Hara, K., Mori, Y., Ide, T., Murakami, K., Tsuboyama-Kasaoka, N., Ezaki, O., Akanuma, Y., Gavrilova, O., Vinson, C., Reitman, M. L., Kagechika, H., Shudo, K., Yoda, M., Nakano, Y., Tobe, K., Nagai, R., Kimura, S., Tomita, M., Froguel, P., Kadowaki, T. (2001). The fat-derived hormone adiponectin reverses insulin resistance associated with both lipoatrophy and obesity. *Nature Medicine*. 7(8), 941–946.

Yan, D., Tu, L., Yuan, H., Fang, J., Cheng, L., Zheng, X., Wang, X. (2017) WBSCR22 confers oxaliplatin resistance in human colorectal cancer. *Scientific Reports.* 7, 15443.

Yau, W. W., Singh, B. K., Lesmana, R., Zhou, J., Sinha, R. A., Wong, K. A., Wu, Y., Bay, B.-H., Sugii, S., Sun, L., & Yen, P. M. (2018). Thyroid hormone (T3) stimulates brown adipose tissue activation via mitochondrial biogenesis and MTOR-mediated mitophagy. *Autophagy*. 15(1), 131–150.

Yoneshiro, T., Wang, Q., Tajima, K., Matsushita, M., Maki, H., Igarashi, K., Dai, Z., White, P. J., McGarrah, R. W., Ilkayeva, O. R., Deleye, Y., Oguri, Y., Kuroda, M., Ikeda, K., Li, H., Ueno, A., Ohishi, M., Ishikawa, T., Kim, K., Chen, Y., Sponton, C. H., Pradhan, R. N., Majd, H., Greiner, V. J., Yoneshiro, M., Brown, Z., Chondronikola, M., Takahashi, H., Goto, T., Kawada, T., Sidossis, L., Szoka, F. C., McManus, M. T., Saito, M., Soga, T., Kajimura, S.. (2019). BCAA catabolism in brown fat controls energy homeostasis through SLC25A44. *Nature*. 572(7771), 614–619.

Zemach, A., McDaniel, I. E., Silva, P., Zilberman, D. (2010) Genome-wide evolutionary analysis of eukaryotic DNA methylation. *Science.* 328, 916-9.

Zeng, H., Dong, A., Hutch, A., Seitova, A., Walker, J.R., Bountra, C., Arrowsmith, C.H., Edwards, A.M., Brown, P.J., Wu, H., S. G. C. (SGC). (2017). The crystal structure of human HMT1 hnRNP methyltransferase-like protein 6 in complex with MTLLE1441. *PDB*.

Zhang, X., Yang, Z., Khan, S. I., Horton, J. R., Tamaru, H., Selker, E. U., Cheng, X. (2003) Structural basis for the product specificity of histone lysine methyltransferases. *Molecular Cell*. 12, 177-85.

Zheng, W., Ibáñez, G., Wu, H., Blum, G., Zeng, H., Dong, A., Li, F., Hajian, T., Allali-Hassani, A., Amaya, M. F., Siarheyeva, A., Yu, W., Brown, P. J., Schapira, M., Vedadi, M., Min, J., Luo, M. (2012) Sinefungin derivatives as inhibitors and structure probes of protein lysine methyltransferase SETD2. *Journal of the American Chemical Society.* 134, 18004-14.

Zilberman, D., Gehring, M., Tran, R. K., Ballinger, T., Henikoff, S. (2007) Genome-wide analysis of Arabidopsis thaliana DNA methylation uncovers an interdependence between methylation and transcription. *Nature Genetics.* 39, 61-9.

Zingaretto, M., Crosta, F., Vitali, A., Guerrieri, M., Frontini, A., Cannon, B., Nedergaard, J., Cinti, S. (2009) The presence of UCP1 demonstrates that metabolically active adipose tissue in the neck of adult humans truly represents brown adipose tissue. *The FASEB Journal*. 23(9), 3113–3120.

Zorbas, C., Nicolas, E., Wacheul, L., Huvelle, E., Heurgué-Hamard, V., Lafontaine, D. L. (2015) The human 18S rRNA base methyltransferases DIMT1L and WBSCR22-TRMT112 but not rRNA modification are required for ribosome biogenesis. *Molecular Biology of the Cell.* 26, 2080-95.

Zou, W., Chen, X., Shim, J. H., Huang, Z., Brady, N., Hu, D., Drapp, R., Sigrist, K., Glimcher, L. H., Jones, D. (2011) The E3 ubiquitin ligase Wwp2 regulates craniofacial development through mono-ubiquitylation of Goosecoid. *Nature Cell Biology.* 13, 69-65.